



ARISTOTLE UNIVERSITY OF THESSALONIKI
FACULTY OF SCIENCES - SCHOOL OF GEOLOGY
DEPARTMENT OF METEOROLOGY AND CLIMATOLOGY



IOANNIS A. TEGOULIAS

Physicist - Meteorologist

IMPLEMENTATION OF AN INNOVATIVE METHODOLOGY FOR THE EVALUATION AND
OPTIMIZATION OF THE WRF MODEL FOR THE STUDY OF CONVECTIVE ACTIVITY
IN THESSALY

PhD Thesis

THESSALONIKI
2020



[Page intentionally left blank]



ΑΡΙΣΤΟΤΕΛΕΙΟ ΠΑΝΕΠΙΣΤΗΜΙΟ ΘΕΣΣΑΛΟΝΙΚΗΣ
ΣΧΟΛΗ ΘΕΤΙΚΩΝ ΕΠΙΣΤΗΜΩΝ -ΤΜΗΜΑ ΓΕΩΛΟΓΙΑΣ
ΤΟΜΕΑΣ ΜΕΤΕΩΡΟΛΟΓΙΑΣ ΚΑΙ ΚΛΙΜΑΤΟΛΟΓΙΑΣ



ΙΩΑΝΝΗΣ Α. ΤΕΓΟΥΛΙΑΣ

Φυσικός - Μετεωρολόγος

ΕΦΑΡΜΟΓΗ ΚΑΙΝΟΤΟΜΟΥ ΜΕΘΟΔΟΛΟΓΙΑΣ ΑΞΙΟΛΟΓΗΣΗΣ ΚΑΙ ΒΕΛΤΙΣΤΟΠΟΙΗΣΗΣ
ΤΟΥ ΜΟΝΤΕΛΟΥ WRF ΓΙΑ ΤΗ ΜΕΛΕΤΗ ΚΑΤΑΓΙΔΟΦΟΡΩΝ ΔΡΑΣΤΗΡΙΟΤΗΤΩΝ
ΣΤΗΝ ΠΕΡΙΟΧΗ ΤΗΣ ΘΕΣΣΑΛΙΑΣ

ΔΙΔΑΚΤΟΡΙΚΗ ΔΙΑΤΡΙΒΗ

ΘΕΣΣΑΛΟΝΙΚΗ

2020



(λευκή σελίδα)



ΙΩΑΝΝΗΣ Α. ΤΕΓΟΥΛΙΑΣ
Φυσικός, MSc Μετεωρολόγος

ΕΦΑΡΜΟΓΗ ΚΑΙΝΟΤΟΜΟΥ ΜΕΘΟΔΟΛΟΓΙΑΣ ΑΞΙΟΛΟΓΗΣΗΣ ΚΑΙ ΒΕΛΤΙΣΤΟΠΟΙΗΣΗΣ
ΤΟΥ ΜΟΝΤΕΛΟΥ WRF ΓΙΑ ΤΗ ΜΕΛΕΤΗ ΚΑΤΑΙΓΙΔΟΦΟΡΩΝ ΔΡΑΣΤΗΡΙΟΤΗΤΩΝ ΣΤΗΝ
ΠΕΡΙΟΧΗ ΤΗΣ ΘΕΣΣΑΛΙΑΣ

Εκπονήθηκε στον Τομέα Μετεωρολογίας και Κλιματολογίας του Τμήματος
Γεωλογίας Α.Π.Θ.

Υποβλήθηκε στο Τμήμα Γεωλογίας Α.Π.Θ. τον Μάρτιο του 2020

Ημερομηνία Προφορικής Εξέτασης: 27/04/2020

Αριθμός Παραρτήματος Επιστημονικής Επετηρίδας Τμήματος Γεωλογίας Ν°: 200

Τριμελής Συμβουλευτική Επιτροπή

Θεόδωρος Καρακώστας, Ομότιμος Καθηγητής, Επιβλέπων
Πρόδρομος Ζάνης, Καθηγητής, Μέλος Τριμελούς Συμβουλευτικής Επιτροπής
Ιωάννης Πυθαρούλης, Αναπλ. Καθηγητής, Μέλος Τριμελούς Συμβουλευτικής
Επιτροπής

Εξεταστική Επιτροπή

Θεόδωρος Καρακώστας, Ομότιμος Καθηγητής
Πρόδρομος Ζάνης, Καθηγητής
Ιωάννης Πυθαρούλης, Αναπλ. Καθηγητής
Αριστείδης Μπαρτζώκας, Καθηγητής
Αθανάσιος Αργυρίου, Καθηγητής
Θεόδωρος Μαυρομμάτης, Αναπλ. Καθηγητής
Πετρούλα Λουκά, Επίκουρη Καθηγήτρια



© Ιωάννης Α. Τεγούλιας, Φυσικός, MSc Μετεωρολόγος, 2020

Με επιφύλαξη παντός δικαιώματος.

ΕΦΑΡΜΟΓΗ ΚΑΙΝΟΤΟΜΟΥ ΜΕΘΟΔΟΛΟΓΙΑΣ ΑΞΙΟΛΟΓΗΣΗΣ ΚΑΙ ΒΕΛΤΙΣΤΟΠΟΙΗΣΗΣ ΤΟΥ ΜΟΝΤΕΛΟΥ WRF ΓΙΑ ΤΗ ΜΕΛΕΤΗ ΚΑΤΑΙΓΙΔΟΦΟΡΩΝ ΔΡΑΣΤΗΡΙΟΤΗΤΩΝ ΣΤΗΝ ΠΕΡΙΟΧΗ ΤΗΣ ΘΕΣΣΑΛΙΑΣ. – *Διδακτορική Διατριβή*

© Ioannis A. Tegoulis, Physicist, MSc Meteorologist, 2020

All rights reserved.

IMPLEMENTATION OF AN INNOVATIVE METHODOLOGY FOR THE EVALUATION AND OPTIMIZATION OF THE WRF MODEL FOR THE STUDY OF CONVECTIVE ACTIVITY IN THESSALY. – *Ph.D. Thesis*

Citation:

Τεγούλιας Ι.Α., 2020. Εφαρμογή Καινοτομου Μεθοδολογιας Αξιολογησης και Βελτιστοποιησης του Μοντελου WRF για τη Μελετη Καταιγιδοφορων Δραστηριοτητων στην Περιοχη της Θεσσαλιας. Διδακτορική Διατριβή, Τμήμα Γεωλογίας Α.Π.Θ., Αριθμός Παραρτήματος Επιστημονικής Επετηρίδας Τμ. Γεωλογίας No 200, 160 σελ.

Tegoulis I. A., 2020. Implementation of an innovative methodology for the evaluation and optimization of the WRF model for the study of convective activity in Thessaly. Ph.D. Thesis, School of Geology, Aristotle University of Thessaloniki, Annex Number of Scientific Annals of the School of Geology No 200, 160 pp.

Απαγορεύεται η αντιγραφή, αποθήκευση και διανομή της παρούσας εργασίας, εξ ολοκλήρου ή τμήματος αυτής, για εμπορικό σκοπό. Επιτρέπεται η ανατύπωση, αποθήκευση και διανομή για σκοπό μη κερδοσκοπικό, εκπαιδευτικής ή ερευνητικής φύσης, υπό την προϋπόθεση να αναφέρεται η πηγή προέλευσης και να διατηρείται το παρόν μήνυμα. Ερωτήματα που αφορούν τη χρήση της εργασίας για κερδοσκοπικό σκοπό πρέπει να απευθύνονται προς το συγγραφέα.

Οι απόψεις και τα συμπεράσματα που περιέχονται σε αυτό το έγγραφο εκφράζουν το συγγραφέα και δεν πρέπει να ερμηνευτεί ότι εκφράζουν τις επίσημες θέσεις του Α.Π.Θ.



To my family



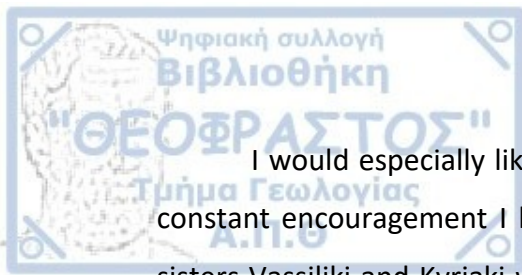
[Page intentionally left blank]



This PhD dissertation has been carried out at the Department of Meteorology and Climatology, Faculty of Sciences, Aristotle University of Thessaloniki.

I would like to thank my supervisor, Emeritus Professor Theodore Karacostas for guiding and supporting me over the years. He has set an example of excellence as a researcher, mentor and instructor. He helped me in bad and good times beyond his supervisor role. I would like to thank my advisory committee members. I am grateful to my friend Ioannis Pytharoulis for his guidance, ideas and support on atmospheric modeling. I am thankful to Prodromos Zanis for his overall support. His scientific paradigm is worth following. I would like to thank the other members of the examination committee, Prof. Aristidis Bartzokas, Prof. Athanasios Argyriou, Assoc. Prof. Theodoros Mavrommatis and Assist. Prof. Petroula Louka for their consideration, ideas and support.

Special thanks goes to my close associates and friends Dimitrios Bampzelis, Stergios Kartsios and Stylianos Kotsopoulos for their full support in the completion of my thesis. Late thanks to Prof. Charalambos Sahsamanoglou who attracted me in the science of Meteorology, to my beloved Prof. Apostolos Flocas who unfortunately wasn't able to see me completing my thesis, and to Prof. Christos Balafoutis for his encouragement during the difficult years. To Prof. Petros Pennas who knew the way to make you love what you do. To Prof. Panayiotis Maheras that took me a lot of time to finally understand. To the rest of the current and former members of the Department of Meteorology and Climatology, with whom I had a fruitful cooperation throughout my long presence in Meteoroskopeio. To my supervisors and colleagues in KEME-ELGA for the facilitations they offered me during the last stages of my work. A particular thanks goes to all of the postgraduate students of the Department throughout the years who, by posing questions to me, gave me the opportunity to widen my knowledge in areas I would never deal with, on my own. A special thanks to all that people who, without knowing it, inspired me with their way to go on with my thesis and finally bring it to an end.



I would especially like to thank my amazing family for the love, support, and constant encouragement I have gotten over the years. My mother Foteini and my sisters Vassiliki and Kyriaki who after the loss of my father Apostolos tried and kept our family united and strong.

This PhD thesis was funded by a 3.5year PhD fellowship from National Scholarship Foundation. Partial funding was provided by the European Union (European Regional Development Fund) and Greek national funds, through the action "COOPERATION 2011: Partnerships of Production and Research Institutions in Focused Research and Technology Sectors" (contract number 11SYN_8_1088 - DAPHNE) in the framework of the operational programme "Competitiveness and Entrepreneurship" and Regions in Transition (OPC II, NSRF 2007-2013).

I thank NCAR, ECMWF and NCEP for providing the WRF-ARW numerical weather prediction model, the operational gridded analyses, and the sea-surface temperature data, respectively. I would like also to thank the Hellenic National Meteorological Service (<http://www.hnms.gr/>) for providing the surface observations and KEME-ELGA for providing radar data. For analysis and visualization purposes, the NCAR Command Language (NCL; v.6.5.0) was utilized. For the statistical evaluation the Model Evaluation Tools (METv6.0) was used. Model Evaluation Tools (MET) was developed at the National Center for Atmospheric Research (NCAR) through grants from the National Science Foundation (NSF), the National Oceanic and Atmospheric Administration (NOAA), the United States Air Force (USAF), and the United States Department of Energy (DOE). NCAR is sponsored by the United States National Science Foundation.



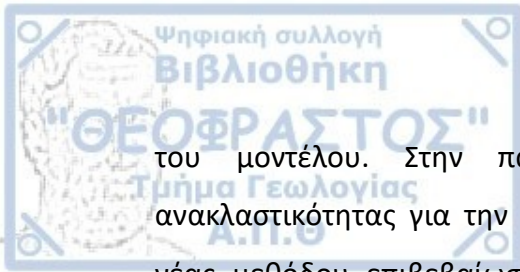
Abstract

The present PhD dissertation investigated the capability of a state of the art numerical prediction model to represent convective activity in the region of Thessaly, Central Greece. The mesoscale meteorological model Weather Research and Forecasting (WRF), was tested in order to discover the optimal configuration able to simulate convective events. An ensemble of twelve different model configurations was put under test, simulating days with high convective activity. The impact of microphysics (MP), cumulus convection (CU) and planetary boundary layer (PBL) schemes was investigated and the best performing combination was chosen. Three MP schemes (Ferrier, WRF single-moment 6-classes, and Goddard), two CU schemes (Kain Fritsch and Betts-Miller-Janjić) and two PBL (Yonsei University and Mellor-Yamada- Janjić) were tested. In the first stage, results of the simulations for seven individual cases were statistically evaluated against surface observations and radar data using classic statistical methods. The best performing setup was chosen and further evaluated in the second stage by widening the experimental sample. Thirty six more cases were selected and classified according to the prevailing synoptic conditions. Statistics were obtained for every synoptic type assuring that the selected setup performs adequately in every case. The final stage involved the application of a novel statistical method for the evaluation of the original ensemble of simulations. The new method belongs to the spatial methods, that do not perform a point to point evaluation, but they rather try to distinguish similarities between the observed and forecast fields. The particular method employed, Method for Object Based Diagnostic Evaluation (MODE), uses objects, discrete entities inside the field, and examines their characteristics. The similarity of the characteristics between the observed and forecast objects, as expressed by the appropriate metrics, provides the performance of the model. In the present study the field of reflectivity was used to derive the objects. The result of this novel method confirmed that the model setup, selected primarily using classic statistical methods has the best performance according to the new method too. This way the WRF-ARW model, with this configuration, can be a useful tool in every situation where a high convective event should be studied employing a numerical weather prediction model.



Περίληψη

Η παρούσα διδακτορική διατριβή διερεύνησε την ικανότητα ενός αριθμητικού μοντέλου πρόγνωσης καιρού στην αναπαράσταση καταιγιδοφόρων δραστηριοτήτων στην περιοχή της Θεσσαλίας. Το μετεωρολογικό μοντέλο μέσης κλίμακας WRF, δοκιμάστηκε προκειμένου να βρεθεί η βέλτιστη διαμόρφωση ικανή να προσομοιώνει την καταιγιδοφόρο δραστηριότητα. Ένα σύνολο δώδεκα διαφορετικών διαμορφώσεων του μοντέλου τέθηκε υπό δοκιμή, προσομοιώνοντας ημέρες με υψηλή καταιγιδοφόρο δραστηριότητα. Εξετάστηκε η επίδραση των σχημάτων μικροφυσικής (MP), ανωμεταφοράς (CU) και πλανητικού οριακού στρώματος (PBL) και επιλέχθηκε ο συνδυασμός με τις καλύτερες επιδόσεις. Χρησιμοποιήθηκαν τρία σχήματα μικροφυσικής (Ferrier, WSM6 και Goddard), δύο σχήματα ανωμεταφοράς (Kain Fritsch και Betts-Miller-Janjic) και δύο σχήματα οριακού στρώματος (Yonsei University και Mellor-Yamada-Janjic). Στο πρώτο στάδιο, τα αποτελέσματα των προσομοιώσεων αξιολογήθηκαν στατιστικά για επτά μεμονωμένες περιπτώσεις χρησιμοποιώντας παρατηρήσεις επιφάνειας και δεδομένα ραντάρ με τη χρήση κλασικών στατιστικών μεθόδων. Η συνδυασμός με τις καλύτερες επιδόσεις επιλέχθηκε και αξιολογήθηκε περαιτέρω στο δεύτερο στάδιο διευρύνοντας το πειραματικό δείγμα. Προστέθηκαν τριάντα έξι περισσότερες περιπτώσεις και ταξινομήθηκαν σύμφωνα με τις επικρατούσες συνοπτικές συνθήκες. Λαμβάνοντας στατιστικά για κάθε συνοπτικό τύπο διασφαλίστηκε ότι ο επιλεγμένος συνδυασμός παράγει ικανοποιητικά αποτελέσματα σε κάθε περίπτωση. Το τελευταίο στάδιο αφορούσε την εφαρμογή μιας νέας στατιστικής μεθόδου για την αξιολόγηση του αρχικού συνόλου προσομοιώσεων. Η νέα μέθοδος ανήκει στις χωρικές μεθόδους, οι οποίες δεν εκτελούν αξιολόγηση σημείο προς σημείο, αλλά προσπαθούν να διακρίνουν τις ομοιότητες μεταξύ των παρατηρούμενων και των προσομοιωμένων πεδίων. Η συγκεκριμένη μέθοδος που χρησιμοποιείται, η Μέθοδος για τη Διαγνωστική Αξιολόγηση Βάσει Αντικειμένων (MODE), χρησιμοποιεί αντικείμενα, διακριτές οντότητες μέσα στο πεδίο, και εξετάζει τα χαρακτηριστικά τους. Η ομοιότητα μεταξύ των παρατηρούμενων και των προσομοιωμένων αντικειμένων, όπως αυτή εκφράζεται χρησιμοποιώντας τις κατάλληλες μετρικές, χαρακτηρίζει την απόδοση



του μοντέλου. Στην παρούσα μελέτη χρησιμοποιήθηκε το πεδίο της ανακλαστικότητας για την εξαγωγή των αντικειμένων. Το αποτέλεσμα αυτής της νέας μεθόδου επιβεβαίωσε ότι η διαμόρφωση του μοντέλου, που επιλέχθηκε αρχικά με κλασσικές στατιστικές μεθόδους, έχει την καλύτερη απόδοση και σύμφωνα με τη νέα μέθοδο. Με αυτό τον τρόπο το μοντέλο WRF-ARW, με τη συγκεκριμένη διαμόρφωση μπορεί να είναι ένα χρήσιμο εργαλείο στη μελέτη καταιγιδοφόρου δραστηριότητας στην περιοχή της Θεσσαλίας.





Table of Contents

Chapter 1 1

Introduction

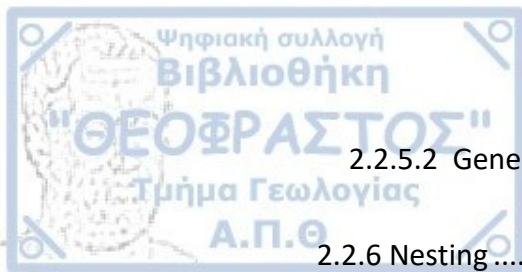
1.1 Numerical Weather Prediction Basics	1
1.2 Aim - Objectives	4
1.3 Thesis Outline.....	5

Chapter 2 7

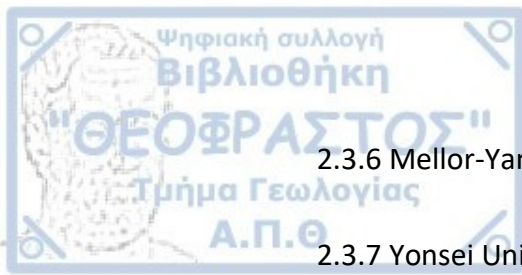
The Weather Research and Forecasting (WRF) Model

Overview and parameterizations used

2.1 Introduction	7
2.2 The ARW Dynamics Solver	9
2.2.1 Governing equations.....	9
2.2.2 Map projections	11
2.2.3 Model discretization	12
2.2.3.1 Temporal discretization	12
2.2.3.2 Spatial discretization	13
2.2.4 Turbulent mixing and model filters	14
2.2.5 Model initialization	14
2.2.5.1 The WRF preprocessing system	15



2.2.5.2 Generation of initial and lateral boundary conditions	16
2.2.6 Nesting	17
2.2.6.1 Nesting options	17
2.2.6.2 Staggering and feedback.....	20
2.2.6.3 Integration sequence	21
2.2.7 The ARW Physics	21
2.2.7.1 Microphysics	22
2.2.7.2 Cumulus parameterization	23
2.2.7.3 Surface Layer.....	23
2.2.7.4 Land surface model.....	24
2.2.7.5 Planetary Boundary Layer.....	24
2.2.7.6 Radiation	25
2.2.7.7 Physics interactions	25
2.3 Cumulus Convection, Microphysics and Planetary Boundary Layer	26
2.3.1 Kain-Fritsch cumulus convection scheme.....	27
2.3.2 Betts-Miller-Janjic cumulus convection scheme	29
2.3.3 Ferrier microphysics scheme	31
2.3.4 WRF Single-Moment 6-class microphysics scheme.....	32
2.3.5 Goddard Cumulus Ensemble microphysics scheme	34

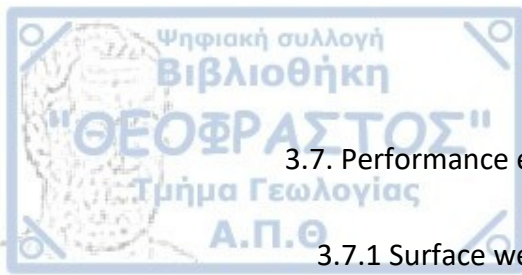


2.3.6 Mellor-Yamada- Janjić boundary layer scheme.....	35
2.3.7 Yonsei University boundary layer scheme.....	37

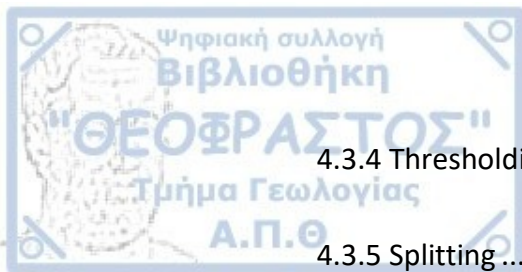
Chapter 3 **39**

Sensitivity studies and model performance

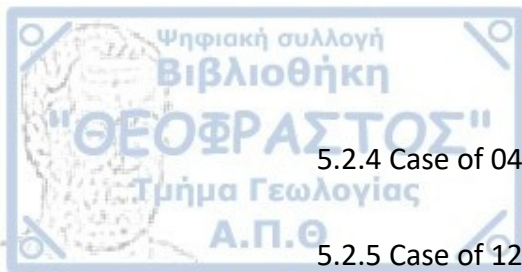
3.1 Introduction	39
3.2 Upper-air synoptic circulation types.....	41
3.3 Case Selection	46
3.4 Numerical Model setup	47
3.5 Verification data: Weather stations, Radar data and TITAN	50
3.6 Sensitivity results	52
3.6.1 Performance at domain D02.....	52
3.6.2 Cloud Characteristics at domain D03.....	56
3.6.2.1 Cloud Height.....	58
3.6.2.2 Maximum Reflectivity	58
3.6.2.3 Cloud Area.....	61
3.6.3 Daily cycle at domain D03.....	61
3.6.3.1 Case of July 20 2010.....	63
3.6.3.2 Case of August 4 2010.....	63
3.6.4 General Evaluation of the sensitivity experiments.....	64



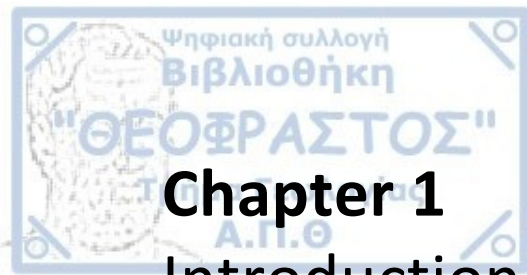
3.7. Performance evaluation of the selected scheme combination.....	65
3.7.1 Surface weather station evaluation.....	65
3.7.2 Characteristics of simulated and measured convective activity	73
3.7.2.1 Maximum reflectivity.....	73
3.7.2.2 Average Storm area	74
3.7.2.3 Cloud Top	77
3.7.3 General Evaluation of the selected setup.....	79
Chapter 4	81
Spatial methods for Numerical Weather Prediction Evaluation	
4.1 Introduction	81
4.2 Description of spatial methods.....	83
4.2.1 Neighborhood approaches	83
4.2.2 Scale Separation/Decomposition.....	83
4.2.3 Feature/Object Methods	84
4.2.4 Field deformation Methods.....	87
4.2.5 Summary characteristics.....	87
4.3 The Method for Object Based Diagnostic Evaluation - MODE.....	88
4.3.1 Objects definition.....	88
4.3.2 Resolving Objects.....	89



4.3.4 Thresholding	91
4.3.5 Splitting	92
4.3.6 Restoring the Data	93
4.3.7 Attributes	93
4.3.7.1 Fitted Attributes.....	94
4.3.7.2 Area Attributes.....	96
4.3.7.3 Distance Attributes	97
4.3.7.4 Intensity Attributes	98
4.3.7.5 Ratio Attributes.....	98
4.3.8 Fuzzy Logic	98
4.3.9 Matching and Merging.....	100
4.3.10 Parameters values selection	101
Chapter 5	103
Application of Method for Object Based Diagnostic Evaluation	
5.1. Introduction	103
5.2 Application for selected cases	108
5.2.1 Case of 19/06/2010	108
5.2.2 Case of 27/06/2010	111
5.2.3 Case of 20/07/2010	114



5.2.4 Case of 04/08/2010	117
5.2.5 Case of 12/09/2010	120
5.2.6 Case of 25/09/2010	123
5.2.7 Agregate statistics for the six days	126
5.3 Discussion.....	128
Chapter 6	131
Summary - Conclusions	



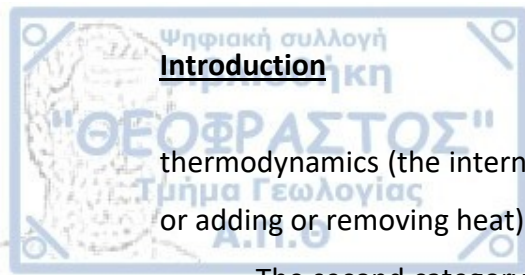
Chapter 1

Introduction

During the previous century the science of Meteorology was greatly benefited from the advances in the Numerical Weather Prediction (NWP) models. Complex physical processes, once inconceivable by the human mind, were able to be simulated by meteorological models and thus became common knowledge for the meteorologists. Various scales phenomena, from planetary waves to microphysical interactions inside the clouds, were described and incorporated into the models. Several scientists and research groups started using the models for operational and research work. This large user's base tried and succeeded to improve the models' prediction ability, through their common scientific effort. The recent advent of powerful computers, providing ample computing power, allowed the analytical representation of more physical problems and the use of grid spacings much smaller than the previous years (Bauer et al., 2015). The arithmetic models hold a prominent position in almost every atmospheric scientist's toolbox using them in a variety of meteorological and climatologically applications. This disperse use raises the necessity of proper adaptation of the used model to the specific needs of every application.

1.1 Numerical Weather Prediction Basics

The numerical representation of dynamical, physical, energy and chemical processes in the atmosphere can be characterized as an atmospheric model. A wide number of equations, corresponding to natural laws governing the atmospheric processes is solved in every model. Those natural laws fall into two categories. The first one includes basic laws of thermodynamics and hydrodynamics. The conservation of mass (mass cannot be created or destroyed), the second law of Newton (the momentum can only be changed by a force) and the first law of



thermodynamics (the internal energy of a system can only change by providing work or adding or removing heat).

The second category includes laws dealing with the absorption and reflection of long wave and short wave radiation, the evaporation and condensation of water, the turbulent transfer of heat and momentum (Jacobson, 2005). All atmospheric processes are represented by differential equation systems, including non linear terms, in the form of partial derivatives in time and space (Pielke, 2013)

$$\frac{\partial u_i}{\partial t} = -u_j \frac{\partial u_i}{\partial x_j} - \frac{1}{\rho} \frac{\partial p}{\partial x_i} - g \delta_{i3} - 2 \varepsilon_{ijk} \Omega_j u_k \quad \text{Newton 2}^{\text{nd}} \text{ law} \quad (1.1)$$

$$\frac{\partial \rho}{\partial t} = -\frac{\partial \rho u_j}{\partial x_j} \quad \text{Conservation of mass} \quad (1.2)$$

$$\frac{\partial \theta}{\partial t} = -u_j \frac{\partial \theta}{\partial x_j} + S_\theta \quad \text{Conservation of heat} \quad (1.3)$$

$$\frac{\partial q_n}{\partial t} = -u_j \frac{\partial q_n}{\partial x_j} + S_{qn} \quad \text{Conservation of water content} \quad (1.4)$$

where

$$\theta = T_v \left(\frac{1000}{p} \right)^{R_d / c_p} \quad \text{Potential temperature} \quad (1.5)$$

$$p = \rho R_d T_v \quad \text{Law of ideal gas} \quad (1.6)$$

$$T_v = T(1 + 0.61 q_3) \quad \text{Virtual temperature} \quad (1.7)$$

Equations 1.1 to 1.7 form a system of non linear partial differential equations with dependent variables ρ (density), θ (heat), T (temperature), T_v (Virtual temperature), p (pressure), u_i (3d velocities), q_n (water mass) and independent variables t (time), x, y, z (space coordinates). The Kronecker's delta is represented by δ_{ij} and the unit antisymmetric tensor by ε_{ijk} . Ω refers to the earth's angular velocity while S_q and S_θ in terms of change of humidity and heat respectively.

The differential equations are solved using numerical methods in a grid of one to three dimensions. Time and space difference techniques are employed in the solution of the above mentioned equations (Pielke, 2013). The common practice is to replace the partial derivatives of the above equations by finite differences.

Bjerknes (1904) while outlined the principle of such a thought, did not prescribe the details of practically realizing it. Lewis Fry Richardson (1922) was the first to put this idea into practice. He portrayed the organization of the “computers” (in the literal form of the word) needed to perform his simulations and found out that “64.000 computers would be needed to race the weather for the whole globe”. His thought inspired many artists to draw sketches picturing this envision (Fig. 1.1). It took him 2 years to perform the calculations and his forecast was a total failure. He predicted a change in pressure of 145hPa in 6 hours. Today, knowing the assumptions he made and what led to this failed forecast we can give him the credit he deserves for his ground breaking effort. In 1949 Charney, using the ENIAC, the first multi-purpose programmable electronic digital computer, performed the first successful “forecast” (Charney et al., 1950). From then on the evolution of numerical

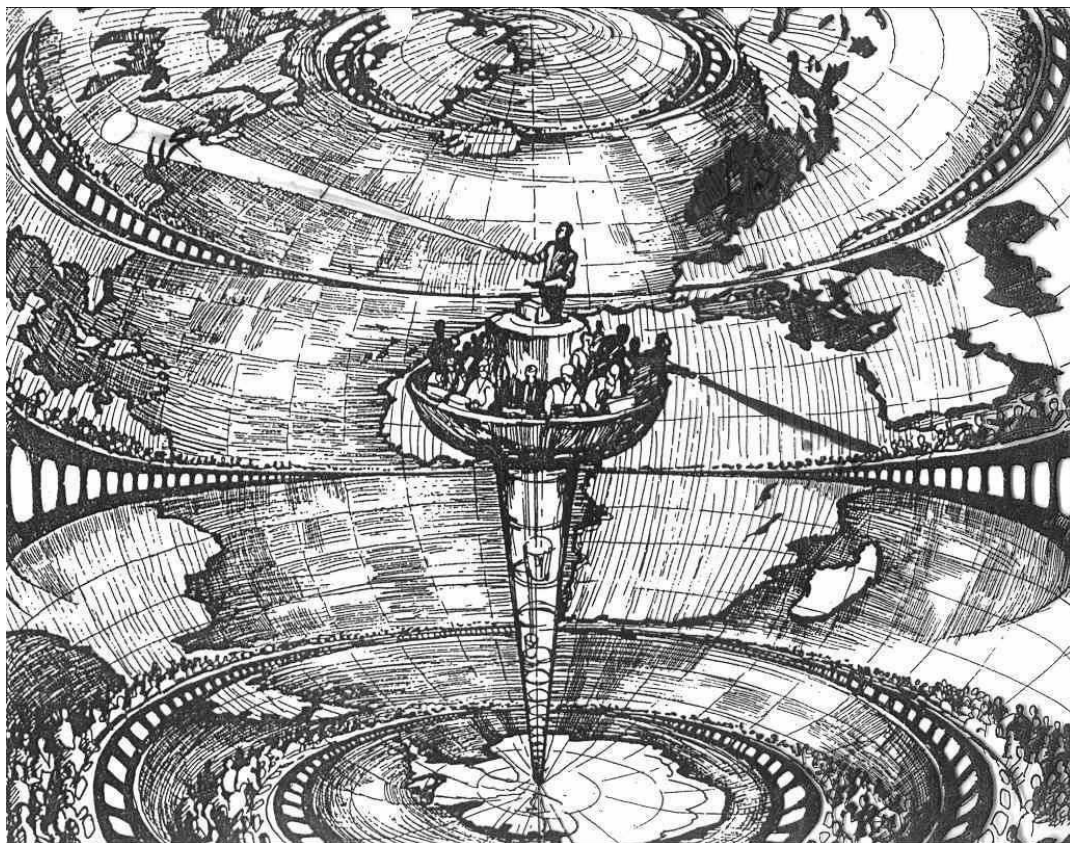
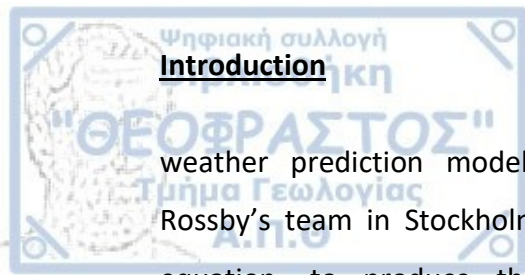


Figure 1.1. An artist’s impression of Richardson’s Forecast Factory (A. Lannerbäck, Dagens Nyheter, September 22, 1984, Stockholm). Adopted from Lynch (2006).



weather prediction models was continuous. In September 1954, Carl-Gustav Rossby's team in Stockholm used the Charney's model, based on the barotropic equation, to produce the first operational forecast. Operational numerical forecasting began in the USA in 1955 in the Joint Numerical Weather Prediction Unit a joint effort of the US Air Force, the US Weather Bureau and the US Naval Weather Service. Today every meteorological service in the world makes use of a numerical model for its every day forecasts. Furthermore every organized University Department or Research Center in the area of Meteorology employs such a model for educational purposes.

1.2 Aim - Objectives

The main aim of the current study is to evaluate the performance of the Weather Research and Forecasting (WRF) numerical model and propose the best combination of its parameterizations, which should be used for the forecast of convective events that shall take place in the area of Thessaly, in central Greece. This study was part of the research project named "DAPHNE" aiming to tackle the problem of drought in this area, by examining the possibility of a rain enhancing program through Weather Modification (Karacostas et al., 2015). The scheduling of the flights would require an a priori good knowledge of the possibility of convective activity in the area. A numerical weather prediction model tuned to perform its best obeying to those requirements would be the best tool in this manner.

In order to fulfill this target three subtasks were created.

1. The first task involves the selection of various WRF parameterizations and the realization of simulations in certain days on which the performance of the model will be evaluated.

2. The second task deals with the primary evaluation of the model's performance using traditional statistic measures.

3. The third task intends on re-assessing the model's performance using for the first time in Greece a novel technique belonging to the spatial methods of forecast evaluation.



By carrying out those tasks a valuable and tested tool would then be in the hands of the Weather Modification operators helping them to plan the everyday operations program.

1.3 Thesis Outline

The current thesis is structured in 6 chapters including the current:

Chapter 2 describes the meteorological model WRF that was employed in this study. Dynamical and physical aspects of the model are presented; implementation steps required for the integration of the model are discussed. The microphysics, cumulus convection and boundary layer schemes used in this study are further analyzed.

In Chapter 3 the primary evaluation of the model is performed using weather station and radar data. In the first step a small number of cases is selected and simulations are performed using a large number of parameterization combinations. The best performing setup is selected and further evaluated by adding more simulated cases in the evaluation sample. Another feature is introduced, since the new cases are categorized by the synoptic type that prevailed over the area in each case.

In Chapter 4 the theoretical basis of the novel Method for Object based Diagnostic Evaluation (MODE), belonging to the spatial methods of model evaluation is presented and analyzed.

Chapter 5 hosts the application of the MODE using the radar reflectivity to derive “objects” from both, the radar and the simulations.

Finally, Chapter 6 includes the summary and conclusions of this thesis.





Chapter 2

The Weather Research and Forecasting (WRF) Model Overview and parameterizations used

2.1 Introduction

In the late 1990s five renowned US agencies collaborated with the common goal of developing a next-generation mesoscale forecast and assimilation system. The system ought to be flexible enough to be used for both operational and research applications, with portable code able to run from personal computers to systems counting thousand of processor cores. It had to be modular in such a way that every new scientific knowledge could be incorporated easily into the main core of the model. Appreciating the importance of the initial conditions its creators foresaw the need of being able to ingest every current and future source of observations.

Soon after its public release in 2000 its user's base started to grow rapidly. Today with almost forty thousand registered users in every continent of the earth, WRF is the most extensively used numerical atmospheric model in the world. WRF is used in forecast applications as an operational tool, in long term studies as a climate model (Coppola et al., 2018; Katragkou et al., 2015), in research and education of future meteorologists. Its derivatives, consisting of the main model coupled with another specialized model are used in fire weather modeling, (WRF-Fire, Coen, 2013; Kartsios, 2020), atmospheric chemistry (WRF-Chem, Fast et al., 2006; Grell et al., 2005), Hydrology (WRF-Hydro, Gochis et al., 2015), hurricane studies (Hurricane-WRF, Tallapragada *et al.*, 2014)), idealized simulations and even more. Thousand of scientific papers in peer review journals dilute every part of it, helping in advancing its quality.

A pictorial representation of WRF's principal components is presented in Fig. 2.1. The dynamic solvers, together with the physics packages interfacing with the

The WRF Model - Overview and parameterizations used

solvers, initialization filters, WRF-Var and WRF-Chem are wrapped around by the WRF Software Framework (WFS) that acts as the coordinator of those components.

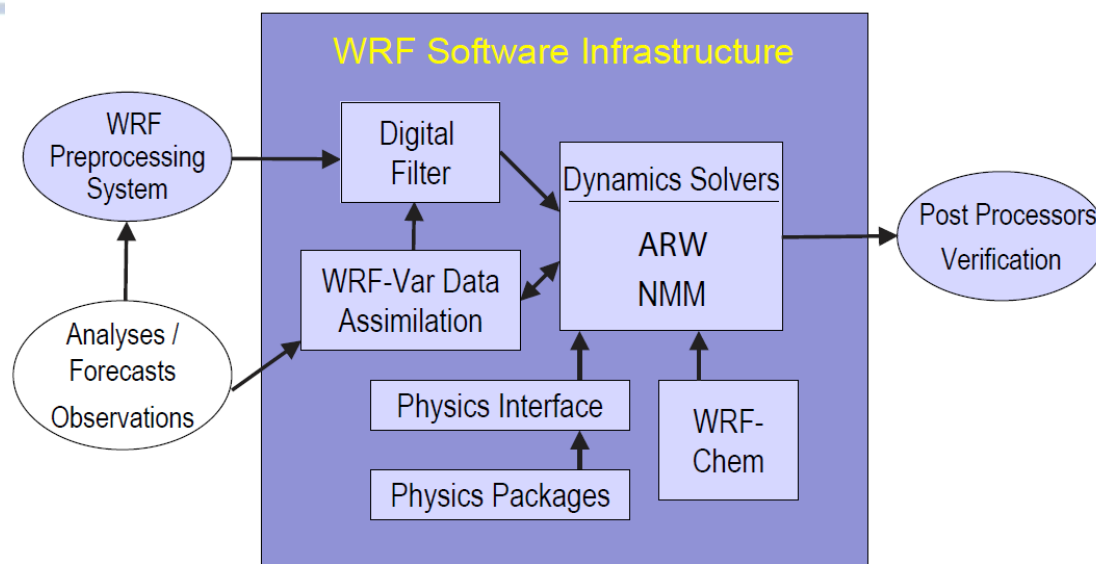


Figure 2.1. WRF system components (adopted from Skamarock *et al.*, 2008).

Up to 2016 two dynamic solvers were developed in parallel. The Advanced Research WRF (ARW) solver maintained by NCAR and the Nonhydrostatic Mesoscale Model (NMM) solver developed at NCEP. From 2016 onward the development of NMM solver stopped due to inadequate funding. In the present study the ARW solver was employed and the description that follows deals with this solver.

The WRF-ARW is routinely integrated in the Department of Meteorology and Climatology (<http://meteo.geo.auth.gr>), School of Geology, Aristotle University of Thessaloniki in Greece, for more than twelve years. Its results are available daily at <http://meteo3.geo.auth.gr/WRF/home.html>.

A large number of scientific contributions have been produced during those years by members of the Department (Bampzelis *et al.*, 2015; Karacostas *et al.*, 2018; Kartsios *et al.*, 2017, 2015, 2014b, 2014a; Katragkou *et al.*, 2015; Krestenitis *et al.*, 2017; Pytharoulis *et al.*, 2015a, 2015b, 2014a, 2018, 2016; Stolaki *et al.*, 2012; Tegoulis *et al.*, 2017, 2014a, 2014b)

2.2 The ARW Dynamics Solver

2.2.1 Governing equations

The nonhydrostatic, compressible Euler equations form the base of the ARW dynamics solver. Variables with conservation properties are used to transform the equations in flux form, following Ooyama's (1990) technique. The terrain-following hydrostatic-pressure vertical coordinate proposed by Laprise (1991) formulate further the equations. The mass vertical coordinate η used in the ARW solver is another form of the σ coordinate used in many hydrostatic models and is defined as

$$\eta = \frac{p_h - p_{ht}}{\mu} \quad (2.1)$$

with

$$\mu = p_{hs} - p_{ht} \quad (2.2)$$

where p_h is the hydrostatic component of the pressure and p_{ht} and p_{hs} are the pressure at top boundaries and surface respectively (Fig. 2.2). From its definition μ represents the mass per unit area at point (x,y) for the entire atmospheric column.

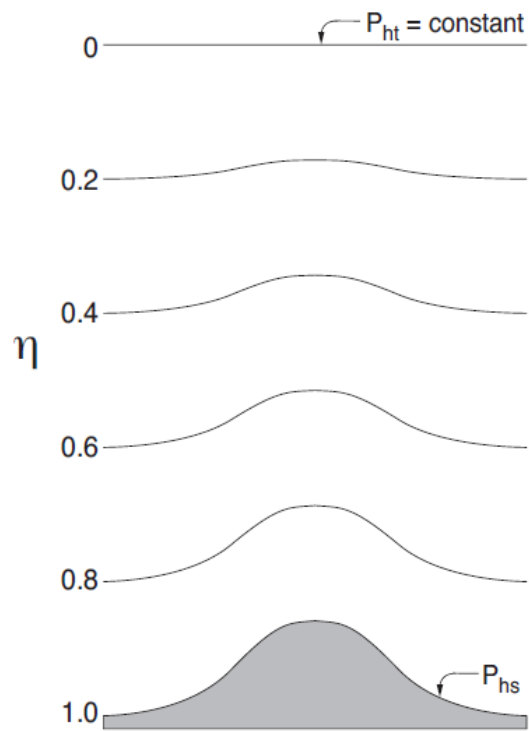


Figure 2.2. ARW η coordinate (adopted from Skamarock *et al.*, 2008).

The WRF Model - Overview and parameterizations used

Prognostic equations cast in conservative form are generally expressed as

$$\frac{d\mu k}{dt} = F_k \quad (2.3)$$

where d/dt is the total derivative and F_k corresponds to sources and sinks related to variable k .

Using the vertical coordinate η from 2.1 we can define the variables in flux form

$$\mathbf{V} = \mu \mathbf{v} = (U, V, W), \quad \Omega = \mu \dot{\eta}, \quad \Theta = \mu \theta \quad (2.4)$$

with $\mathbf{v} = (u, v, w)$ the vector of the two horizontal and one vertical velocities, $\omega = \dot{\eta}$ and θ is the potential temperature.

With the use of the above introduced variables the Euler equations in flux form are now:

$$\frac{\partial U}{\partial t} + (\nabla \cdot \mathbf{V}u) - \frac{\partial}{\partial x}(p\varphi_\eta) + \frac{\partial}{\partial \eta}(p\varphi_x) = F_u \quad (2.5)$$

$$\frac{\partial V}{\partial t} + (\nabla \cdot \mathbf{V}v) - \frac{\partial}{\partial y}(p\varphi_\eta) + \frac{\partial}{\partial \eta}(p\varphi_y) = F_v \quad (2.6)$$

$$\frac{\partial W}{\partial t} + (\nabla \cdot \mathbf{V}w) - g \left(\frac{\partial p}{\partial \eta} - \mu \right) = F_w \quad (2.7)$$

$$\frac{\partial \Theta}{\partial t} + (\nabla \cdot \mathbf{V}\theta) = F_\theta \quad (2.8)$$

$$\frac{\partial \mu}{\partial t} + (\nabla \cdot \mathbf{V}) = 0 \quad (2.9)$$

$$\frac{\partial \varphi}{\partial t} + \mu^{-1} [(\mathbf{V} \cdot \nabla \varphi) - gW] = 0 \quad (2.10)$$

where p is the pressure and $\varphi = gz$ is the geopotential. The terms F_u , F_v , F_w and F_θ account for phenomena related to earth rotation, geometric spherical projections and unresolved subgrid processes. The parameterizations used in the model take care of the effect of these terms on the explicitly resolved variables.

Adding the relation which diagnoses the inverse density α

$$\frac{\partial \varphi}{\partial \eta} = -\alpha \mu \quad (2.11)$$

and the equation of state

$$p = p_0 \left(\frac{R_d \theta}{p_0 \alpha} \right)^\gamma \quad (2.12)$$

creates the full set of equations which are the core of WRF.

The above equations are formulated for dry air. The inclusion of moisture further alters the equations, retaining the conservation equation for dry air and describing the course of each hydrometeor with a prognostic equation of its mixing ratio.

2.2.2 Map projections

Since the earth has a spherical surface and it's easier to present and analyze meteorological variables in a plane, a relation should be found that translates spherical surface points to plane surface points. This translation which is known with the familiar term projection should retain as much as possible of the characteristics of the original surface to the projected surface. WRF supports various projections with the more commonly used in mid-latitudes the Lambert Conformal (LC). The LC projection is isotropic meaning that the ratio of grid spacing in x and y dimension over the earth's surface is the same in the whole domain.

To account for the change between the actual distance between two grid points in earth's surface Δx (Δy) and the distance in the computational grid ΔX (ΔY) the map factor m is introduced

$$\Delta X = m_x \Delta x \Rightarrow \Delta x = \frac{\Delta X}{m_x} \quad (2.13)$$

$$\Delta Y = m_y \Delta y \Rightarrow \Delta y = \frac{\Delta Y}{m_y} \quad (2.14)$$

for x and y distances respectively.

Using the map factors the governing equations are rewritten in projected form. Care is also taken that the right hand side terms of equations 2.5-2.12 take into account curvature and Coriolis effects.

2.2.3 Model discretization

2.2.3.1 Temporal discretization

The physical processes analyzed in the WRF model fall into two separate categories according to their time scale. Low frequency, meteorologically significant and high frequency acoustic modes. Those temporal scales are separated and integrated using two different time steps in order to improve computational efficiency. This time split integration uses a short time step to integrate high frequency modes and a longer time step to integrate low frequency waves. The slow meteorologically significant modes use a third order Runge-Kutta time integration scheme - RK3 (Wicker and Skamarock, 2002) while a smaller time step is employed in high frequency modes to retain numerical stability.

The Runge-Kutta methods, developed in the first years of the twentieth century, include implicit and explicit iterative methods. If the model equations are defined as $\Phi_t = R(\Phi)$ where $\Phi = (U, V, W, \theta, \varphi', \mu', Q_m)$ are the prognostic variables of the model, a solution from $\Phi(t)$ to $\Phi(t+\Delta t)$ with the RK method requires 3 separate steps:

$$\Phi^* = \Phi^t + \frac{\Delta t}{3} R(\Phi^t) \quad (2.15)$$

$$\Phi^{**} = \Phi^t + \frac{\Delta t}{2} R(\Phi^*) \quad (2.16)$$

$$\Phi^{t+\Delta t} = \Phi^t + \Delta t R(\Phi^{**}) \quad (2.17)$$

where Δt is the time step for the low frequency modes (dt in model namelist) and the superscripts denote time levels. The smallest time step for both the low and high frequency modes is set in such a way that no instabilities occur in the integration of the model

In real situations the RK3 time step is governed by the advective Courant number

$$C = U \frac{\Delta t}{\Delta x} \quad (2.18)$$

and the choice of the advection scheme. Wicker and Skamarock (2002) calculated the maximum one dimensional stable values, C_{max} , for the Courant numbers for every combination of time integration scheme and order of discretization of the advection terms. For three-dimensional advection the above calculated Courant numbers must be multiplied by $1/\sqrt{3}$ and the time step must satisfy the following equation

$$\Delta t_{max} < \frac{C_{max}}{\sqrt{3}} \frac{\Delta x}{u_{max}} \quad (2.19)$$

where u_{max} is the maximum velocity likely to occur in the simulation. The most common places for maximum horizontal velocities are the jet stream areas, while high vertical velocities could be reached in convective updrafts. Taking these into account and providing headroom for maximum stability, the proposed time step of integration is three to six times (in seconds) the grid spacing (in kilometers).

2.2.3.2 Spatial discretization

A C staggered grid shown in Figure 2.3, is used for the spatial discretization in the ARW solver. Normal velocities are staggered one-half grid length from the thermodynamic variables. Geopotential ϕ is defined in correspondence of w

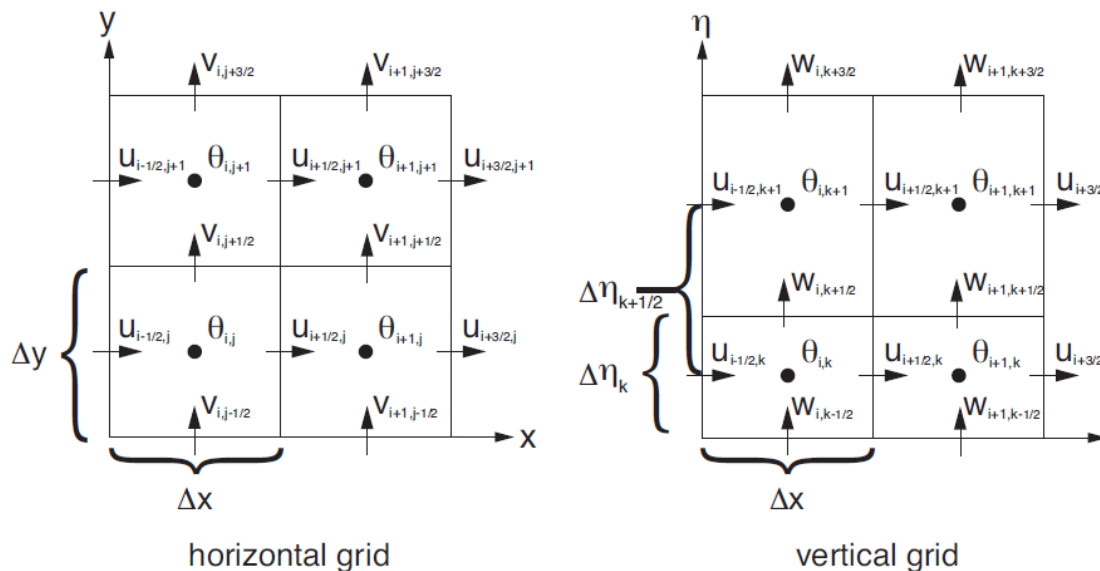


Fig 2.3. Horizontal and vertical grids of the WRF-ARW (adopted from Skamarock *et al.*, 2008)



The WRF Model - Overview and parameterizations used

velocities while the moisture, column mass, diagnostic variables used in the model, pressure p and inverse density α , are computed at points of thermodynamic variables. Staggered grids permit the evaluation of certain partial derivatives over a smaller grid interval, thus increasing artificially the spatial resolution and decreasing truncation errors (Haltiner and Williams, 1980). The vertical discretization is performed either automatically and the user just sets the number of required vertical levels, or setting explicitly every vertical level with the constrain that $\eta=0$ at model top and $\eta=1$ at the surface and there is monotonical increase between the top and the surface.

2.2.4 Turbulent mixing and model filters

Numerous formulations are used in the WRF-ARW solver for turbulent mixing and filtering. A number of these filters are responsible for the elimination of numerical issues. Divergence damping filters acoustic modes from the solution, and polar filtering helps in lowering the time step restriction which is the result of converging grid lines of the latitude-longitude grid. Unresolved subgrid turbulent processes are catered by energy removing filters. These filters are only triggered when no planetary boundary layer scheme is used. When a PBL scheme is used vertical mixing is parameterized within the PBL physics scheme.

2.2.5 Model initialization

In order to perform simulations for real cases, as in the current study, initial conditions and, for any limited area numerical simulation, lateral boundary conditions, are required. The first step in the procedure is to define the integration domain. That includes the location of the domain, the projection to be used, the grid spacing of the parent and the possible nested domains.

Then a dedicated software package, named the WRF pre-processor system (WPS), is used in order to provide the ARW with

- input data on the correct horizontal and vertical staggering,
- hydrostatically balanced reference state and perturbation fields and

- metadata dealing with information, such as the date, grid physical characteristics, and projection details.

2.2.5.1 The WRF preprocessing system

Global data for meteorological fields and geographical data in GRIB (GRIdded Binary) format are the usual input for WPS. The use of WPS transforms them in a form suitable for input to the real data cases interpolation program (REAL), which is then used to generate the initial and boundary conditions for the model.

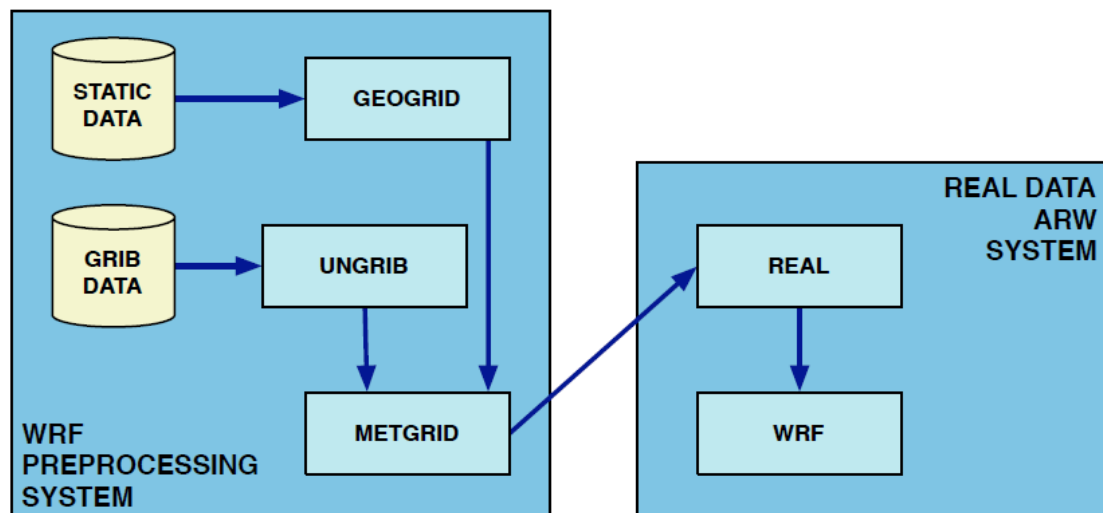


Fig 2.4. Schematic of the WPS package and the data flow between its components (Adopted from Skamarock *et al.*, 2008).

Figure 2.4 depicts the interaction between the WPS components and the data flow in and out of them. Letters in the light blue rectangles indicate program names. GEOGRID is the first program used, responsible for the interpolation of static data (e.g. Coriolis parameter, terrain elevation, land-use type, land/water mask, albedo, map scale factors) into the selected domain. UNGRIB is then used to decode the three dimensional GRIB formatted meteorological data into an intermediate data format. The data outputs of both GEOGRID and UNGRIB are then passed as inputs to the METGRID program. METGRID performs horizontal interpolation into the selected domain in every level (including the surface) of the UNGRIB output data. In this stage the WPS is finished and the WPS output data are ready to be processed by the REAL program. Those data contain among others three-dimensional fields of temperature,

relative humidity and the horizontal components of momentum rotated to the model projection.

2.2.5.2 Generation of initial and lateral boundary conditions

In the next stage the REAL program proceeds in the vertical interpolation and extrapolation of its input data creating the model's initial conditions. It also creates the lateral boundary conditions file for the most coarse/parent domain. Due to their mission they are also called relaxation or nudging boundary conditions. As can be

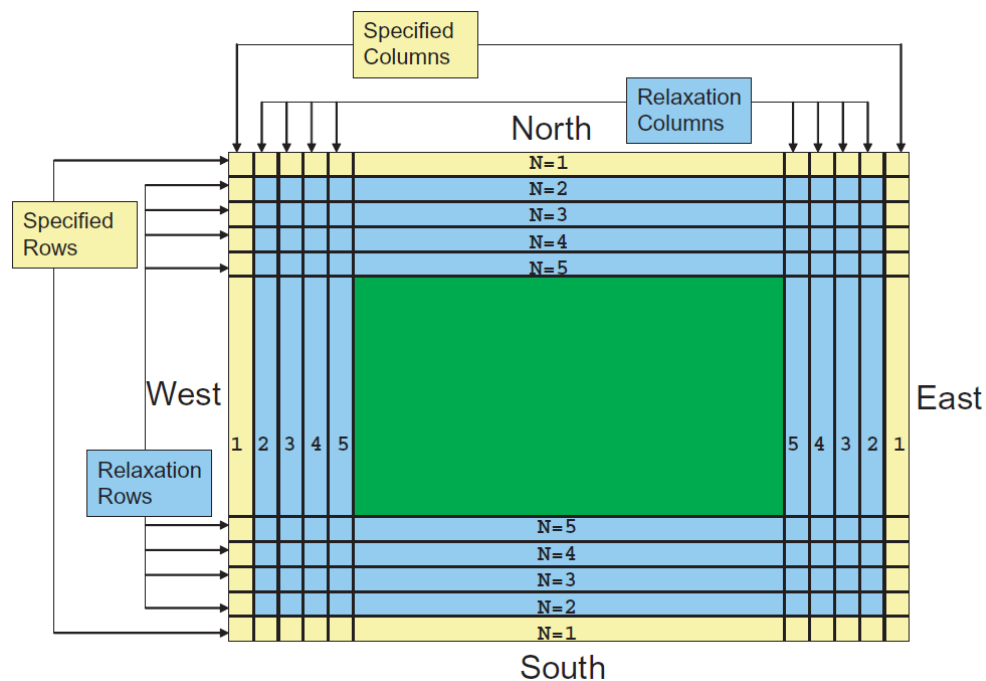


Figure 2.5. Specified and relaxation zones for a grid with a single specified row and column, and four rows and columns for the relaxation zone. These are typical values used for a specified lateral boundary condition for a real-data case (Adopted from Skamarock *et al.*, 2008).

seen in Fig 2.5, WPS creates a specified zone (depicted in yellow) by temporal interpolation of the external forecast or analysis. The width of the zone is user specified but its default value is set to 1. The inner zone (depicted in light blue) is the relaxation zone. A gradual relaxation or nudging of the large-scale forecast to the model happens in this area. The lateral boundary condition file contains values that

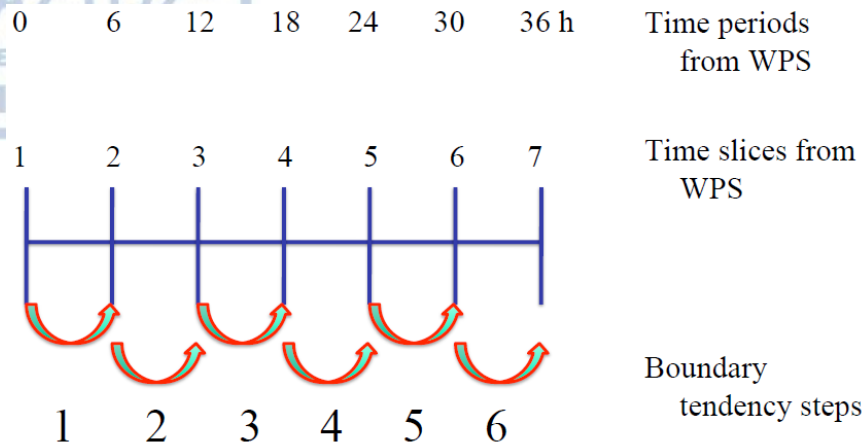


Figure 2.6. Lateral boundary condition times (adopted from Gill, 2015).

are valid at the initial time of the lateral boundary time and tendency terms to get to the next boundary time period. This way the boundary layer file holds one less time period than was processed by WPS (Fig. 2.6)

2.2.6 Nesting

The idea of nesting in numerical prediction models is vital when the study should be focused over a region of interest. The WRF-ARW supports horizontal nesting giving the opportunity to introduce one or more additional grids into the simulation. The nested domains are rectangular and are contained and referred to the coarser (parent) within which they are nested.

2.2.6.1 Nesting options

WRF-ARW gives the options to perform nested simulations using either 1-way nesting or 2-way nesting (Table 2.1). The multiplicity of the way has to do with the interaction of the coarse and fine grid. The common factor between the two types of nesting is that the coarser domain always provides lateral boundary conditions to the finer domain. In 1-way nesting this is the only interaction between the two grids. In a 2-way nesting simulation grids points belonging to the coarse grid, located inside the fine grid, take values from the solution of the fine grid. In this manner there is a 2-way information exchange (coarse domain provides later boundary conditions to

The WRF Model - Overview and parameterizations used

the fine domain, fine domain solutions replace coarse domain solution inside the fine domain) leading to the 2-way naming of the simulation.

Table 2.1. One way and 2 way nesting options in the ARW (Adopted from Skamarock et al., 2008).

1 way ARW Simulation		2 way ARW Simulation
<i>Two consecutive ARW simulations</i>	<i>Concurrent ARW simulation with two domains</i>	<i>Concurrent ARW simulation with two domains</i>
1) Run coarse grid (CG) simulation	1) Both CG and FG simulations run within the same WRF	Both CG and FG simulations run within the same WRF
2) Process CG for initial condition (IC) for fine grid (FG)	2) FG LBC from CG at each coarse time step	2) FG LBC from CG at each coarse time step
3) Process CG for lateral boundary condition (LBC) for FG	3) CG integrates one time step, then the FG integrates up to the same time	3) CG integrates one time step, then the FG integrates up to the same time
4) Run FG simulation		4) Feedback FG to CG

In a nested simulation the fine grid may be initialized in several ways:

- The coarse grid provides both the meteorological and terrestrial grid variables to the fine grid through interpolation
- The fine grid variables are taken from an external file containing meteorological and terrestrial data in high resolution.
- The static data fields are initialized from an external high resolution file while the meteorological fields are interpolated from the coarse grid. The advantage of the fine resolution static fields is obvious in this case. This was the way that the simulations were performed in this study.

For a gradual transition from coarse boundary conditions to local scale modeling, multiple nesting must take place. Dudhia (personal communication) urge the use of intermediate coarse domains to avoid abrupt steps in the nesting. The

coarse domains are computational cheap and provide better relaxation in the meteorology fields.

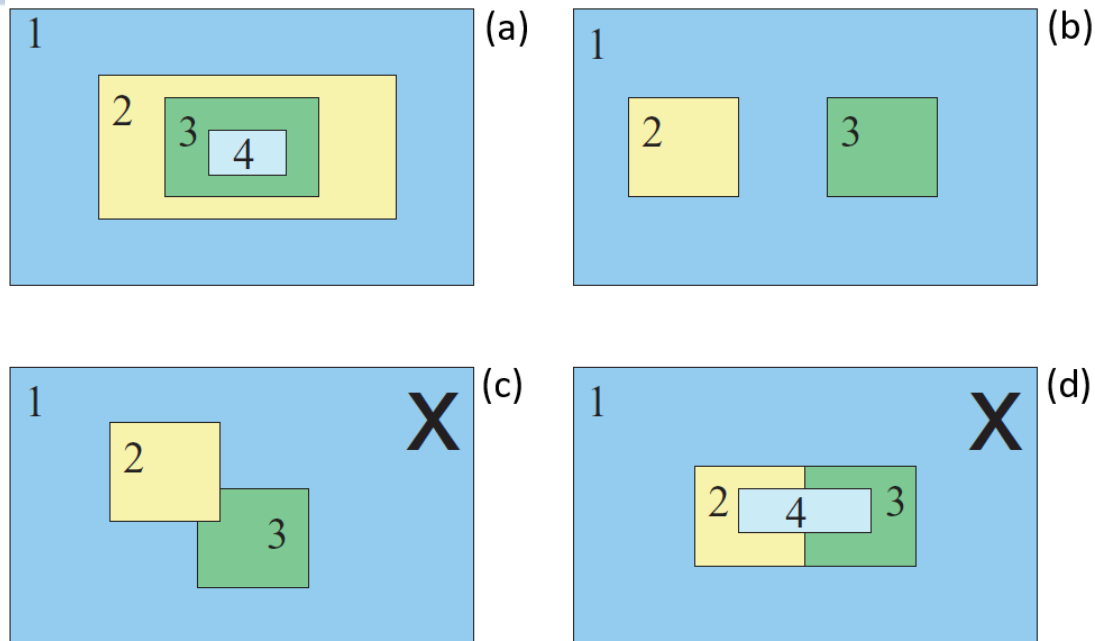


Figure 2.7. Nested grids examples: (a) Telescoping nests, (b) Nested domains on the same level sharing the same parent grid, (c) Overlapping grids: Not acceptable, (d) Fine grid with two parent domains: Not acceptable (Adopted from Skamarock *et al.*, 2008).

The coarse domain in a nested simulation is typically called the *parent* domain while the nested grid is called the *child* grid. When multiple nesting is employed one specific domain may be the child of coarser domain and the parent of a finer domain. Figure 2.7 presents various nest configurations. In Figure 2.7a the most common use of nested grids is presented: a telescopic nest with a depth of four. The coarser domain contains three more levels on nesting. Two or more fine nests may be contained in a parent nest (Fig. 2.7b) provided that the fine nests do not overlap. In this case (Fig. 2.7c) the nesting is not permitted. Finally a fine grid can only have one parent. This is another disallowed case (Fig 2.7d).

The ratio of the grid spacing between the parent and child domains must be an integer. Typical values for the ratio are one to three (1:3) or one to five (1:5). An odd ratio is preferred over an even ratio. This ratio also defines the ratio between the integration time step (dt) of each domain. Same level childs could have different

ratios to the parent domain. In this context the ratio of grid 2 to grid 1 in Fig 2.7b may be 1:5 and the ratio of grid 3 to grid 1 may be 1:3.

2.2.6.2 Staggering and feedback

The grid staggering used by the WRF-ARW is an Arakawa-C type staggering. In this type of staggering the thermodynamic, mass, chemistry and scalar variables are located at the center of the grid and the momentum variables u and v are normal to the respective cells' faces (Fig 2.8). The components of horizontal velocity are averaged values across the respective face of the grid cell. For the variables at mass points their value represents the mean for the whole cell.

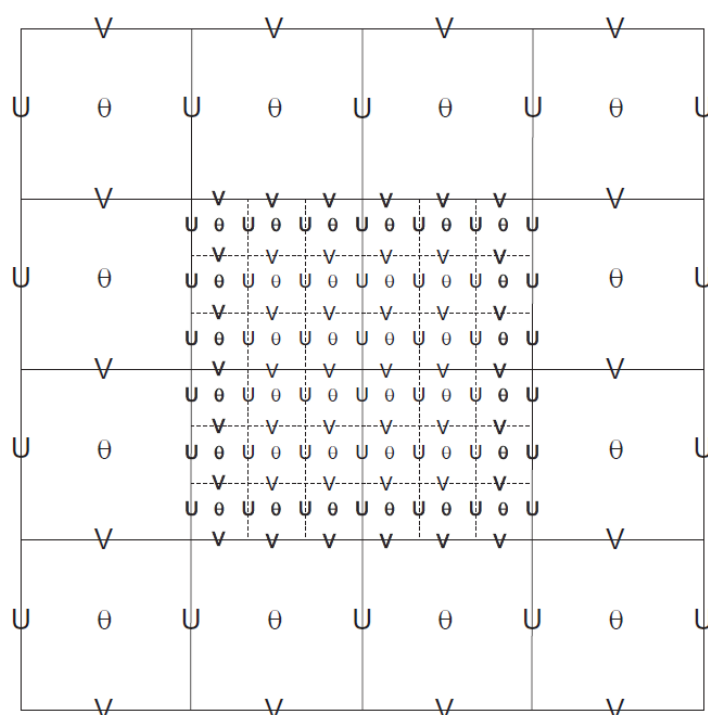


Figure 2.8. Arakawa-C staggering shown part of the coarse grid and an embedded nest domain with a 3:1 grid size ratio. Boundaries of the coarse grid are depicted with solid lines while dashed lines denote fine-grid cells boundaries (Adopted from Skamarock *et al.*, 2008).

As mentioned above odd ratios are preferred when preparing a simulation. That is because in this case the staggering imposes that there is always a coincident point between the coarse grid and the fine grid for both the mass and momentum

points. This is clearly evident in Figure 2.8. The coincident point for mass variables is in the center of the fine grid cell, while for the horizontal momentum this point lies along the grid boundaries.

In order to preserve the mean values of both mass and momentum variables across the nests, feedback mechanisms are employed. Referring to figure 2.8 for mass points the mean of the nine mass points of the fine grid is received by the coarse grid. The mean of the three wind values of the fine grid, along the coarse and fine grid coincident face, are fed to the coarse grid.

2.2.6.3 Integration sequence

The grid's integration is recursive. Upon completion of each grid's time step the existence of a child nest is queried. If the child's nest run/no run flag is high the run continues with calculations in the child nest up to the time that the parent grid has already been integrated. After that the execution continues to the coarse's grid next time step.

2.2.7 The ARW Physics

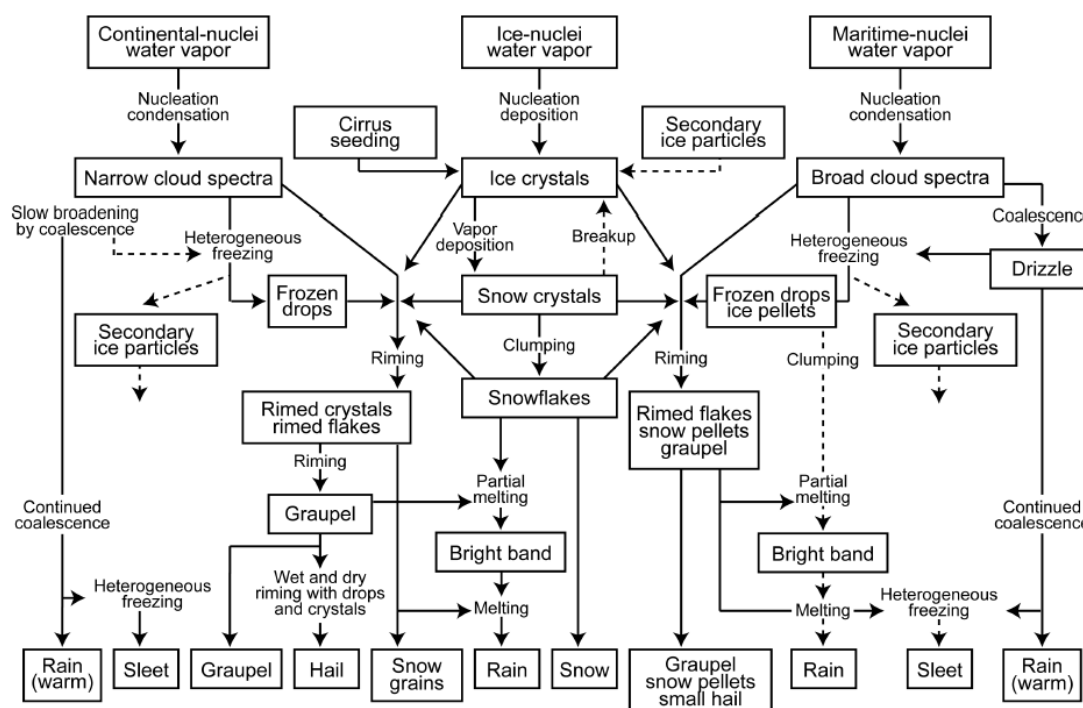
The WRF-ARW has a multitude of physics options which may be combined in order to perform a simulation. The selection of physics used, together with the meteorological and geographical data that will create the initial and boundary conditions, paired with the domain selection, form what is commonly known as the setup of the model for a particular simulation.

The physics categories that the user may choose fall into the following categories: (1) microphysics, (2) cumulus convection parameterization, (3) planetary boundary (and its companion surface layer) parameterizations, (4) land surface physics, and (5) radiation

For each category several choices exist. The total number of setups that may be created by only altering the different physics schemes and their parameters is over two million (Gill, 2015).

A short description of the role of each physics category and the way it is implemented in the model will be presented here while in the next subchapter the microphysics, cumulus and boundary layer schemes used in this study will be presented in more detail.

Microphysics includes explicitly resolved water vapor, cloud and precipitation processes. Figure 2.9 presents the complexity of the interactions analyzed by a complex microphysics scheme. Depending on the scheme complexity a number of two to six separate mixing ratios may be calculated. Cloud water (Q_c), Rain (Q_r), Cloud Ice (Q_i), Snow (Q_s), Graupel (Q_g) and Hail (Q_h). In higher moment schemes apart from the mass variables their corresponding number concentrations are calculated. The microphysics scheme is called by the ARW solver at the end of each



22

model time step to make sure that the saturation balance is accurate for the updated temperature and moisture. For convection allowing simulations, schemes with mixed phase physics are preferable, despite their computational cost.

2.2.7.2 Cumulus parameterization

Cumulus schemes are used for grid columns that contain convective clouds. Their purpose is to account for vertical convective fluxes that are unresolved by the model. The cumulus scheme is responsible for identifying column conditions that will make the scheme to be triggered, i.e. to diagnose when an individual column of air is considered convectively unstable. The triggering of cumulus scheme removes instability from the atmosphere since the subsidence around the triggered column warms and dries its surroundings.

Cumulus convection parameterization is probably needed for simulations with grid spacing larger than 10km since the model cannot resolve the smaller processes. In simulations with grid spacing smaller than 3km the use of cumulus parameterization is generally not proposed, but there are cases where the early triggering of the convection provides better results. The grid spacing from 3 to 10km is the gray zone where the cumulus parameterization may be used in case by case analysis.

2.2.7.3 Surface Layer

The surface layer schemes are employed in the calculation of friction velocities, exchange coefficients and diagnostics of 2m temperature and moisture as well as 10m winds. The planetary boundary layer scheme then uses them to calculate surface stress and the land surface model scheme to deduct surface heat and moisture fluxes. In case of water surfaces the SL scheme calculates the surface fluxes and surface diagnostic fields itself. Not every surface layer scheme can be combined with every planetary boundary layer scheme. The Monin-Obukhov similarity theory (Monin and Obukhov, 1954) is the basis for all surface schemes. The main differences between the schemes are the stability functions and the roughness lengths.

2.2.7.4 Land surface model

The land surface models receive atmospheric information from the SL schemes, radiative forcing from the radiation schemes and precipitation forcing from the microphysics and cumulus convection scheme. Combining those data with

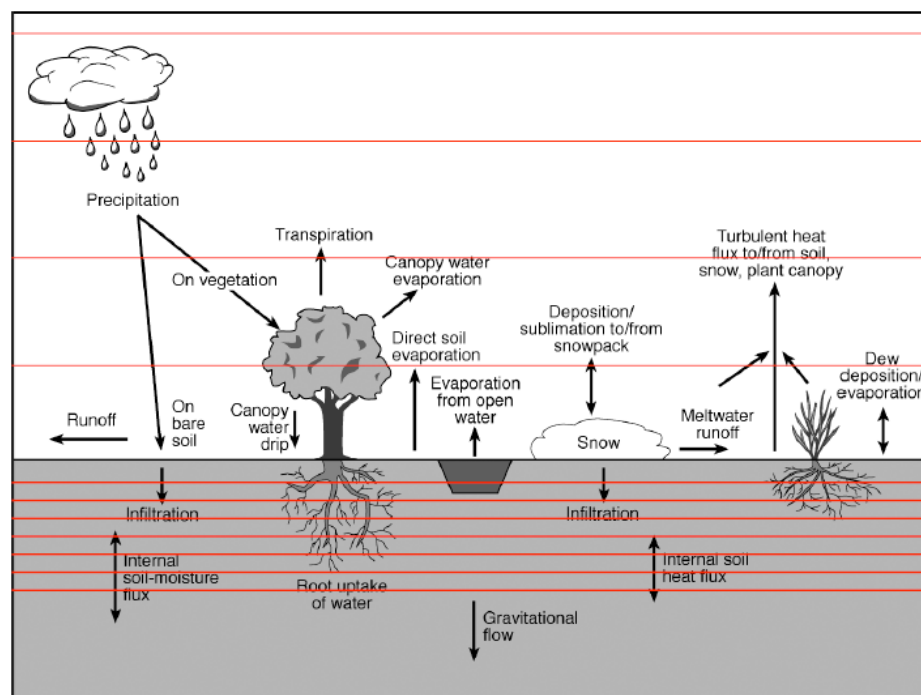


Figure 2.10. Land surface processes (adopted from Dudhia, 2015).

information about land's state variables and land surface properties that are already contained in the model it calculates heat and moisture fluxes over land and sea-ice points. The planetary boundary layer scheme uses those fluxes as bottom boundary conditions for the vertical transport. Figure 2.10 depicts the various processes handled by the land surface scheme.

2.2.7.5 Planetary Boundary Layer

The planetary boundary layer (PBL) schemes takes care of the eddy induced transports, present in the whole atmospheric column, resulting in vertical sub-grid fluxes. The explicit vertical diffusion in the model ceases when a PBL scheme is activated. The surface layer and the land surface schemes feed the PBL scheme with surface fluxes. Atmospheric tendencies of temperature, moisture, including clouds, and horizontal momentum in the entire atmospheric column are calculated by the

PBL scheme which determines the flux profiles in both the stable and the well mixed boundary layer. Resolved eddies and sub-grid scale eddies are considered separate down to a scale of a few hundred meters.

2.2.7.6 Radiation

The radiation schemes regulates the radiative flux divergence induced atmospheric heating, and the downward short-wave and long-wave radiation affecting the ground heat budget. LW radiation comprises of infrared or thermal radiation absorbed and emitted by gases and surfaces. The upward LW emitted radiation is conditioned by the surface emissivity, which is dependent on the land use category and surface temperature. The Sun is the original supplier of the SW radiation which is then absorbed, reflected and scattered in the atmosphere and the surfaces. The surface albedo regulates the reflected SW radiation. Clouds and water content of the atmosphere play an important role in radiation budget together with ozone, carbon dioxide and trace gasses. The available radiation schemes in WRF are column schemes and every grid is integrated independently of its surroundings.

2.2.7.7 Physics interactions

As mentioned earlier, the physics drivers are responsible for the communication between the physics schemes and the ARW solver. To accomplish this task the physics drivers make use of model state variables (e.g., moisture), their related tendencies and surface fluxes.

In Table 2.2 summary of the interactions between the physics of the model is presented. The i symbol corresponds to input of this variable into the respective physics scheme, while the o symbol means that the physics scheme calculates a new value for the selected variable. The surface physics interacts with almost every other scheme providing updates for the land state variables. The same is performed by the microphysics scheme which is executed last in the sequence of integration to provide the updates to the atmospheric state variables. The radiation, cumulus convection and boundary layer schemes are called with a different time step and the tendencies produced are kept constant between successive calls.

The WRF Model - Overview and parameterizations used

Table 2.2. WRF physics interactions (adopted from Skamarock et al., 2008.)

		Radiation	Microphysics	Cumulus	PBL	Surface
Atmospheric	Momentum			i	io	
State or	Potential					
Tendencies	Temperature	io	io	io	io	
	Water Vapor	i	io	io	io	
	Cloud	i	io	o	io	
	Precipitation	i	io	o		
Surface	Longwave Up	i				o
Fluxes	Longwave					
	Down	o				i
	Shortwave					
	Up	i				o
	Shortwave					
	Down	o				i
	Surface					
	Convective			o		i
	Rain					
	Surface					
	Resolved Rain		o			i
	Heat Flux				i	o
	Moisture Flux				i	o
	Surface Stress				i	o

2.3 Cumulus Convection, Microphysics and Planetary Boundary Layer

The numerical weather prediction and climate models represent the effects of the unresolved scale physical processes through parameterizations. These are necessary in order to achieve an accurate modeling of the atmospheric flow. The Weather Research and Forecasting model with the Advanced Research dynamic solver (WRF-ARW) includes a large number of schemes for the parameterization of deep and shallow moist convection, microphysics, planetary boundary layer (PBL) and surface layer processes, shortwave and longwave radiative fluxes, land surface processes etc. (Skamarock et al., 2008; Wang et al., 2014).

The representation of moist convection, microphysics and boundary layer processes is of primary importance, especially during periods favorable for intense convective activity (Yano et al., 2018). The sensitivity of WRF-ARW to the parameterization of these physical processes is investigated in this thesis. The former two kinds of schemes model the sub-grid effects of deep and/or shallow convection and microphysical processes, respectively, and determine the precipitation and the latent heat release. The boundary and surface layer parameterizations calculate the turbulent fluxes and their distribution in the atmospheric column at sub-grid scales (Skamarock et al., 2008). The numerical experiments of this work employ all the twelve (12) combinations of: (a) the Kain-Fritsch and the Betts-Miller-Janjic cumulus schemes, (b) the Eta-Ferrier, the WRF single-moment 6-class and the Goddard microphysics and (c) the Yonsei University and the Mellor-Yamada-Janjic PBL parameterizations with their corresponding surface layers. The main features of these schemes are presented here.

2.3.1 Kain-Fritsch cumulus convection scheme

The Kain-Fritsch cumulus parameterization (KF) was originally developed by Kain and Fritsch (1993, 1990), following the fundamental assumption of Fritsch and Chappell (1980) that convection removes convective available potential energy (CAPE) during a convective time scale. Kain (2004) presents the modifications of the updated form of the scheme, implemented in order to ameliorate its performance in various weather conditions. A CAPE closure is employed using the properties of an entraining air parcel. In convective clouds, the mass flux augmentation is based on the consumption of at least 90% of CAPE. KF provides convective precipitation, tendencies of temperature, specific humidity (parameterizing glaciation processes) and cloud water detrainment to the resolved scales, while it simulates coarsely the transport of momentum (Kain and Fritsch, 1993). A thorough description of this scheme is provided by Mazarakis (2010).

KF is based on “a one-dimensional entraining/detraining plume model” (Kain and Fritsch, 1990) representing entrainment of environmental air and detrainment



The WRF Model - Overview and parameterizations used

of the updraft. Thereby, a 2-way exchange of mass between the environment and the clouds at each model layer is allowed. Mixtures of clear and cloudy air with positive (negative) buoyancy are assumed to rise in the updraft (to detrain into the environment). The entrainment rate of environmental air in the mixing area at the periphery of an updraft is proportional (inversely proportional) to the cloud-base mass flux (radius of the updraft). The net entrainment rate of environmental air is imposed to be at least half of the abovementioned maximum possible environmental air entrainment rate. This modification has prevented the easy activation of deep convection in neutral or slightly unstable conditions and has resulted to a reduction of light precipitation in wide regions and an increase of precipitation maxima, bringing the results closer to observations (Kain, 2004). The cloud radius (1-2 km) is a function of the large-scale convergence through a dependence on the vertical velocity at the lifting condensation level. The introduction of the minimum entrainment rate and the variable cloud radius allow higher (weaker) dilution to be associated with weak (strong) low-level forcing.

Deep or shallow moist convection is triggered when the sum of the temperature of a candidate lower tropospheric air parcel, called the Updraft Source Layer (corresponding to a mixture of a layer at least 60 hPa deep), lifted at its lifting condensation level (LCL) and a temperature perturbation is warmer than the ambient air temperature at the LCL. The temperature perturbation is proportional to the time-averaged grid-scale vertical velocity at the LCL and it is introduced in order to consider the effect of background vertical motion. The parcel ascents taking into account the entrainment, detrainment and water loading. If the cloud-depth exceeds a variable minimum threshold (2-4 km) that depends on the cloud-base temperature, deep precipitating convection will be activated. Otherwise, if none of the candidate lower tropospheric layers qualifies for deep ascent, shallow convection will be triggered. In the latter case, the mass flux at the cloud-base depends on the turbulent kinetic energy below the cloud layer (Kain, 2004).

Downdrafts that transport air with low values of equivalent potential temperature to the lower troposphere, are parameterized by KF. They are considered to develop at a layer 150-200 hPa above the updraft source layer and emanate only from environmental air. In their presence, detrainment initiates below

the top of the updraft source layer. The downdraft may be active until it becomes positively buoyant or it reaches the ground/sea. The strength of its mass flux at the updraft source layer is proportional to the relative humidity deficit at its source layer and on the updraft mass flux at the updraft source layer. The relative humidity of the downdraft is 100% within the cloud, while it decreases linearly (20% per km) below the cloud base.

2.3.2 Betts-Miller-Janjić cumulus convection scheme

The Betts-Miller-Janjić convective parameterization (BMJ) is based on the original Betts-Miller scheme (Betts, 1986; Betts and Miller, 1986) and the important modifications introduced by (Janjić, 1994). Moreover, BMJ has been optimized during its multi-year operational use in NCEP as part of ETA numerical weather prediction model (Janjić, 2000). A detailed description of the updated BMJ parameterization is provided by Baldwin et al. (2002), while a summary of its latest features in WRF-ARW model can be found in Skamarock et al. (2008).

It is a lagged static convective adjustment scheme which has been created to represent directly the atmospheric conditions after deep convective activity, avoiding the uncertainties associated with an indirect determination of them using complex algorithms (Betts and Miller, 1993). The basic idea behind its development came from numerous observations of convective clouds during tropical experiments. They have shown that the state of the atmosphere after deep convection is nearly moist adiabatic, through the sub-cloud layer's equivalent potential temperature. Thereby, such pre-defined "reference" atmospheric profiles are employed in the implementation of the scheme. BMJ provides convective precipitation (associated with deep convection), as well as tendencies of temperature and moisture, but no cloud water to the grid-scale (Baldwin et al., 2002).

In the scheme, moist convection may be activated by the most unstable parcel of air of the lowest 200 hPa of the troposphere, if it is buoyant at least at some vertical levels. Its LCL and the highest model level at which the parcel is



The WRF Model - Overview and parameterizations used

positively buoyant (following moist adiabatic lifting) determine the cloud base and top, respectively.

If the cloud depth is larger than 200 hPa, the scheme checks the activation of deep convection. Reference (first-guess) profiles of temperature and specific humidity are created using pre-existing soundings observed in the vicinity of deep convection (Betts, 1986) together with the “cloud efficiency” parameter (Janjić, 1994). The cloud efficiency is a non-dimensional function of entropy change, mean cloud temperature and precipitation at a single time-step. Janjić, (1994) introduced the application of a range of equilibrium states, generating the first-guess profile as a function of two extreme ones, a moist and a dry profile corresponding to low and high cloud efficiency, respectively. The specific cloud efficiency of the candidate grid-point at each timestep determines its first-guess profiles of temperature and humidity. The latter are adjusted (shifted in a thermodynamic diagram) appropriately in order to achieve conservation of enthalpy in the cloud layer. In this way, the released latent heat will be associated with removal of water vapor from the cloud layer and precipitation at the surface. In this case, deep convection is activated at this grid-point and the model adjusts to the final reference profiles of temperature and humidity at a relaxation time that also depends on the cloud efficiency. Baldwin et al. (2002) showed that the activation of deep convection by the BMJ scheme is strongly dependent on the moisture of the cloud layer. Downdrafts are parameterized at the grid-points with deep convection using a simple scheme (Betts and Miller, 1993). Their source layer is located near 850 hPa and their low-level outflow is considered to take place at the 3 lowest model levels. They are considered to be unsaturated, unless their inflow is saturated.

Shallow non-precipitating convection is evaluated for activation when the modeled cloud depth is smaller than 200 hPa or the reference profiles generated by the abovementioned check of deep convection result to negative precipitation (after the conservation of enthalpy), provided that various additional criteria are met (Baldwin et al., 2002; Janjić, 1994). The cloud base remains the same, but the cloud top is defined as the level with the fastest reduction of relative humidity in a depth of 200 hPa above the base. The temperature and humidity profiles are adjusted to reference profiles that correspond to observed soundings in shallow cumulus or

stratocumulus. The effect of modeled shallow convection is to warm (cool) and dry (moisten) the cloud base (aloft), as in reality.

2.3.3 Ferrier microphysics scheme

Ferrier or “Eta Grid-scale Cloud and Precipitation scheme released in 2001” (EGCP01) is a bulk microphysical parameterization originally implemented in the Meso Eta model of NCEP (Ferrier et al., 2002; Rogers et al., 2001). In bulk schemes, semi-empirical particle size distributions (usually gamma or exponential) are employed to represent the microphysical properties of the clouds (Khain et al., 2015). Ferrier is a good candidate scheme for operational numerical weather prediction systems (e.g. Katsafados et al., 2012; Pytharoulis et al., 2014b), because of its efficacy in various weather conditions (exhibiting a good/satisfactory performance) and its low computational cost (Ferrier et al., 2002). Lookup tables are used in order to store the results of complex calculations (e.g. for precipitation processes) and achieve computational efficiency.

The parameterization predicts the specific humidity of the water vapor and the total condensate, which includes cloud water (small not-falling droplets), cloud ice (small crystals of ice), rain and precipitation ice. The latter comprises of snow, graupel and sleet depending on its density. The scheme determines the fractional contribution of ice condensates (sum of cloud ice and precipitation ice) to the total condensate and that of rain to the liquid hydrometeors (Ferrier et al., 2002). The information of the different hydrometeors is stored in different arrays locally in order to be used only internally by the microphysics scheme. The water vapor and the total condensate are advected, but not the different hydrometeors.

The triggering of cloud condensation depends on a critical value of the relative humidity which is a function of grid spacing and tends to 100% at fine resolutions. In line with other high-resolution models, the condensation algorithm follows Asai (1965).

The precipitation that falls at the surface includes rain, freezing rain and snow (actually precipitation ice). The precipitation fluxes are integrated downwards from

the top of the cloud. They are partitioned in a fraction that remains in the grid-box (proportional to its vertical size) and the rest that fall from the bottom of the grid-box. The microphysical processes that take place in the grid-box modify the specific humidity of precipitation in the grid-box and the precipitation flux at the bottom of the box. The processes of deposition of water vapor and riming of supercooled water droplets are taken into account in the calculation of the density of precipitation ice (Skamarock et al., 2008). Its mean size depends on temperature, in line with the observations of Ryan (1996). The ice crystals of cloud ice are assumed to have a fixed mean radius of 25 μ m. Rain, cloud ice and precipitation ice particles are assumed to be exponentially distributed. The parameterization allows the occurrence of mixed-phase conditions (only ice) at cloudy conditions with air temperatures above (below) -30°C (Skamarock et al., 2008). Various microphysical processes and their latent heating/cooling are represented: vapor condensation, evaporation of cloud, autoconversion to form rain, evaporation of rain, collection of cloud droplets by rain, riming of supercooled water on ice, freezing of supercooled water, ice deposition, ice melting and sublimation, evaporation from wet ice.

2.3.4 WRF Single-Moment 6-class microphysics scheme

WRF Single-Moment 6-class (WSM6) is a bulk microphysical parameterization developed by Hong and Lim (2006). It is a single-moment scheme (like Ferrier), thus, only the mass concentration (specific humidity) of each microphysical species is predicted explicitly. It is an extension of the WRF Single-Moment 3-class (WSM3) and WRF Single-Moment 5-class (WSM5) microphysical schemes (Hong et al., 2004; Hong and Lim, 2006). WSM3 assumes simple-ice processes, forecasting only the three (3) variables of water vapour, cloud water/ice and rain/snow in line with Dudhia (1989) who considered the existence of cloud water and rain (cloud ice and snow) in positive (sub-zero) temperatures. No supercooled water or mixed-phase processes are parameterized. WSM5 upgrades the previous scheme by forecasting separately five (5) species (water vapour, cloud water, rain, cloud ice and snow) and permitting the existence of supercooled water and mixed-phase processes (Hong and Lim 2006).

Comparing the three, WSM6 is more suitable for fine resolution numerical weather prediction (Skamarock et al., 2008; Wang et al., 2014) increasing the rainfall amount and its peak intensity (Hong and Lim, 2006).

WSM6 predicts the specific humidity of six (6) water variables: water vapour, cloud water, rain, cloud ice, snow and graupel. An important improvement relative to WSM5 is the addition of graupel and the parameterization of its related processes according to Rutledge and Hobbs (1984) and Lin et al. (1983). The graupel number concentration, as a function of its diameter, is assumed to follow an exponential distribution. The formula of Locatelli and Hobbs (1974) was adopted for the calculation of the terminal velocity of graupel. The ice microphysics follow the methodology of Hong et al. (2004).

A wide range of microphysical processes are accounted for the production/dissipation of each hydrometeor Hong and Lim (2006). These processes are considered in two different regimes, depending on whether the temperature is warmer or colder than 0°C.

The microphysical processes of cloud water in WSM6 are: (a) aggregation: formation of rain via autoconversion of cloud water, (b) accretion: collection of cloud water by rain, snow and graupel, (c) freezing: both homogeneous and heterogeneous freezing are parameterized, using a critical temperature of -40°C, (d) condensation and evaporation, and (e) melting: cloud ice becomes cloud water via melting.

The parameterized microphysical processes of cloud ice are: (a) initiation of cloud ice crystals: nucleation of ice from water vapor, (b) aggregation: snow formation through autoconversion of cloud ice, (c) accretion: collection of cloud ice by rain, snow and graupel, (d) freezing: both homogeneous and heterogeneous freezing are parameterized with a critical temperature of -40°C, (e) deposition and sublimation, and (f) melting.

The parameterized microphysical processes for the rain are: (a) autoconversion: formation of rain via autoconversion of cloud water, (b) accretion, (c) freezing to form graupel, (d) evaporation and condensation, and (e) melting.

The parameterized microphysical processes of snow are: (a) aggregation: formation of snow because of aggregation of ice crystals, (b) accretion, (c)



The WRF Model - Overview and parameterizations used

deposition/sublimation, (d) melting: the accretion of rain and cloud water by snow enhances its melting, and (e) evaporation of snow that melts.

The parameterized microphysical processes of graupel are: (a) aggregation: formation of graupel through autoconversion of snow, (b) accretion, (c) freezing: rain freezes to form graupel, (d) deposition of water vapor or sublimation, (e) melting of graupel which can increase due to the accretion of cloud water and rain in temperatures above 0°, and (f) evaporation of graupel that melts in a sub-saturated environment (relative to water) with temperature above 0°C.

2.3.5 Goddard Cumulus Ensemble microphysics scheme

Goddard is the microphysical parameterization of the Goddard Cumulus Ensemble model (Tao et al., 2014; Tao and Simpson, 1993). It is a bulk single-moment scheme, suitable for fine resolution weather forecasts (Wang et al., 2014), which has been developed by the Goddard Space Flight Center of NASA.

The scheme is based mainly on the parameterization of Lin et al. (1983) and the upgrades of Rutledge and Hobbs (1984) on the representation of the physics of graupel. In the default version, Goddard includes prognostic equations for the mass content (specific humidity) of six (6) variables: water vapor, cloud water, rain, cloud ice, snow and graupel. Mixed-phase processes are included. The numerous studies performed with this parameterization either using the Goddard Cumulus Ensemble model (e.g. Lang et al., 2007) or by incorporating the scheme in other NWP models (e.g. in MM5 and WRF), have resulted to various modifications/improvements.

The user of WRF-ARW model has the option to integrate the scheme with hail instead of graupel (McCumber et al., 1991; Tao et al., 2003; Wang et al., 2014). The density of graupel is lower than that of hail, while a higher number of small (large) particles are associated with graupel (hail) (Skamarock et al., 2008). Regarding the ice microphysics, there are two additional options to run Goddard only with (a) cloud ice and snow (without graupel/hail) or (b) cloud ice and graupel in extreme conditions (Wang et al., 2014).

The saturation technique has been revised in order to prevent sub-saturation in cloudy grid-points and super-saturation in clear conditions (Tao et al., 2003). The major assumptions of the followed methodology of Tao et al. (1989) are: (a) At temperatures between 0°C and a critical value (between -30°C and -40°C), the saturation mixing ratio of water vapor is a mass weighted value of the saturation mixing ratios over ice and liquid water. Only liquid water (cloud ice) is present at temperatures above 0°C (below the critical value). (b) Under mixed-phase supersaturation, the excess water vapor is condensed/deposited into cloud water/ice. In sub-saturated conditions, the cloud water (ice) evaporates (sublimates). The condensation/deposition and evaporation/sublimation rates are linear functions of the temperature (between 0°C and the critical sub-zero value).

The computation of the transfer rates of the processes that are not related to evaporation, sublimation and melting is based on one thermodynamic state. In this way, the equal treatment of these microphysical processes is ensured (Tao et al., 2003). Otherwise, one microphysical process would be activated first, affecting the temperature and moisture before the activation of another process. An additional improvement is related to the assurance of the water budget in the microphysical computations (Skamarock et al., 2008).

Finally, it is noted that Tao et al. (2003; their Table 3) suggested that tuning is needed for the optimum use of the Goddard parameterization in different environments.

2.3.6 Mellor-Yamada-Janjić boundary layer scheme

The Mellor-Yamada- Janjić turbulence parameterization (hereafter MYJ) was originally developed by Mellor and Yamada (1982) and later was updated and significantly improved for research and operational use by Janjić, 2001, 1994, 1990). It employs a 1.5 order closure (Stensrud, 2011) with local vertical mixing and predicts turbulent kinetic energy. The N-th order closures parameterize the unknown N+1 order correlations in terms of the lower moment predicted terms (Cohen et al., 2015). In the case of non-integer order schemes, e.g. 1.5-order, 1st order moments



The WRF Model - Overview and parameterizations used

are diagnosed for a number of variables and 2nd order moments for others (Tymvios et al., 2018). In a local scheme, the variables at a level are affected only by the ones at adjacent vertical levels.

Janjić (2001) provided a solution to the singularity problem of the original scheme that appeared when the turbulent kinetic energy (TKE) tended to vanish (e.g. Gerrity et al., 1994). Not only the TKE and the master length scale are required to be positive, but also a maximum value is imposed to the master length scale. The master length scale is estimated within the atmospheric boundary layer following Mellor and Yamada (1974), Miyakoda and Sirutis (1977) and Janjić (1994, 1990). Above the boundary layer, it is a percentage of the vertical grid spacing. In MYJ, the lowest model level height at which the production of TKE cannot balance dissipation determines the height of the boundary layer. Janjić (2001) suggested that the upper value of the master length scale must be “proportional to the square root of twice the TKE and a function of large-scale buoyancy and shear” in order to be able to implement this parameterization without a singularity issue in stable and unstable regimes.

The MYJ parameterization is implemented in conjunction with the Eta surface layer scheme which follows the similarity theory (Monin and Obukhov, 1954). During free convection and zero wind speed, the singularity problem is corrected through the methodology of Beljaars (1995), in which part of the surface buoyancy is transformed into kinetic energy. An important feature of the Eta surface layer scheme is the use of a viscous sublayer. This is a near surface layer which is so thin that there is no room for the development of turbulence. Therefore, the momentum, heat and moisture are transported through molecular diffusion. In the presence of the viscous sublayer, the surface energy fluxes are weaker because the molecular diffusion is much weaker than turbulence.

Over the land, the viscous sublayer is parameterized using the formula of Zilitinkevich, (1995) which defines the roughness height of temperature and humidity relative to the one for momentum (Janjić, 2001). Three difference regimes are considered over water grid-points: (a) smooth and transitional, (b) rough and (c) rough with spray (Janjić, 2019, 1994). The depth of the viscous sublayer as well as the roughness length is a function of the friction velocity (Janjić, 1994). Heat and

moisture (momentum) are transported through this sublayer in the first two (one) regimes. Janjic (1994) presented the improvements due to combination of this scheme with updates on the MYJ and BMJ schemes of Eta model, on the precipitation. Pytharoulis, (2008) provided evidence about the effect of this sublayer on the surface fluxes of heat and moisture, as well as on temperature and precipitation over the Mediterranean sea, through numerical experiments with the SKIRON/Eta model.

2.3.7 Yonsei University boundary layer scheme

The turbulence parameterization of the Yonsei University (YSU, Hong et al., 2006) is an upgraded version of the widely used MRF boundary layer scheme (Hong and Pan, 1996) suggesting a revised treatment of the vertical diffusion. It uses a first order closure with nonlocal vertical mixing within the planetary boundary layer (Cohen et al., 2015), that is the variables at a specified level are determined from the ones at multiple (and not just from the adjacent) levels. The local approach is followed above the mixed layer.

YSU parameterization has been developed in order to treat various deficiencies of the MRF, related with too much mixing in windy conditions that results to a drier lower boundary layer, much deeper boundary layer height, weak mixing in a convection-dominated boundary layer, weakening of the convective inhibition that affects the simulated precipitation etc. (Hong et al., 2006). The new scheme treats the entrainment at the top of the boundary layer explicitly, via an additional term for the entrainment flux at the inversion layer. Moreover, it follows the "nonlocal K" approach of Troen and Mahrt (1986) taking into account the countergradient fluxes for potential temperature and momentum, but not for moisture. The large eddies are considered in the turbulence diffusion equations through a gradient correction factor.

In the definition of the boundary layer top, a critical value of zero (0) is assumed for the bulk Richardson number. Thereby, the boundary layer height is found through the investigation of the stability, taking into account the perturbation



The WRF Model - Overview and parameterizations used

in the potential temperature because of the surface buoyancy flux (Hong et al. 2006).

The surface layer is parameterized by the MM5 scheme. It is based on Monin-Obukhov similarity theory (Jiménez et al., 2012) and uses the stability functions of Dyer and Hicks (1970), Paulson (1970) and Webb (1970) in order to calculate the transfer coefficients. Four stability regimes are considered, depending on the bulk Richardson number (Zhang and Anthes, 1982): (a) stable conditions, (b) damped mechanical turbulence, (c) forced convection and (d) free convection. The wind speed at the lowest model level and thus the surface fluxes are enhanced, using a convective velocity (Beljaars, 1995) and a subgrid velocity (Mahrt and Sun, 1995; only for grid spacings greater than 5 km). A viscous sublayer (Carlson and Boland, 1978), up to the height of the roughness length over the water and 0.01 m over land, is employed in the computation of the transfer coefficient for moisture. Over water the roughness length is related to the friction velocity (Skamarock et al., 2008).

Finally, in the default version the drag coefficient is a monotonically increasing function of the wind speed (Green and Zhang, 2013). However, according to Donelan (2004) and Powell et al. (2003) this is not valid over the sea for wind speeds greater than 33 m/s. Moreover, the dissipative heating is not considered in the calculation of the sensible heat fluxes. Two additional options, with modified roughness lengths and exchange coefficients as well as with dissipative heating, are available in WRF-ARW model (Green and Zhang, 2013; Wang et al., 2014). Pytharoulis et al. (2018) investigated the sensitivity of a simulated medicane (that developed in November 2014) on these options.



Chapter 3

Sensitivity studies and model performance

The first statistical evaluation of the numerical studies performed in the framework of the current dissertation is presented in this chapter. The focus is on convective activity simulations with the WRF model. Characteristic cases belonging to various synoptic conditions are examined in order to have a more representative sample of storm days. The study aims on identifying the best performing of the different setups engaged to conduct the simulations without first examining their synoptic forcing. The impact of different WRF physics schemes employed on the simulation of convective activity over Thessaly is assessed. Three microphysics schemes, two planetary boundary layer schemes (with their corresponding surface schemes) and two cumulus convection schemes were tested. After the selection of the most appropriate setup, the performance of the model is assessed again with the inclusion of more test cases and the drawing of conclusions related to the synoptic conditions of each case. Surface weather observations from weather stations, along with radar data, were used for the evaluation. Particular emphasis was given on mean sea level pressure, surface temperature, surface relative humidity and surface winds, when using station data and on geometrical/morphological characteristics of clouds, when using radar data.

3.1 Introduction

The central part of Greece -which mainly belongs to the administrative area of Thessaly-, is one of its main agricultural production areas. As Greece is an agricultural country the production of the Thessaly plain has a major influence in country's socio-economic status and plays a crucial role in its financial life.

With an area of almost 14.000 km² and places where the elevation is below mean sea level pressure (dried lakes in the south east part) up to a little less than



Sensitivity studies and model performance

3000m (in the south part of mount Olympus) Thessaly occupies the eastern part of central Greece. Following the Mediterranean climate type, precipitation mainly occurs during the cold period (from October to April), while during summer the small amounts of precipitations mainly come from small duration and high intensity convective events. Apart from the described high inter-annual variation, the Pindus Mountains located in Thessaly's west part, combined with the eastward moving atmospheric circulation, results in high spatial heterogeneity of the precipitation regime. Low elevation areas in the east accept around 420mm while in high elevation areas in the west precipitation exceeds 2.000mm (Flocas, 1994). Those characteristics that could classify the eastern plain area as semi-arid, have not yet reduce in a sizable way the agricultural production. Fruits (like apples, pears, cherries) and agricultural commodity products (as wheat, cotton, maize, etc) make up the area's production. The intensification of the applied agricultural activities, leads to further exploitation of underground water, which combined with the reluctance of farmers to perform good irrigation methods has led to significant water deficit in the area presented as lowering of the underground water levels (Petalas et al., 2005).

As population increases and irrigation absorbs during the demanding warm period of the year more and more water, drought is an imminent threat presenting its signs in the last decades over the area (Tzabiras et al., 2016). The DAPHNE research project that was active from 2013 to 2015 tried to propose a methodology to tackle the problem of drought in the area. Using Weather Modification (Karacostas et al., 2015) favorable atmospheric conditions could be identified and convective clouds could be characterized as being candidates for assisted production of rain/snow through cloud seeding. The same effect could have been the collateral benefit of melting hailstones and their transformation into raindrops. The in advance knowledge of the atmospheric conditions, when dealing with convective scale phenomena, could only be realized using a state-of-the-science numerical weather prediction model configured in such a way, able to maximize its performance in analyzing moist convection in the area of interest.

Atmospheric models are built having in mind that they will deal with a huge number of scales from local turbulence in the scale of centimeters to synoptic scale

40

in mid-latitude weather systems and even more in planetary waves (Grabowski et al., 2019). In the work of Ćurić and Janc (2011a,b), who examined storms in Serbia from 1981 to 1995 using convection allowing numerical weather models, the total convective precipitation was effectively resolved by the models. In recent studies by Pytharoulis et al. (2016) and Lompar et al. (2017) extreme storms, that happened in Greece and Serbia respectively, accompanied by large amount of precipitation were simulated with the WRF numerical weather model.

For convection scale numerical simulations the microphysics scheme used plays an important role in the proper representation of the storms (Clark et al., 2012; Lean et al., 2008; Roberts and Rutledge, 2003; Stein et al., 2015; Weisman et al., 2008). The boundary layer structure as represented by the selected boundary layer scheme is a key factor in convective storm initiation, structure, and development. The boundary layer scheme regulates the onset of the convection scheme and together with the convection scheme adjust the vertical instability (Möbis and Stevens, 2012). Finally convection scheme also acts as a mean of regulating the available convection potential in a starting storm (Roberts and Rutledge, 2003).

3.2 Upper-air synoptic circulation types

Synoptic types classification has been globally used from many researchers (Hess and Brezowsky, 1977; Lamb, 1972; Muller, 1977), attempting to identify air-mass properties with circulation patterns and their connection with the appearance of certain weather events over a place. Likewise, several Greek researchers dealt with producing synoptic types over Greece using different calculation methods (Karacostas, 2003; Karacostas et al., 2018, 1992; Kassomenos et al., 1998; Maheras et al., 2000). In this study, the classification method proposed by (Karacostas, 2003) and (Karacostas et al., 2018) is used for classifying each day into certain atmospheric schemes using ECMWF gridded analysis data. It is a manual classification scheme based on synoptic charts of the upper atmospheric isobaric surfaces of 300hPa, 500hPa and 700hPa along with the presence of the trough/ridge axis and its position/orientation.

A brief description of the synoptic types used in this study follows:

Sensitivity studies and model performance

Open Long Wave trough (OPTR): This synoptic type is characterized by the presence of a slow-moving long wave trough dominating the area of interest (Fig. 3.1). Sometimes the long wave trough might be stationary. In this synoptic situation the upper airflow over the area is generally light, having a northwest to west wind direction. Air masses prevailing over the area are generally characterized as moderately unstable. An accompanying surface low sometimes associated with frontal activity is situated to the east or southeast of the area of interest. In case of evident baroclinic zone, this is placed between the trough line and the surface low pressure system. An anticyclone is generally positioned northwest of the area of interest. As a result to that, a north-west wind flow is observed over the surface.

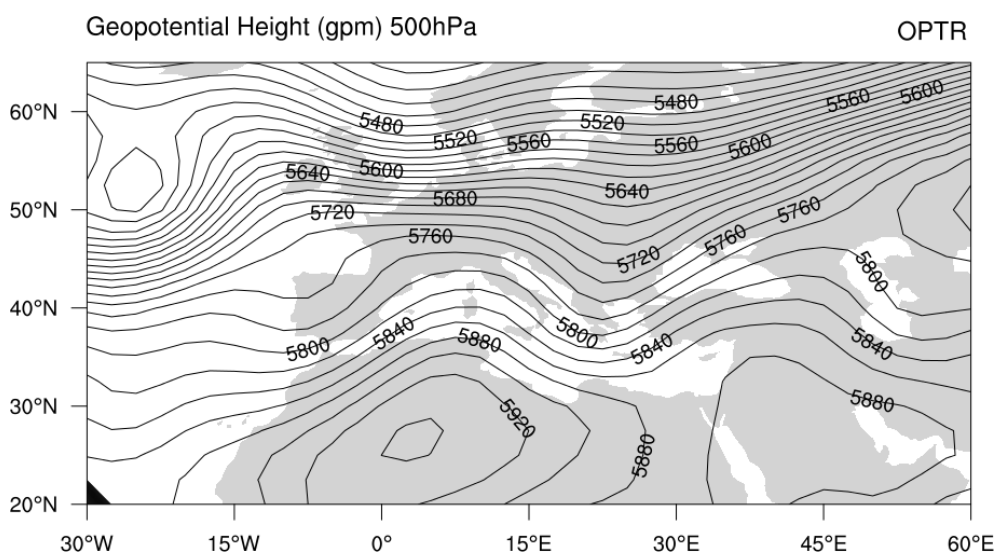


Figure 3.1. Geopotential height at 500hPa during OPTR circulation type.

Closed Long Wave trough (CLO): If one or more closed geopotential height lines are observed in the upper air synoptic charts this synoptic situation is named CLO (Fig. 3.2). This synoptic type is similar with OPTR synoptic type, but in this case, a more organized trough with easily observed developed baroclinic zone is present resulting in deeper and well-organized associated surface low pressure system. In this case air masses over the area are almost unstable, as a result of cold air advection due to the trough. Surface winds have a northerly component. Frequent thunderstorm is observed over the area, especially during the warm period of the year.

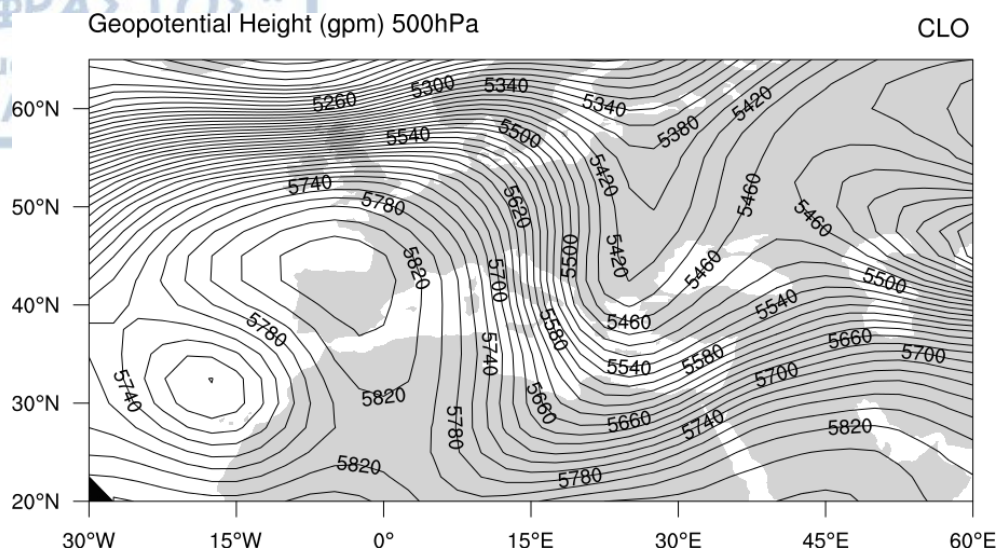


Figure 3.2. Geopotential height at 500hPa during CLO circulation type.

Cut-Off Low (CUT): This synoptic situation is described as the mature stage of both OPTR and CLO, formerly described, synoptic types. Closed contour lines are observed, resulting in a cut-off upper air low pressure system which is separated from the main westerly upper air flow (Fig. 3.3). This synoptic system presents almost no inclination from bottom to top of the atmosphere. Usually within these situations the kinetic energy of the weather system has been converted into dynamic energy. The associated surface low pressure system, which is almost vertically situated below the upper air cut-off low, remains longer time over the area producing scattered thunderstorm activity.

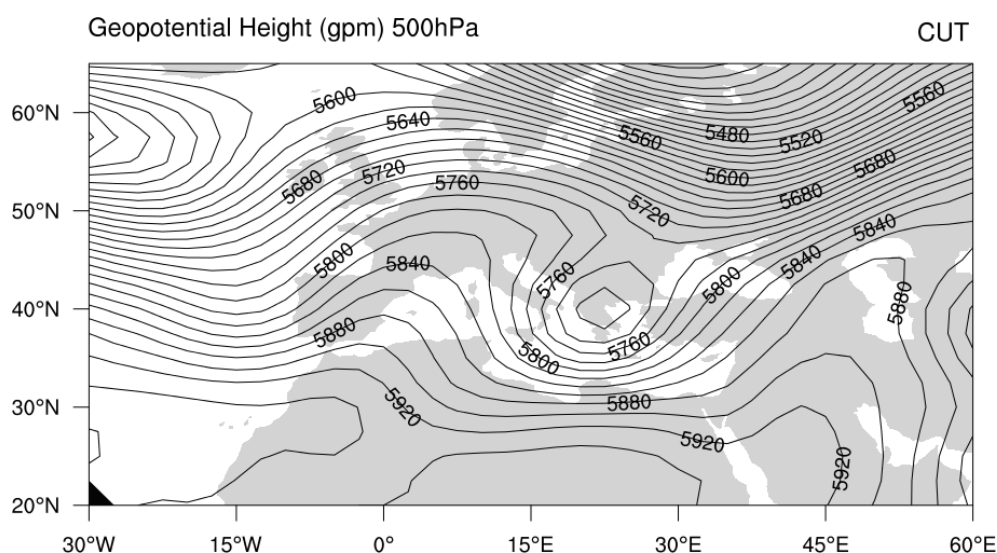


Figure 3.3. Geopotential height at 500hPa during CUT circulation type.

North-West flow (NW): At this synoptic type a long wave ridge is located west or northwest of the area of interest. Usually a long wave trough is situated to east or southeast of the area as well (Fig. 3.4). Sometimes, the resulting northwest flow is embedded with a number of short-wave troughs and ridges following the main northwest air flow. The presence of an aligned baroclinic zone over or east of the area is also evident. At the surface, a low pressure system is present to the east and a high pressure system to the north or northwest of the area. A northwest to southeast cold front appears sometimes, as the result of the embedded upper air short wave trough. Due to upper cold air advection the air mass becomes more destabilized resulting in frequent thunderstorm activity. According to the orientation of the trough axis the airflow ranges from westerly to northerly directions.

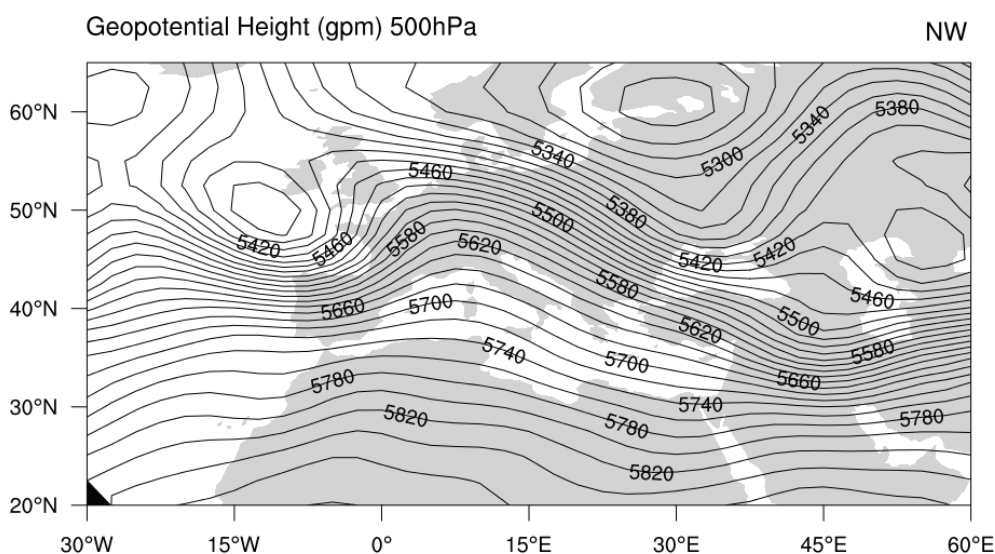


Figure 3.4. Geopotential height at 500hPa during NW circulation type.

South-West flow (SW): This synoptic type is characterized by the presence of a long wave trough situated to the west or southwest of the area of interest (Fig. 3.5). Accordingly, a long wave ridge to the east or northeast of the area is also present. As a result to that, a southwest flow prevails over the area, sometimes coupled with a series of embedded short wave troughs and ridges. The baroclinic zone is usually aligned over, or to the east of the area of interest. At the surface, a low-pressure system is observed to the east or northeast and a high-pressure system to the south or southwest of the area. A warm front is sometimes observed, embedded to the southwest to northeast airflow, as a result of the upper air short

wave trough. Alike with SW synoptic type, the orientation of the trough axis tilts airflow from southerly to westerly directions.

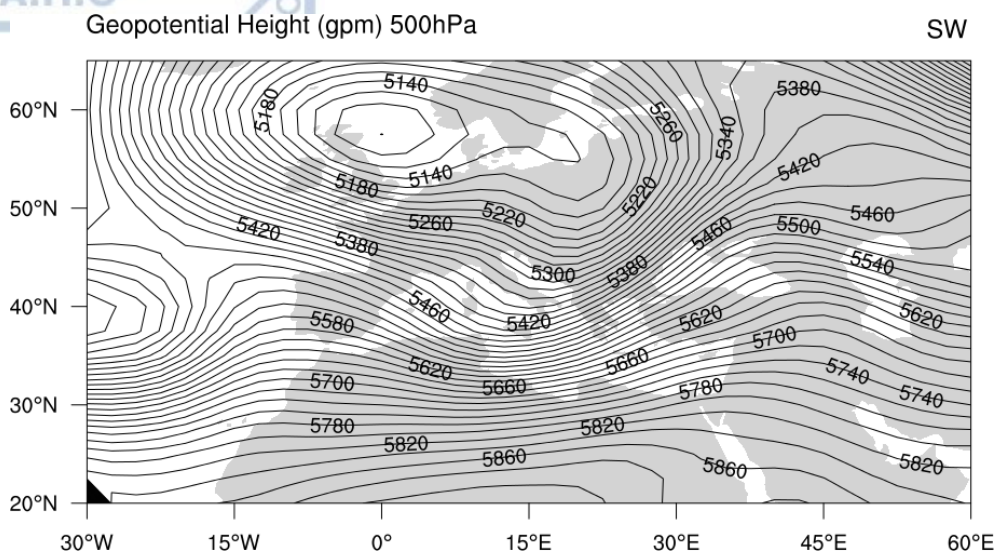


Figure 3.5. Geopotential height at 500hPa during SW circulation type.

Zonal flow (ZON) (Fig. 3.6): This synoptic type is the outcome of the presence of a low amplitude trough to the west and north of the area and a low amplitude ridge to the east and south. According to the pressure gradient, the resulting westerly winds vary in strength. Within this flow, embedded short waves are developed and move quite rapidly, passing over the area. Surface low pressure systems and associated frontal zones are generally moving from west to east having,

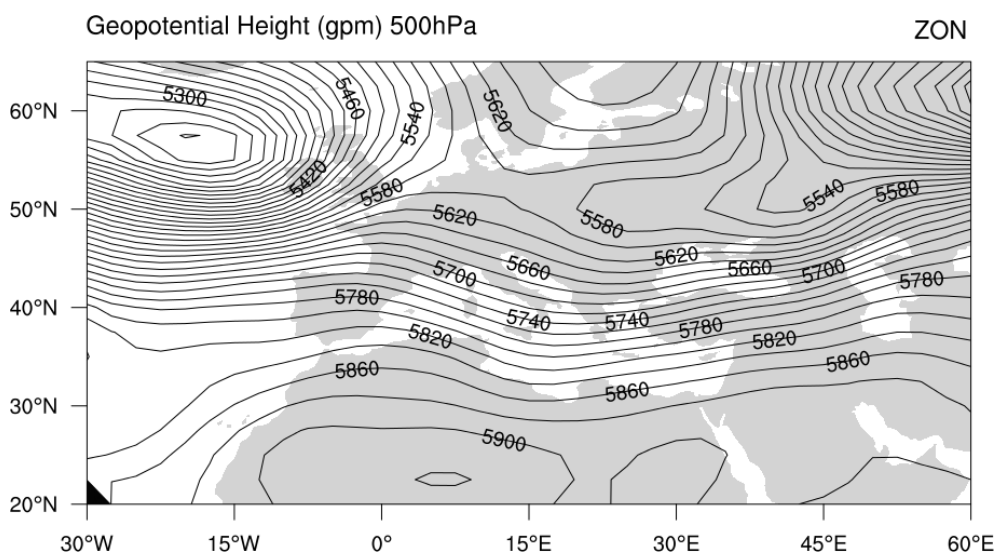


Figure 3.6. Geopotential height at 500hPa during ZON circulation type.

under the upper level baroclinic zone, cold air masses to the north and the warm air masses to the south.

According to Yarnal (1993) there are two main ways for circulation type classification. Circulation to environment and environment to circulation. In the first way the atmospheric circulation classification occurs first and then a relation is established with an environmental phenomenon. In the second method, the circulation classification is carried based on observed parameters of environmental phenomena. In the present study the second approach was adopted. Moreover, the manual synoptic classification scheme proposed by Karacostas et al. (1992) and Karacostas (2003) was used.

3.3 Case Selection

A two step procedure was chosen for the final selection of the model setup to be used at the operational runs of the DAPHNE research project.

In the first stage, seven (7) characteristic cases from year 2010 were selected and simulations were performed with variable model setups (12 different setups, explained later in section 3.4). This way a total number of $7 \times 12 = 84$ simulations were performed and evaluated to reach the preliminary decision about the setup to be used. The selected days that were chosen are presented in Table 3.1.

Table 3.1. Dates of the simulated cases during the first stage of the selection procedure

19/06/2010	27/06/2010	20/07/2010	04/08/2010
12/09/2010	20/09/2010	25/09/2010	

Stepping up on the synoptic classification of the upper air circulation types, the initial number of selected cases was raised to thirty-six (36). Six cases from every different upper-air synoptic circulation type were selected (Table 3.2) for days that convective activity affected the examined area. For these days simulations were performed with the setup selected in the first stage and evaluated.

Table 3.2. Dates of the simulated cases during the second stage of the selection procedure categorized by synoptic type

Zonal (ZON)	19/09/2007 24/09/2008 06/07/2009
	13/09/2009 17/09/2009 19/06/2010
Northwest (NW)	14/06/2007 25/05/2009 04/07/2009
	19/09/2009 23/05/2010 18/07/2010
Southwest (SW)	04/06/2008 15/05/2009 17/04/2010
	15/05/2010 04/08/2010 25/09/2010
Open Trough (OPTR)	09/06/2008 03/07/2009 06/09/2009
	20/04/2010 07/07/2010 20/09/2010
Closed Low (CLO)	02/09/2007 27/09/2008 22/05/2010
	22/06/2010 27/06/2010 12/09/2010
Cut-off Low (CUT)	24/05/2007 28/06/2009 29/06/2009
	05/06/2010 11/07/2010 20/07/2010

This way the performance of the selected setup was tested for consistency in a broader sample of convective days. The familiarity to the characteristics of the area of interest in terms of the local weather and environment, assisted by previous radar based climatological studies in the examined area (Bampzelis and Karacostas, 2016, 2014) provided the required assurance for the representativeness of the selected cases.

3.4 Numerical Model setup

The meteorological model used is the WRF-ARW model, version 3.5.1 (WRF-ARW Version 3.5.1 (Skamarock et al., 2008; Wang et al., 2014, thoroughly described in Chapter 2). Three nested domains were used (Fig. 3.7). The coarser domain (D01) with grid spacing of 15Km x 15km covers Europe and a large part of Northern Africa (301x261 grid points). Synoptic scale characteristics can be captured in detail in this resolution. The middle domain (D02) with grid spacing of 5km (grid ratio 1:3) covers Greece, the lower Balkans and part of Asia Minor (253x253 grid point). Finally the finest domain (d03) has a grid spacing of 1.67Km and is centered over Thessaly

Sensitivity studies and model performance

(201x171 grid points). The top level of the model was located at 50 hPa. The model sigma levels number was set to thirty-nine (39). Variable vertical resolution was used with coarser resolution in the upper levels and layers close to each other at the boundary layer. Ten minutes output interval was set for the innermost domain (D03), as a mean to capture the fast evolving field of radar reflectivity.

Table 3.3. Model Setups used in the study

Experiment	Microphysics	Boundary layer	Surface layer	Convection (D01 and D02)
ETA-KF-YSU	ETA	YSU	MM5	KF
ETA-KF-MYJ	ETA	MYJ	ETA	BMJ
ETA-BMJ-YSU	ETA	YSU	MM5	KF
ETA-BMJ-MYJ	ETA	MYJ	ETA	BMJ
WSM6-KF-YSU	WSM6	YSU	MM5	KF
WSM6-KF-MYJ	WSM6	MYJ	ETA	BMJ
WSM6-BMJ-YSU	WSM6	YSU	MM5	KF
WSM6-BMJ-MYJ	WSM6	MYJ	ETA	BMJ
GOD-KF-YSU	Goddard	YSU	MM5	KF
GOD-KF-MYJ	Goddard	MYJ	ETA	BMJ
GOD-BMJ-YSU	Goddard	YSU	MM5	KF
GOD-BMJ-MYJ	Goddard	MYJ	ETA	BMJ

In order to find the best performing mix of physics schemes, a number of 12 combinations was tested (Table 3.3). Three (3) microphysics (mp) schemes were employed in the simulations: Ferrier-ETA (ETA, mp_physics=5) which is the operational microphysics scheme in NCEP, simple, fast, but yet efficient scheme with diagnostic mixed-phase processes. WRF Single Moment 6-class (WSM6, mp_physics=6) which is suitable for high-resolution simulations, cloud water, rain, ice, snow and graupel are represented in separate variables (Wang et al., 2014). Goddard (GOD, mp_physics=7) which also classifies ice, snow and graupel in separate variables. Two planetary boundary layer schemes: Yonsei University (YSU, bl_pbl_physics=1) which is a non local-K vertical mixing scheme with explicit entrainment. Mellor-Yamada-Janjić (MYJ, bl_pbl_physics=2), a local closure scheme

that predicts turbulent kinetic energy. Finally two cumulus parameterization schemes were used only in the two outer nests (D01, D02): Kain-Fritsch (KF, cu_physics=1) addresses deep and shallow convection. Betts-Miller-Janjić (BMJ, cu_physics=2), the operational ETA scheme aiming at a well-mixed profile through column moist adjustment (Wang et al., 2014). The physics schemes are better described in chapter 2 of the present dissertation.

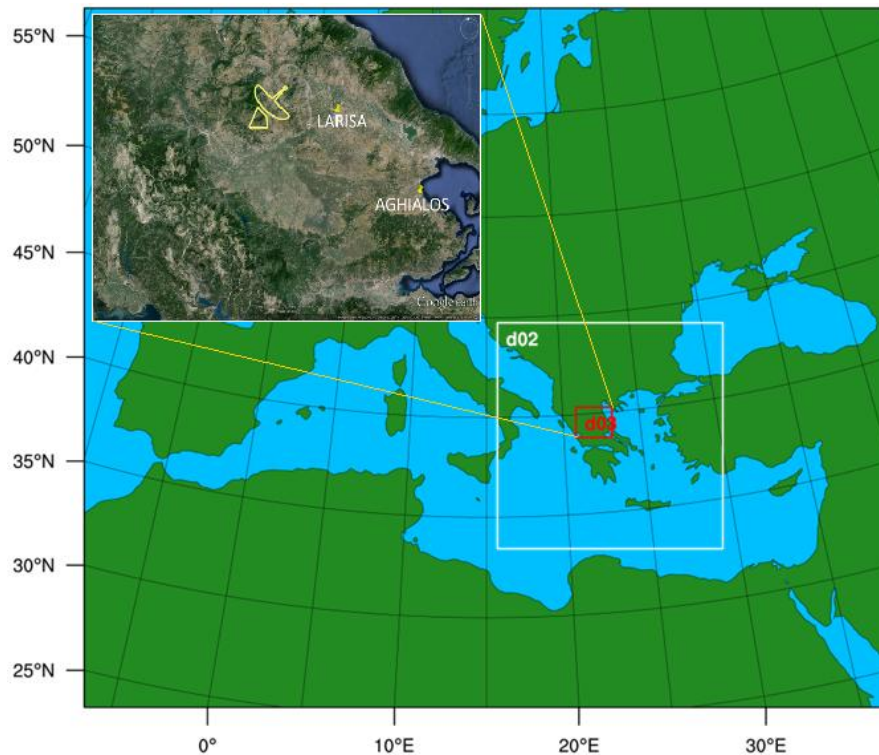


Figure 3.7. Model domain setup used by WRF-ARW in the numerical experiments. (inline picture presents innermost domain topography, radar position and stations used in model validation in D03).

The Rapid Radiative Transfer Model application for Global (RRTMG, ra_sw_physics=4) climate models (Iacono et al., 2008) was used for both the longwave and shortwave radiation. The surface layer scheme employed was dependent on the boundary layer scheme selected. MM5 similarity (sf_clay_physics=1) based on Monin-Obukhov with Carlson-Boland viscous sub-layer and standard similarity functions from lookup tables when Yonsei University boundary layer scheme was selected, and Eta similarity based on Monin-Obukhov with Zilitinkevich thermal roughness and standard similarity functions from lookup



Sensitivity studies and model performance

tables when Melor-Yamada-Janjić boundary layer scheme was selected (Wang et al., 2014). Surface physics was represented by the NOAH (NCEP/Oregon State University/Air Force/Hydrologic Research Lab) Unified model (sf_surface_physics=2, Chen & Dudhia, 2001)

The resolution of 5km falls in to the grey zone for the use of parameterized convection. Prior use from the writer and other researchers suggests that this is not uncommon in everyday use of meteorological models for operational purposes in grid spacings of this order of magnitude in Greece and other Mediterranean Sea regions (Kotroni and Lagouvardos, 2004; Lagouvardos et al., 2013; Pytharoulis et al., 2016; Sindosi et al., 2012)

Data from the European Centre for Medium-Range Weather Forecasts (ECMWF), at a horizontal resolution of $0.25^{\circ} \times 0.25^{\circ}$ was used as initial and boundary conditions. Their temporal resolution was six hours and they consisted of operational analyses (and not forecast products) to avoid the error inherent to forecast products. National Center for Environmental Prediction (NCEP) SSTs was retrieved at horizontal resolution of $\sim 0.083^{\circ} \times 0.083^{\circ}$ and they were kept constant for the whole simulation. Topography and the land-use data were provided by USGS (United States Geological Survey) at the fine-resolution of $30'' \times 30''$.

For every selected day, data from the 12:00 UTC cycle of the previous day from ECMWF was used for the initialization of the model. The forecast horizon was 36 hours, thus reaching the 24:00UTC for the day of interest. For every case chosen it was checked that convective activity for both the simulations and observation was already over at that time. The first 12 hours were used for model spin-up and a net duration of 24 hours (00:00UTC to 24:00UTC for the selected day) was used for the analysis.

3.5 Verification data: Weather stations, Radar data and TITAN

Data provided by the Hellenic National Meteorological Service (HNMS) was used for the statistical evaluation of the model performance in the domain D02 over Greece. Meteorological data were available every three hours and the corresponding forecast values were extracted from the simulations. For Larissa and Aghialos (Fig.

3.7) hourly data were used for statistical evaluation in D03. The fields of 2 m air temperature (TEMP), 2 m air relative humidity (RH), mean sea-level pressure (MSLP) and wind speed at 10 m (WIND) was used for the evaluation.

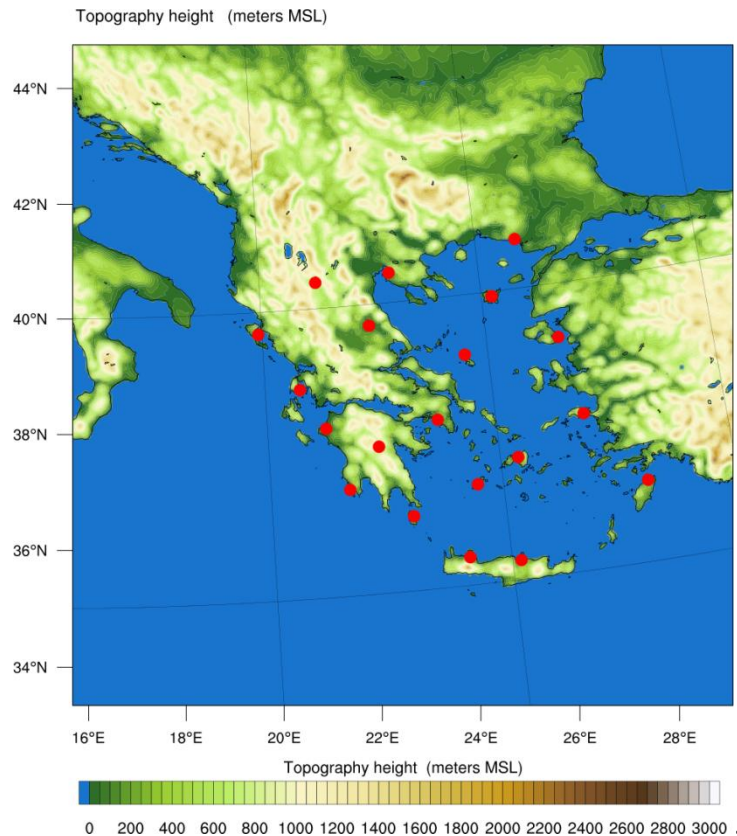


Figure 3.8. Detailed topography (m) of the model domain D02. Overplotted with red dots the meteorological stations of the Hellenic National Meteorological Service, which were used in the validation of D02 simulations.

A C-band (5cm) weather radar located in the center-north west part of the examined area is the source of the radar data. It takes around 3.5 minutes for the radar to cover the area around it at 26 levels, with the lowest being at 1km and the highest at 19.75km. The field of reflectivity is interpolated at a grid having a resolution of 750m in each dimension. Taking account for the cone of silence, a circle with diameter of 30 km was created and the data contained in the circle were not considered for analysis. The convective cells are identified using TITAN (Thunderstorm Identification, Tracking, Analysis, and Nowcasting) software (Dixon and Wiener, 1993). TITAN is a software suite used in real time for operational purposes in weather modification applications, and in archived mode for post



Sensitivity studies and model performance

analysis of past cases, providing identification, tracking and forecasting of convective cells taking as input data raw reflectivity measurements from a weather radar. By setting a threshold on the reflectivity value one can identify a storm as a three dimensional entity satisfying the criterion. Roberts & Rutledge (2003) proved that setting the threshold to 35dBz acquired a satisfying correlation with the development of mature cumulonimbus clouds. The Greek National Hail Suppression Program (Karacostas, 1989, 1984) uses the same threshold for the initiation of cloud seeding operations. For the purposes of this study cloud top, cloud base, area and maximum reflectivity were produced by TITAN.

The 10 minutes outputs from D03 of the model were the initial data for the calculations of the convective activity in the area of interest. The same 35dBz threshold employed in the radar data was used for the model results. Convective activity was considered to occur when the composite (maximum throughout the atmospheric column) reflectivity, in the model was higher than 35 dbz. Valid data were considered those that were contained on a 140km x 140km region centered on the weather radar (Liopraso, 39.674°N, 21.837°E) and laying outside the cone of silence of the radar (3.7 inline). The NCEP Unified Post Processing module of WRF (UPP; Wang et al., 2014) was used to compute model's reflectivity in every model time step and then by using the 35dBz criterion to calculate the cloud's top and area. The last step was to transform both radar and model data into hourly data by taking into account maximum reflectivity, average area and maximum cloud top that happened through the examined hour.

3.6 Sensitivity results

3.6.1 Performance at domain D02

Using data provided by the 20 stations of HNMS presented in Fig. 3.8 the model's statistical evaluation was performed using the Model Evaluation Tool (METv.60, Brown et al., 2017) The plots were created using NCL (NCAR Command Language, UCAR/NCAR/CISL/TDD, 2018). Three-hourly values exported from the available meteorological messages and the corresponding model values were considered. Using the distance weighted mean interpolation method with data from

the four closest grid points, the forecasted values at the station location were obtained.

Fig. 3.9 presents the mean error ME (a) and mean absolute error MAE (b) for mean sea level pressure. The model underestimates the MSLP in every case. There is a clear distinction between the two cumulus schemes. Simulations performed using

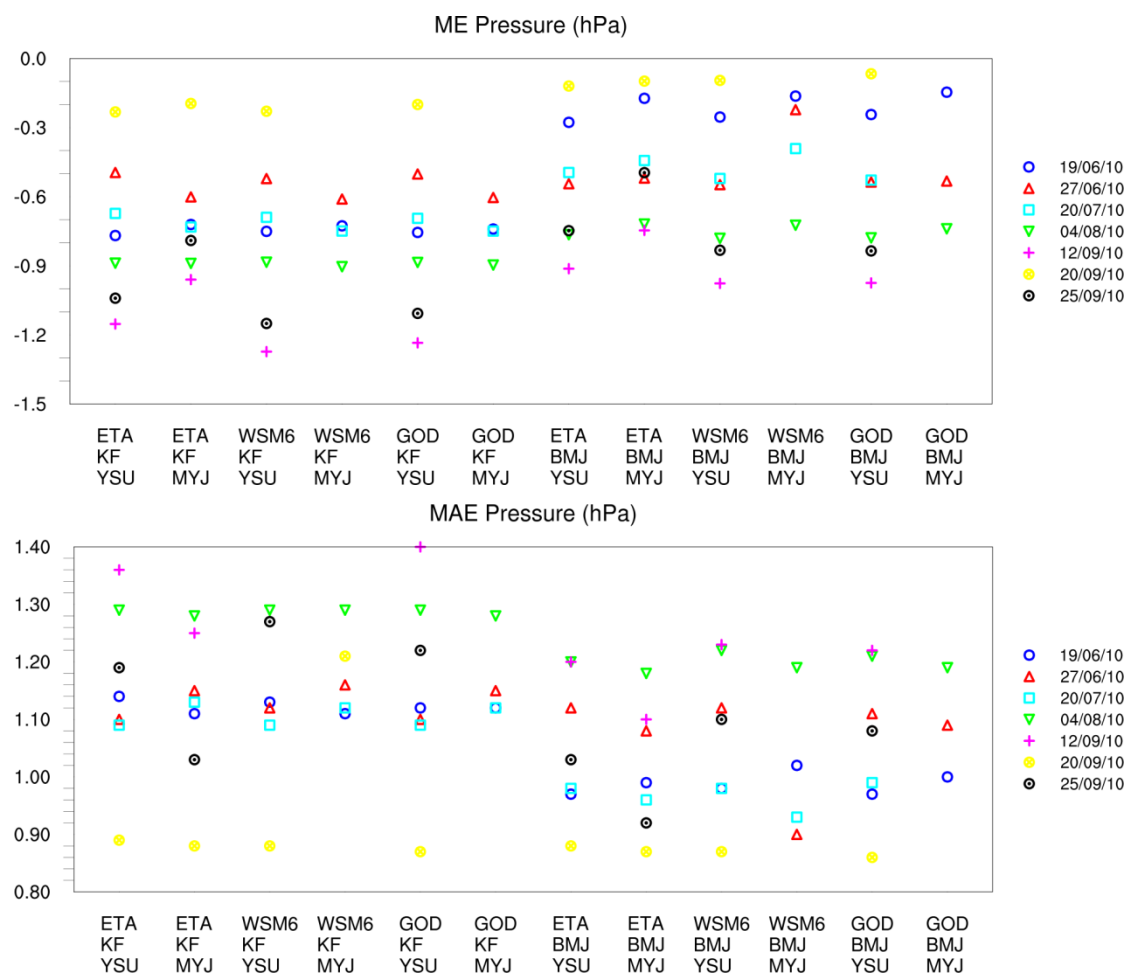


Figure 3.9. The Mean Error (a) and Mean Absolute Error (b) of mean sea-level pressure forecasts of WRF-D02 over Greece in the twelve sets of experiments (See Table 3.3 for more info on the specific model setups).

the Kain-Fritsch cumulus scheme have a systematically bigger mean error. The values of mean error range from -1.3hPa to -0.2hp for KF cumulus scheme and from -1.0hPa to -0.1hPa for BMJ scheme. The simulations performed using YSU boundary layer scheme correspond to those presenting the bigger values. They also have wider spread than the cases simulated using the BMJ boundary layer scheme. The mean absolute error has the same behavior with values ranging from 0.8hPa to 1.4hPa. It is

Sensitivity studies and model performance

worth noting that the case of 20/09/2010 presents the best results in every simulation while the worst represented case is the one of 12/09/2010. This was a case which led to model crashes in at least two simulations. Some simulations (mainly using Goddard microphysics) presented erratic results and are not shown in the graph (and the subsequent graphs for the other parameters).

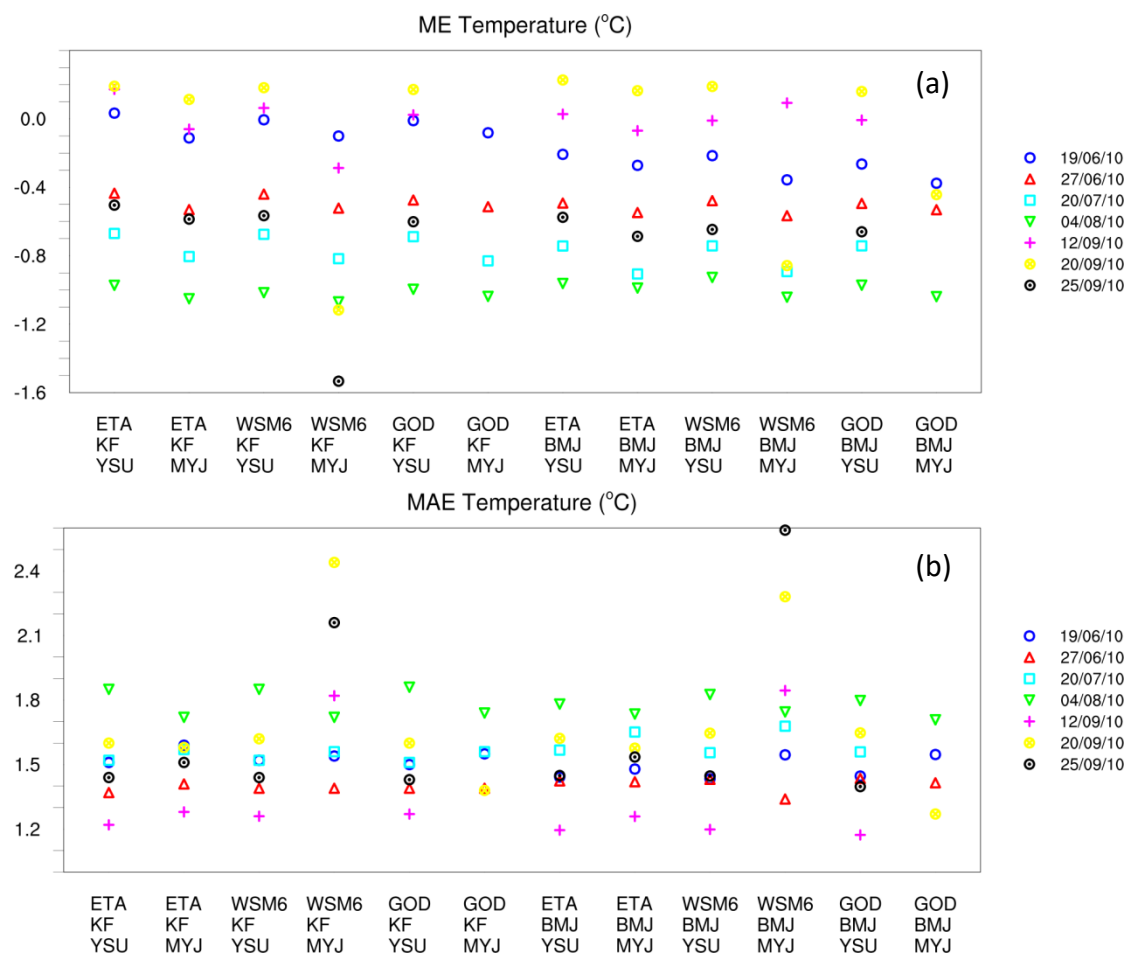


Figure 3.10. The Mean Error (a) and Mean Absolute Error (b) of 2m air temperature forecasts of WRF-D02 over Greece in the twelve sets of experiments (See Table 3.3 for more info on the specific model setups).

Temperature ME and MAE are presented in Fig 3.10a and 3.10b respectively. The ME shows values from 0.1K to -1.1 (with one outlier at -1.6K). There is no systematical error related to the cumulus scheme as in MSLP but there is a distinction based on the BL scheme. Better results are obtained on the simulations using the YSU boundary layer scheme. The WSM6-KF-YSU and the WSM6-BMJ-YSU model setups present the smaller overall MAE with values from 1.3K to 1.8K while

their spread of values is also the smallest. On the opposite side the WSM6-KF-MYJ and WSM6-BMJ-MYJ model setups came out with the worst results reaching values of MAE close to 2.6K almost double the mean values of the other setups. The relative humidity results of the simulation exhibit the greatest dependence on the boundary layer scheme used, which is evident from the successive ups and downs in Fig. 3.11a and 3.11b presenting the ME and MAE of relative humidity. Relative humidity is over estimated in almost every case. In the cases where YSU boundary layer was used the values of ME ranges from -1.0% to 5.8%. On the other hand when MYJ scheme was used the values of ME are all positive from 1.9% to 8%. The MAE values range from 7.9% to 11.1% for simulations performed using the YSU BL scheme compared to 9.0% to 13.0% with the MYJ BL scheme.

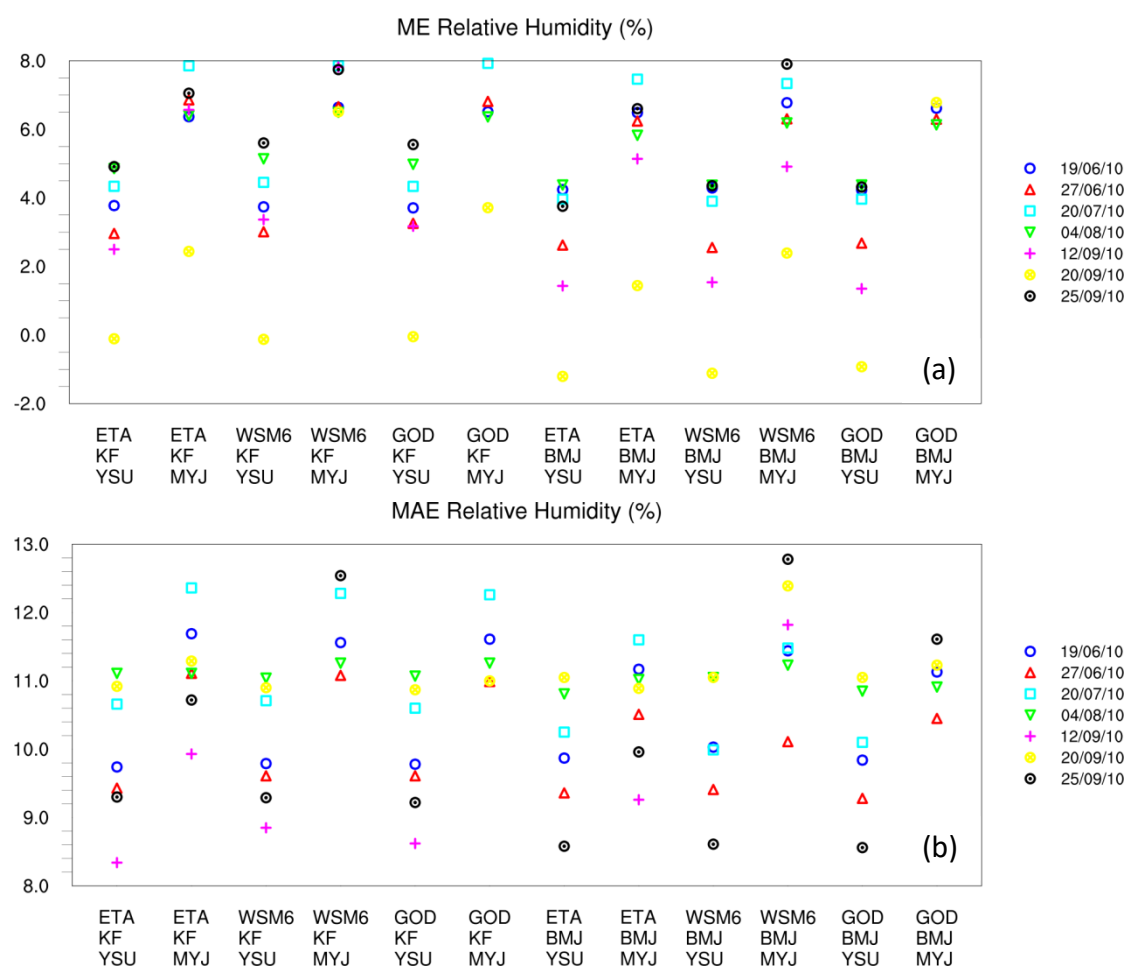


Figure 3.11. The Mean Error (a) and Mean Absolute Error (b) of 2m relative humidity forecasts of WRF-D02 over Greece in the twelve sets of experiments (See Table 3.3 for more info on the specific model setups).

Sensitivity studies and model performance

Finally WRF overestimated the wind speed as is shown in Fig 3.12. The mean error (Fig. 3.12a) ranges from 0.4m/s to 1.9m/s. The dependence on the boundary layer scheme used is noticeable for wind speed too. The YSU boundary layer simulations have a ME reaching 1.6m/s and in only 2 cases 1.7m/s. The BMJ

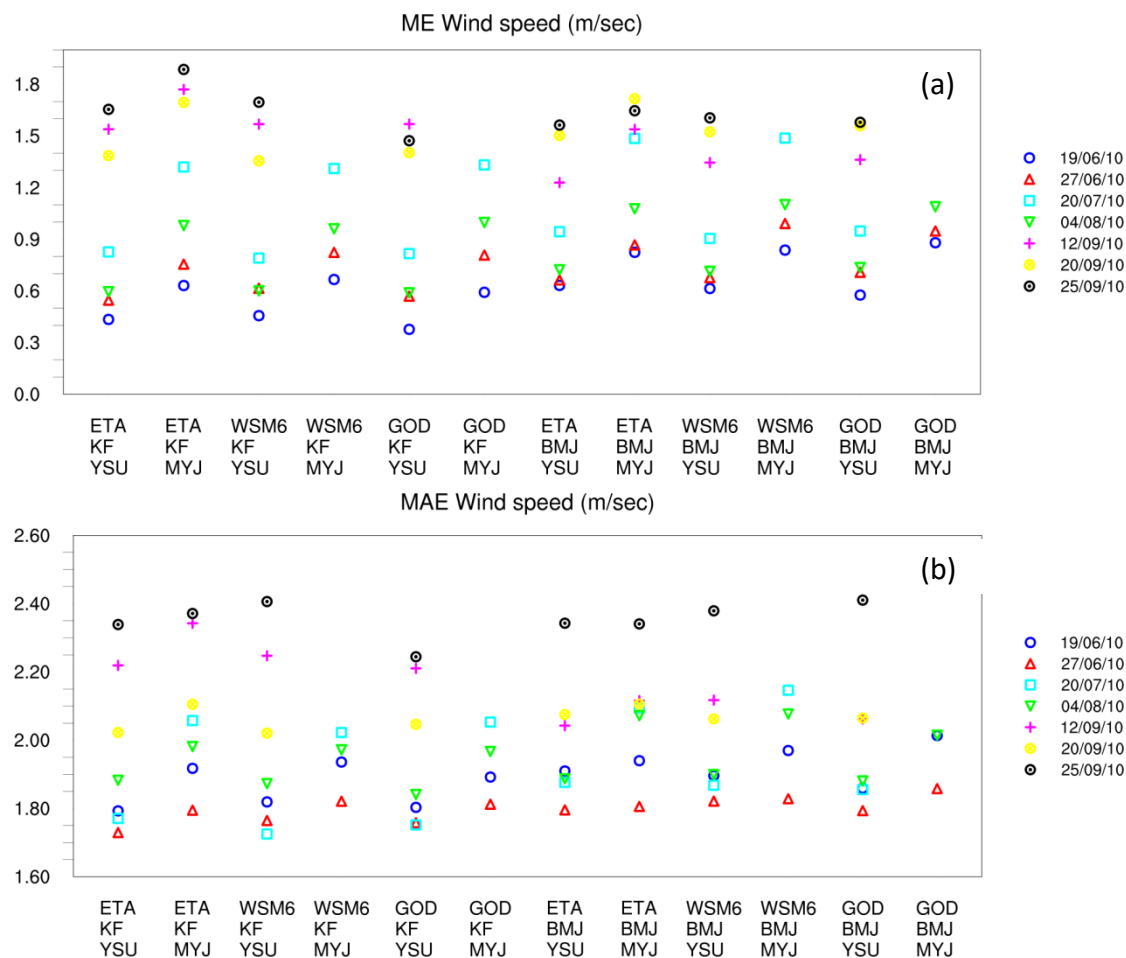


Figure 3.12. The Mean Error (a) and Mean Absolute Error (b) of 10m wind speed forecasts of WRF-D02 over Greece in the twelve sets of experiments (See Table 3.3 for more info on the specific model setups).

boundary layer simulations reach values from 0.7m/s to 1.9m/s. The BMJ cumulus scheme coupled with MYJ boundary layer scheme presents the biggest mean ME for all the cases. That high value of ME is the result of high values in all the cases and not a result of outliers indicating as systematic unmatched combination.

3.6.2 Cloud Characteristics at domain D03

The characteristics of the simulated convective activity in WRF-D03 and those measured by the radar for a typical case are shown in Fig. 3.13 to Fig. 3.15 as

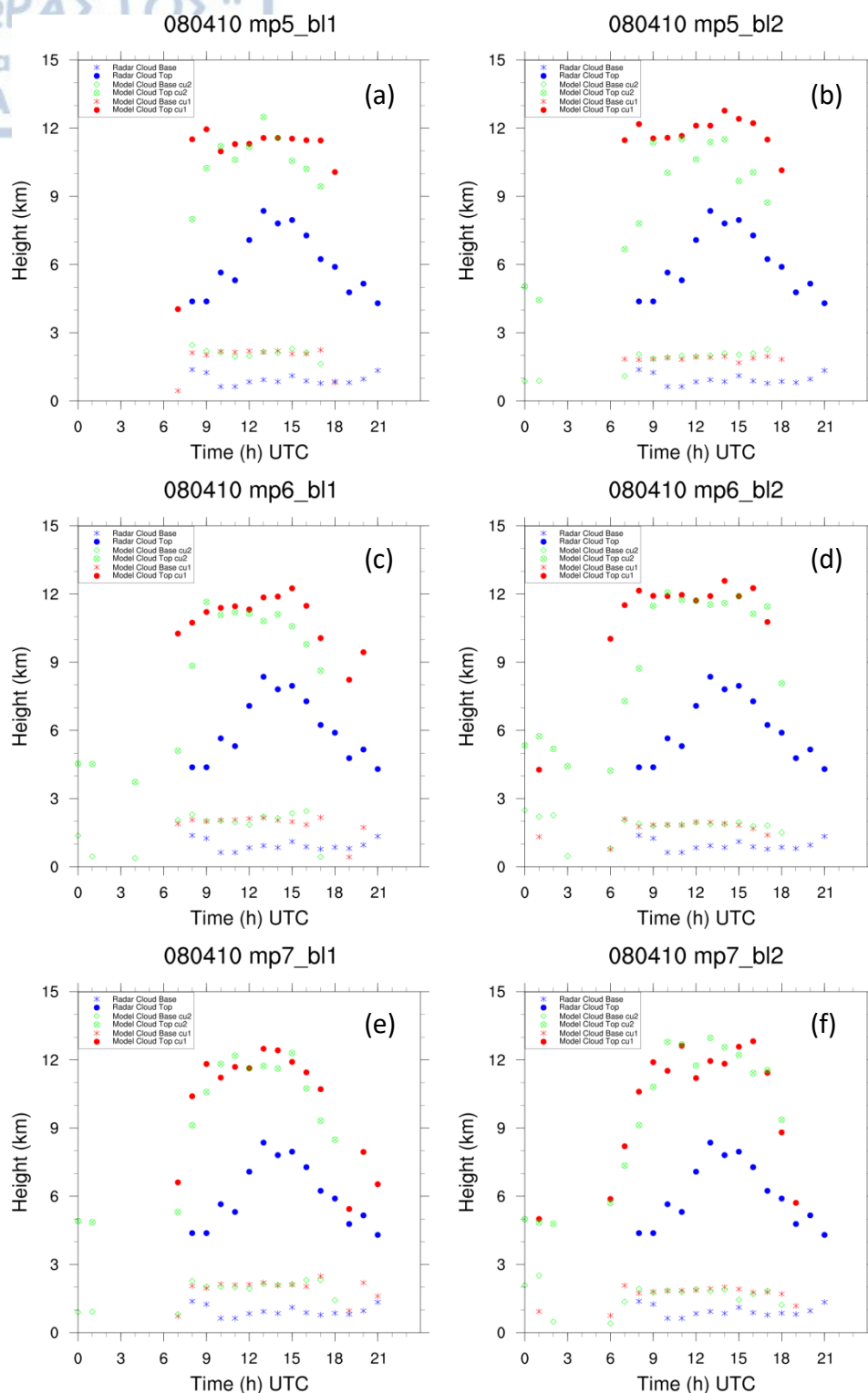


Figure 3.13. Cloud top and base for WRF-D03 grid points with composite reflectivity greater than 35 dBz (for August 4, 2010). Blue markers represent radar measurements, green markers model results for KF convection scheme and red markers results for BMJ convection scheme used in WRF D01 and WRF D02.



Sensitivity studies and model performance

represented by cloud top, cloud base, maximum reflectivity and cloud area. In the analysis the results are presented in relation to the cumulus scheme, even if cumulus convection was not used in D03. The cumulus convection scheme used refers to D01 and D02.

3.6.2.1 Cloud Height

In every simulation the model over estimated the cloud height. The simulations present a more rapid growth of the cloud than the one calculated by the radar data. For Ferrier microphysics (mp5) from the time that the cloud has reached reflectivity of more than 35dBz its top height remains almost constant. This is more pronounced in the KF (cu=1) than in BMJ (cu=2) simulation (Fig. 3.13a and 3.13b). The WSM6 (mp=6) simulations present a variation in top height, more evident when KF cumulus scheme is used. The timing of the maximum height is well simulated (Fig 3.13c). The simulations using the BMJ cumulus scheme (Fig. 3.13c and 3.13d) show an onset of light convective activity (reflectivity more than 35dBz in lower heights) three to five hours before the actual start of the activity. The Goddard microphysics (mp=7) simulations overestimate more than the other setups the cloud height reaching 14km. Furthermore the Goddard scheme coupled with MYJ boundary layer scheme (bl=2) causes a rapid evolution of the convective activity that ends at least 1.5 hour earlier than the other setups (Fig. 3.13f). The cloud base is almost independent of the setup used and is calculated at about 2km, almost double the one measured from the radar data.

3.6.2.2 Maximum Reflectivity

Maximum reflectivity (simulated and measured) is shown in Fig. 3.14. All simulations results are in close agreement with the maximum reflectivity measured from the radar. The simulations using the Ferrier microphysics (Fig 3.14a and 3.14b) present smaller reflectivity in the beginning of the activity but soon reach the actual values measured. The onset of the activity is well represented but the end of the activity is sharper and while the radar measures reflectivity more than 35dBz the model predict smaller values, less than 35dBz. When WSM6 is the microphysics scheme employed in the simulations the reflectivity is overestimated by 2-4dBz

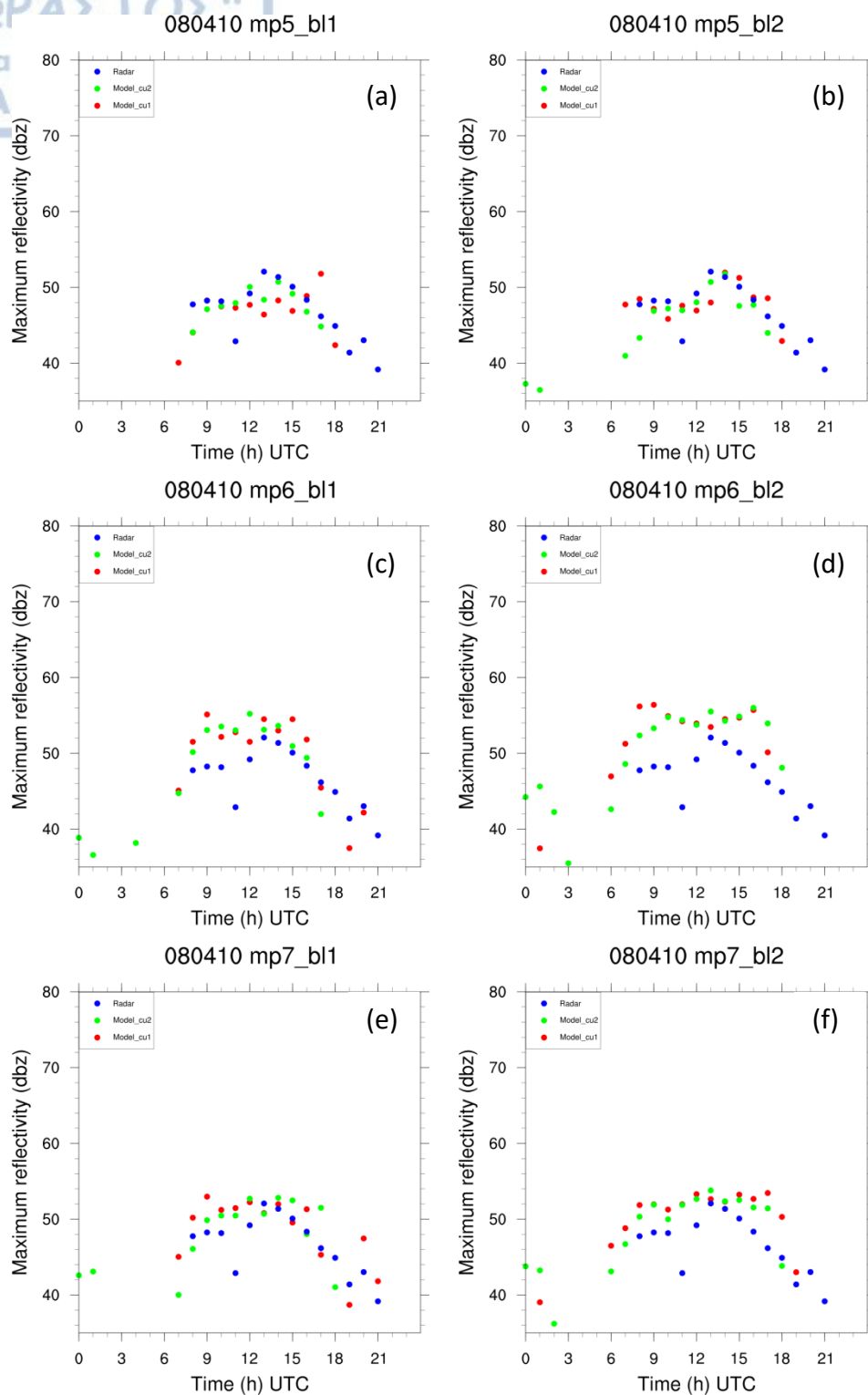
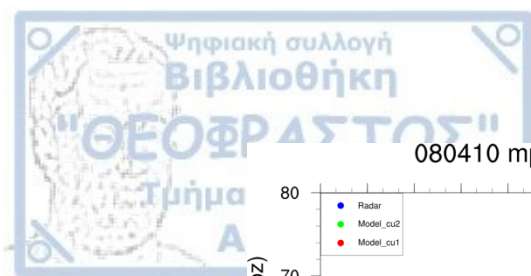


Figure 3.14. Maximum reflectivity in WRF-D03 grid points with composite reflectivity greater than 35 dBz (for August 4, 2010). Blue markers represent radar measurements, green markers model results for KF convection scheme and red markers results for BMJ convection scheme used in WRF D01 and WRF D02.

Sensitivity studies and model performance

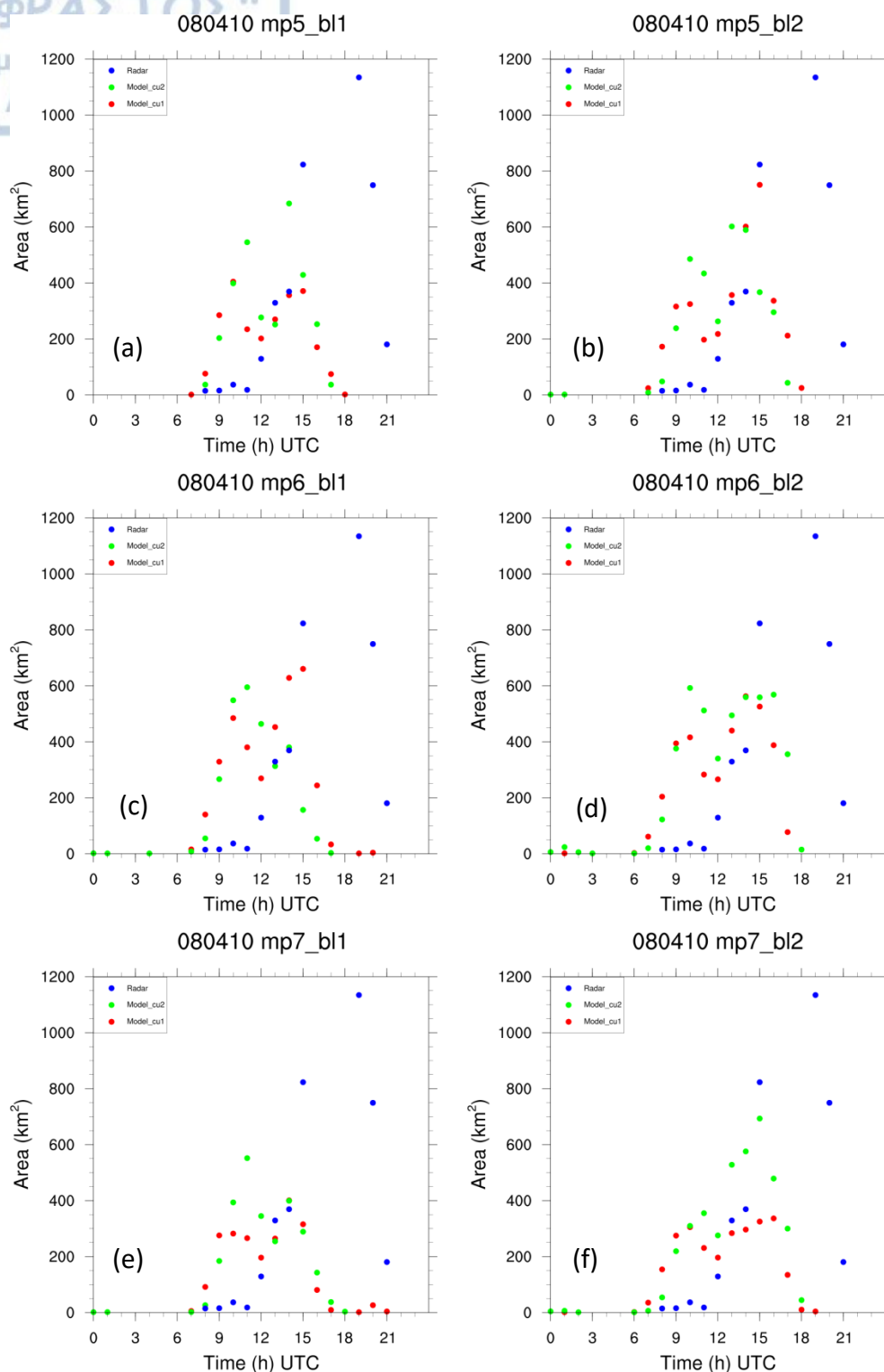


Figure 3.15. Cloud area in WRF-D03 grid points with composite reflectivity greater than 35 dBz (for August 4, 2010). Blue markers represent radar measurements, green markers model results for KF convection scheme and red markers results for BMJ convection scheme used in WRF D01 and WRF D02.

when the YSU boundary layer scheme is used (Fig. 3.14c) and by 2-5dBz when the MYJ boundary layer scheme is used (Fig. 3.14d). The temporal evolution is well replicated especially when the YSU boundary layer scheme is coupled with KF cumulus convection scheme (used in D01 and D02). Good agreement in reflectivity values is attained in Goddard simulations (Fig. 3.14e and 3.14f). The coupling with YSU boundary layer scheme results in convection start and end time match, with simulated reflectivity very close to the measured by the radar throughout the event. The use of MYJ boundary layer keeps the simulated reflectivity higher during the event with a subsequent rapid fall before the actual end of the event, as this is measured by the radar.

3.6.2.3 Cloud Area

The area of the cloud as simulated by the model and calculated using TITAN from radar data is shown in Fig. 3.15. The onset of the activity is properly predicted by the simulations in most of the model setups. The raise in cloud area is far more progressive in the calculated area (radar) than in the simulations. In the first half of the event (the true duration of the event is based on the radar measurements) the simulated area reaches values up to 600km^2 while the calculated one is much less ($<100\text{km}^2$). In the second half of the event the calculated area increases up to 1200km^2 while the simulated start to decrease and falls to almost zero about at the $\frac{3}{4}$ of the event duration. The Ferrier simulations (Fig. 3.15a and 3.15b) present the lowest overall area while the Goddard (Fig. 3.15e and 3.15f) the highest. The WSM6 simulations (Fig 3.15c and 3.15d) present the same temporal evolution with the radar but with a time shift due to the fastest evolution of the convective activity in the simulations. The maximum area from the WSM6-YSU simulations reaches half the area of the calculated from the radar data.

3.6.3 Daily cycle at domain D03

The performance of the model simulations was assessed in the innermost domain WRF-D03 using data from two stations located in the area, namely Larissa and Aghialos (their position is shown in Fig. 3.7). Due to the limited number of

Sensitivity studies and model performance

trustworthy weather stations in the area the performance of the model was checked examining the daily cycle of T2m (temperature at 2m) and RH (relative humidity at 2m). As in WRF-D02 some simulations produced extreme results and were discarded from analysis. Typical results for 2 days (20/07/2010 and 04/08/2010) are presented in the following pages. As in the previous section, for results presented in relation to the cumulus scheme, this refers to the cumulus convection scheme used in D01 and D02 since no cumulus convection parameterization was used in D03.

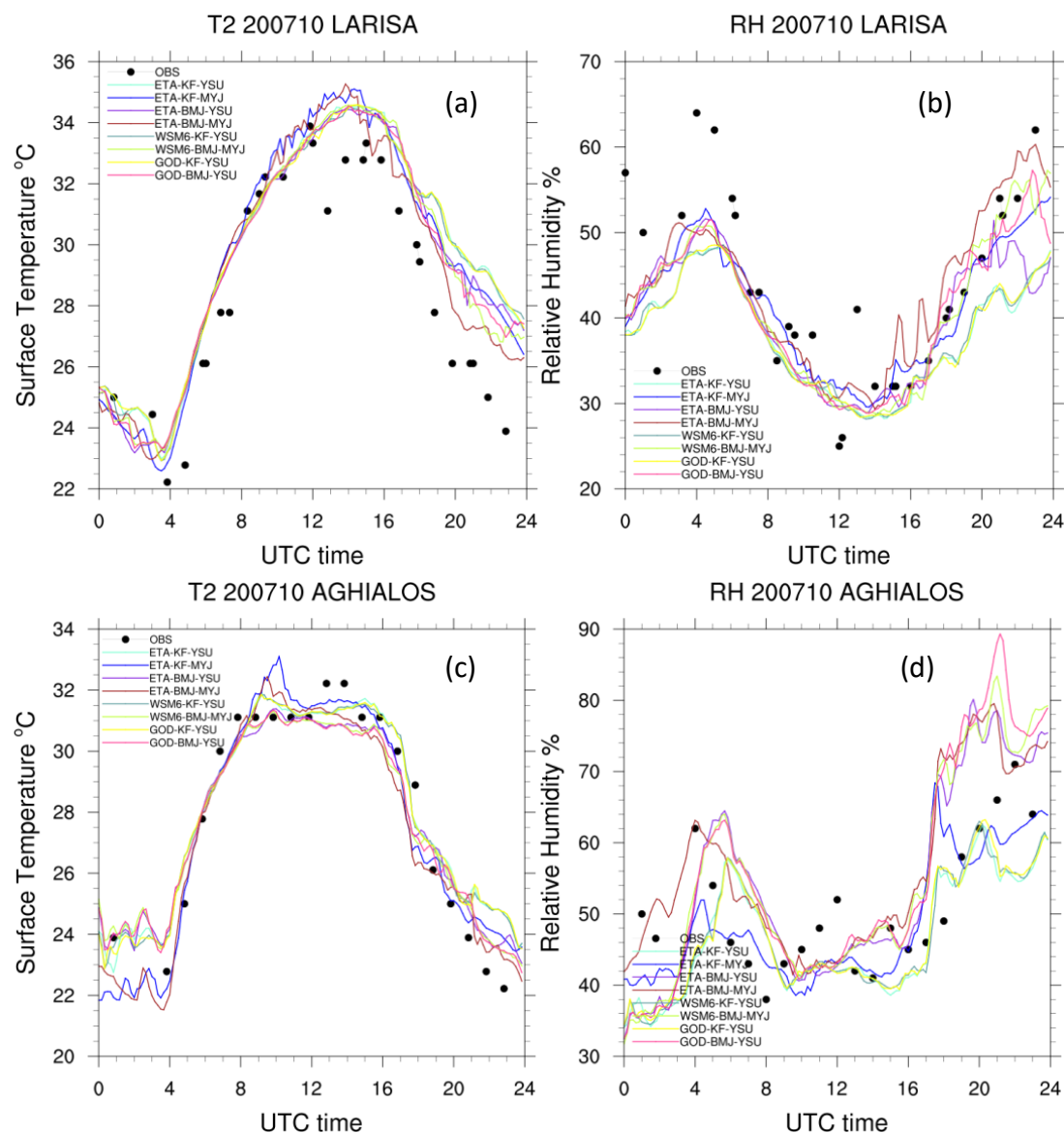


Figure 3.16. Daily cycle of measured and simulated 2m temperature and relative humidity in WRF-D03 for 20-07-2010 at Larisa (a and b) and Anghialos (c and d).

3.6.3.1 Case of July 20 2010

The daily cycle of 2m temperature and relative humidity for 20/07/2010 is presented in Fig. 3.16. For Larisa the combination of Ferrier microphysics, Betts-Miller-Janjic Cumulus and Mellor-Yamada-Janjic boundary layer scheme is better in representing maximum and minimum temperatures (Fig. 3.16a). The WSM6-KF-YSU setup does not predicts the extreme temperatures but shows an overall better behavior, following the observed values during the whole day. As for RH all simulations fail to predict the high values of relative humidity during the first morning hours but adequately follow the daily cycle (Fig. 3.16b). For Anghialos, which is located closer to the sea, the WSM6- KF-YSU setup predicts the midday temperatures without the overestimation shown in other experiments from 8UTC to 12UTC (Fig. 3.16c). The experiments using the Ferrier microphysics present low ability to predict the night temperatures. For RH the experiments using the WSM6 microphysics scheme have the most consistent representation of the measured values (Fig. 3.16d). On the other hand the use of Ferrier microphysics scheme shows the biggest deviations during the night time.

3.6.3.2 Case of August 4 2010

Figure 3.17 presents the daily cycle of T2m and RH for Larissa and Anghialos for 04/08/2010. All experiments show a good agreement in T2m for Larissa during the day time but the same is not true for night time (Fig. 3.17a). WSM6 based experiments show the smallest deviations during the midday, followed by Ferrier based experiments. The experiments that use Goddard microphysics present substantial inconsistencies during the midday and afternoon. RH for Larissa is well represented from the first morning hours till the afternoon but after 17:00UTC the errors are increasing (Fig. 3.17b). For Anghialos's temperature the main characteristic is that all the experiments miss by almost 2.5K (2.5k to 3.5) the maximum afternoon temperature while they are quite accurate in the morning and the early night hours. Relative humidity daily cycle is well captured during the first morning hours by the experiments using Ferrier microphysics (Fig. 3.17d).

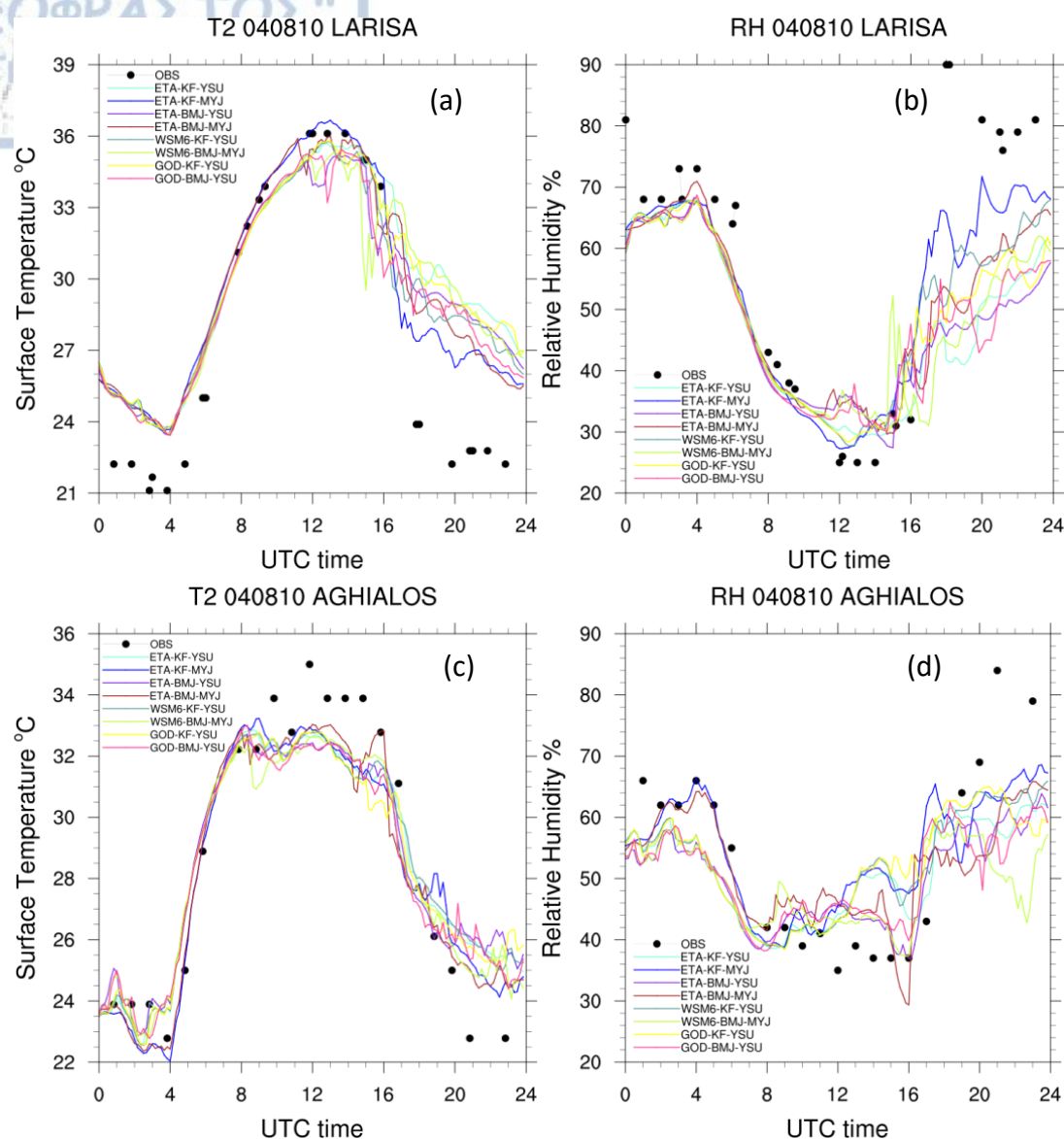


Figure 3.17. Daily cycle of measured and simulated 2m temperature and relative humidity in WRF-D03 for 04-08-2010 at Larisa (a and b) and Anghialos (c and d).

Goddard microphysics based experiments present the highest deviations for the whole day while WSM6 based experiments have the lowest overall deviations during the whole day, especially when WSM6 is coupled with YSU boundary layer scheme.

3.6.4 General Evaluation of the sensitivity experiments

From the twelve (12) performed set of experiments the ones employing Goddard microphysics scheme showed the worst statistics and biggest deviations in

WRF-D02 and WRF-D03 regardless the boundary layer and cumulus scheme coupled to. The experiments using Ferrier microphysics and especially when coupled with MYJ boundary layer showed some good results in WRF-D02. The coupling of Ferrier to YSU on the other hand proved to exhibit worst statistics than the former configuration. Talking about cumulus convection schemes (employed in WRF-D01 and WRF-D02 only) the KF showed overall better behavior both in results for WRF-D02 and WRF-D03. The coupling of WSM6 microphysics to YSU boundary layer and KF cumulus convection scheme showed the most consistent statistics overall in all cases (and those not presented here) and was selected for further evaluation in an enlarged sample of cases.

3.7. Performance evaluation of the selected scheme combination

3.7.1 Surface weather station evaluation

The same number of 20 stations of the Hellenic National Meteorological Service (HNMS), presented in Fig. 3.8, was the source for statistical evaluation of the selected model configuration (WSM6 microphysics, YSU boundary layer and KF cumulus schemes) in the inner domain of Greece (WRF-D02) This time the verification was carried out categorizing the selected cases according to the prevailing upper-air synoptic circulation types presented in section 3.2. The tool used to perform the statistics calculation was again the Model Evaluation Tool (MET 6.0, Brown et al., 2017). The time increment of the used meteorological data was three hours. The meteorological parameters examined were 2 m air temperature (TEMP), 2 m air relative humidity (RH), mean sea-level pressure (MSLP) and wind speed at 10 m (WIND). Using the distance weighted mean interpolation method with data from the four closest simulated grid points the value at the station location was obtained. Starting from Fig. 3.18 up to Fig. 3.21 the calculated statistics are pictured while Table 3.4 and Table 3.5 tabulate their actual values.

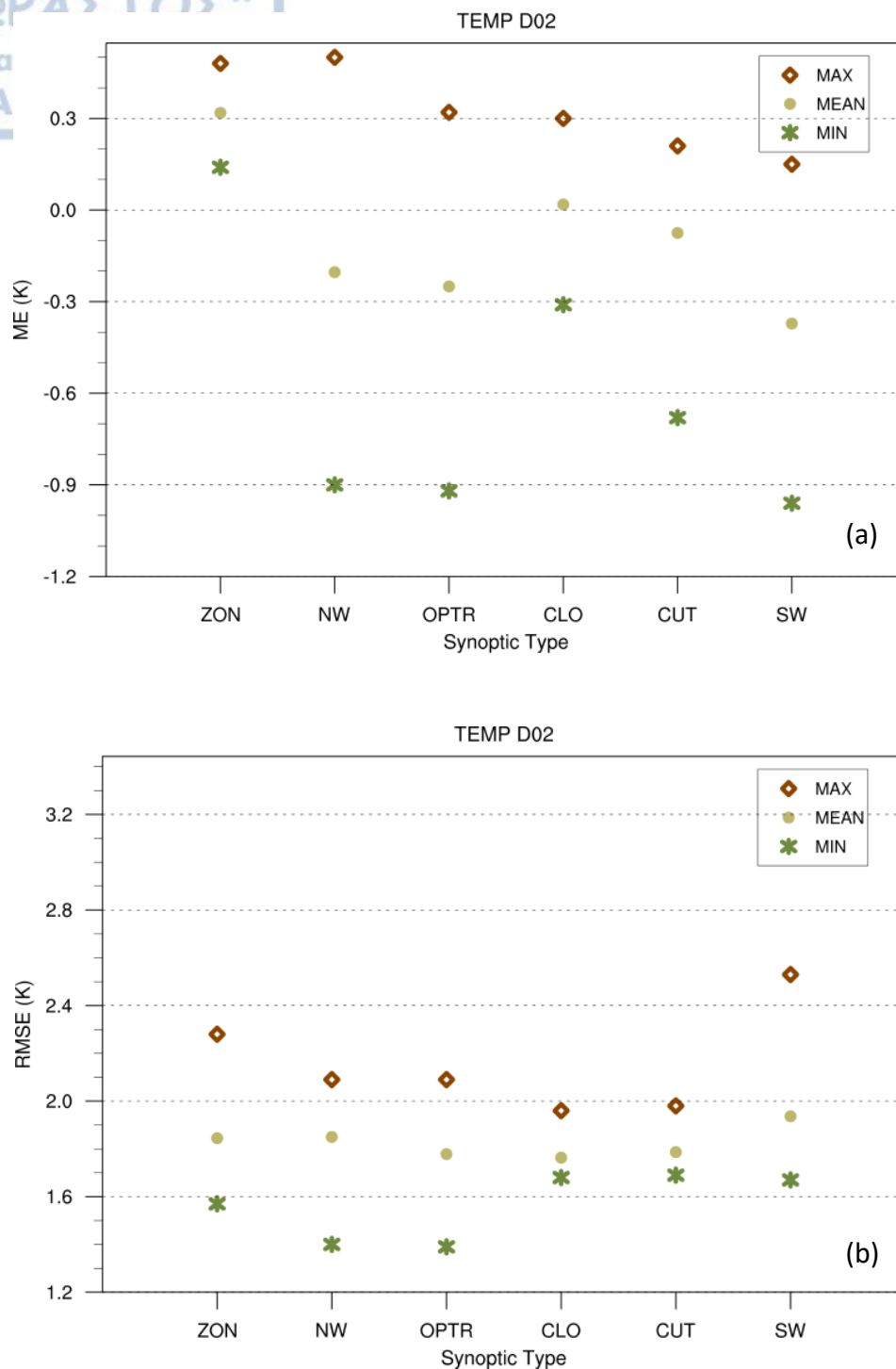


Figure 3.18. The minimum, average and maximum Mean Error (ME; model - observations) (a) and Root Mean Square Error (RMSE) (b) for 2m air temperature (TEMP) in relation to the upper-air synoptic circulation type for the inner domain (WRF-D02).

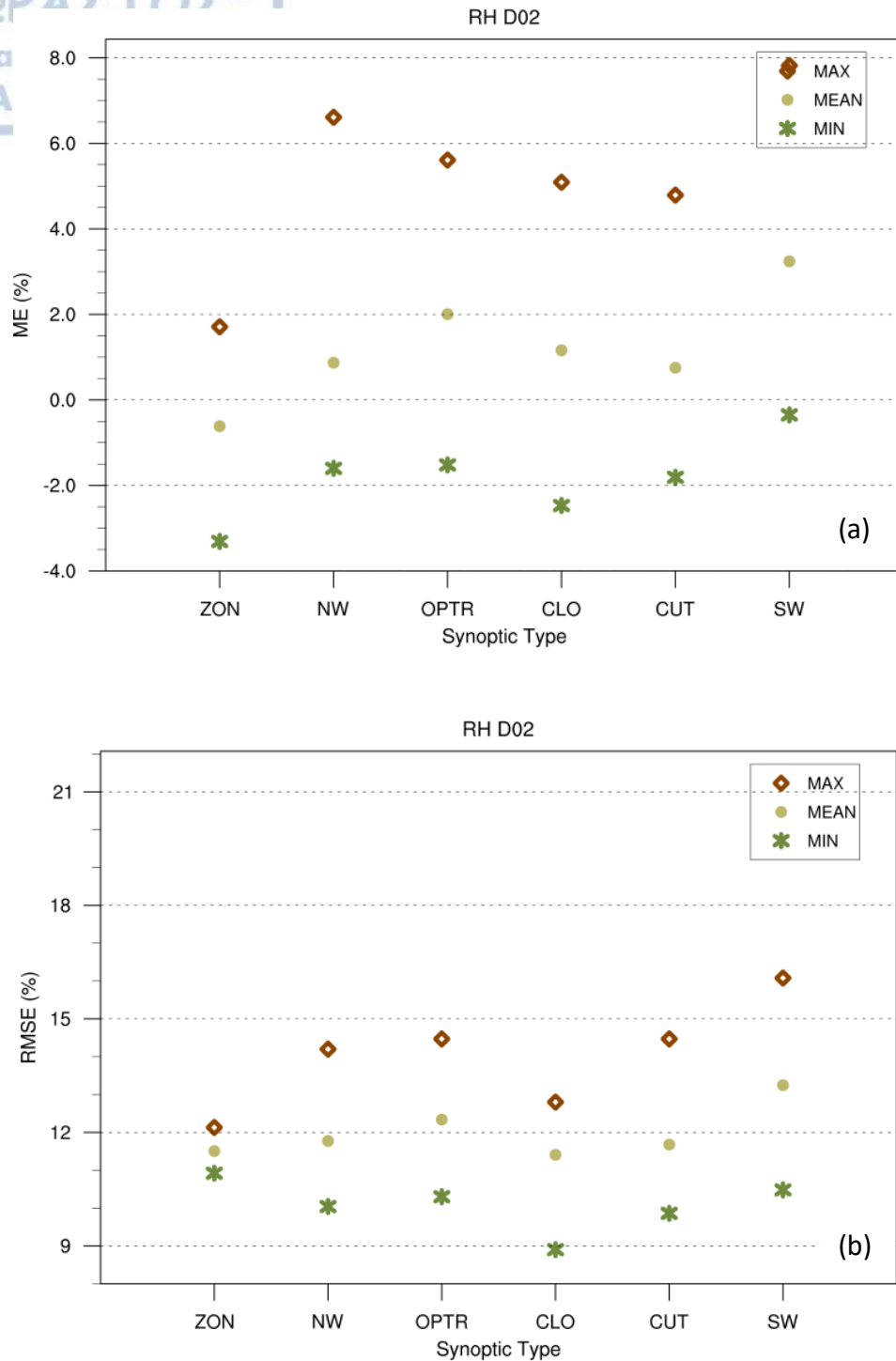


Figure 3.19. The minimum, average and maximum Mean Error (ME; model - observations) (a) and Root Mean Square Error (RMSE) (b) for 2m relative humidity (RH) in relation to the upper-air synoptic circulation type for the inner domain (WRF-D02).

Fig. 3.18 presents the Mean Error (ME) (Fig. 3.18a) and the Root Mean Square Error (RMSE) (Fig. 3.18b) of 2m air temperature by reference to the upper air synoptic types. The results shown are the aggregated statistics from all the six cases selected in each synoptic type. Minimum, mean and maximum values of ME and RMSE are shown. The maximum value of temperature overestimation is 0.5K in ZON type (Fig. 3.18a) which is the only type that the average ME is strongly positive (0.3K). The other types (NW, OPTR, CUT and SW) show an underestimation in TEMP ranging from -0.4K to -0.1K while the CLO type has an ME of almost 0K. The RMSE (Fig. 3.18b) presents its higher value in SW type (1.9K) while for all the other types the RMSE values are very close to 1.8K (1.8 ± 0.5 K).

With the exception of ZON synoptic type which has an average ME of -0.6% (underestimation) and a small spread of values (Fig. 3.19a, max ME=1.7, min ME=-3.3) the RH is overestimated for the rest of the synoptic types. Closely correlated to TEMP the ME of SW type is the largest (3.2%) and so does its RMSE reaching a value of 13.3%. ZON, NW, OPTR, CLO and CUT synoptic type show an RMSE of $11.9 \pm 0.5\%$ (Fig. 3.19b).

An underestimation of mean sea-level pressure is obvious in all synoptic types (Fig. 3.20a). The ME ranges from -0.2hPa in SW type to -1.0hPa for CUT synoptic type. The RMSE takes values from 1.3 in SW synoptic type to 1.6 in CLO type (Fig. 3.20b) The ZON and SW types present the lowest spread of RMSE (max RMSE – min RMSE = 0.4hPa).

Regarding the 10m wind speed, it is systematically overestimated. The lowest value of ME is calculated for OPTR (ME=0.5m/s). The highest value corresponds to ZON synoptic type (ME=0.8m/s). It must be noted that the spread of the ME is uniform throughout the synoptic types. The ZON, NW and CUT synoptic types present values of RMSE less than 2.5m/sec and spread less than 0.5m/sec. The CLO synoptic type has the highest RMSE (2.8m/sec) and the highest spread (min RMSE=2.3m/sec and max RMSE= 3.4 m/sec).

Pytharoulis et al. (2014) performed verification of the operational runs of the Department of Meteorology and Climatology of AUTH for a domain with grid spacing of 5km x 5 km. Their results come in agreement with the current findings, and in fact the selected configuration of the current study performs slightly better.

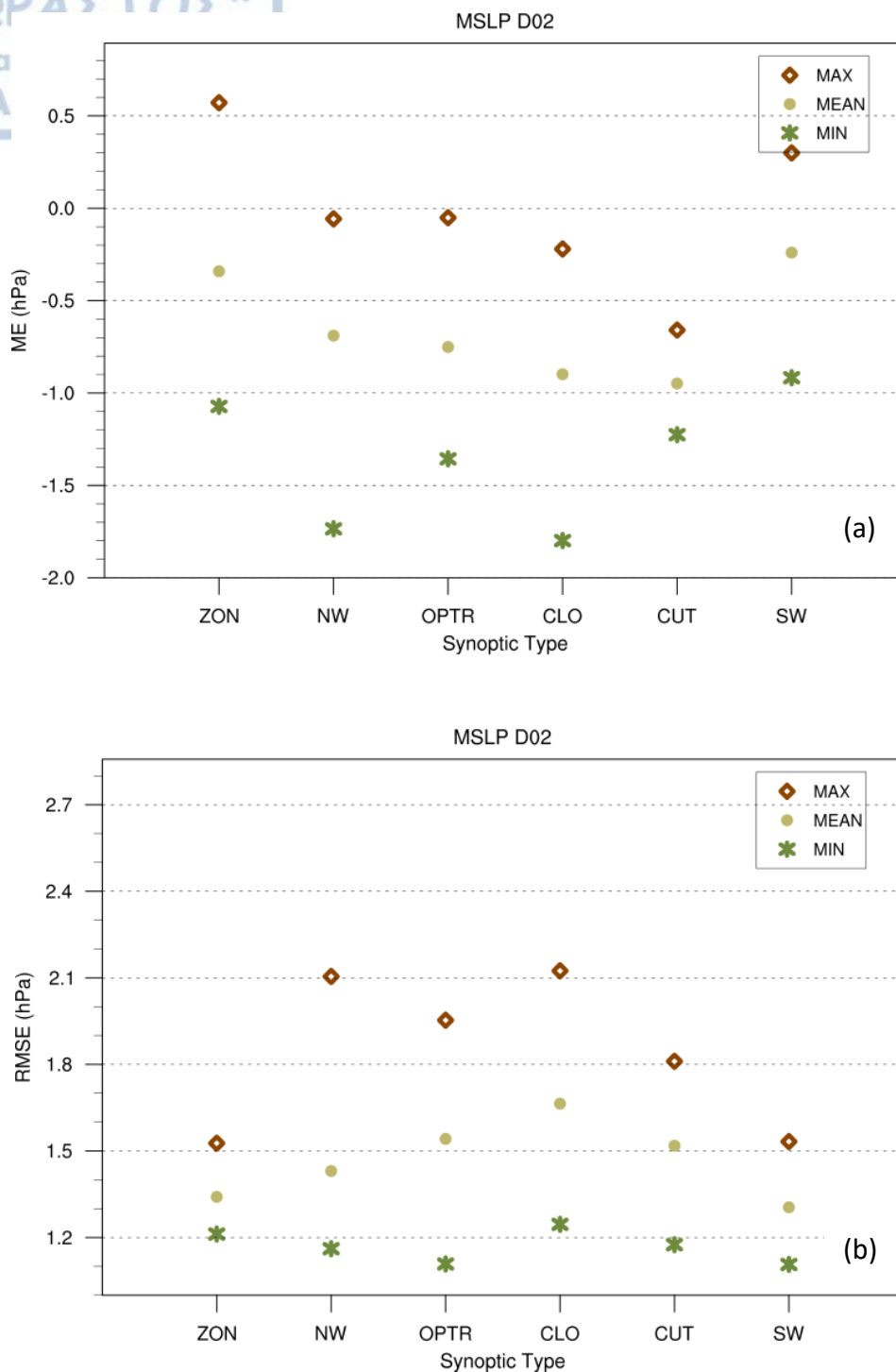


Figure 3.20. The minimum, average and maximum Mean Error (ME; model - observations) (a) and Root Mean Square Error (RMSE) (b) for mean sea level temperature (MSLP) in relation to the upper-air synoptic circulation type for the inner domain (WRF-D02).

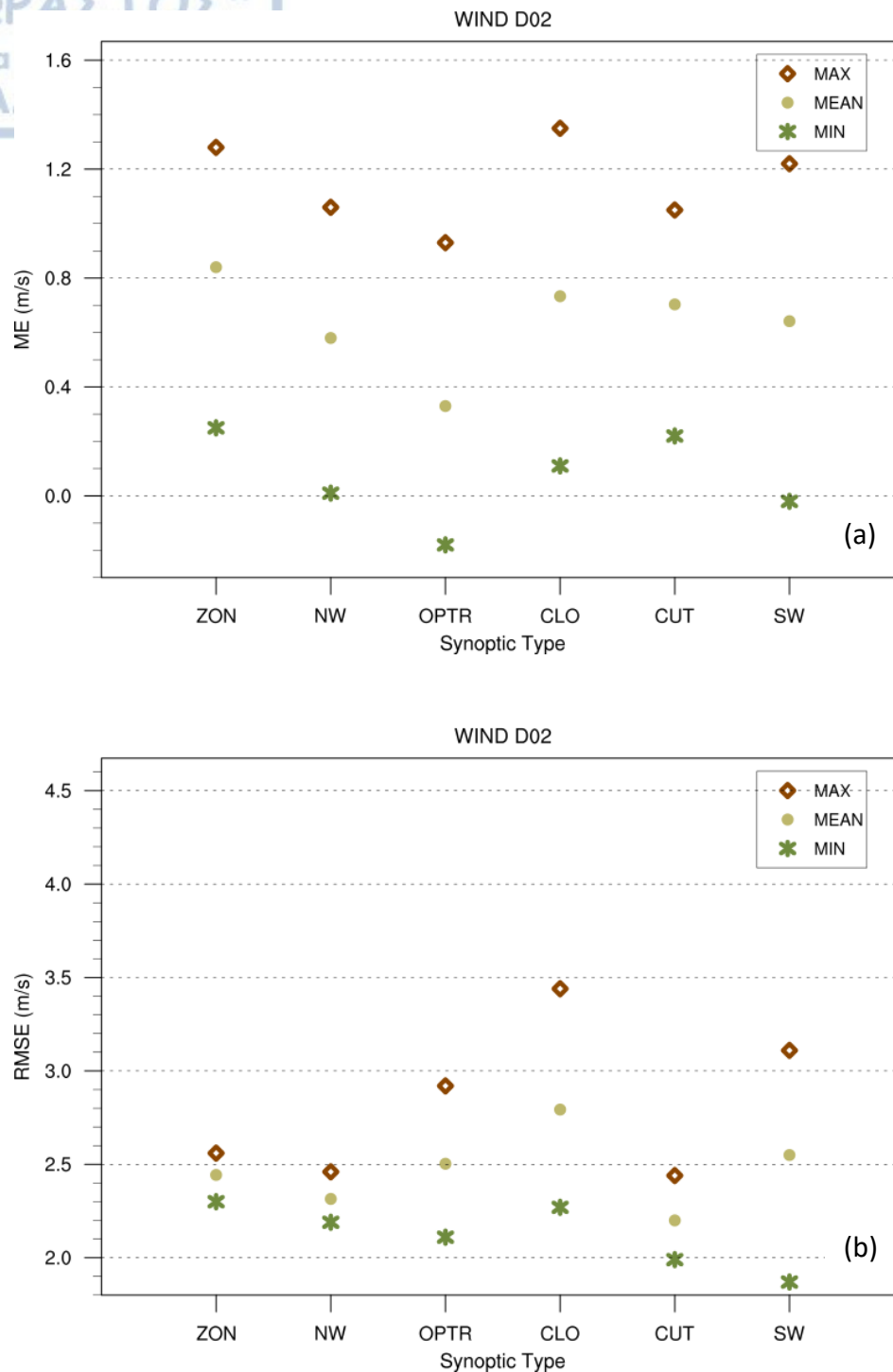


Figure 3.21. The minimum, average and maximum Mean Error (ME; model - observations) (a) and Root Mean Square Error (RMSE) (b) for wind speed at 10m (WIND) in relation to the upper-air synoptic circulation type for the inner domain (WRF-D02).

Table 3.4 Minimum, average and maximum Mean Error (ME; model - observations), Mean Absolute Error (MAE) and Root Mean Squared Error (RMSE), for 2m air temperature (TEMP), 2m air relative humidity (RH), mean sea-level pressure (MSLP) and wind speed at 10m (WIND), for each upper-air synoptic circulation type at D02.

		ZON	NW	OPTR	CUT	CLO	SW
TEMP_ME (K)	MIN	0.1	-0.9	-0.9	-0.3	-0.7	-1.0
	AVERAGE	0.3	-0.2	-0.3	0.0	-0.1	-0.4
	MAX	0.5	0.5	0.3	0.3	0.2	0.2
TEMP_MAE (K)	MIN	1.3	1.1	1.1	1.3	1.4	1.3
	AVERAGE	1.5	1.5	1.5	1.4	1.4	1.6
	MAX	1.8	1.7	1.7	1.6	1.6	2.1
TEMP_RMSE (K)	MIN	1.6	1.4	1.4	1.7	1.7	1.7
	AVERAGE	1.9	1.9	1.8	1.8	1.8	1.9
	MAX	2.3	2.1	2.1	2.0	2.0	2.5
RH_ME (%)	MIN	-3.3	-1.6	-1.5	-2.5	-1.8	-0.4
	AVERAGE	-0.6	0.9	2.0	1.2	0.8	3.2
	MAX	1.7	6.6	5.6	5.1	4.8	7.8
RH_MAE (%)	MIN	8.8	7.9	8.2	7.3	8.1	8.4
	AVERAGE	9.2	9.4	9.9	9.2	9.3	10.7
	MAX	9.5	11.3	11.7	10.8	11.2	13.1
RH_RMSE (%)	MIN	10.9	10.0	10.3	8.9	9.9	10.5
	AVERAGE	11.5	11.8	12.3	11.4	11.7	13.3
	MAX	12.1	14.2	14.5	12.8	14.5	16.1

Sensitivity studies and model performance

Table 3.5 Minimum, average and maximum Mean Error (ME; model - observations), Mean Absolute Error (MAE) and Root Mean Squared Error (RMSE), for mean sea-level pressure (MSLP) and wind speed at 10m (WIND), for each upper-air synoptic circulation type at D02.

		ZON	NW	OPTR	CUT	CLO	SW
MSLP_ME (Pa)	MIN	1.1	-1.7	-1.4	-1.8	-1.2	-0.9
	AVERAGE	-0.3	-0.7	-0.7	-0.9	-1.0	-0.2
	MAX	0.5	-0.6	-0.5	-0.2	-0.7	-0.3
MSLP_MAE (Pa)	MIN	0.9	-0.8	0.9	1.0	1.0	0.9
	AVERAGE	1.1	1.2	1.3	1.4	1.3	1.1
	MAX	1.2	1.8	1.6	1.8	1.5	1.2
MSLP_RMSE (Pa)	MIN	1.2	1.1	1.1	1.2	1.2	1.1
	AVERAGE	1.3	1.4	1.5	1.6	1.5	1.3
	MAX	1.5	2.1	1.9	2.1	1.8	1.5
WIND_ME (m/s)	MIN	0.3	0.0	-0.2	0.1	0.2	0.0
	AVERAGE	0.8	0.6	0.3	0.7	0.7	0.6
	MAX	1.3	1.1	0.9	1.4	1.1	1.2
WIND_MAE (m/s)	MIN	1.9	1.8	1.7	1.8	1.6	1.6
	AVERAGE	2.0	1.9	2.0	2.2	1.8	2.0
	MAX	2.1	2.0	2.3	2.7	2.0	2.4
WIND_RMSE (m/s)	MIN	2.3	2.2	2.1	2.3	2.0	1.9
	AVERAGE	2.4	2.3	2.5	2.8	2.2	2.6
	MAX	2.6	2.5	2.9	3.4	2.4	3.1

3.7.2 Characteristics of simulated and measured convective activity

The relative frequency distribution of maximum reflectivity, covered area by storms and maximum cloud height, integrated in hourly intervals, calculated from the domain WRF-D03 of the simulations and radar data is presented in Figures 3.22 to 3.24 as a function of the synoptic types. In every grid point of the domain the simulated reflectivity field was compared to the threshold value of 35dBz. The highest level at which the reflectivity was over the threshold was considered as the cloud top.

3.7.2.1 Maximum reflectivity

For ZON synoptic type (Fig. 3.22a) the distribution of model reflectivity is bimodal while the measured one is unimodal. A small maximum around 42 dBz represents 18% of the distribution and a second largest maximum around 52dBz accounts for 22% of the distribution. The maximum of the measured distribution is around 42dBz and is responsible for 50% of the distribution.

In NW synoptic type (Fig. 3.22b) the modeled and the measured reflectivity present common characteristics. In both cases a small amount of less than 15% of the distribution has reflectivity values up to 45dBz. From 45dBz to 55dBz both the simulated and the measured reflectivity accounts for more than 70% of the distribution.

The similarity continues in OPTR synoptic type too. The primary maximum for both simulated and measured reflectivity is around 52dBz (Fig. 3.22c). Even small deviations in percentages between simulated and measured values exist up to 50 dBz, the cumulative contribution of reflectivity <50dBz reaches the value of 50%.

In CLO synoptic type the distributions are unimodal in both the measured and the simulated distribution (Fig. 3.22d). The maximum in measured reflectivity is at 48dBz and has a value of 25% while in simulated reflectivity the maximum is at 55dBz with a value of 24%.

In CUT synoptic type the major part of the simulated reflectivity lies between 45dBz and 55dBz with a maximum at 53dBz accounting for 22% of the distribution

(Fig. 3.22e). The measured distribution has two maximums, one at 45dBz (15% of the distribution) and one at 50dBz (28% of the distribution).

Finally the SW distributions present entirely different results between the measured and simulated reflectivity (Fig. 3.22f). The modeled reflectivity presents an almost uniform distribution from 40dBz to 57dBz with a small maximum at 51dBz (20% of the distribution). The measured distribution has a major maximum at 45dBz which with its lateral columns (42dBz to 47dBz) accounts for almost 70% of the distribution.

3.7.2.2 Average Storm area

The general overview of Fig. 3.23 reveals that the majority of storms that were observed in the area and those simulated by the model have an area of up to 460km². In rare cases (less than 3%) there may reach up to 5000km².

For ZON type the first bin class (up to 460km²) accounts for 70% and 85% for simulated and modeled storms respectively (Fig. 3.23a). In the second bin class (460km² to 920km²) 10% of the measured storms fall in this category and 18% of the simulated ones. In NW synoptic type (Fig. 3.23b) the area distribution follows the same pattern as in ZON. The only difference is the occurrence of around 10-12% of storms measuring more than 2000km² in both measured and simulated calculated area

In OPTR synoptic type (Fig. 3.23c) the first bin class is the key category. Around 80% of both measured and simulated storms fall within this category and 95% has an area of less than 2000km². Apart from the usual predominance of the first bin class, in CLO synoptic type the model simulated almost 28% of the storms to have area of 460km² to 1300km² (Fig. 3.23d). The percentage of the radar measured storms that cover the same area is 20%.

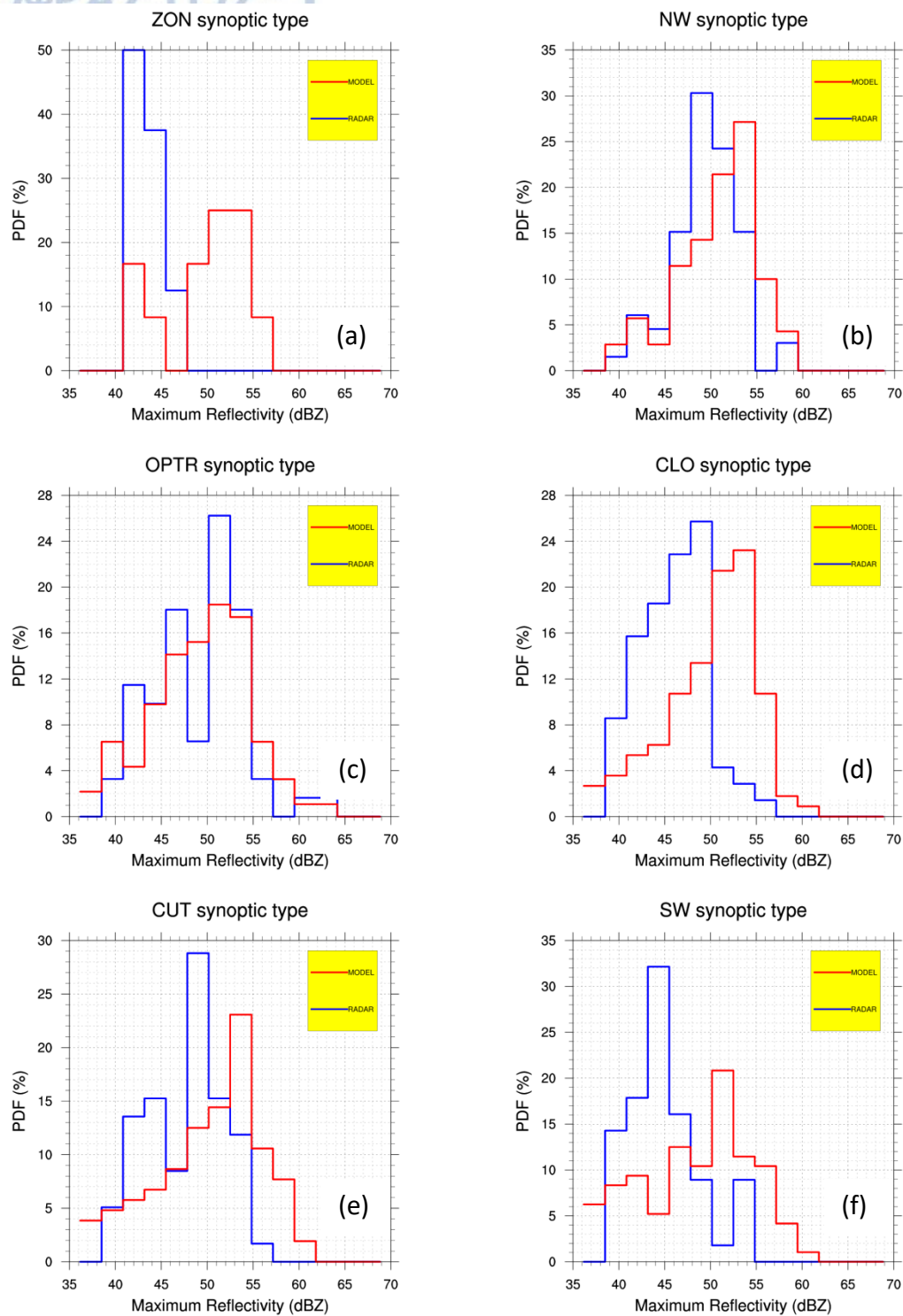


Figure 3.22. Relative frequency distribution of maximum reflectivity (dBz) at hourly intervals in WRF-D03 and radar data, for every synoptic type.

Sensitivity studies and model performance

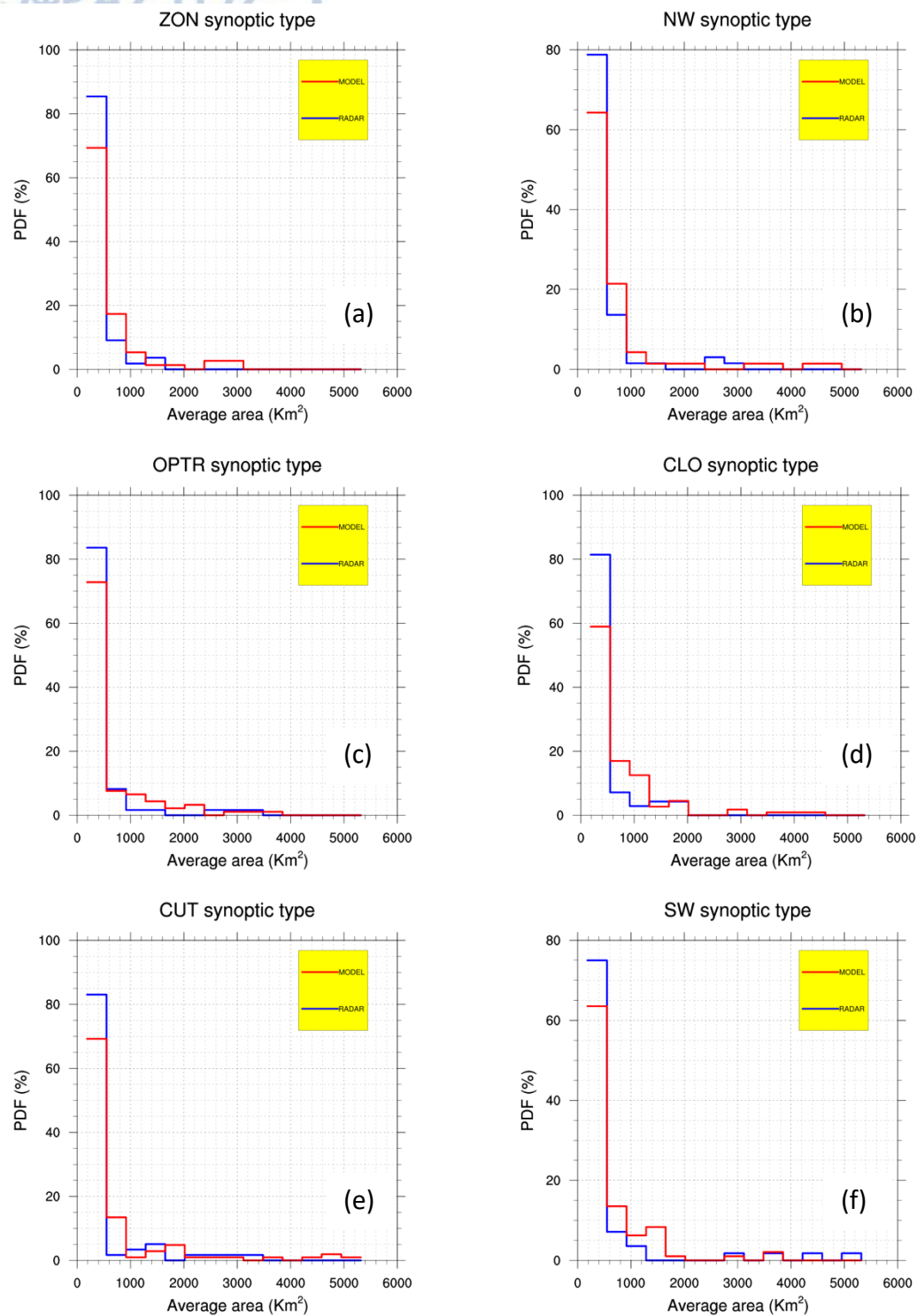
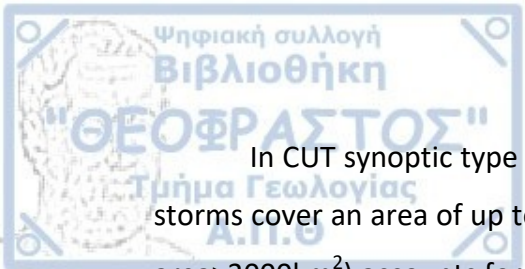


Figure 3.23. Relative frequency distribution of average storms area (km²) at hourly intervals in WRF-D03 and radar data, for every synoptic type.



In CUT synoptic type (Fig 3.23e) 70% and 83% of the simulated and measured storms cover an area of up to 430km^2 respectively. The tail of the distribution (storm area $>3000\text{km}^2$) accounts for 7% in simulated storms and 3% for measured ones. That means that extended storms covering more than 20% of the examined area lasted for at least one hour. Similar results are can be drawn for the SW synoptic type (Fig. 3.23f). Storms with area from 160km^2 to 2000km^2 are responsible for 19% of the activity in the area according to the model and 13% according to the radar measurements. A respectable percentage (~5%) of the measured storms has an area more than 4200km^2 .

3.7.2.3 Cloud Top

In regard to the cloud top the statistical distributions reveal the following:

In ZON synoptic type the measured (radar) heights have a dominant maximum in 6km (Fig. 3.24a) which accounts for 74% of the total storms. This is the maximum measured height since the percentages drop to 0 over this limit. The simulated heights present another image, with heights from 3km to 10km being responsible for more than 90% of the storms while the rest has height of up to 11km.

The plot for NW synoptic type (Fig. 3.24b) presents unimodal distributions with similar characteristics but shifted from one another. The measured distribution has the maximum at a height of 8km accounting for 46% of the storms, while for the simulated ones the maximum of the distribution is located at 12km and accounts for the same percentage.

For OPTR synoptic type (Fig. 3.24c) the model simulated distribution is bimodal with one maximum at 4km (27% of the storms) and the second (smallest) one at 12km (19% of the storms). The distribution of the measured heights has its wide maximum at 6-8km responsible for 86% of the storms.

Storms belonging to the CLO synoptic type (Fig. 3.24d) exhibit similar characteristics for both measured and simulated height. The maximum is located from 4 to 7km and accounts cumulatively for 75% in radar measured storms and 66% in simulated storms.

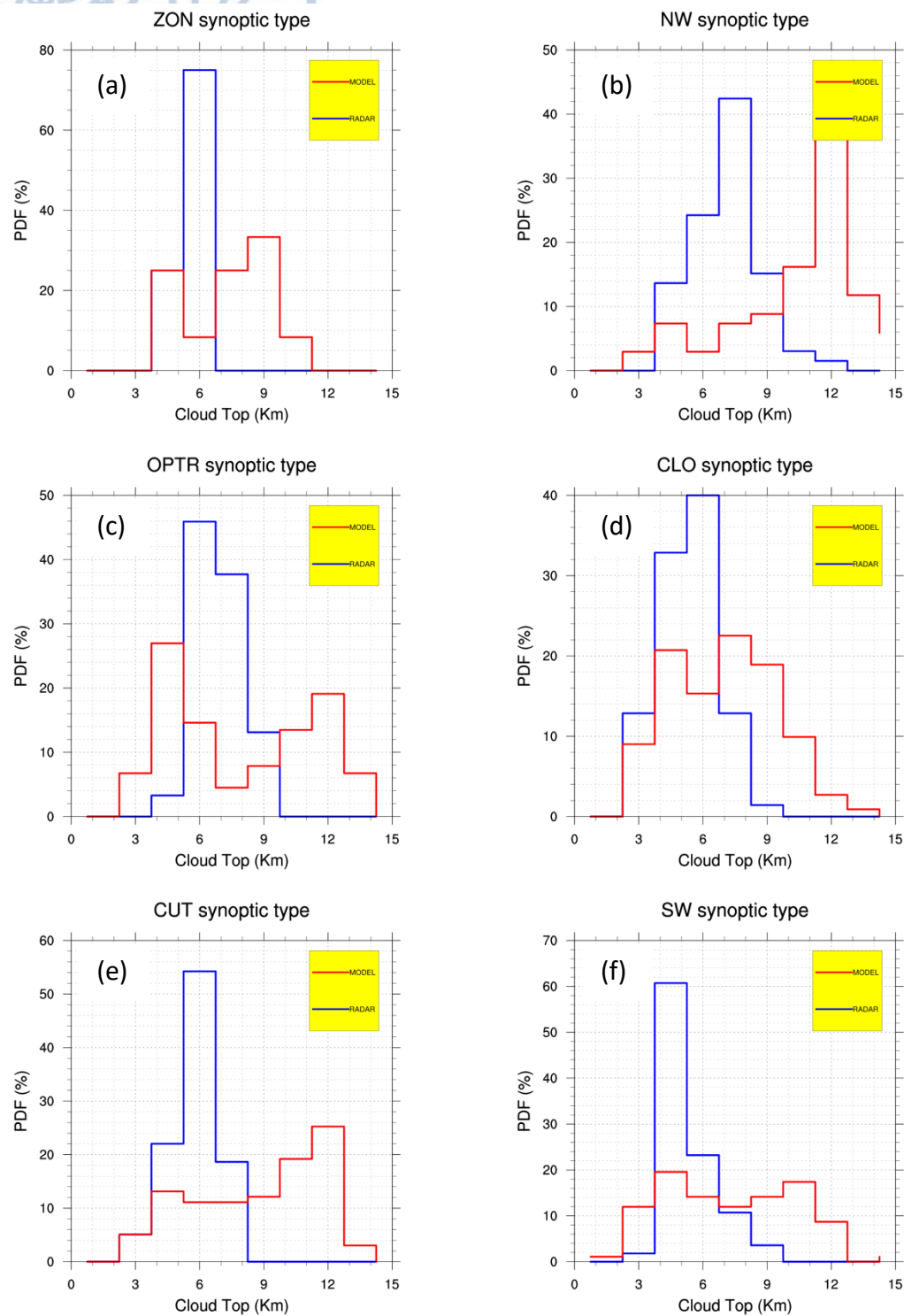


Figure 3.24. Relative frequency distribution of cloud top (km) at hourly intervals in WRF-D03 and radar data, for every synoptic type.

Simulations for the CUT synoptic type resulted in storms with cloud tops from 2.5 km to 13.5km, with more of them being over 9km (Fig 3.24e). The measured storms have a sharp maximum at 6km with two side lobes from 4 to 8km which includes all the storms.

Finally, the SW synoptic type (Fig 3.24f) has also a maximum at 4.5km (60% of the measured storms). The simulated storms present a wide bimodal distribution with two same height maximums accounting for 20% of the storms each. The first one is at 4km and the second one is at 10km

Overall WRF produced storms with higher reflectivity and more extended in horizontal and vertical dimension than the measured from the meteorological radar

Gallus and Pfeifer (2008) who examined five microphysical schemes in their study found a similar behavior with the meteorological model producing scattered areas with intense convective activity but a limited amount of areas with light reflectivity.

3.7.3 General Evaluation of the selected setup

New simulations were performed for cases categorized upon the prevailing synoptic condition for the examined day. The selected setup used the WSM6 microphysics, the Kain-Fritsch cumulus convection and the Yonsei University boundary layer scheme. This setup went under evaluation for both surface and cloud parameters

The classic statistics of ME and RMSE were used for surface parameters. For temperature at 2m (T2m) a small underestimation (RMSE \approx 1.7K) was apparent for almost all of the synoptic types examined. The relative humidity at 2m (RH2m) showed the expected opposite behavior (overestimation of about 12%). Mean sea level pressure was systematically underestimated while the RMSE had values from 1.3hPa to 1.6hPa. Higher values than those observed was the result of the simulations in all the synoptic types for wind at 10m. All the aforementioned results are satisfactory since they fall close to outcomes of previous studies in the area (Katsafados et al., 2012; Pytharoulis et al., 2014a).



Sensitivity studies and model performance

For cloud parameters a different approach was taken. Frequency distributions of maximum reflectivity, maximum cloud height and storm area, observed and simulated, were compared. Regarding the maximum reflectivity the cases of the ZON and SW synoptic types presented the biggest differences. The NW and OPTR simulation representatives formed distributions almost identical to the observed ones. For the area parameter there was a distinction between synoptic types leading to extensive convective activity (NW, SW) and those leading to small area storms (CUT, ZON). The model performed satisfactory since there was close resemblance between the observed and simulated distributions. Finally for observed cloud tops, the observed distributions are always unimodal, while the simulated distributions present mainly bimodal views, with the dominant mode higher than the observed.



Chapter 4

Spatial methods for Numerical Weather Prediction Evaluation

4.1 Introduction

The evolution of forecasting systems based on numerical weather prediction models gave them the ability to resolve mesoscale and smaller scale phenomena in extremely high detail. The models are now able to provide more realistic forecasts than the old coarse models, and even more their usefulness is increased since their observed intensities are better reproduced (Kain et al., 2006). The enhanced representation of specific fields (precipitation) can help forecasters better predict the evolution of convective activity (Weisman et al., 2008).

This general sense, common between scientists, faces various obstacles when has to be proven. Despite the indisputable progress, high resolution forecasts have difficulties in entirely matching local features of the observed phenomena. If a feature is observed but forecasted spatially offset from the observation the “double penalty” problem arises. This problem is called this way because the offset in the forecast creates an error that is counted two times. In the place where the feature is observed but not forecasted and in the place where the feature is forecasted but not observed. The forecasts may present an intuitively good quality for a forecaster but local scale errors are the dominant factor in the calculation of the overall error (Mass et al., 2002).

Fine scale disparities between observations and forecasts, not apparent in the assessment of low resolution forecasts, become prominent when traditional point to point verifications statistics (Jolliffe and Stephenson, 2005; Wilks, 1995) are used in fine scale simulations. Concerns about the representativeness of data provided by weather stations are increased, when performing statistic verification in fine grid scale (Tustison et al., 2001).

The availability of new sources of data (gridded radar fields and high resolution satellite data), the necessity to perform verification directed to specific needs, pushed scientists to take new roads and develop new strategies in forecast verification. Ensemble forecasting brought up the idea of probability distribution evaluation of the forecasts. Extreme values in meteorological phenomena, appearing more in the recent years, gave the opportunity to test long used methods in other sciences (e.g. economics) in these phenomena. Even more the new direction in verification is to provide meaningful results in the final users of numerical forecasts and not only in model developers and testers. In this context, given that a final user is concerned more about a forecast for a his limited area, forecasts with –maybe– compensating errors may present bigger value for the location of interest than forecasts giving statistically superior results (Ebert, 2009).

Following those needs, several new methods of verification have been proposed. Of special interest are those methods performing the verification between two gridded datasets, one observed and one forecasted. Almost all of the aforementioned methods belong to one of the next categories: a) neighborhood (of fuzzy), b) scale decomposition (or scale separation), c) object based (or features based) and d) field deformation. The scale separation methods employ band pass filters to identify the performance of the forecast in different spatial scales (Gilleland et al., 2010). Neighborhood verification techniques (the initial name was “fuzzy techniques”) measure the strength of the agreement with varying distance between a point observation and its surroundings (Ebert, 2008). Feature based approaches discover features in the observed and forecasted fields and compare their characteristics (Casati et al., 2008). Finally the field deformation methods alter the forecast field to make it look as much as possible to the observed (Keil and Craig, 2007).

In most of the previous methods the observed and verification fields must be available in a continuous grid, without missing values. Therefore they are ideal candidates for radar or satellite derived data. A brief analysis of the main representatives of each method will be presented in the next sections. The Method for Object Based Evaluation (belonging to the object based methods) that was used in the next chapter will be presented in detail in a specific section.

4.2 Description of spatial methods

4.2.1 Neighborhood approaches

In this approach single point data are compared to the values of points in their “neighborhood”. Starting from points close to each other the distance between the compared data gradually increases until a satisfying skill is reached. The simplicity of the method, the similarity of the scores used with those of traditional methods, and the ability to spot the scale at which the forecast has its best performance are the main advantages of the method.

One broadly used method of this type is the Fractional Skill Score (FSS) (Roberts and Lean, 2008). The statistic takes values from 0 to 1 (no skill to full skill) but for large enough samples, a value of $FSS > 0.5$ represents a skillful forecast. FSS has been used to assess the skill of long term precipitation forecasts (Mittermaier et al., 2013), convection permitting simulations (Ekström and Gilleland, 2017; Nachamkin and Schmidt, 2015) and operational ALADIN-CZ runs (Zacharov et al., 2019). Stratman *et al.* (2013) compared the results of FSS with traditional scores using the field of reflectivity $> 35\text{dBz}$ and found that the FSS provided an assessment consistent with experts’ impression of forecast skill.

4.2.2 Scale Separation/Decomposition

These techniques isolate features present in each scale of the examined phenomenon using a single band spatial filter. This way the verification is performed in each case separately providing information about the dependence of error on scale and the ability of the forecast to properly represent the selected scale of the phenomenon (Gilleland et al., 2009). Contrary to the neighborhood methods the scale separation manipulations retain the whole information contained in the examined field, lost with the smoothing performed with the neighborhood methods, and the original field can be recreated again.

The intensity scale (IS) method (Casati et al., 2004) is one method falling into this category and provides skill estimates as a function of intensity and spatial scale. Using a bootstrapping approach Casati (2010) improved the method providing

confidence intervals for aggregated IS statistics. Marzban and Sandgathe (2009) used the variogram plots of observed and forecasted fields to compare the distributions of their spatiotemporal scale structures.

Finally Weniger *et al.*, (2017) used wavelets (Eckley *et al.*, 2010) to verify the ensemble prediction system (COSMO-DE-EPS, Gebhardt *et al.*, 2011; Peralta *et al.*, 2012) operated by the German Meteorological Service. He concluded that while the method performs well in distinguishing between different cases it faces problems following the temporal evolution into the same case.

4.2.3 Feature/Object Methods

The feature based approach uses techniques employed in the science of image interpretation and pattern recognition. The forecasts are examined as they were images and features are extracted using image analysis methods. Every method uses its own strategy in i) the isolation of a separate feature contained in the whole image, ii) whether some features appearing to be split belong to a wider one and must be treated as one, iii) the way the establish relations between features of the observed and forecasted fields and finally iv) the measures used to quantify the relations.

The first method of this family that was described by (Ebert and McBride, 2000) was the “contiguous rain areas” (CRAs). In this method the features are identified as the union of areas in the forecast and observed fields, in which the field values surpass a pre selected limit. The examined qualities of the objects are the location of occurrence, their shape and the intensity of their values. Tartaglione *et al.* (2005) used this method to compare rain gauge observations with high resolution simulations during a heavy rain event, in the Island of Cyprus and found that the domain size plays a crucial role in the results. Grams *et al.* (2006) examined the sensitivity of the method in the selection of the limit to characterize the areas, together with the smallest area that the features might have to be included in the analysis. They concluded that the raising of the limit creates representativeness concerns for the derived objects. The same method was used by Ebert and Gallus (2009) in a set of artificial and real cases (Ahijevych *et al.*, 2009) to find out that the

method provides meaningful results for the intensities of the forecasted value (rain). Recently the effect of horizontal grid size of the simulations in the method was examined (Mariani and Casaioli, 2018) to conclude that the CRA analysis is highly sensitive to both the temporal and spatial resolution.

Marzban and Sandgathe (2006, 2008) proposed the cluster analysis (CA) technique in which a large dataset is categorized into a number of clusters minimizing the internal spread of the cluster and maximizing its distance from the other clusters. To assess timing errors Marzban et al. (2008) performed the method using time lags between the observed and forecast fields to find out that in general the models are “on time”. Finally Marzban *et al.* (2009) pointed out that it is still difficult to decide which is the best measure of distance between the clusters that should be used to characterize the error.

Nachamkin (2004) supported that intense phenomena as heavy precipitation and convection should be verified separately, since their verification in the context of a more general model verification lessens their added value. He used the composites method to verify strong winds and found out that his method performs well up to 66h of lead time. The method creates composite of similar events, putting them on a common grid for both forecast and observed fields. Then the two composite fields are compared using different metrics, such as their probability density functions. Nachamkin *et al.* (2005) employed this method to evaluate precipitation forecasts concluding that the dimension of the created common grid plays an important role in the final statistics. The application of this method to the set of artificial and real cases (Ahijevych et al., 2009) revealed that this method performs better when a sufficient number of cases are “composited”.

The method of SAL (Structure, Amplitude, Location) introduced by Wernli (Wernli et al., 2008) derives objects by selecting continuous grids satisfying a criterion, which is directly related to the local maximum of the field. Three components representing the Structure (large/flat of small/peaked), Location (distance between the forecasted and observed objects, but also within the area of the objects) and Amplitude (weighted difference in the intensity between the objects) summarize the methods metrics. The SAL method results are strongly influenced by the domain chosen for the verification (Wernli et al., 2009). Weniger

and Friederichs (2016) combined the SAL with three external optical identification algorithms and found that the threshold level set to the studied algorithms induces high sensitivity and unstable behavior of object dependent SAL scores. Lawson and Gallus (2016) employed the method using the composite reflectivity to derive objects, and found that the method is quite sensitive to limit selection. Wałaszczek et al. (2017) pointed out that the method can capture the model tendency to underestimate total cloud amount. Radanovics et al. (2018) checked the ensemble (eSAL) version of SAL to describe the performance of the ensemble forecasts conducted for the summer period of 2007 in the Alpine region. In their study Gofa (Gofa et al., 2018) used the SAL method for the evaluation of Mediterranean and Greek area forecasts with different grid spacing and found that the component providing more information about the model skill is resolution dependant.

The Gaussian Mixture Model (GMM) method (Lakshmanan and Kain, 2010) tries to place Gaussian functions into an image in such a way that the final result resembles the forecast's image. The parameters of the Gaussians used together with their number may convey information about the scale in which the verification takes place, the orientation and the intensities of the features in the forecast.

Finally the last presented feature based method -and the one used in the current thesis -is the **Method for Object based Diagnostic Evaluation–MODE** (Brown et al., 2004; Davis, Brown and Bullock, 2006). The method will be thoroughly presented in the next subchapter. In this method objects are identified through a rather complex procedure and their attributes are used to provide useful metrics for the interpretation of the models' performance. The application of the method (Davis et al., 2006b) proved that the method is able to distinguish and provide detailed information about the characteristics of convective rain systems happening in the US. Furthermore using as input data forecasts from the NMM and ARW versions of WRF they concluded that the ARW performs slightly better than the NMM in intense events. Another use of the method, this time using cloud cover to derive objects, showed the great importance of the threshold choice in the final results. Cassola et al. (2015) verified an ensemble of simulations using various microphysics schemes for heavy precipitation events using traditional methods and MODE. They found that single moment class schemes perform better than double moment schemes in the

selected cases. In his two works Bytheway (Bytheway and Kummerow, 2015; Bytheway et al., 2017) assessed the performance of the High Resolution Rapid Refresh - HRRR (ESLR) model of the national Weather Service and highlighted the differences between HRRRv1 and HRRRv2. Griffin et al. (2017) used MODE to conclude that 1-h forecasts of clouds in HRRR are more accurate than the 0-h analyses. He ascribed that to the better representation of large clouds by the model.

4.2.4 Field deformation Methods

The fourth broad category of spatial methods works in the whole field in contrast to the feature based methods focusing on individual features within the field. The forecast field undergoes spatial processing, aiming in close resemblance of the transformed field to the observed field. The spatial processing needed is expressed with the suitable metrics (Zinner et al., 2008) and their values are estimated. Keil and Craig (2007) used the forecast quality measure (FQM) as a metric and the improved displacement and amplitude score (DAS) to account better for the false alarms (Keil and Craig, 2009). The optical flow suggests that the transformation of one image to another can be represented by the flow of a liquid. Marzban and Sandgathe (2010) used this technique (known from image processing community) pretending that the initial and the processed field in this method is the succession of two images to assess the quality of MM5 surface pressure forecasts. A variation of the method employs the wrapping of the image/field and in this case the image wrapping statistic (IWS) is used as the metric. This statistic was used to test the cases of Ahijevych *et al.* (2009) with great success in simple geometric cases and adequate results in real cases.

4.2.5 Summary characteristics

In Table 4.1 the information conveyed by each method on several aspects of verification is presented. We can see that all methods are able to identify intensity errors. Structure errors are only captured by the feature based methods. The field deformation and feature base methods can spot location errors too. Finally neighborhood and scale separation methods are capable of defining the resolution in which the forecast has sufficient skill.

Spatial methods for Numerical Weather Prediction Evaluation

Table 4.1. Summary of the information that each spatial verification method category can convey (adopted from Gilleland *et al.*, 2010)

	Skillful scales	Location Errors	Intensity Errors	Structure Errors	Occurrence (hit, miss, false alarms
Neighborhood	Yes	No	Yes	No	Yes
Scale Separation	Yes	No	Yes	No	Yes
Features Based	No	Yes	Yes	Yes	Yes
Field deformation	No	Yes	Yes	No	No

4.3 The Method for Object Based Diagnostic Evaluation - MODE

4.3.1 Objects definition

As discussed in the previous section MODE belongs to the object based methods of evaluation. The first question coming into mind is how we can define objects in the sense of the method. Objects are specific parts of a field presenting special interest for a study. This field may be an observed field or a forecasted one. Rain, pressure, clouds and radar reflectivity are mainly analyzed using MODE.

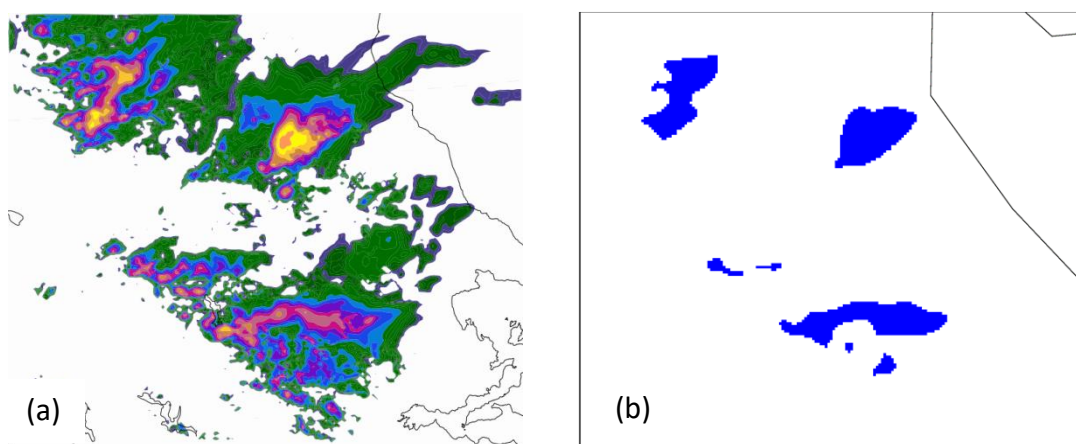


Figure 4.1. Raw reflectivity field (a) and derived objects (b) using the 35dBz threshold for an arbitrary day.

Figure 4.1 presents an example of objects using simulated radar reflectivity field. Warm colors (Fig, 4.1a, purple to orange) depict reflectivities > 35dBz used to

derive objects (Fig. 4.1b). These objects are approximately the areas that a forecaster would focus during a routine view of the images. MODE analyze these objects (in observed and forecasted fields), quantify their characteristics and compare them to express the degree of agreement between them. Objects belonging to the same field representing a single phenomenon may be merged to form a cluster. Objects belonging to different fields (i.e. forecast and observation) may be matched corresponding to a hit in the classic statistic methods.

4.3.2 Resolving Objects

The first stage in the MODE is the resolution of objects, the transformation of raw field to object field (Fig. 4.2).



Figure 4.2. How are the objects resolved?

A human eye would intuitively select the most interesting parts in an image and focus on them. The computer programming of such an intuition is difficult or even impossible to achieve. To circumvent this limitation the method uses the convolution-thresholding approach portrayed in Fig. 4.3.

In MODE the working grid G is simply a set of $N_x N_y$ points without taking into account the grid spacing. All grids points are referenced to the start of the grid and no anchor point is defined for it.

The first step in the resolution of objects is the convolution. Convolution is an operation on two functions, which returns another function. In image processing the convolution is used to implement various digital filters. In MODE the convolution

Spatial methods for Numerical Weather Prediction Evaluation

operation acts as a weighted average function. The raw field is subjected to the effect of the convolution filter. The filter has one adjustable parameter which is the radius of influence (R).

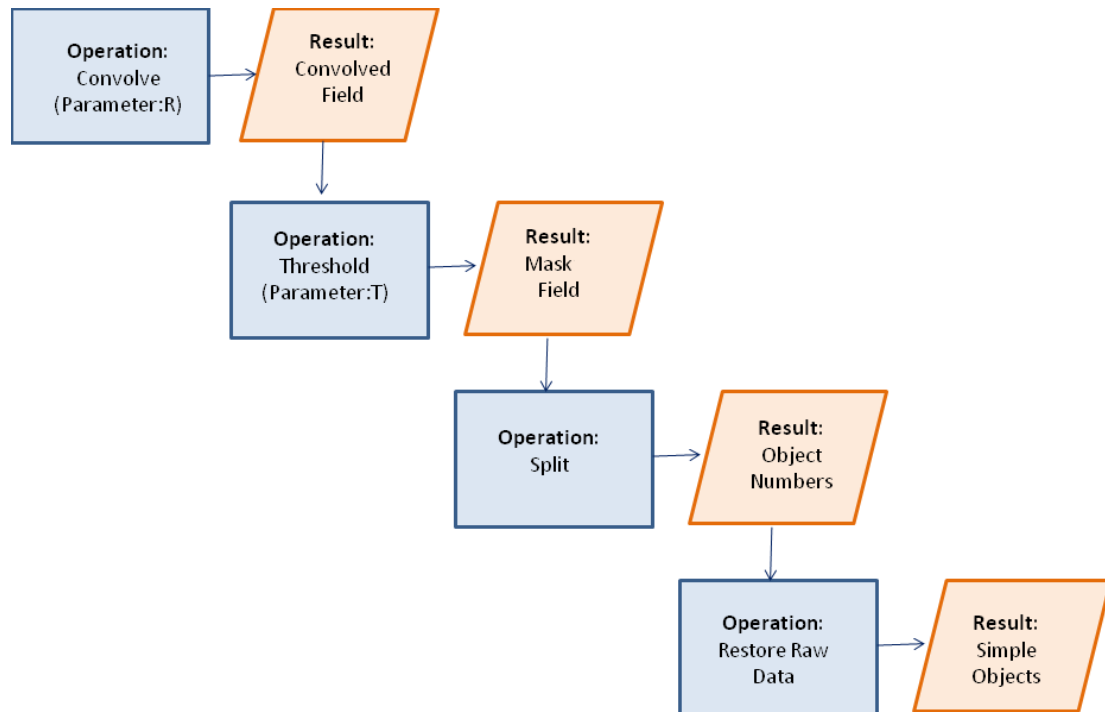


Figure 4.3. Flowchart for resolving objects

If we denote by x and y the coordinates of the grid G , by $f(x, y)$ the raw field, the convolved field $C(x, y)$ is given by

$$C(x, y) = \sum_{(x', y') \in G} f(x', y') \phi(x - x', y - y') \quad (4.1)$$

and the convolution filter function ϕ is given by

$$\phi(x, y) = \begin{cases} H & \text{if } \sqrt{x^2 + y^2} \leq R \\ 0 & \text{otherwise} \end{cases} \quad (4.2)$$

The height H of the filter satisfies the following relation

$$\int_G \phi = \pi R^2 H = 1 \quad (4.3)$$

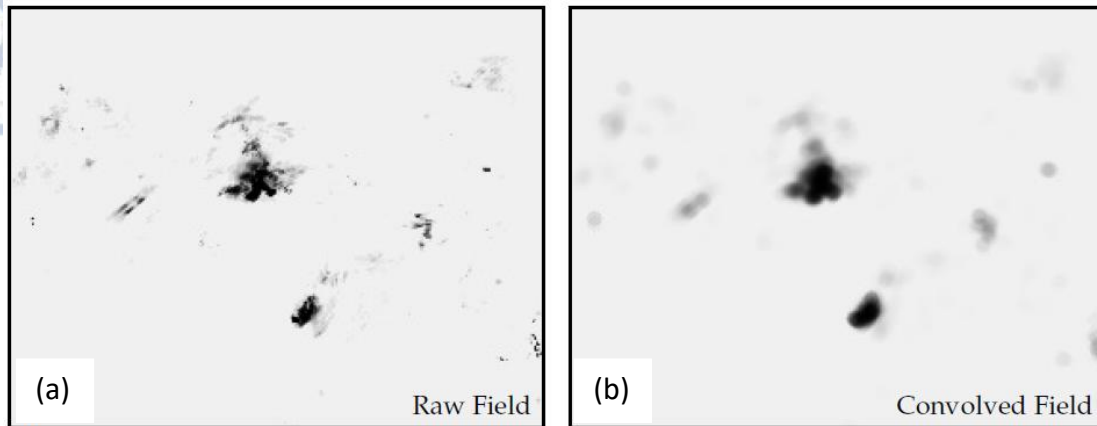


Figure 4.4. Field before and after convolution (adopted from Bullock *et al.*, 2016)

Figure 4.4 presents the raw (a) and convolved (b) field. We can see that fine spatial details are faded just like applying a low pass filter. That is because the filter acts as a moving average in spatial scale. It can be proven that the final value of the convolved field $C(x,y)$ in position (x,y) is the average in its neighborhood, confined by the radius R . Two convolution properties can be further proved: It is commutative and it preserves the total amount in the field, as a result of equation 4.3.

4.3.4 Thresholding

The next manipulation that the field undergoes is the thresholding. This is a process producing the mask field M :

$$M(x,y) = \begin{cases} 1 & \text{if } C(x,y) \geq T \\ 0 & \text{otherwise} \end{cases} \quad (4.4)$$

where T is the threshold. The new field is now the object field which contains grids for which $M = 1$. The objects will be constructed using only those grids. The geometrical properties of the objects can be calculated from the mask field M . But other properties of the objects cannot be derived since the original data values are not present in the mask field.

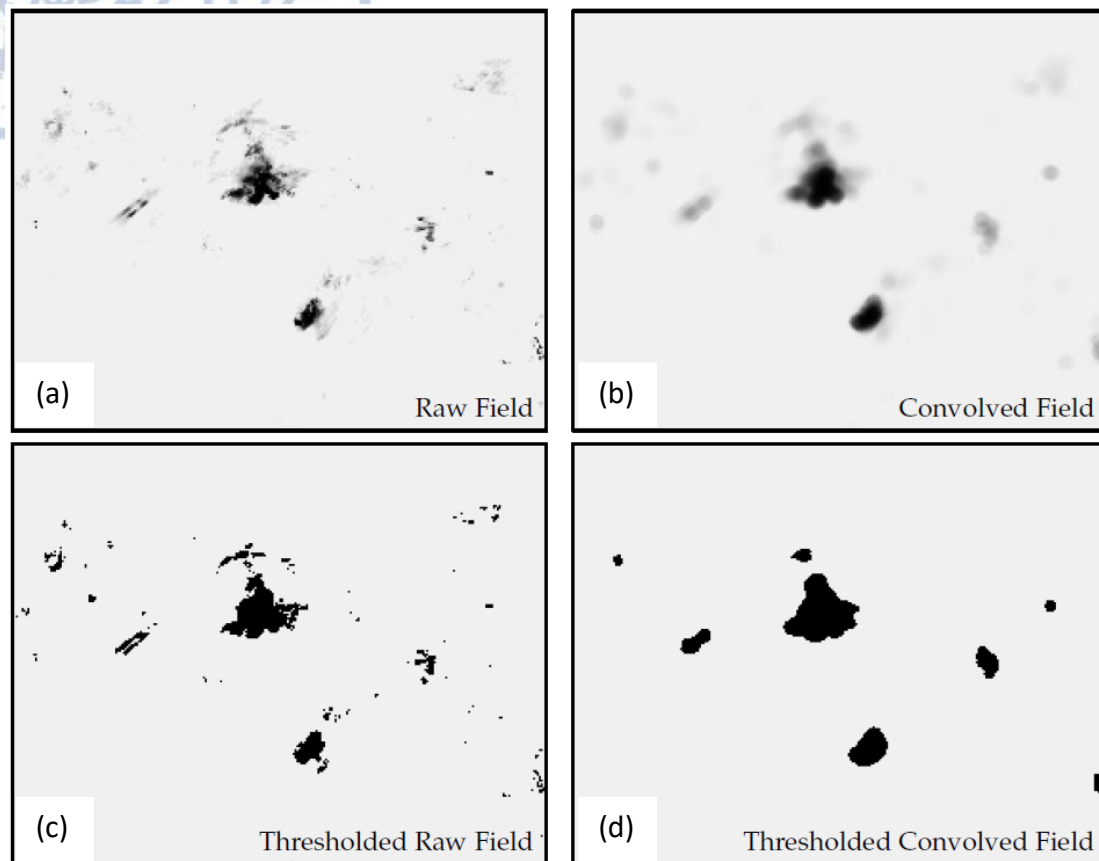


Figure 4.5. Results of thresholding the raw and the convolved field (adopted from Bullock *et al.*, 2016)

Figure 4.5 presents the result of thresholding the raw field (Fig. 4.5a) and the convolved field (Fig. 4.5b), providing the explanation on why the convolution step was performed. The thresholding of the raw field produces a noisy field (Fig.4.5c), with numerous small components of questionable value. On the other hand thresholding the convolved field results in lower number of objects, with better defined edges and a considerably larger size (Fig. 4.5d). The image they present matches better to the one that the human eye would gain trying to distinguish the original images' areas of interest.

4.3.5 Splitting

The idea of object creation is depicted in Figure 4.6. Green dots represent points (x,y) which after the thresholding were assigned a value of $M(x,y)=1$. Grids having such a grid in their lower left corner (blue grids) are used to create the

objects. Three separate objects are visible in this field and are numbered sequentially (Fig. 4.6, right side). This process of finding the pieces belonging to the same object and, and assigning numbers to the objects is called splitting.

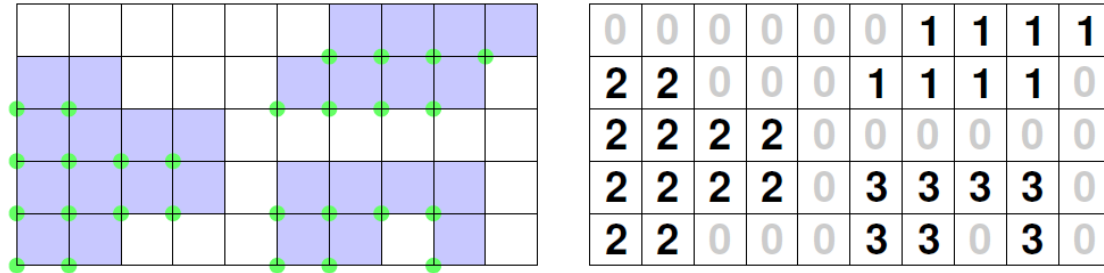


Figure 4.6. Numbering simple objects (adopted from Bullock *et al.*, 2016)

Simple geometrical properties of the objects may be calculated in this stage. For example the area of an object is the number of the grids that constitute the object (In Figure 4.6 the object #3 has an area of 7).

4.3.6 Restoring the Data

In order to be able to calculate properties of the objects associated with their intensity, the original field values should be restored. The object field B is defined by

$$B(x, y) = \begin{cases} f(x, y) & \text{if } M(x, y) = 1 \\ 0 & \text{otherwise} \end{cases} \quad (4.5)$$

This way properties like percentiles of intensities or intensity-weighted centroids may be calculated.

4.3.7 Attributes

MODE does not perceive objects the way a human does. That's way the method uses the idea of Attributes to characterize the objects. Such quantities, measured or calculated, provide meaningful information about spatial features or properties of the objects.

Two categories of attributes are defined for the objects. The first one deals with individual objects. Single objects derived from either the observation or

forecast field. The most common example in this category is the object's area. The second kind of attributes is defined for object pairs. For example if we take an object from the forecast field and one from the observed field we can find the area of the union of two objects. As in classic statistics ratios and differences are used for the quantification of the results. Ratios present the advantages of being scale insensitive since they are dimensionless.

There are attributes calculated directly from the objects, and attributes which involve a goodness-of-fit criterion to be "fitted" to the objects. In the next paragraphs those two types of attributes will be presented.

4.3.7.1 Fitted Attributes

The *centroid* of an object is the geometric center of the object (Fig. 4.7a). Using this attribute we can define its location with a point, despite the fact that an object covers a larger area around its centroid.

The *axis* (Fig. 4.7b) specifies the overall spatial orientation of the object. It can provide information about the evolution of the phenomenon that the object represents.

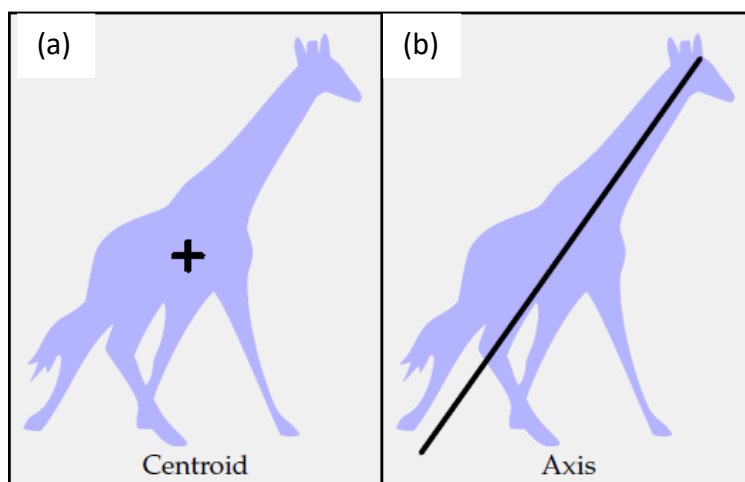


Figure 4.7. Centroid and Axis (adopted from Bullock *et al.*, 2016)

The *length* and *width* of an object is defined as the length and width of a fitted rectangle as shown in Fig. 4.8. The fitted rectangle should satisfy two criteria: i) it should be the smallest one enclosing the object and ii) the object's axis must be parallel to the long sides of the rectangle.

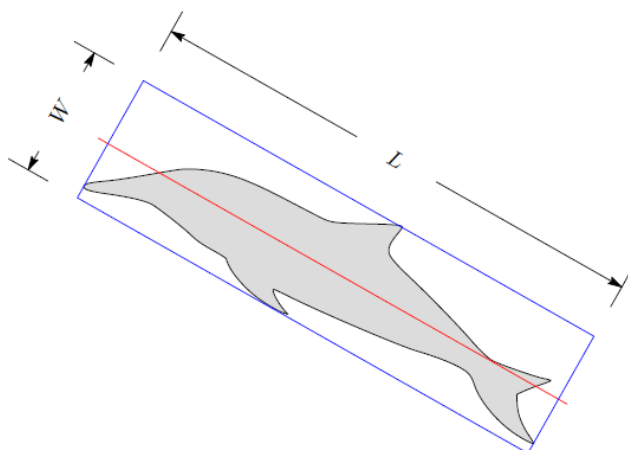


Figure 4.8. Length and width (red line indicating object's axis, adopted from Bullock *et al.*, 2016)

The *curvature* of an object can be defined by finding the circle of best fit to the curve of the object. This is done using the least squares approach. The curvature of the object is the curvature of the fitted circle. The center of curvature of the object is the center of the fitted circle (Fig. 4.9) .

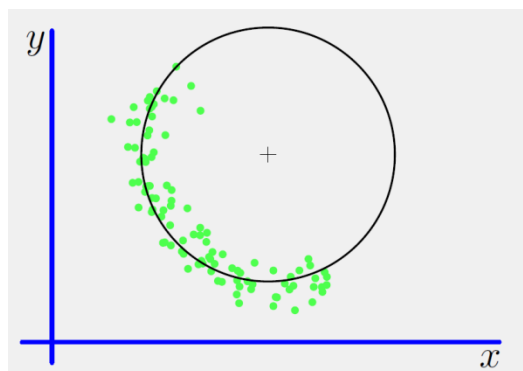


Figure 4.9. Curvature (adopted from Bullock *et al.*, 2016)

The next attribute is the *convex hull*. In geometry a region is thought to be convex if the line that joins every two points of the region lies entirely inside the region. In Figure 4.10 the ellipse is convex, but the star shaped region is not. A line joining point A to point B will pass from areas out of the star. The convex hull of a region is the smallest convex region that contains the given region. A rubber band

running around the star is a practical representation of its convex hull. For example the convex hull of the star in the right part of Figure 4.10 is the red rhombus surrounding it.

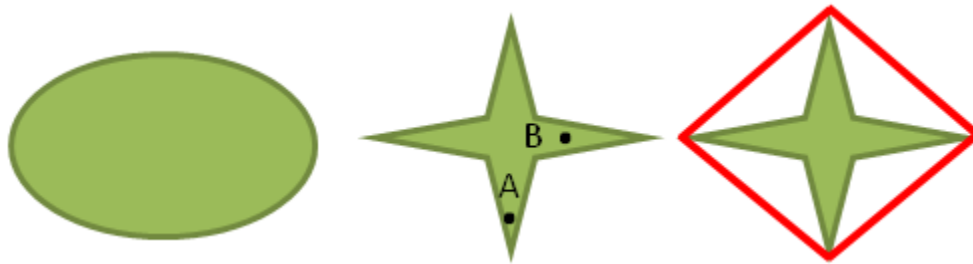


Figure 4.10. Illustration of convexity

4.3.7.2 Area Attributes

Area characterizes the size of an object. In case of pair of objects it characterizes the amount of overlap. Figure 4.11 presents three different measures for two overlapping objects. In the left part the union counts the total area of both the objects. The intersection (Fig. 4.11, middle part) counts the area of the overlapping portion of the objects (zeroed out, in non overlapping objects). Finally the symmetric difference is the total area minus the overlapping area.

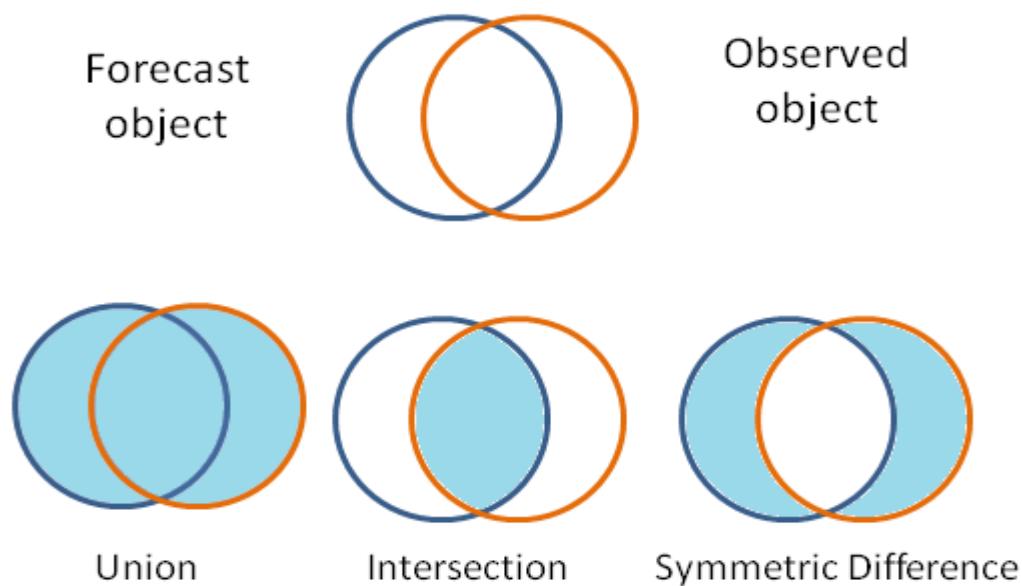


Figure 4.11. Area attributes

Object *complexity* provides a measure of how complicated an object is.

MODE measures the complexity as the difference between the area of the object and the area of its convex hull:

$$Complexity = \frac{A_{hull} - A_{object}}{A_{hull}} \quad (4.6)$$

Complexity can take values from 0 (if the object is convex, meaning that the objects area and its convex hull area are the same) to <1. Figure 4.12 presents objects with increasing complexity: penguin (a) $c=0.2$, bird (b) $c=0.26$, giraffe (c) $c=0.58$ and spider (d) $c=0.79$)

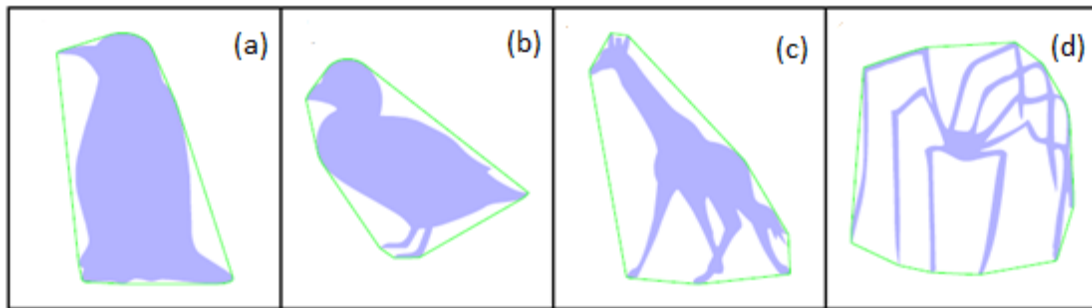


Figure 4.12. Object Complexity (adopted from Bullock *et al.*, 2016)

4.3.7.3 Distance Attributes

Distance attributes measure how close or far are two objects. In this manner distance attributes are always pair attributes. *Centroid distance* is the distance between the centroids of two objects and is usually computed applying the Cartesian formula. For two objects with centroid coordinates (x_1, y_1) and (x_2, y_2) it is

$$distance = \sqrt{(x_1 - x_2)^2 + (y_1 - y_2)^2} \quad (4.7)$$

Convex hull distance is the shortest distance between a point on one object's convex hull and a point on the other object's convex hull. For overlapping convex hulls this distance is zero. If instead of the convex hull we use the actual boundaries

of the objects the resulting distance is called *boundary distance*. In a similar way the boundary distance is equal to zero for touching objects.

4.3.7.4 Intensity Attributes

Attributes computed from the raw field are called *intensity-based attributes*. MODE calculates the 10th, 25th, 50th, 75th and 90th intensity percentiles, together with one user specified percentile. Moreover, MODE calculates the sum of the intensity values for every object.

4.3.7.5 Ratio Attributes

Ratio attributes compare the values of an attribute for a forecast object and the same attribute for an observed object. Ratios are dimensionless, and in this way do not depend on the grid spacing.

If A_f is the area of a forecast object and A_o the area of an observed object the *area ratio* is defined as

$$\text{Area ratio} = \frac{\min(A_f, A_o)}{\max(A_f, A_o)} \quad (4.8)$$

In a similar manner *complexity ratio* is defined as

$$\text{Complexity ratio} = \frac{\min(C_f, C_o)}{\max(C_f, C_o)} \quad (4.9)$$

4.3.8 Fuzzy Logic

The attributes defined in the previous section can be used to characterize and compare forecasts with observations. Another way of using them is to associate certain forecast and observed objects with each other with the help of pair attributes. In MODE this is accomplished with the use of MODE's fuzzy engine based in the principles of fuzzy logic.

Not all values of an attribute are equally important for MODE. To relate an attribute and its interest value, MODE uses functions called *interest maps*. Their input is an attribute value and their output is a number, the interest value. Interest values are bounded in the range of 0 to 1, with 0 corresponding to no interest and 1 to full interest.

An interest map is formulated in such a way that it represents the real feel of the phenomenon it is related to. We are more interested in objects that are close enough, but from over a value our interest starts to fall since the objects are considered separate and their distance does not matter. This is captured in Fig. 4.13a where the centroid distance interest map is pictured. On the other hand ratio attributes have high interest when they are close to 1; that is when the attribute of the forecast and observation have values that are close to each other (Fig. 4.13b).

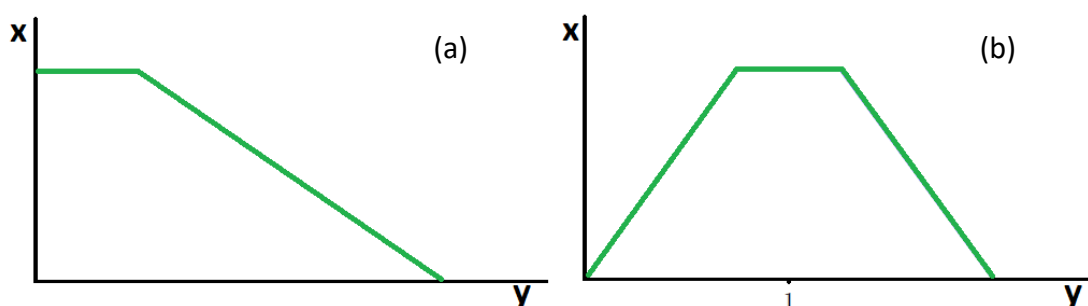


Figure 4.13. Interest map for centroid distance (a) and area ratio (b)

In a similar way to the interest maps MODE defines the *confidence maps*, which express the level of confidence in the calculated value of an attribute. Suppose we have a wind vane to provide us the wind direction. In very low wind speeds the uncertainty in the wind vane measurement is very high; its confidence is very low. This example demonstrates the idea that the value of one attribute (wind speed) dominates the confidence for another attribute (wind direction)

If we use a number of attributes, apart from the importance that the values of an attribute themselves have (as expressed by the interest map), we ought to specify which attribute as a whole is more important in our analysis. This role is given to scalars, called *weights*. A large weight of a particular attribute tells MODE that this attribute is more important than others for the purposes of matching and merging. If we are more interested in the distance between two objects than their area ratio we

will give higher weight to the distance attribute. Weights they can take any positive value since they are set for each attribute relative to the others.

The attribute values, the associated weights, interest maps and confidence maps are combined into a single scalar value, the total interest.

$$T(a) = \frac{\sum_i w_i C_i(a) I_i(a)}{\sum_i w_i C_i(a)} \quad (4.10)$$

Where $\alpha=(\alpha_1, \dots, \alpha_n)$, α_i , w_i , C_i and I_i the value, weight, confidence map and interest map of i^{th} attribute respectively.

By introducing the above quantities MODE is able to take advantage of the human knowledge since their values are not arbitrary set but they are dictated by the human experience. If we decide to give bigger merit to an attribute we can just increase its weight or alter its interest map.

4.3.9 Matching and Merging

The initial step of MODE creates simple objects. While useful information can be retrieved from the study of simple objects, the pursuit of relation between objects can provide additional information. MODE associates objects via matching and merging, employing the fuzzy engine with predetermined criteria.

Matching is the association of an observed object with a forecast object to create a pair. The two objects belong to different fields. Merging is the grouping of objects together to create a cluster. In this case the objects belong to the same field. Several convective cells may belong to the same multi-cell thunderstorm. Thus, it makes sense to treat these individual cells as a single cluster object.

The attributes of simple objects are calculated from the beginning and are used in the fuzzy engine to perform matching and merging. Single attributes are then again calculated for clusters and pair attributes are calculated for pairs of single objects or pairs of clusters

MODE supports two types of merging. The first simple (yet effective) method is the double thresholding. In addition to the initial threshold, a second, lower, threshold can be specified for object merging. Fig. 4.14 portrays this method. Using the initial threshold three objects were derived. Using the second threshold the objects are all contained in the area surrounded by the lower threshold and can be merged creating a cluster.

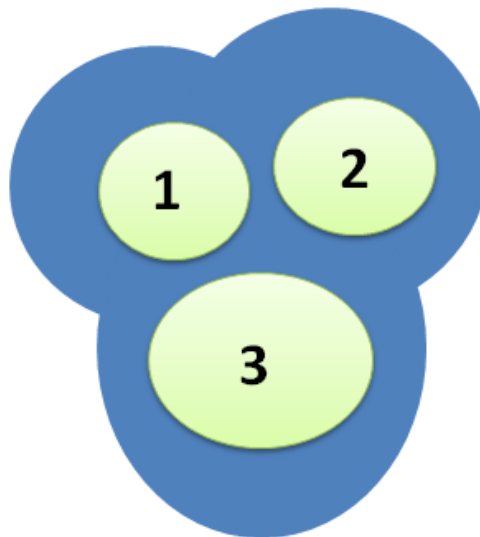


Figure 4.14. Double threshold merging

In the fuzzy engine merging method the field is duplicated and given to a new created fuzzy engine as both a forecast and observed field. The new engine then performs matching and merging on the original and artificially created field.

4.3.10 Parameters values selection

The convolution radius R is the radius of influence in an averaging filter. The convolution effect is to smooth the field's data. High spatial frequencies are attenuated; high intensity areas are "flattened" and spread out.

For small values of R the objects retain much of the spatial detail. As the radius R increases, the resulting objects become more smooth-featured, and there are fewer of them. At higher radiuses only high intensity, large objects are identifiable.

The threshold is the other MODE parameter that determines how objects are resolved in the raw data field. The increase in the threshold results in less objects to be resolved. Even more the size of the objects becomes smaller as there are less grids satisfying the greater criterion.

A graphic representation of the dependence of objects characteristics on threshold and radius selection is presented in Fig 4.15. Large objects are derived with low values of threshold, and small objects with higher thresholds. Highly smoothed objects is the result of high values of convolution radius, while smaller values produce highly textured objects

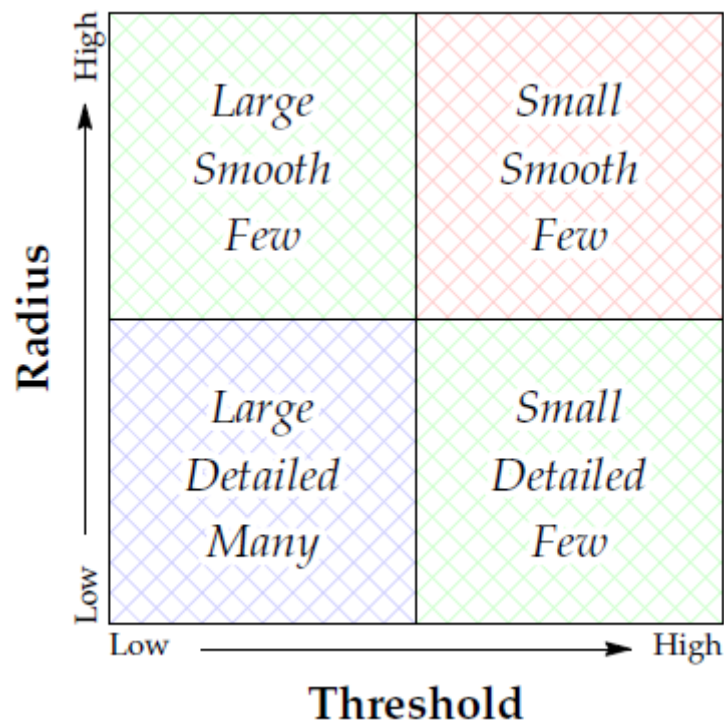
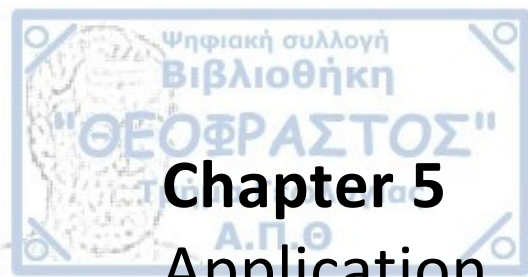


Figure 4.15. Varying the convolution radius and threshold (adopted from Bullock *et al.*, 2016)



Chapter 5

Application of Method for Object Based Diagnostic Evaluation

5.1. Introduction

In Chapter 3 of the current dissertation statistics calculated using station data (point statistics) and weather radar was used to statistically evaluate the performance of the set of twelve parameterization setups of the WRF model in a limited number of cases. The selected setup was then further evaluated by adding more cases in the sample and by providing statistics separated by synoptic type that each case belonged to. Those statistics proved that the selected setup can be used for the study of convective activity.

In this chapter, the Method for Object Based Diagnostic Evaluation (MODE) will be employed in the same number of twelve parameterization setups and its results will be put side to side to the results of chapter three. This time, as the method dictates, the radar and model data will be used to derive “objects” and results will be drawn by examining their characteristics.

The primary parameter examined is reflectivity (dBz) as measured by the radar and calculated by the model. Volume scans of reflectivity are processed by TITAN software and composite reflectivity is provided as the final product to be used in the method. The NCEP Unified Post Processing module of WRF (UPP; Wang et al., 2016) was used to compute model’s composite reflectivity from the raw model results. Ten minutes time-steps were used for both radar and model data. The finer grid radar data were interpolated to the model’s D03 domain coarser grid, using the conservative method to avoid elimination of high values of reflectivity due to smoothing.

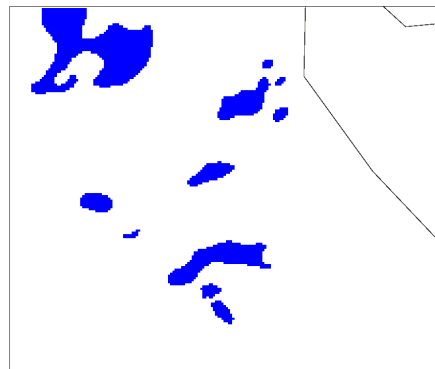
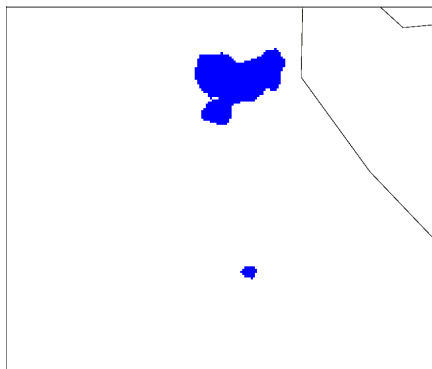
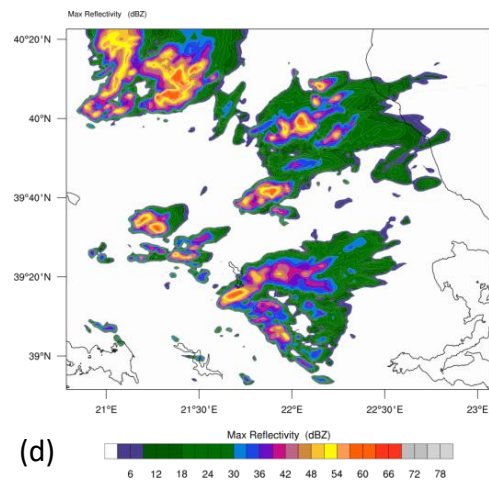
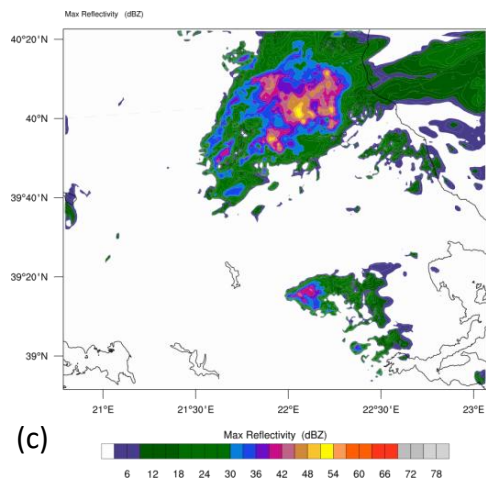
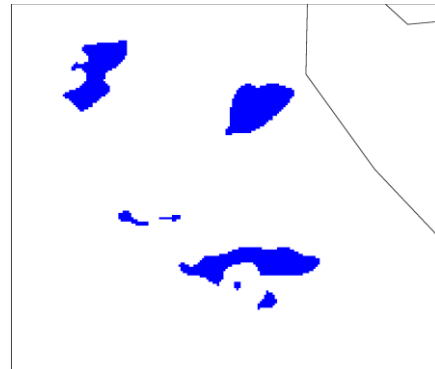
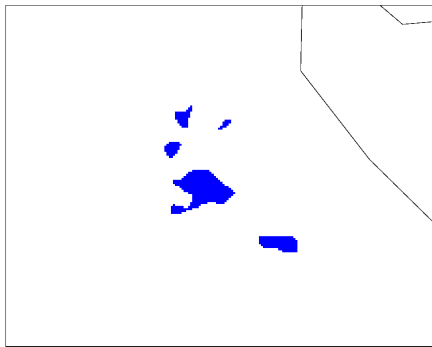
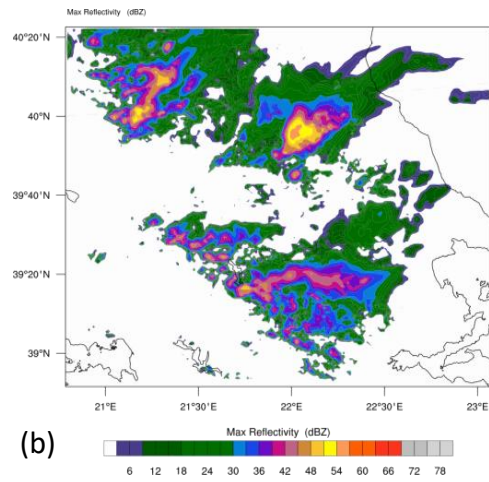
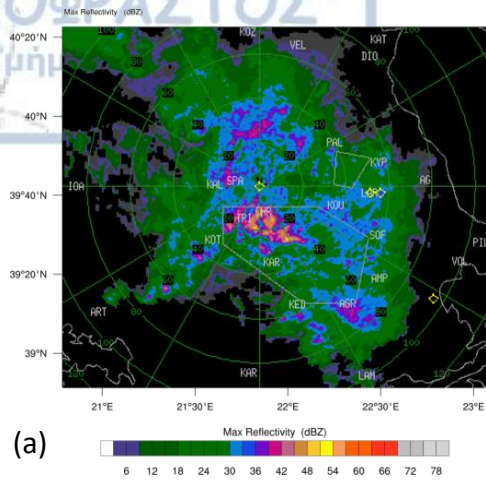
The whole method was carried out using the Model Evaluation Tool (METv6.0, Brown et al., 2017). MET provides the MODE tool to perform the initial analysis on the primary data and the MODE-Analysis tool for the post processing of

the MODE results. The MODE tool has tunable parameters that must be set depending on the particular application of the method. Those parameters in MODE method are almost scale insensitive, meaning that almost all of them are set according to the grid spacing of the analyzed fields. More details about the parameters are discussed in chapter 4 containing the theoretical background of the method.

In the current application the parameter of convolution radius applied to smooth the raw field was set to 4 ($\text{conv_radius}=4$), meaning 4 times the grid spacing of the analyzed field. Since the convective phenomena affecting the area are rather size limited a higher value would result in excessive smoothing and the consecutive unification of the separate storms. The accepted percentage of grid points with valid data for the thresholding was set to 50% ($\text{vld_thresh}=0.5$). With a percentage of bad data higher than this threshold the convolved value will be bad data also. No upper limit was set for the maximum intensity of the field ($\text{inten_perc_value}=100$). That means that even the highest reflectivity values were included in the analysis. As a final step to avoid the noise induced in the analysis by very fine scale phenomena, the derived objects should at least cover 10 grid points ($\text{area_thresh}\geq 10$) to be included in the analysis.

To examine the sensitivity of the method to the selection of the convolution threshold, the method was employed using three threshold values. In the first case the value of 35dBz ($\text{conv_thresh}\geq 35$) was used to derive the objects. This comes in accordance to the statistical evaluation performed in chapter three. A higher value of 45dBz was the second choice. With values of reflectivity higher than 45dBz the possibility of hail in the ground as a result of a heavy thunderstorm is greatly increased. Finally the third threshold used was 40dBz since initial results with the 45 dBz threshold indicated a reduced number of detected objects.

To compare the characteristics of the objects (Fig 5.1 presents typical images of raw field and derived objects) specific attributes were selected and their values were plotted for every experiment and convolution threshold value. It must be noted that the comparison was performed in the objects for the whole period of the



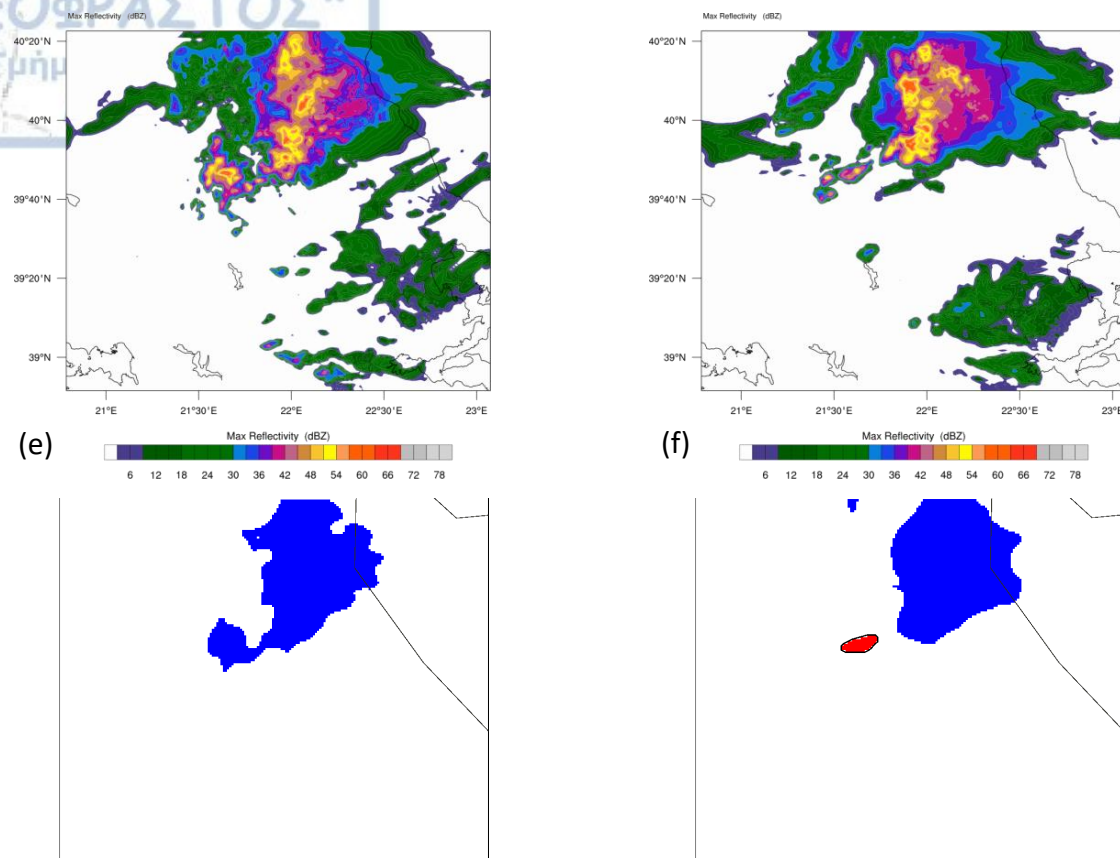


Figure. 5.1. Composite reflectivity and derived objects using the 35dBz threshold as observed by the radar (a) and computed from model (WRF-03) for five of the experiments, namely ETA-KF-YSU (b), ETA-BMJ-MYJ (c), WSM6-KF-YSU(d) WSM6-BMJ-YSU (e) and GOD-BMJ-YSU (f) for 12/9/2010 18:30 (± 20 min).

phenomenon duration without taking into account its temporal evolution. A small delay in the prediction of the convective activity by the model would result in misleading results by the method. That is, if the model was able to successfully predict the intensity and spatial evolution of the convective activity but missed the actual time, the method would indicate poor model performance.

The first two attributes examined was the object area and the object area threshold. The object's area is an attribute calculated after the convolution stage. The object's area threshold is the area of the object which contains grid points of the raw field (before the convolution step) satisfying the criterion of the object definition (in our case 35dBZ, 40dBz, 45dBz). While those two first attributes seem to provide

similar information their comparison provides information about the right selection of convolution radius. A small convolution radius would result in almost identical values of the two attributes, while a large value would result in the quantization of the object's area in confined intervals prescribed by this convolution radius.

The third attribute examined is the complexity of the object. The complexity is defined as the "ratio of the difference between the area of an object and the area of its convex hull divided by the area of the convex hull" (METv6.0, Brown et al., 2017) The complexity is a unitless quantity. It is a measure of the internal structure of the object. Small values of complexity mean that the object has areas of convective activity that are continuous and cover the whole area of the object while small values indicate patches of activity, located inside the object that are just close enough to be contained in the same object.

The fourth attribute is the median value of the 75 percentile of the reflectivity values. The intensity values of each object are sorted in an ascending order. For each object identified throughout the duration of the convective activity the 75 percentile of its reflectivity is calculated. Then the median value is extracted from the values of all the objects. This attribute can give some insights about how well the model predicts the intensity of the convective activity. Its value was found to lie in the mid forty dBz, a value of reflectivity that is enough to characterize the convective activity quite severe. Should we were interested in the maximum reflectivity, a higher percentile could be used. But this higher percentile would only inform us about the extreme values contained in the object.

In the next pages results for six cases (the same of the first part of chapter 3, one case was discarded since the derived objects were not adequate for further analysis) and the aggregate results are presented and discussed. The MODE results analysis is preceded by a brief synoptic and dynamic analysis for each case.

Whenever a cumulus scheme is referred, this is employed in WRF-D01 and WRF-D02 since no cumulus parameterizations was used in WRF-D03.

5.2 Application for selected cases

5.2.1 Case of 19/06/2010

The case of convective activity that occurred on June 19, 2010 affected the whole of Thessaly, and is characterized by the presence of zonal circulation over the area (Fig. 5.2a). The isothermal line of -14°C crosses Greece at 500hPa. The zonal circulation induces an eastern flow over Greece. In the lower troposphere (850hPa) a zone of negative divergence (convergence) is located over eastern Thessaly

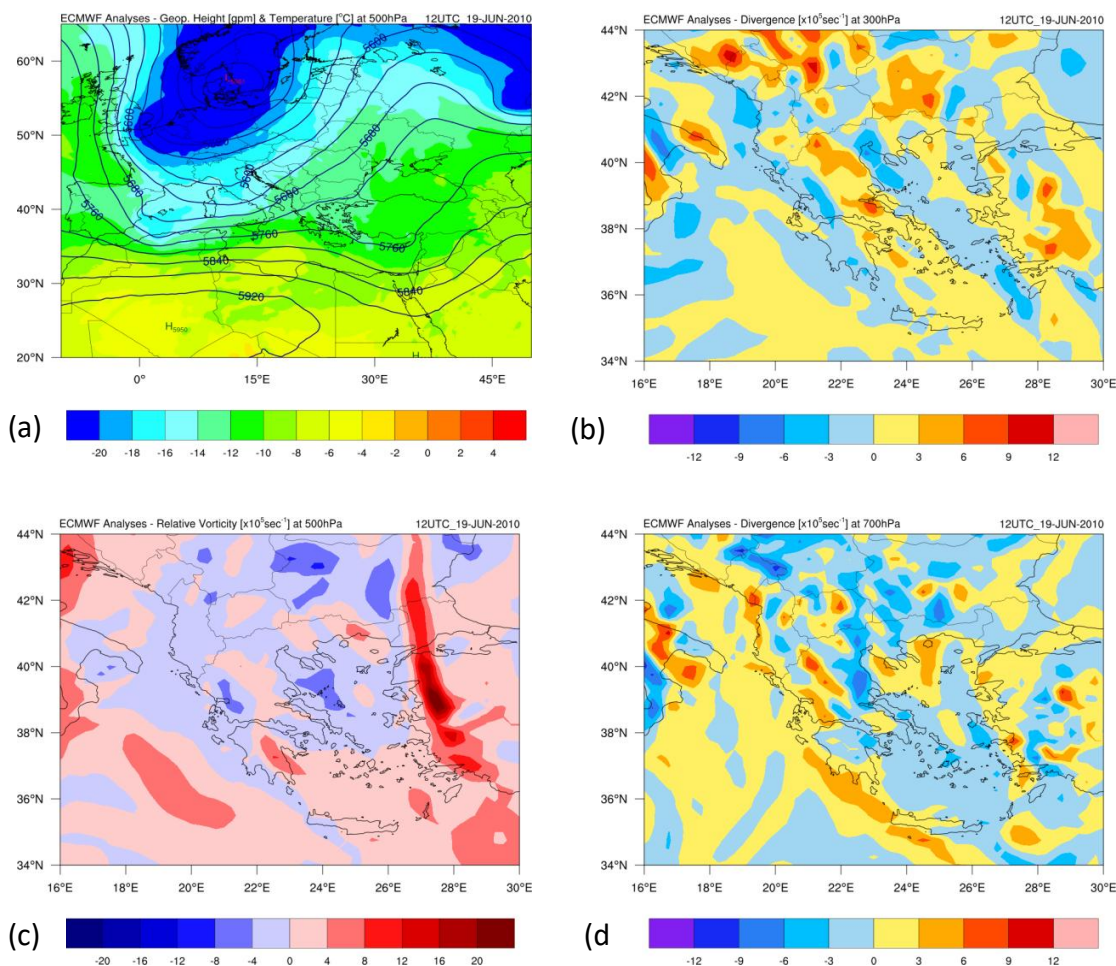


Figure 5.2. Geopotential height (contours) and temperature (shaded) at 500hPa (a), wind divergence at 300hPa and 700hPa (b) and (d) respectively, and relative vorticity at 500hPa (c), at 12:00UTC, in 19/06/2010.

(Fig 5.2d) with values reaching $-8 \times 10^{-5} \text{s}^{-1}$. In the upper troposphere (300hPa) moderate divergence can be observed in the same area and further north (Fig 5.2b). The relative vorticity map at 500hPa (Fig 5.2c) reveals positive values of vorticity

($2 \times 10^{-5} \text{ s}^{-1}$) over the western part of Thessaly and small negative values in the far eastern part.

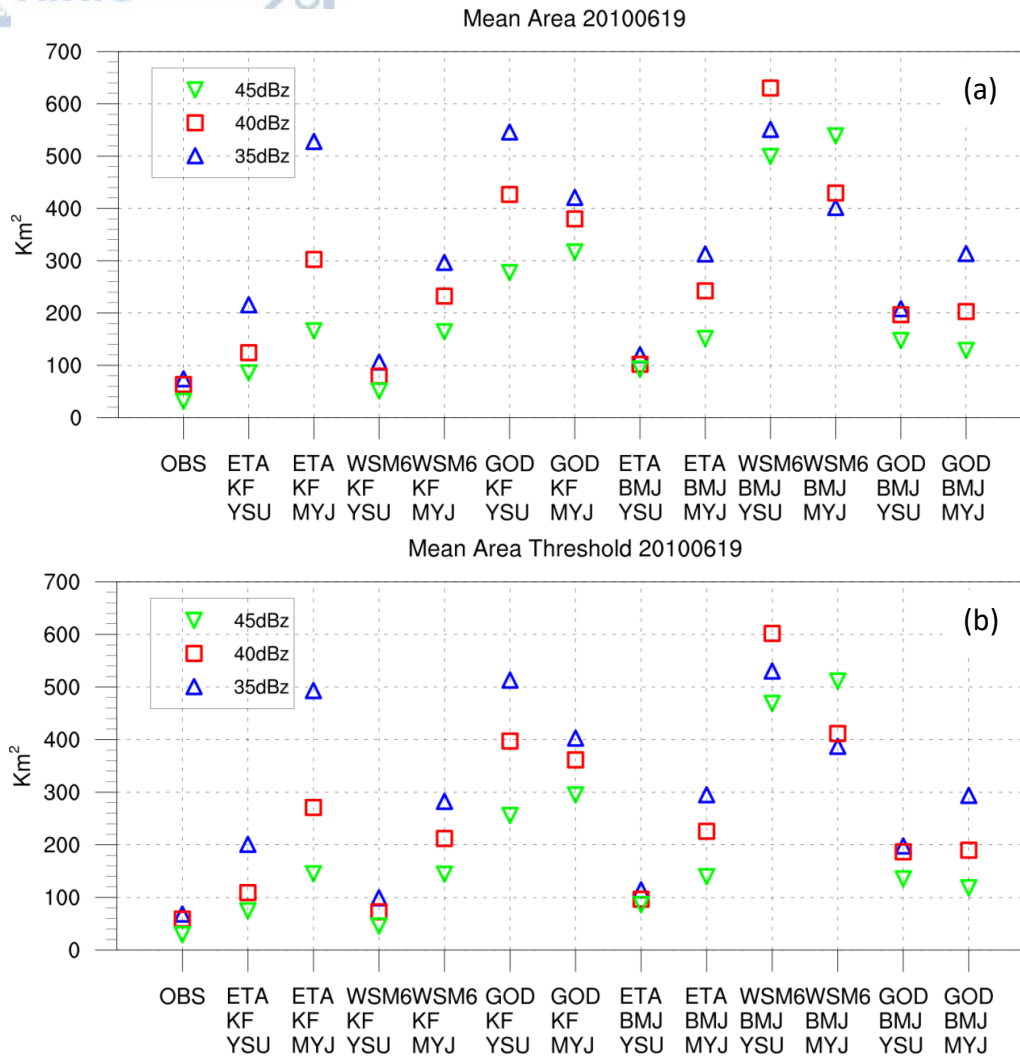


Figure 5.3. Mean area (a) and mean threshold area (b) attributes for the objects derived from observed and simulated values of reflectivity for all model setups for 19/06/2010.

The mean area of the observed objects is in the order of $70 \pm 10 \text{ Km}^2$. The change in the convolution threshold has limited effect in the area of the observed objects (Fig. 5.3a). The simulations that use the MYJ boundary layer scheme produce objects with consistently larger area. The objects produced using the WSM6-KF-YSU and ETA-BMJ-YSU simulations have areas that are closer to the observed ones. The same is true for the area threshold values also (Fig 5.3b). Simulations using the Goddard microphysics produce objects with much larger areas. The WSM6-BMJ-YSU

Application of Method For Object Based Diagnostic Evaluation

experiment produces objects with eight times bigger area than the observed. Regarding the median intensity, the simulations using the KF cumulus convection scheme produce objects with intensity from 45 to 48dBz (with the exception of Goddard based simulations) while the simulations employing the BMJ scheme produce objects with 2-3dBz higher reflectivity (Fig 5.4a). The observed median intensity ranges from 48dBz (for the 35dBz threshold) to 54dBz (for the 45 dBz threshold). The direct effect of convolution threshold (higher threshold – higher median intensity) is evident in all the simulations. Finally the mean complexity of the observed objects ranges from 0.12 for the 35dBz threshold to 0.15 for the 45dBz threshold (Fig 5.4b). For the modeled objects the mean complexity is systematically higher, especially with experiments using the MYJ boundary layer scheme.

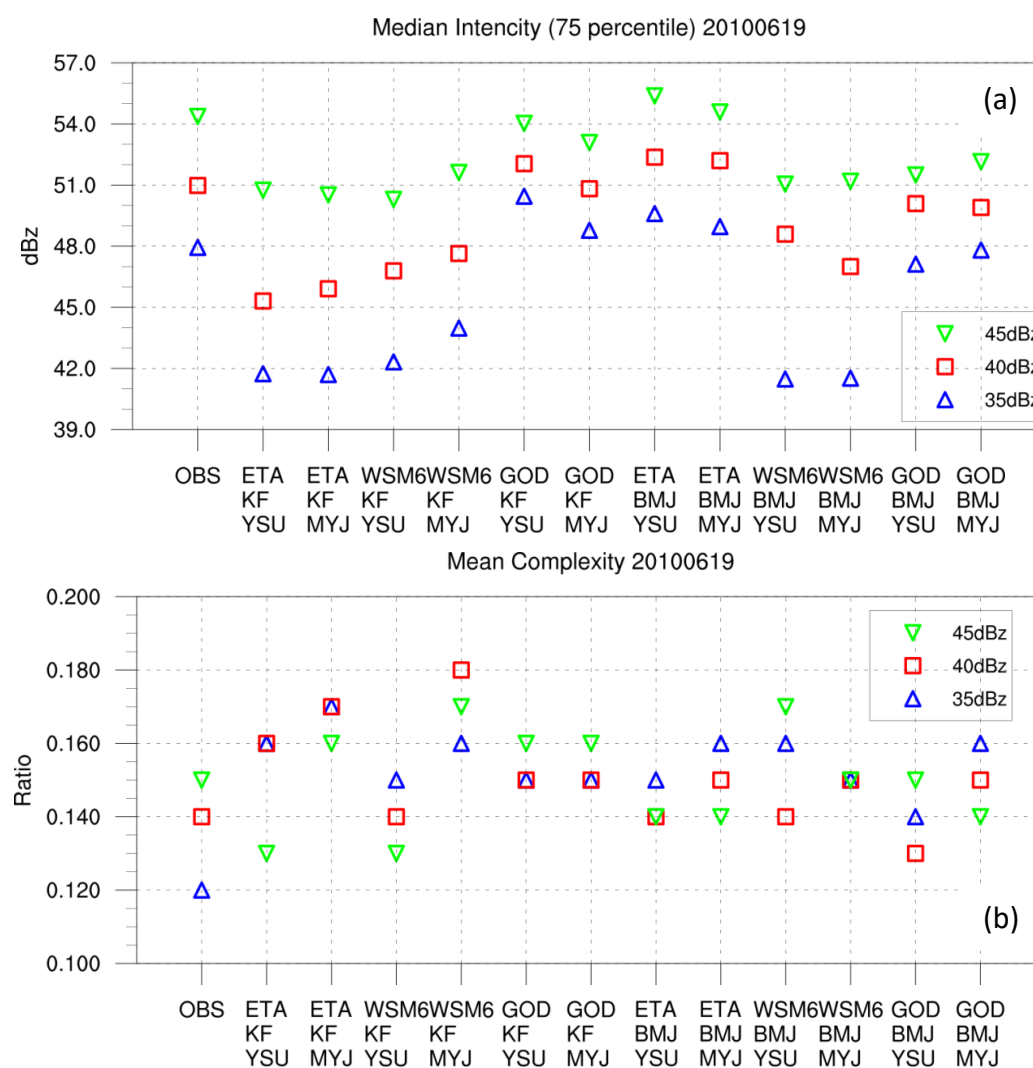


Figure 5.4. As in Fig. 5.3 but for median intensity (75th percentile) (a) and mean complexity (b) attributes.

5.2.2 Case of 27/06/2010

The synoptic type of CLO characterizes the case of 27 June 2010. An area of low pressure extends over the lower Balkans with its center (5680gpm) over southern Bulgaria (Fig 5.5a). A cold lake is clearly visible over the area extending from Ionian Sea to the Black Sea with temperatures reaching -18°C . The relative vorticity over Thessaly is close to zero with small negative values over its eastern part and small positive values over its central part (Fig 5.5c). Highly positive values of vorticity exist over western Ionian Sea. Large values of divergence exist in the upper troposphere over southern Thessaly enhancing upward vertical movements (Fig 5.5d and Fig 5.5d).

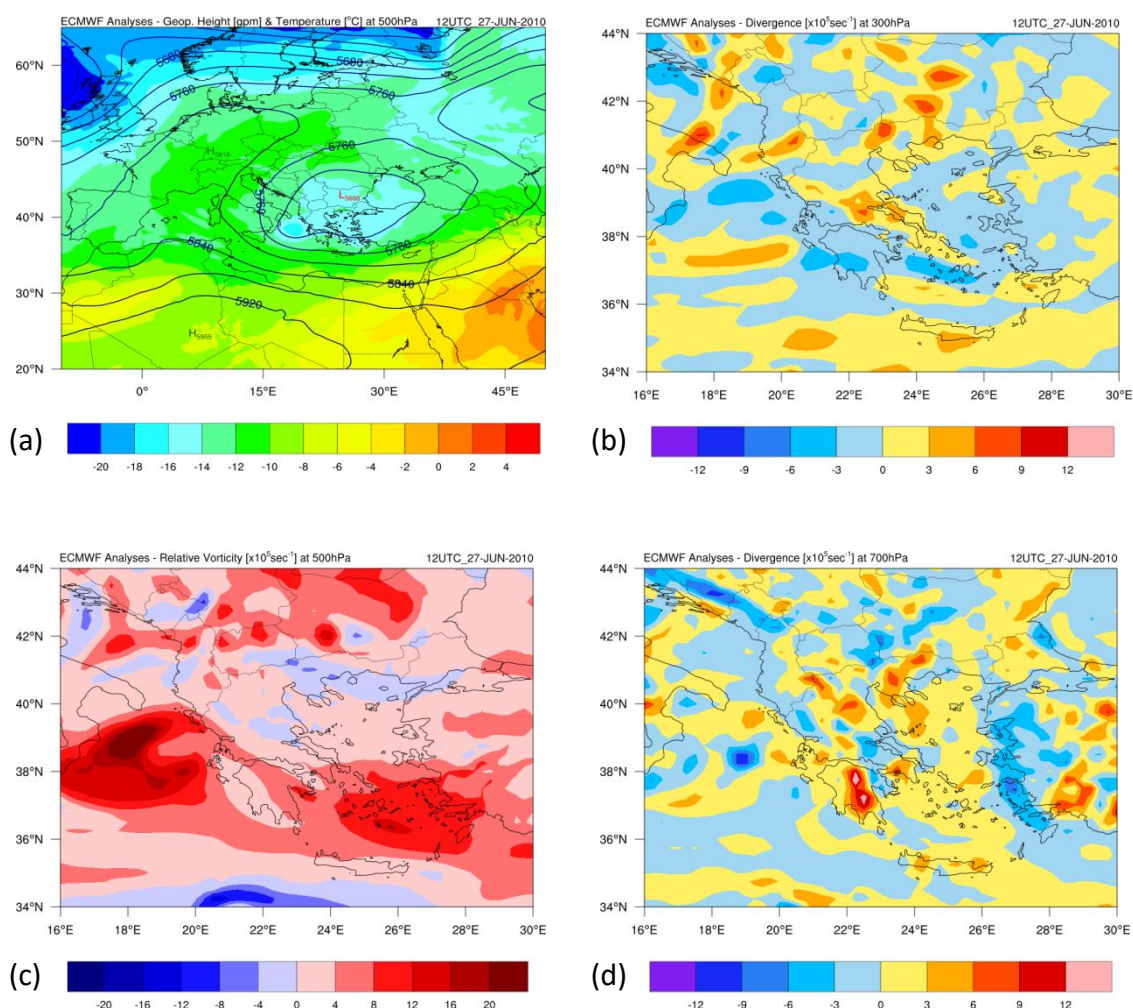


Figure 5.5. Geopotential height (contours) and temperature (shaded) at 500hPa (a), wind divergence at 300hPa and 700hPa (b) and (d) respectively, and relative vorticity at 500hPa (c), at 12:00UTC, in 27/06/2010.

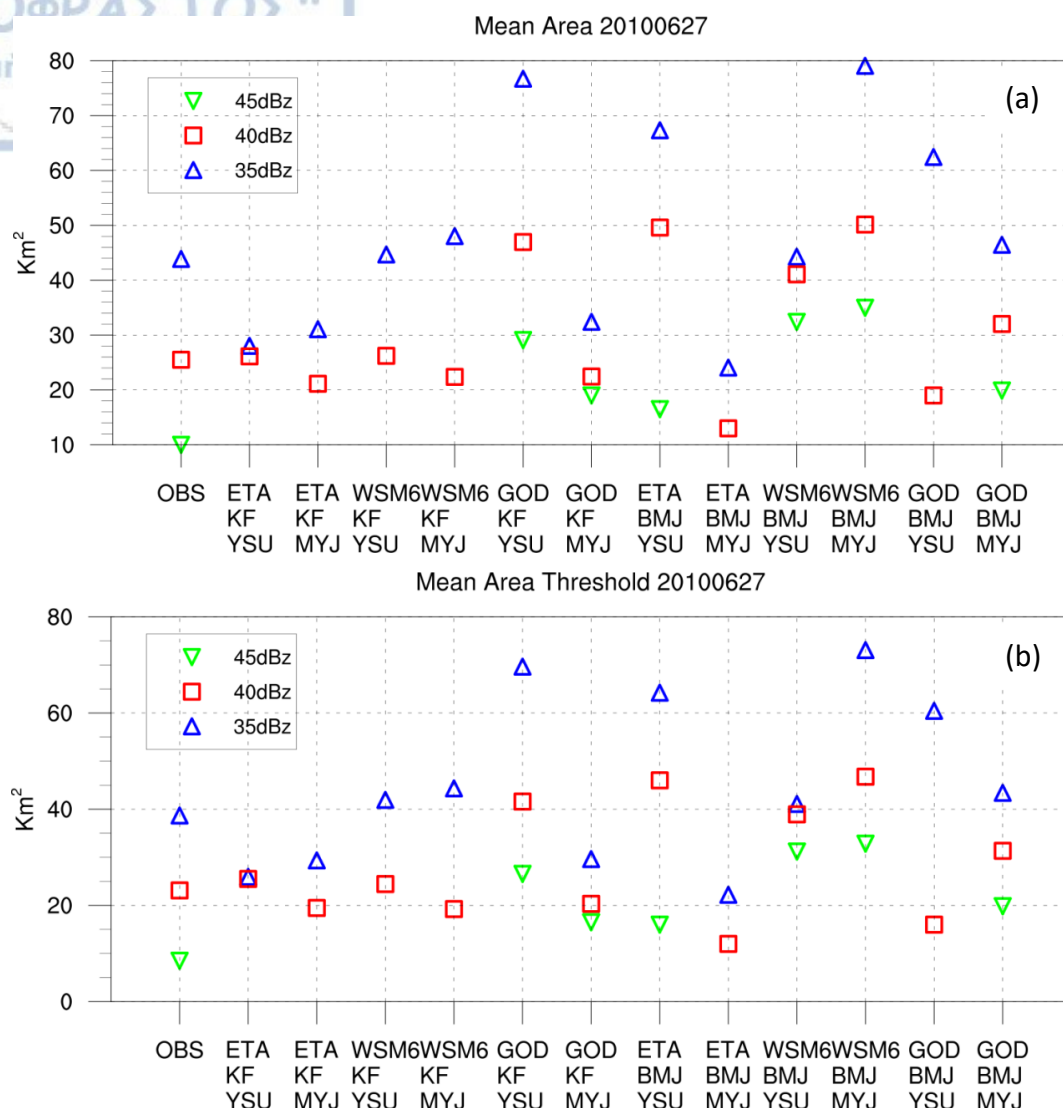


Figure 5.6. Mean area (a) and mean threshold area (b) attributes for the objects derived from observed and simulated values of reflectivity for all model setups for 27/06/2010.

The radar derived objects for the case of 27/06/2010 have a mean area 40km^2 when the threshold of 35dBz is used, that plummets to just over 10km^2 when the higher threshold of 45dBz is employed (Fig. 5.6a). This higher threshold leads the method to find no objects when the KF cumulus scheme is employed (Goddard experiments excluded). In all the experiments the change in threshold from low (35dBz) to high (45dBz) leads in a sharp decrease in both area and area threshold (Fig. 5.6b). The experiments using the WSM6 microphysics and KF cumulus scheme provide area values closest to the observed. The intensity graph shows a high value

of 55dBz when the 45dBz threshold is used far away from the 43dBz when the 35dBz threshold is employed (Fig. 5.7a). This means that there is a large number of grid points with reflectivity between 35dBz and 45dBz that draws the mean intensity value close to 43dBZ. The experiments that use the BMJ cumulus scheme have higher intensity values from the one using the KF cumulus scheme. Once again the KF scheme combined with the WSM6 microphysics and YSU boundary layer provides the smallest deviations from the observed values in both the 35dBZ and 40dBZ threshold. Finally, with the exception of the Goddard scheme experiments the complexity of the model derived objects is in accordance with the observed ones (Fig. 5.7b).

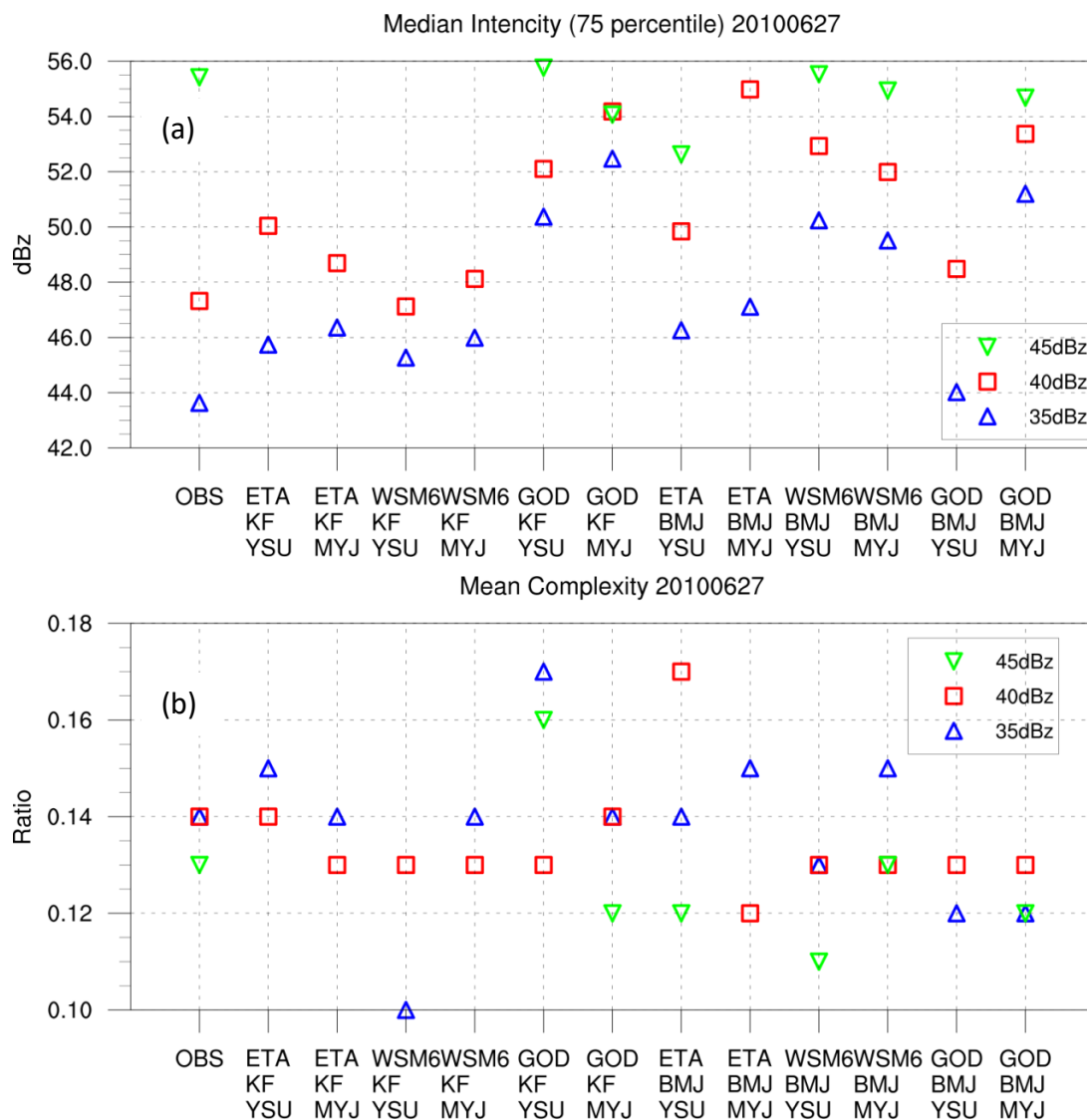


Figure 5.7. As in Fig. 5.6 but for median intensity (75th percentile) (a) and mean complexity (b) attributes.

5.2.3 Case of 20/07/2010

The case of July 20, 2010 started with a closed low over the area that was followed by a North West flow. Temperature at 500hPa in 00:00UTC (not shown) reveals a cold air mass over the area that started to get warmer from 12:00UTC. This is in agreement with the observed mild convective activity that appeared in the western part of the area, with the storms having a south east heading, and was terminated early in the evening. The relative vorticity map at 500hPa shows positive values over the examined area. At the 700hPa level strong convergence assisted by divergence at the 300hPa level favored the convective motions in the area.

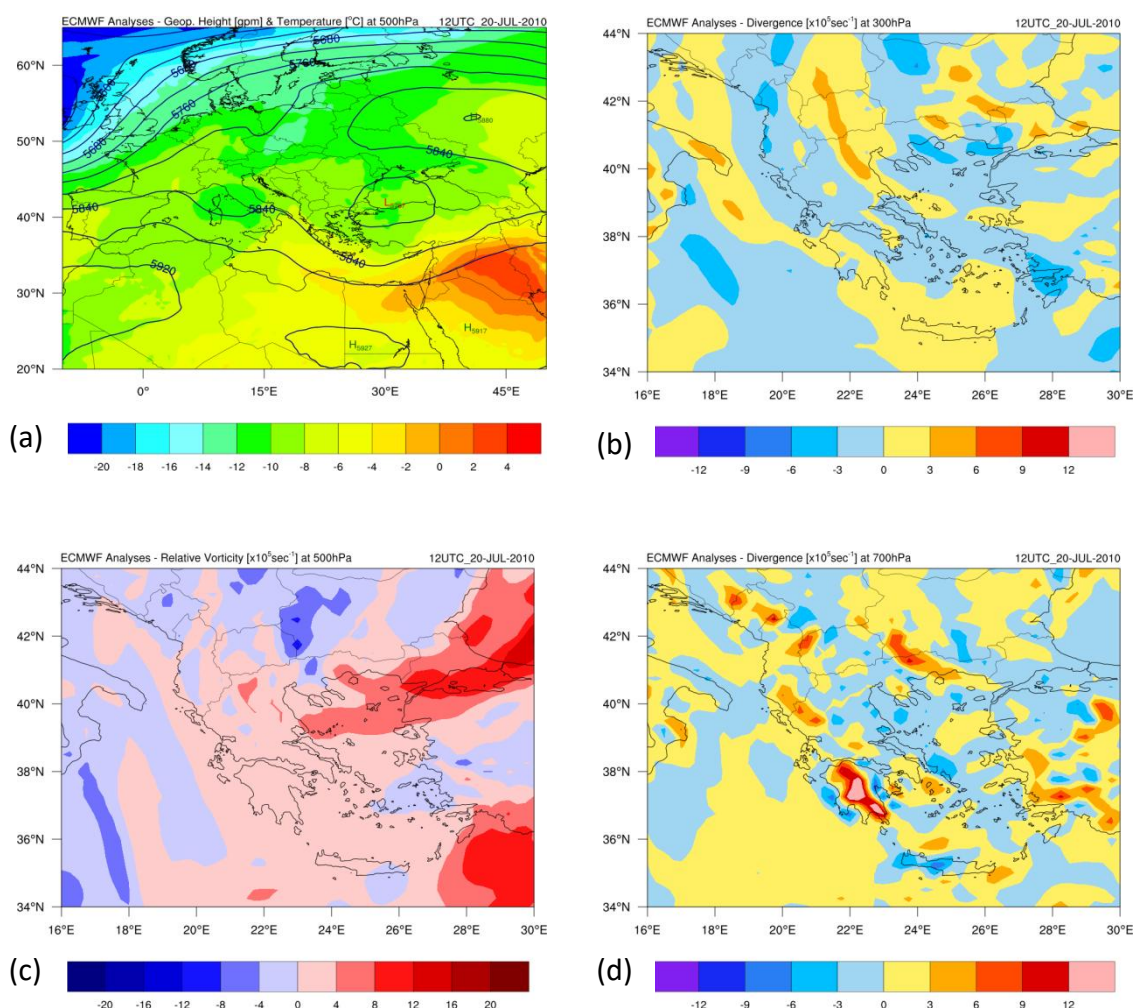


Figure 5.8. Geopotential height (contours) and temperature (shaded) at 500hPa (a), wind divergence at 300hPa and 700hPa (b) and (d) respectively, and relative vorticity at 500hPa (c), at 12:00UTC, in 20/07/2010

The observed mean area of convective activity is in the order of 20km^2 . In all but three of the experiments setting the threshold to 45dBz resulted in the detection of no objects (Fig 5.9a). The WSM6 microphysics scheme combined with BMJ cumulus and MYJ boundary layer schemes produced unrealistic storms with area four times the observed ones. KF cumulus when employed with YSU boundary layer and without Goddard microphysics provided a reasonable representation of both mean area and mean area threshold (fig 5.9b). The observed Mean Area threshold (for 35dBz) is 25km^2 while the simulated object's values range from 13km^2 to 40km^2 .

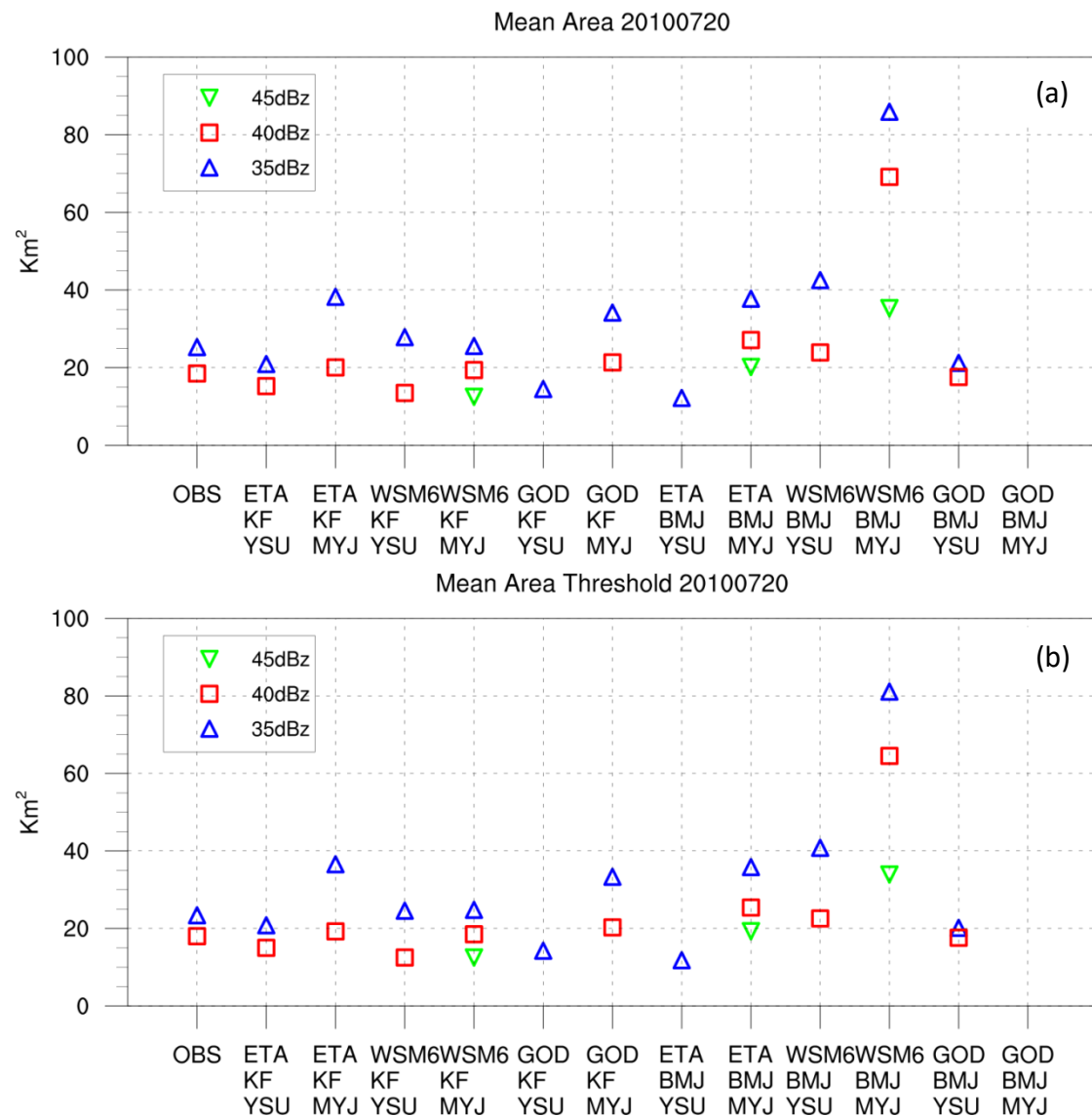


Figure 5.9. Mean area (a) and mean threshold area (b) attributes for the objects derived from observed and simulated values of reflectivity for all model setups for 20/07/2010.

Application of Method For Object Based Diagnostic Evaluation

The mean intensity for the observed objects is at 45dBz when the 35dBz threshold is used and jumps to 50dBz for the 45dBz (Fig 5.10a). The mean intensity of the objects for the simulations lies between 46dBz (once again the WSM6-KF-YSU experiment provides the best results) to 52dBz (not surprisingly for an experiment using the Goddard microphysics scheme). The complexity of the observed objects is 12% for the 35dBz threshold and 18% for the 40dBz threshold (Fig 5.10b). That means that grid-points having reflectivity more than 40dBz are more scattered than those with reflectivity more than 35dBz increasing the complexity. More over the complexity of the objects is higher on the experiments using the BMJ cumulus convection scheme.

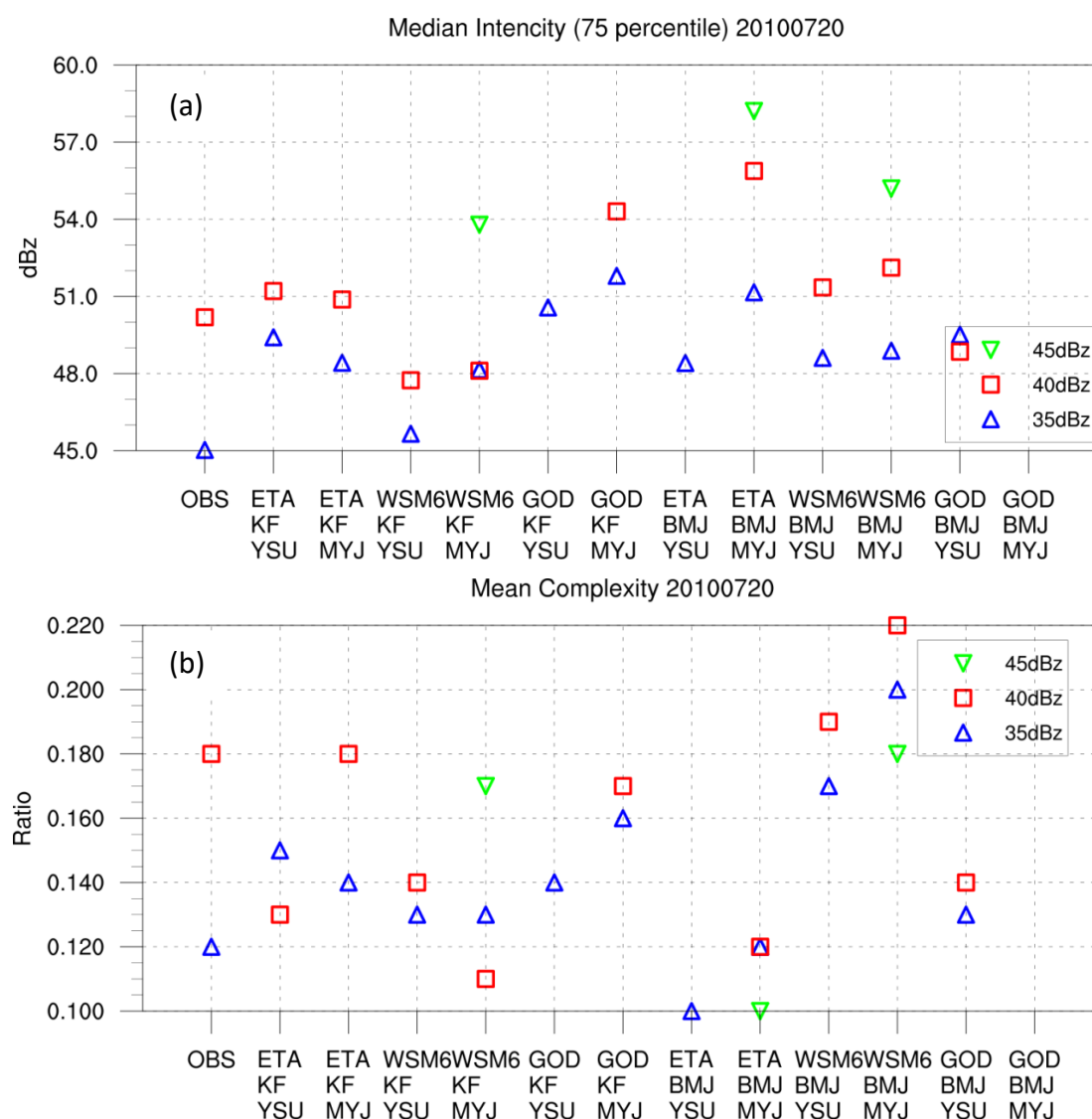


Figure 5.10. As in Fig. 5.9 but for median intensity (75th percentile) (a) and mean complexity (b) attributes.

5.2.4 Case of 04/08/2010

The convective activity started around 13:00 UTC in the western part of the area and reached its highest intensity from 15:00UTC to 19:00UTC in its western part. At trough approached Greece from the west and SW flow affected the area (Fig 5.11a). A drop in temperature of about 6°C was observed at 500hPa. Values of vorticity around 0 are shown in the 12:00UTC map with positive values as high as 12×10^{-5} to the west (Fig. 5.11c). Strong convergence occurs over Thessaly at 700hPa with high values of divergence around it (Fig 5.11d). At 300hPa values of divergence down to -6×10^{-5} exist over the area with strong convergence to the northwest of the area (Fig.5.11b).

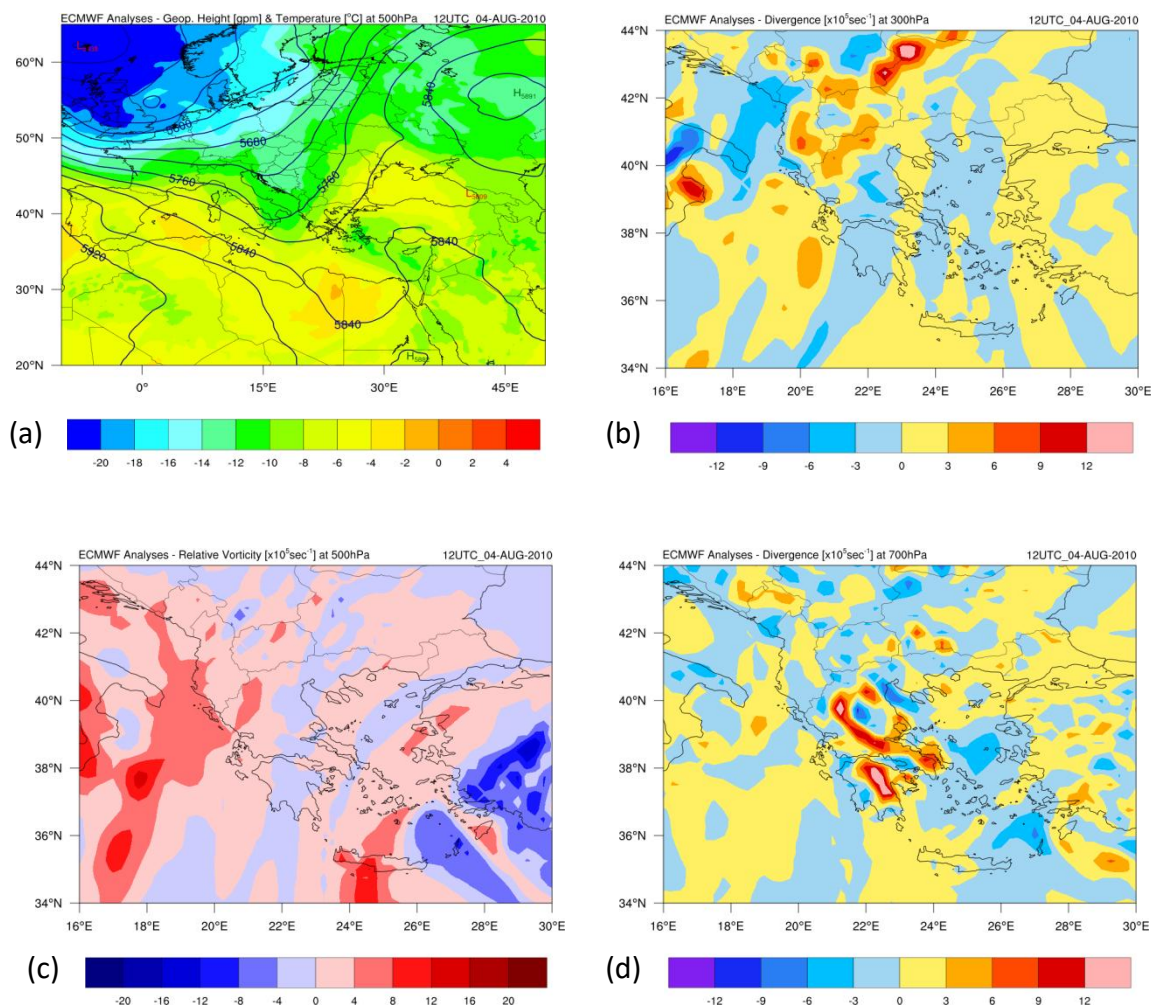


Figure 5.11. Geopotential height (contours) and temperature (shaded) at 500hPa (a), wind divergence at 300hPa and 700hPa (b) and (d) respectively, and relative vorticity at 500hPa (c), at 12:00UTC, in 04/08/2010.

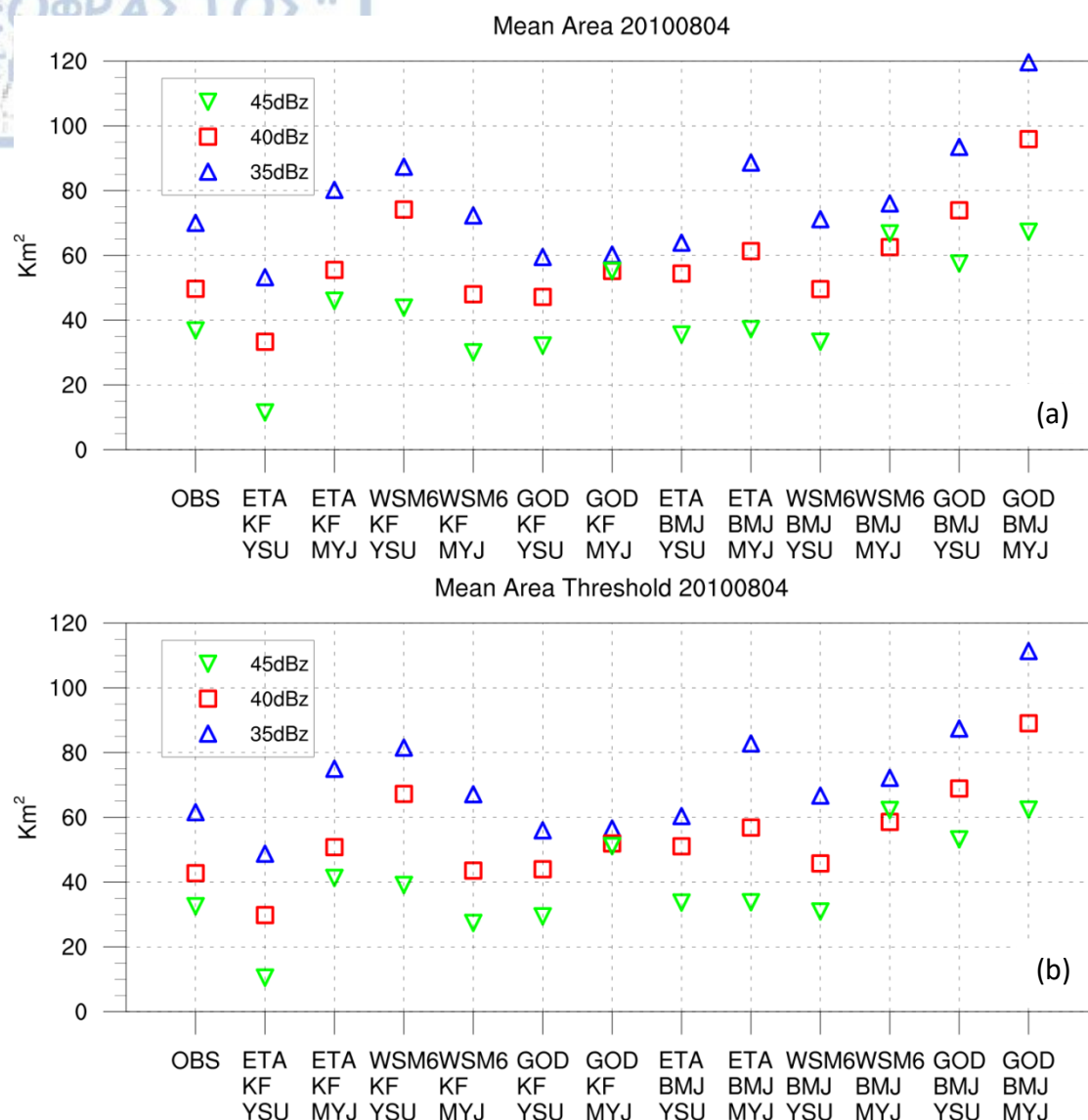


Figure 5.12. Mean area (a) and mean threshold area (b) attributes for the objects derived from observed and simulated values of reflectivity for all model setups for 04/08/2010.

In all the simulations and the observation the mean area of the derived objects follows the threshold value set in the most consistent way, i.e higher threshold leads always to higher mean area (Fig 5.12a). This was to be expected since the storms that were observed this day had the closest view to a textbook example (from the examined cases); Compact cells with decreasing reflectivity from the center of the activity to its outer limits. This was also true for most of the simulations. The area of the observed objects was from 60km^2 (35dBz threshold) to 33km^2 (45dBz threshold). The combination of KF cumulus convection with MYJ

boundary layer gave the best results in both mean area and mean area threshold (Fig. 5.12b). In the median intensity the simulations performed using the KF cumulus scheme (with the exception of those using the Goddard microphysics) provided better results from those using the BMJ scheme. Those using the BMJ cumulus scheme resulted in object's median intensity from 4dBz to 6dBz higher than the observed ones in every threshold used (Fig. 5.13a). In the complexity attribute the ETA microphysics based experiments gave the best results (close to observed) for lower threshold while the WSM6-KF-YSU did the same for the higher threshold (Fig. 5.13b).

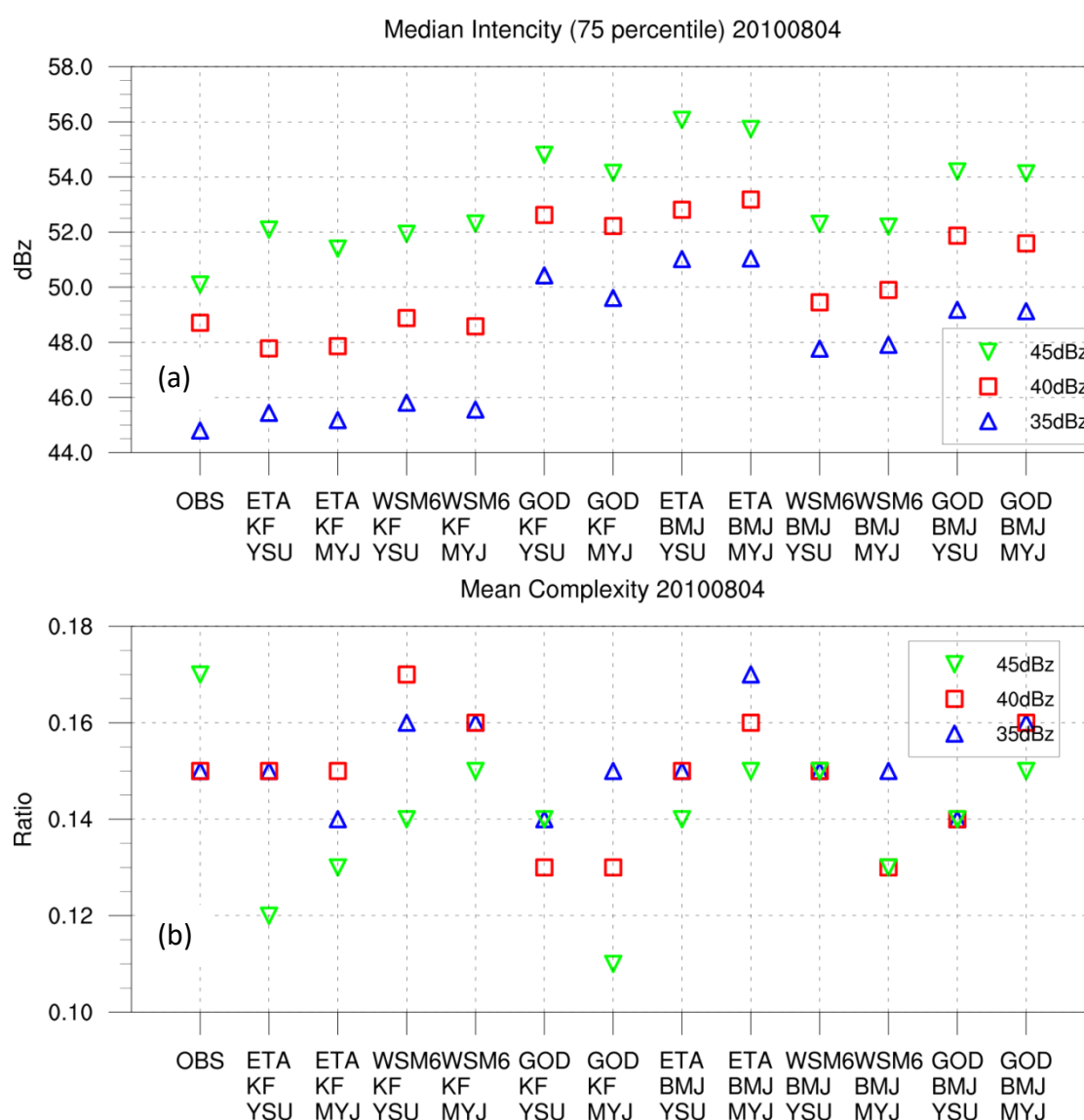


Figure 5.13. As in Fig. 5.12 but for median intensity (75th percentile) (a) and mean complexity (b) attributes.

5.2.5 Case of 12/09/2010

An extensive low system covers Southeastern Europe, the Balkans and most of Greece with its center ($H=5700\text{gpm}$) over Eastern Macedonia and Thrace (Fig. 5.14a). Another secondary low is located in the South Adriatic Sea accompanied by a cold (-18°C) air mass. The relative vorticity has high positive values over the examined area (Fig 5.14c) and even higher values over the secondary low. In the low troposphere (Fig 5.14d) the divergence is almost zero and in the upper troposphere (Fig 5.14b) the divergence has low negative values (convergence). Thus the main reasons for this day's storms were thermal instability and abundance of relative vorticity.

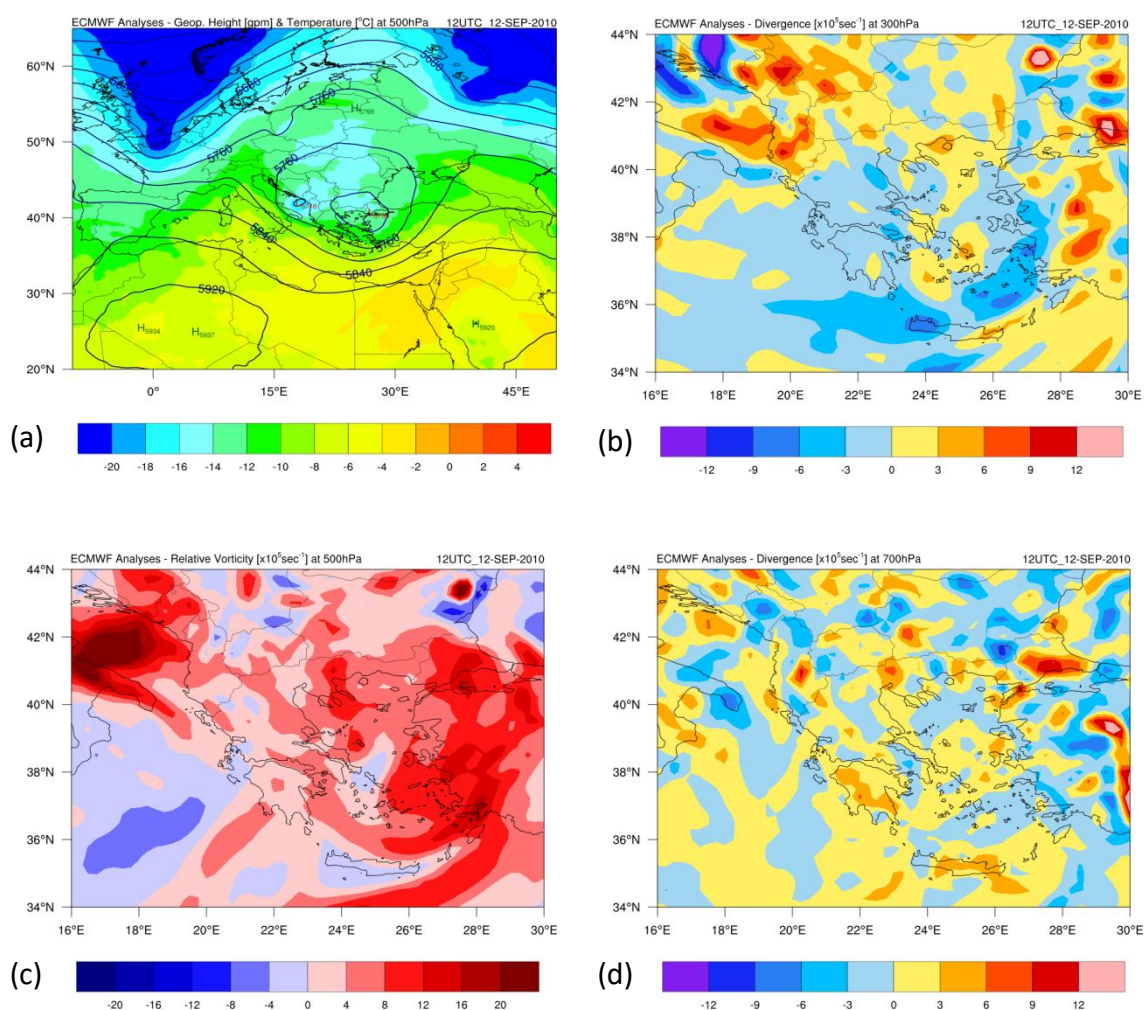


Figure 5.14. Geopotential height (contours) and temperature (shaded) at 500hPa (a), wind divergence at 300hPa and 700hPa (b) and (d) respectively, and relative vorticity at 500hPa (c), at 12:00UTC, in 12/09/2010

The area of the objects is quite large (compared to the other cases) in both the observed and the simulated objects. The convective activity started with great intensity at around 16:00UTC on the northwest part of the area and moved slowly with a southeast heading till 21:00 that seized to exist. The ETA-KF combination with both boundary layer schemes gave the best results for the 35dBz threshold (Fig 5.15a). Overall the observed objects had extended areal coverage but lacked the high values of reflectivity, evident from the fact that no substantial (>10 grid points) object was found when the 45dBz threshold was used. On the other hand most of

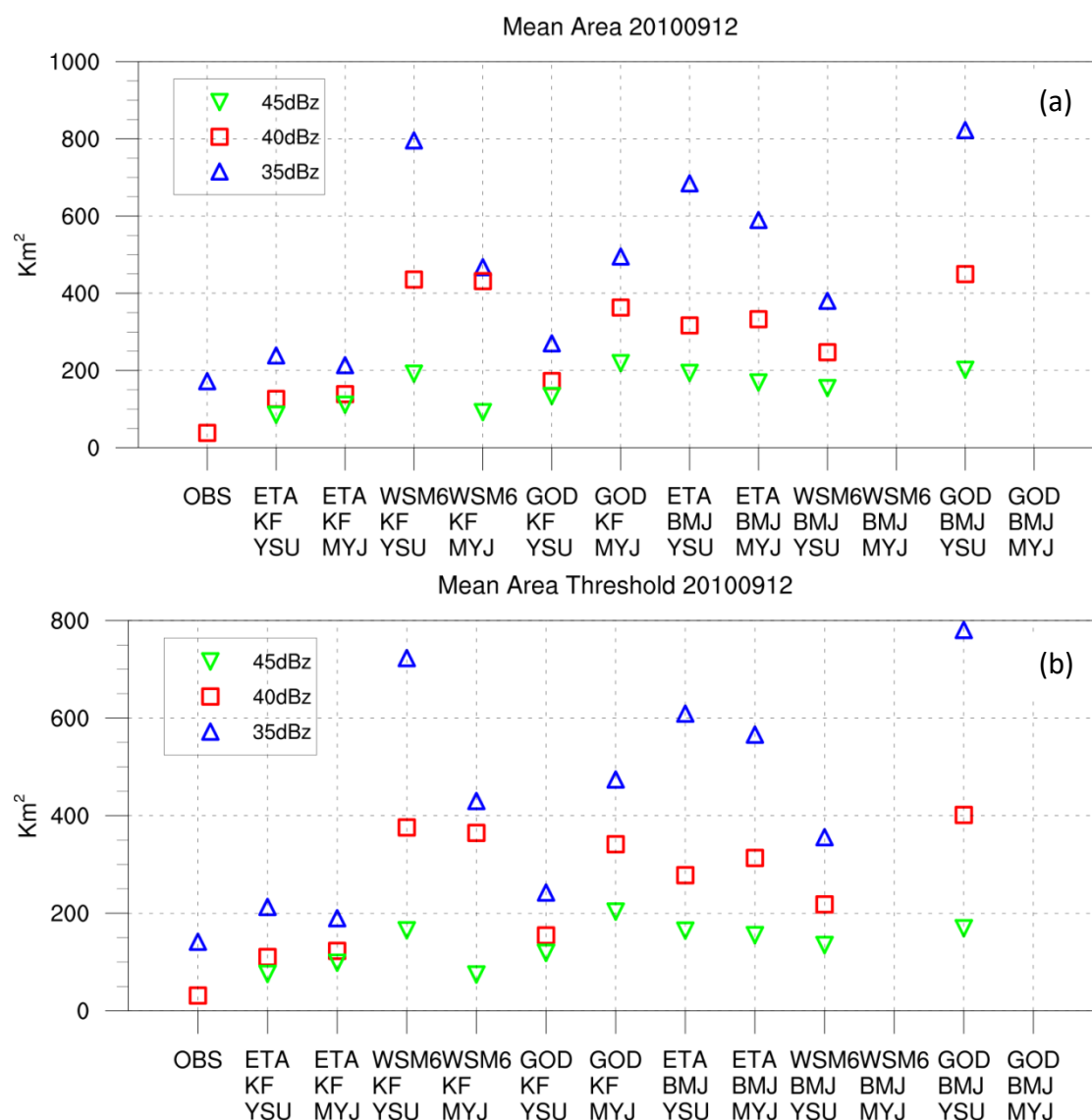


Figure 5.15. Mean area (a) and mean threshold area (b) attributes for the objects derived from observed and simulated values of reflectivity for all model setups for 12/09/2010.

Application of Method For Object Based Diagnostic Evaluation

the simulations produced large objects (area>150km²) having reflectivity higher than 45dBz. The same conclusion about the reflectivity applies to the median intensity since the observed objects have 39dBz median intensity (with the 35dBz threshold) but most of the simulations produce objects with more than 42dBz median intensity (Fig. 5.16a). The complexity of the simulated objects (16%-18%) is close to the observed ones (19%) but only for the 35dBz threshold (Fig 5.16b). The 40dBz threshold produces a denser object with only 13% complexity while the simulated ones start from 16%.

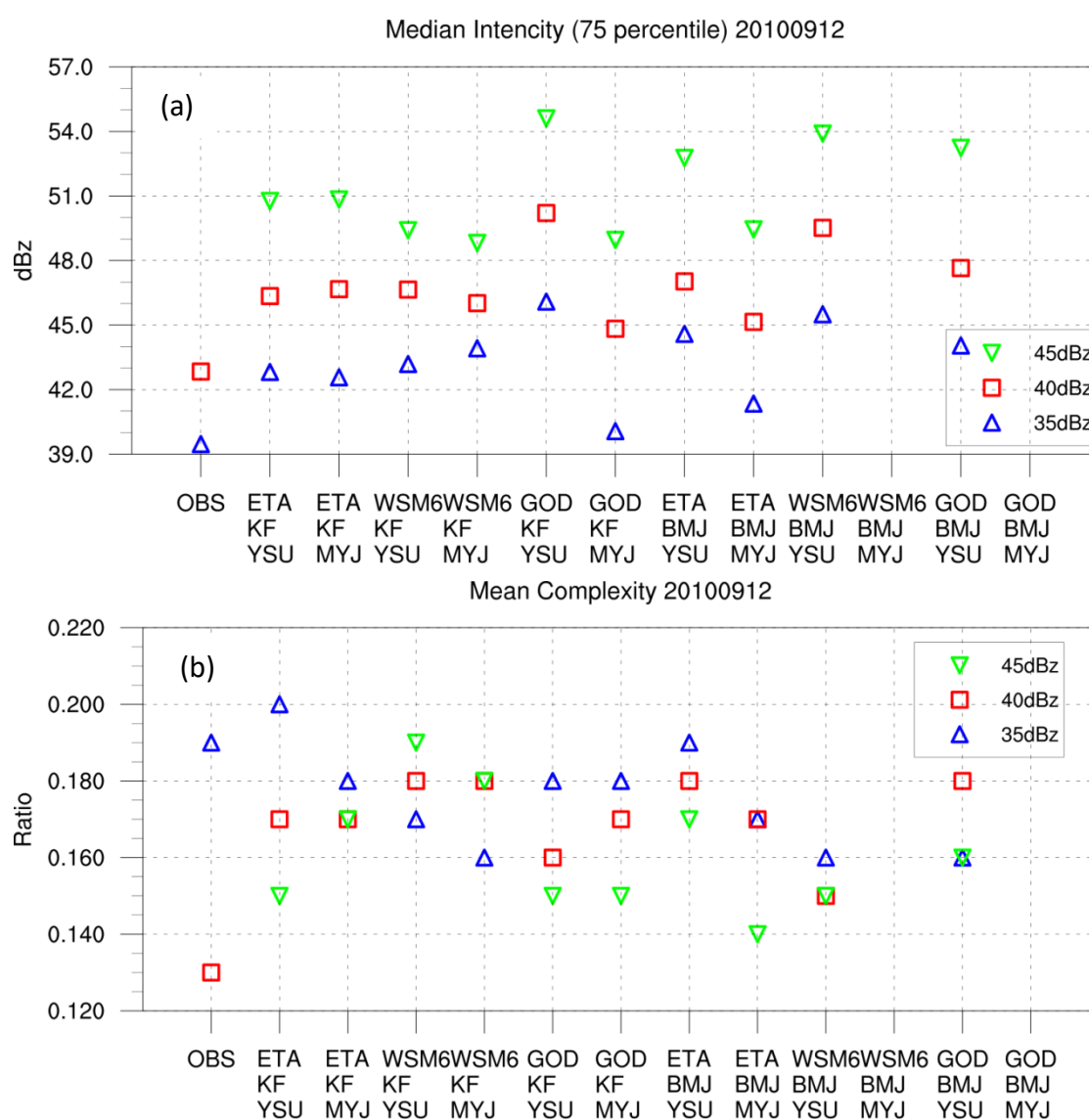


Figure 5.16. As in Fig. 5.15 but for median intensity (75th percentile) (a) and mean complexity (b) attributes.

5.2.6 Case of 25/09/2010

A SW flow dominates the area of Greece during the 9th of July, 2010. The temperature at 500hPa is $10 \pm 2^\circ\text{C}$ over Greece. The vorticity over the area has small negative values a fact that significantly reduced the intensity of the convective activity that day. On the western part of Thessaly strong convergence is present in the lower troposphere (Fig 5.17d) with almost zero divergence in the 300hPa level (Fig 5.17b). In the eastern part small values of divergence appear in both lower and higher troposphere implying entrainment in the middle levels, possibly from the area in the southwest where strong convergence exist in the lower levels.

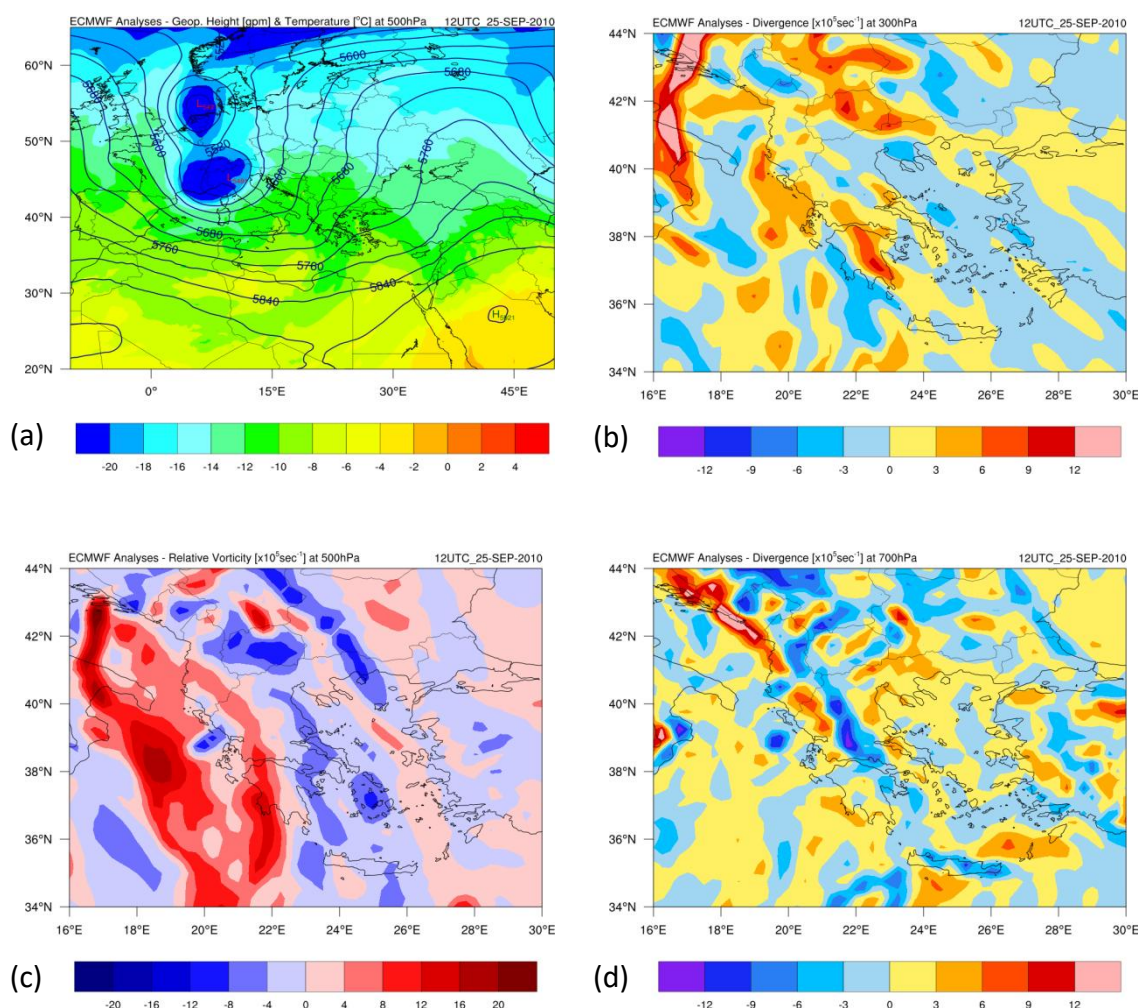


Figure 5.17. Geopotential height (contours) and temperature (shaded) at 500hPa (a), wind divergence at 300hPa and 700hPa (b) and (d) respectively, and relative vorticity at 500hPa (c), at 12:00UTC, in 25/09/2010.

Application of Method For Object Based Diagnostic Evaluation

The mean area of the observed objects is almost 100km² and in the same order are the objects derived from the simulations using the KF cumulus scheme (again with the exception of the GOD-KF-MYJ experiment). The experiments using the BMJ cumulus scheme (Fig 5.18a, right side) produce objects with much larger area, up to 600km². No apparent effect of the boundary layer scheme used can be traced in this case. Once again all the experiments produced sizable objects when using the threshold of 45 dBz, while there are no observed objects that fall into this category.

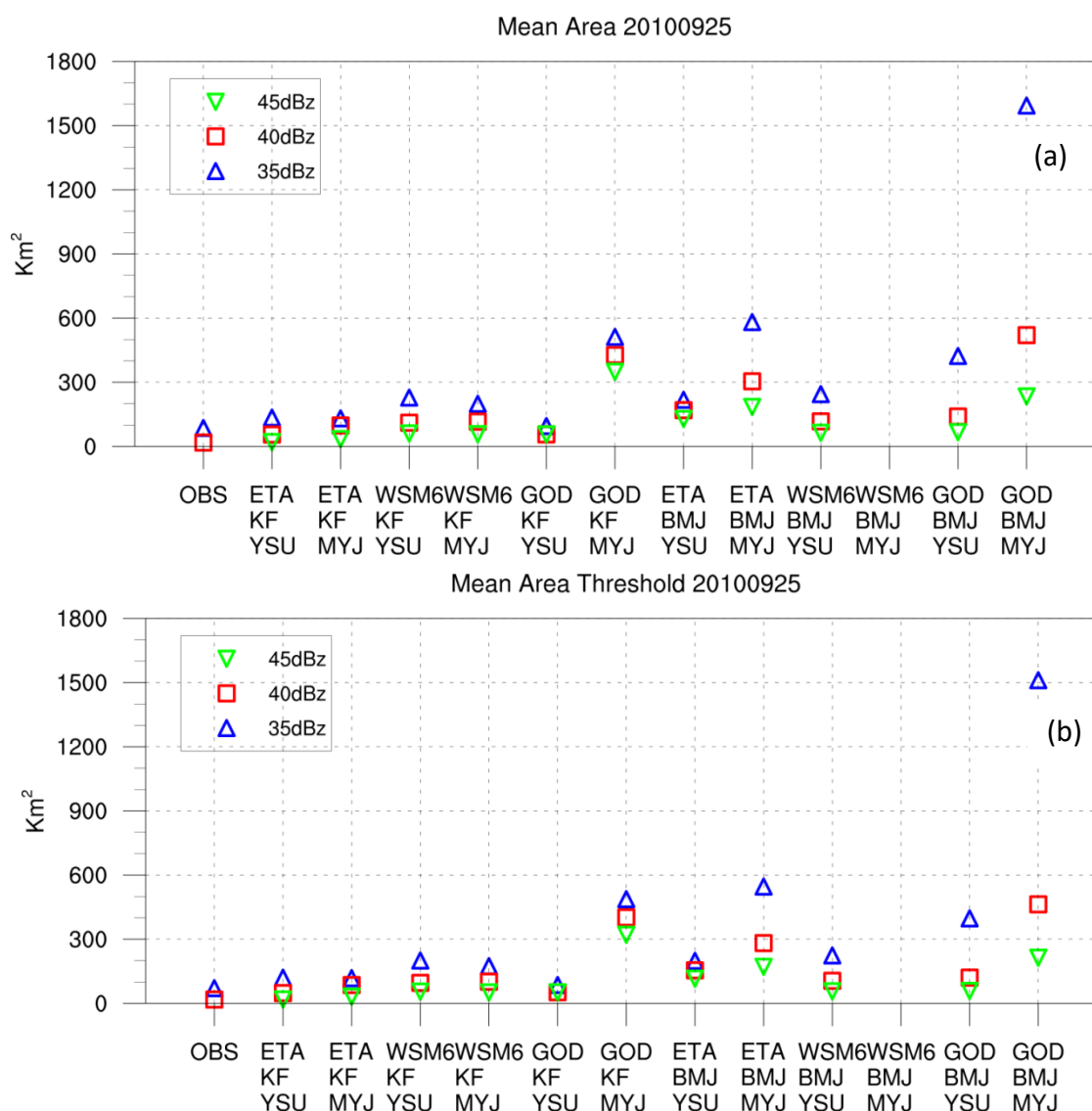


Figure 5.18. Mean area (a) and mean threshold area (b) attributes for the objects derived from observed and simulated values of reflectivity for all model setups for 25/09/2010.

In terms of median intensity the observed one is 38dBz with the 35dBz threshold and 43dBz with the 45 dBz threshold (Fig 5.19a). The objects derived from the simulations have at least 3dBz higher median intensities in both the 35db and 45dBz threshold. Finally the complexity of the observed objects is rather low compared to the simulated ones (Fig 5.19b). The phenomena that occurred that day were rather extensive with continuous areas of activity, but with reduced intensity that fits to the previous remark. The simulated ones had higher area (Fig 5.18a) but more irregular shape as their higher complexity attests (Fig. 5.19b).

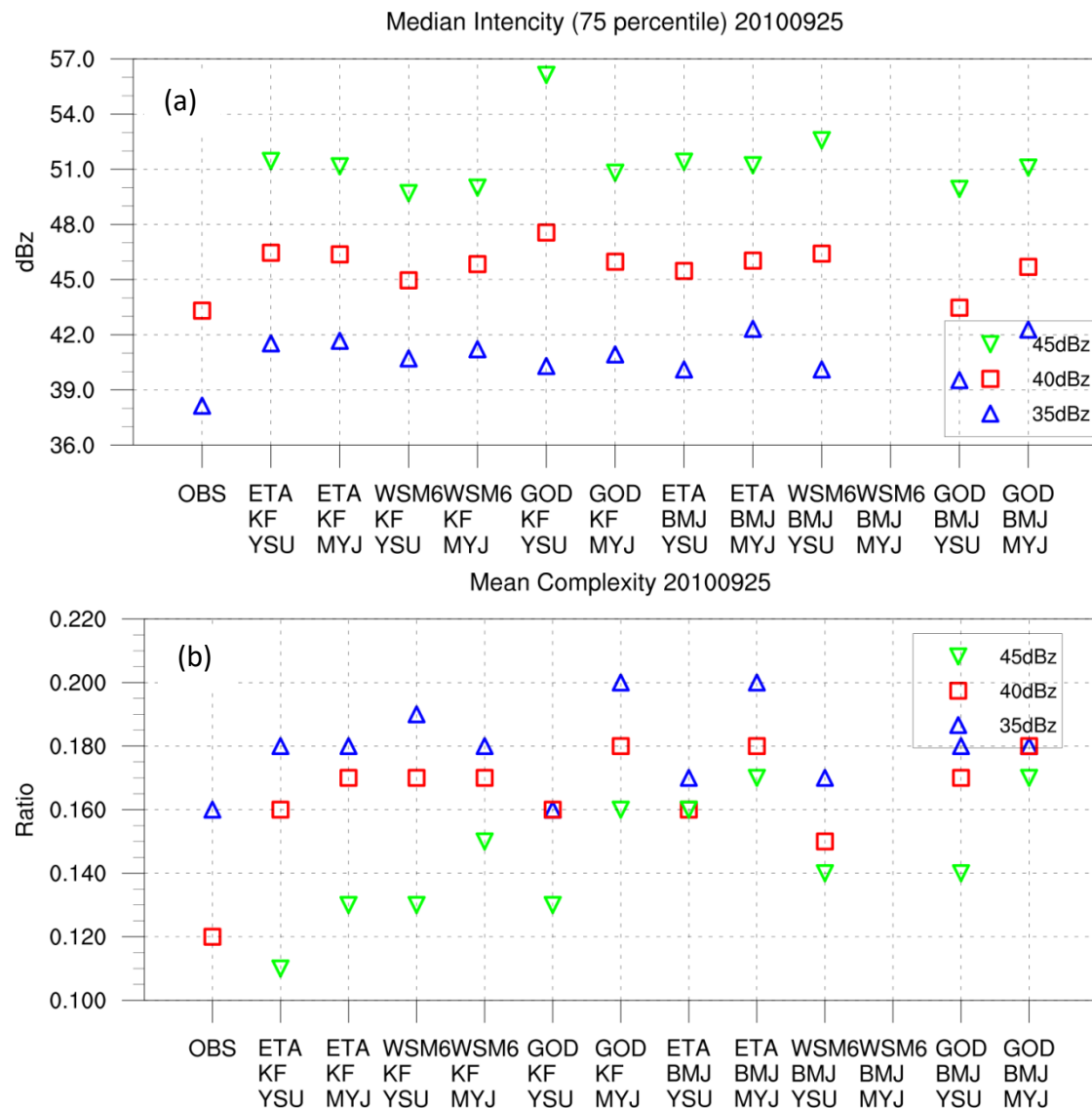


Figure 5.19. As in Fig. 5.18 but for median intensity (75th percentile) (a) and mean complexity (b) attributes.

5.2.7 Agregate statistics for the six days

The aggregate statistics for all the selected cases are shown in figures 5.20 and 5.21. The mean area of the observed objects is 90km² when the 35dBz threshold is used. This almost halves when the higher threshold of 45dBz is used (Fig. 5.20a). Most of the simulations produce objects with areas larger than the observed. The experiments using the KF cumulus scheme produce smaller objects than the experiments employing the BMJ scheme. (with the exception of the experiment using Goddard microphysics) and present smaller spread of values around the

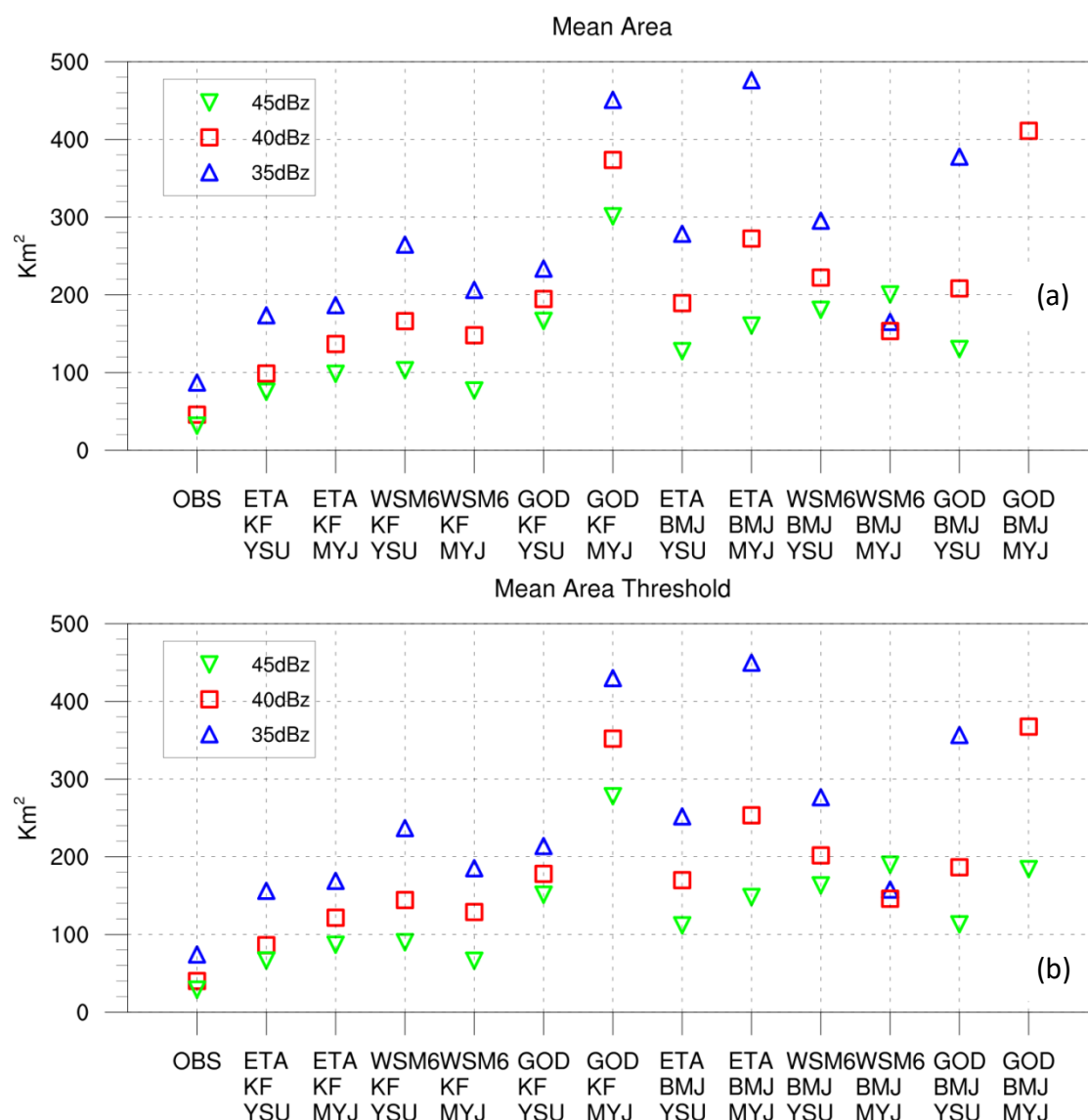


Figure 5.20. Mean area (a) and mean threshold area (b) attributes for the objects derived from observed and simulated values of reflectivity for all model setups for all the examined dates.

mean. The dependence on the convolution threshold is larger in the experiments using the BMJ cumulus scheme indicating that this scheme produces storm with more dispersed reflectivities. Since the sample is bigger in the aggregate statistics the median intensity values have a higher dependence on the convolution threshold (Fig. 5.21a). For the observed objects the median intensity receives values from 42dBz for the low threshold of 35dBz up to 54dBz for the high threshold of 45 dBz. The WSM6-KF-YSU, WSM6-KF-MYJ and ETA-BMJ-YSU experiments have values closer to the observed ones. The apparent good fit of the GOD-KF-MYJ is not real, but it is the result of combining extremes values to the both sides of the calculated mean.

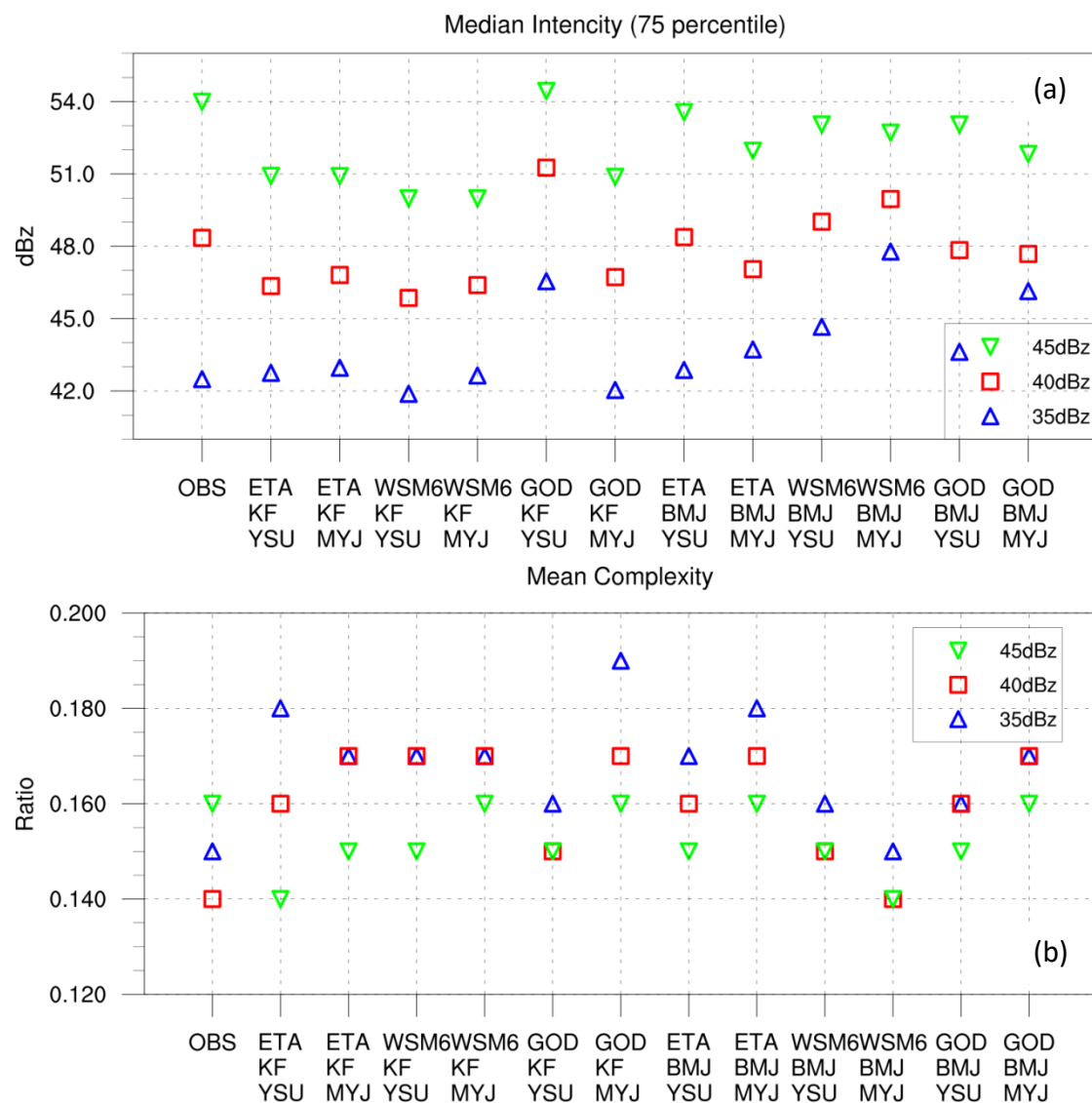


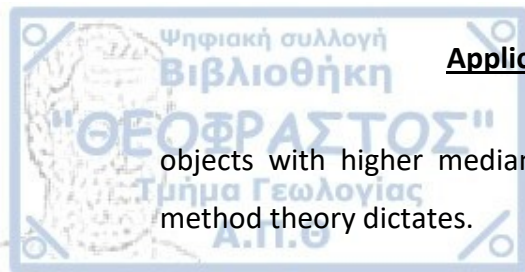
Figure 5.21. As in Fig. 5.20 but for median intensity (75th percentile) (a) and mean complexity (b) attributes.

Finally the complexity values fall in the range of 14% to 16% for the various convolution thresholds (Fig. 5.21b). The simulated derived objects present an overall higher complexity for the low convolution threshold, from 1% to 2%. For the higher convolution radius the complexity has values that are equal or smaller (up to 1% for most of the experiments) than the observed one.

5.3 Discussion

The Method of Object Based Diagnostic Evaluation was used to confirm that the choice of the working setup of the model was indeed right. Composite reflectivity was used to derive objects and their characteristics were compared. The method was employed in the same cases used in Chapter three and a brief synoptic and dynamic description of each case was presented.

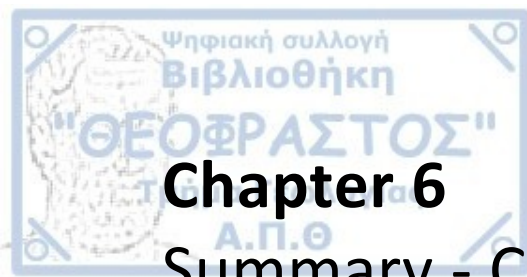
Three values of convolution threshold were used in the method to demonstrate if there is dependence of the final results on the threshold. Due to the different synoptic and dynamic forcing in the examined cases the derived objects had a wide variety of values in every attribute. The area of the observed objects varied from decades to hundreds of km^2 . The same is true for the median intensity ranging from 37dBz to 50dBz. The simulated objects while not extremely accurate per case, showed the same fluctuation with the observed ones. Wherever the observed area was high the corresponding simulated area was also high. The use of Goddard microphysics resulted in the biggest discrepancies between observed and simulated objects. Adequate results were obtained using the ETA-BMJ-MYJ setup while the WSM6-BMJ-MYJ setup caused unrealistic storms (very high areas and intensities). The WSM6-KF-YSU setup provided the most consistent results in both the simulated area and median intensity. Complexity values were close enough in every simulation, except those using the Goddard microphysics scheme. The complexity of the objects was higher when the 45dBz threshold was used, meaning that the areas with reflectivity higher than 45dBz are more scattered in the area. Overall the simulations derived objects that have bigger area and higher median intensity than the observed ones. The raise in the convolution threshold led to



Application of Method for Object Based Diagnostic Evaluation

objects with higher median intensity, smaller area and bigger complexity as the method theory dictates.





Chapter 6

Summary - Conclusions

Numerical weather prediction has made huge steps in the current years assisted by the immense increase in computational power and the ongoing understanding of complex weather phenomena. The widening of available options in the use of numerical weather models brings the user facing the problem of selecting the optimal setup of the model that best fits his needs. This is even more pronounced in the study of convective activity, dealing with events that are intense, fast evolving and have possibly high impact in the society.

The aim of the current study was to evaluate the performance and propose the best combination of parameterizations that should be used in Weather Research and Forecasting (WRF) numerical model for the forecast of convective events that shall take place in the area of Thessaly in central Greece. The research project “DAPHNE” aimed in tackling the problem of drought in this area, examining the possibility of a rain enhancing program through Weather Modification, would be highly benefited by the existence of such an important tool.

An ensemble of twelve different model configurations was put under test, simulating days with high convective activity. The impact of microphysics (MP), cumulus convection (CU) and planetary boundary layer (PBL) schemes was investigated and the best performing combination was chosen. Three MP schemes (Ferrier, WRF single-moment 6-classes, and Goddard), two CU schemes (Kain Fritsch and Betts-Miller-Janjić) and two PBL (Yonsei University and Mellor-Yamada-Janjić) were tested. In the first stage, results of the simulations for seven individual cases were statistically evaluated against surface observations and radar data using classic statistical methods.

This part of the study showed that:

- The experiments employing Goddard microphysics scheme showed the worst statistics and biggest deviations in WRF-D02 and WRF-D03 regardless the boundary layer and cumulus scheme coupled to.



Summary - Conclusions

- The experiments using Ferrier microphysics and especially when coupled with MYJ boundary layer showed adequate results in WRF-D02. The coupling of Ferrier to YSU on the other hand proved to exhibit worst statistics than the former configuration.
- The KF cumulus convection scheme showed overall better behavior both in results for WRF-D02 and WRF-D03.
- The coupling of WSM6 microphysics to YSU boundary layer and KF cumulus convection scheme showed the most consistent statistics overall in all cases.

The best performing setup was chosen and further evaluated in the second stage by widening the experimental sample. Thirty six more cases were selected and classified according to the prevailing synoptic conditions. The selected setup used the WSM6 microphysics, the Kain-Fritsch cumulus convection and the Yonsei University boundary layer scheme. This setup went under evaluation for both surface and cloud parameters. The classic statistics of ME and RMSE were used for surface parameters.

The major conclusions derived from this part of the study are:

- For temperature at 2m (T2m) a small underestimation (RMSE \approx 1.7K) was apparent for almost all of the synoptic types examined.
- The relative humidity at 2m (RH2m) showed the expected opposite behavior (overestimation of about 12%).
- Mean sea level pressure was systematically underestimated while the RMSE had values from 1.3hPa to 1.6hPa.
- Higher values than those observed was the result of the simulations in all the synoptic types for wind at 10m.

All the aforementioned results are satisfactory since they fall close to outcomes of previous studies in the area.

For cloud parameters a different approach was taken. Frequency distributions of maximum reflectivity, maximum cloud height and storm area, observed and simulated, were compared.

- Regarding the maximum reflectivity the cases of the ZON and SW synoptic types presented the biggest differences. The NW and OPTR simulation representatives formed distributions almost identical to the observed ones.
- For the area parameter there was a distinction between synoptic types leading to extensive convective activity (NW, SW) and those leading to small area storms (CUT, ZON). The model performed satisfactory since there was close resemblance between the observed and simulated distributions
- For observed cloud tops, the observed distributions are always unimodal, while the simulated distributions present mainly bimodal views, with the dominant mode higher than the observed.

The final stage involved the application of a novel statistical method for the evaluation of the original ensemble of simulations. The new method belongs to the spatial methods, that do not perform a point to point evaluation, but they rather try to distinguish similarities between the observed and forecast fields. The particular method used, Method for Object Based Diagnostic Evaluation (MODE) uses objects, discrete entities inside the field and examines their characteristics. The similarity of the characteristics between the observed and forecast objects, as this is expressed using the appropriate metrics, provides the performance of the model. In the present study the field of reflectivity was used to derive the objects. The method was employed in the same cases used in Chapter three and a brief synoptic and dynamic description preceded the statistical analysis of each case.

Three values of convolution threshold were used in the method to demonstrate if there is dependence of the final results on the threshold. Due to the different synoptic and dynamic forcing in the examined cases the derived objects had a wide variety of values in every attribute.

- The area of the observed objects varied from decades to hundreds of km². The same is true for the median intensity ranging from 37dBz to 50dBz.



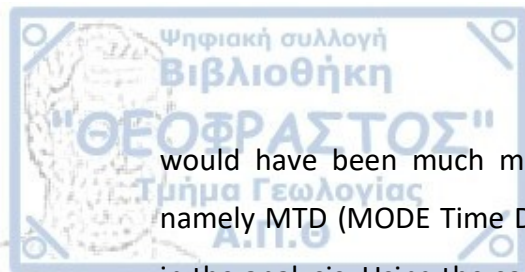
Summary - Conclusions

- The simulated objects while not extremely accurate per case, showed the same fluctuation with the observed ones. Wherever the observed area was high the corresponding simulated area was also high.
- The use of Goddard microphysics resulted in the biggest discrepancies between observed and simulated objects.
- Adequate results were obtained using the ETA-BMJ-MYJ setup while the WSM6-BMJ-MYJ setup caused unrealistic storms (very high areas and intensities).
- The WSM6-KF-YSU setup provided the most consistent results in both the simulated area and median intensity
- Complexity values were close enough in every simulation, except those using the Goddard microphysics scheme. The complexity of the objects was higher when the 45dBz threshold was used, meaning that the areas with reflectivity higher than 45dBz are more scattered in the area.
- The simulations derived objects that have bigger area and higher median intensity than the observed ones.
- The raise in the threshold led to objects with higher median intensity, smaller area and bigger complexity as the method theory dictates.

The result of this novel method confirmed that the model setup, initially selected using classic statistical methods has the best performance according to the new method too. This way the WRF-ARW model with this configuration can be a useful tool in every situation where a high convective event should be studied.

In the course of this study it became obvious that while the model is able to predict the convective activity in the wider area, there was a temporal deviation in the times of actual onset and decay of the activity. For this reason the extended MODE capabilities of matching objects of the forecasted and observed fields was not used in this study, since they would certainly provide a misleading result.

My everyday use of the model, as an operational meteorologist in the National Hail Suppression Program assures me that the model performs satisfactory. If the method had a way to manage those temporal errors the statistical results

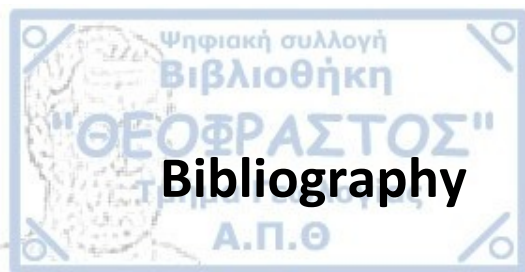


Summary - Conclusions

would have been much more close to my feeling. A recent extension of MODE namely MTD (MODE Time Domain) provides the ability to insert another dimension in the analysis. Using the coordinate of time the MTD can reveal temporal aspects of the examined phenomenon. Unfortunately MTD was in a beta stage for a long time during the analysis of my data and it could not be used with the required confidence in its results.

Now that the method is in stable stage, the next unsolicited step after this study, is the application of MTD in a subsample of the examined cases, in a way to familiarize with the new method. Furthermore the long term target is the creation of a procedure that would automatically quantify the performance of the model in every user specified case using the MODE time domain tool.





Ahijevych, D., Gilleland, E., Brown, B.G., Ebert, E.E., 2009. Application of spatial verification methods to idealized and NWP-gridded precipitation forecasts. Weather Forecast. 24, 1485–1497. <https://doi.org/10.1175/2009WAF2222298.1>

Asai, T., 1965. A Numerical Study of the Air-Mass Transformation over the Japan Sea in Winter. J. Meteorol. Soc. Japan. Ser. II. https://doi.org/10.2151/jmsj1965.43.1_1

Baldwin, M.E., Kain, J.S., Kay, M.P., 2002. Properties of the Convection Scheme in NCEP's Eta Model that Affect Forecast Sounding Interpretation. Weather Forecast. 17, 1063–1079. [https://doi.org/10.1175/1520-0434\(2002\)017<1063:POTCSI>2.0.CO;2](https://doi.org/10.1175/1520-0434(2002)017<1063:POTCSI>2.0.CO;2)

Bampzelis, D., Karacostas, T., 2016. Diurnal distribution of storm characteristics in central Macedonia during the warm season of the year using a C-band weather radar, in: Karacostas, T., Bais, A., Nastos, P.T. (Eds.), Perspectives on Atmospheric Sciences. Springer-Verlag, Berlin Heidelberg, pp. 317–322.

Bampzelis, D., Karacostas, T., 2014. Radar storm characteristics based upon their synoptic situations over Thessaly, in: Conference of Meteorology, Climatology and Physics of the Atmosphere. Conference of Meteorology, Climatology and Physics of the Atmosphere, Heraklion.

Bampzelis, D., Spiridonov, V., Kartsios, S., Pytharoulis, I., Tegoulis, I., Karacostas, T., 2015. Numerical Simulation of Airborne Cloud Seeding for the DAPHNE Precipitation Enhancement Project in Central Greece, in: 95th AMS Annual Meeting, Phoenix, Arizona, January 4–8.

Bauer, P., Thorpe, A., Brunet, G., 2015. The quiet revolution of numerical weather prediction. Nature. <https://doi.org/10.1038/nature14956>

Beljaars, A.C.M., 1995. The parametrization of surface fluxes in large-scale models

under free convection. Q. J. R. Meteorol. Soc. 121, 255–270.
<https://doi.org/10.1002/qj.49712152203>

Betts, A.K., 1986. A new convective adjustment scheme. Part I: Observational and theoretical basis. Q. J. R. Meteorol. Soc. 112, 677–691.
<https://doi.org/10.1002/qj.49711247307>

Betts, A.K., Miller, M.J., 1993. The Betts-Miller Scheme, in: The Representation of Cumulus Convection in Numerical Models. American Meteorological Society, Boston, MA, pp. 107–121. https://doi.org/10.1007/978-1-935704-13-3_9

Betts, A.K., Miller, M.J., 1986. A new convective adjustment scheme. Part II: Single column tests using GATE wave, BOMEX, ATEX and arctic air-mass data sets. Q. J. R. Meteorol. Soc. <https://doi.org/10.1002/qj.49711247308>

Bjerknes, V., 1904. Das Problem der Wettervorhersage, betrachtet vom Standpunkte der Mechanik und der Physik. Meteorol. Zeitschrift 18, 1–7.

Brown, B., Bullock, R., Fowler, T., Gotway, J.H., Newman, K., Jensen, T., 2017. Model Evaluation Tools Version 6.0 (METv6.0) User's Guide. Boulder, Colorado.

Brown, B.G., Bullock, R.R., Davis, C.A., Gotway, J.H., Chapman, M.B., Takacs, A., Gilleland, E., Manning, K., Mahoney, J.L., 2004. New verification approaches for convective weather forecasts. Conf. Aviat. Range, Aerosp. Meteorol. 503–515.

Bullock, R., Brown, B., Fowler, T., 2016. Method for Object- Based Diagnostic Evaluation NCAR Technical Notes NCAR / TN-532 + STR. Boulder, Colorado.

Bytheway, J.L., Kummerow, C.D., 2015. Toward an object-based assessment of high-resolution forecasts of long-lived convective precipitation in the central U.S. J. Adv. Model. Earth Syst. 7, 1248–1264. <https://doi.org/10.1002/2015MS000497>

Bytheway, J.L., Kummerow, C.D., Alexander, C., 2017. A features-based assessment of the evolution of warm season precipitation forecasts from the HRRR model over three years of development. Weather Forecast. 32, 1841–1856.

<https://doi.org/10.1175/WAF-D-17-0050.1>

Carlson, T.N., Boland, F.E., 1978. Analysis of Urban-Rural Canopy Using a Surface Heat Flux/Temperature Model. J. Appl. Meteorol. 17, 998–1013.
[https://doi.org/10.1175/1520-0450\(1978\)017<0998:AOURCU>2.0.CO;2](https://doi.org/10.1175/1520-0450(1978)017<0998:AOURCU>2.0.CO;2)

Casati, B., 2010. New developments of the intensity-scale technique within the spatial verification methods intercomparison project. Weather Forecast. 25, 113–143. <https://doi.org/10.1175/2009WAF2222257.1>

Casati, B., Ross, G., Stephenson, D.B., 2004. A new intensity-scale approach for the verification of spatial precipitation forecasts. Meteorol. Appl. 11, 141–154.
<https://doi.org/10.1017/S1350482704001239>

Casati, B., Wilson, L.J., Stephenson, D.B., Nurmi, P., Ghelli, A., Pocerich, M., Damrath, U., Ebert, E.E., Brown, B.G., Mason, S., 2008. Forecast verification: Current status and future directions, in: Meteorological Applications. <https://doi.org/10.1002/met.52>

Cassola, F., Ferrari, F., Mazzino, A., 2015. Numerical simulations of Mediterranean heavy precipitation events with the WRF model: A verification exercise using different approaches. Atmos. Res. 164–165, 210–225.
<https://doi.org/10.1016/j.atmosres.2015.05.010>

Charney, J.G., Fjörtoft, R., Neumann, J. Von, 1950. Numerical Integration of the Barotropic Vorticity Equation. Tellus. <https://doi.org/10.3402/tellusa.v2i4.8607>

Chen, F., Dudhia, J., 2001. Coupling and advanced land surface-hydrology model with the Penn State-NCAR MM5 modeling system. Part I: Model implementation and sensitivity. Mon. Weather Rev. [https://doi.org/10.1175/1520-0493\(2001\)129<0569:CAALSH>2.0.CO;2](https://doi.org/10.1175/1520-0493(2001)129<0569:CAALSH>2.0.CO;2)

Clark, A.J., Weiss, S.J., Kain, J.S., Jirak, I.L., Coniglio, M., Melick, C.J., Siewert, C., Sobash, R.A., Marsh, P.T., Dean, A.R., Xue, M., Kong, F., Thomas, K.W., Wang, Y.,

- Brewster, K., Gao, J., Wang, X., Du, J., Novak, D.R., Barthold, F.E., Bodner, M.J., Levit, J.J., Entwistle, C.B., Jensen, T.L., Correia, J., 2012. An Overview of the 2010 Hazardous Weather Testbed Experimental Forecast Program Spring Experiment. Bull. Am. Meteorol. Soc. 93, 55–74. <https://doi.org/10.1175/BAMS-D-11-00040.1>
- Coen, J.L., 2013. Modeling Wildland Fires : of the Coupled Atmosphere- Wildland Fire Environment Model (CAWFE). <https://doi.org/10.5065/D6K64G2G>
- Cohen, A.E., Cavallo, S.M., Coniglio, M.C., Brooks, H.E., 2015. A Review of Planetary Boundary Layer Parameterization Schemes and Their Sensitivity in Simulating Southeastern U.S. Cold Season Severe Weather Environments. Weather Forecast. 30, 591–612. <https://doi.org/10.1175/WAF-D-14-00105.1>
- Coppola, E., Sobolowski, S., Pichelli, E., Raffaele, F., Ahrens, B., Anders, I., Ban, N., Bastin, S., Belda, M., Belusic, D., Caldas-Alvarez, A., Cardoso, R.M., Davolio, S., Dobler, A., Fernandez, J., Fita, L., Fumiere, Q., Giorgi, F., Goergen, K., Güttler, I., Halenka, T., Heinzeller, D., Hodnebrog, Ø., Jacob, D., Kartsios, S., Katragkou, E., Kendon, E., Khodayar, S., Kunstmann, H., Knist, S., Lavín-Gullón, A., Lind, P., Lorenz, T., Maraun, D., Marelle, L., van Meijgaard, E., Milovac, J., Myhre, G., Panitz, H.-J., Piazza, M., Raffa, M., Raub, T., Rockel, B., Schär, C., Sieck, K., Soares, P.M.M., Somot, S., Srnc, L., Stocchi, P., Tölle, M.H., Truhetz, H., Vautard, R., de Vries, H., Warrach-Sagi, K., 2018. A first-of-its-kind multi-model convection permitting ensemble for investigating convective phenomena over Europe and the Mediterranean. Clim. Dyn. <https://doi.org/10.1007/s00382-018-4521-8>
- Ćurić, Mladjen, Janc, D., 2011. Comparison of Modeled and Observed Accumulated Convective Precipitation in Mountainous and Flat Land Areas. J. Hydrometeorol. 12, 245–261. <https://doi.org/10.1175/2010JHM1259.1>
- Ćurić, M., Janc, D., 2011. Analysis of predicted and observed accumulated convective precipitation in the area with frequent split storms. Hydrol. Earth Syst. Sci. 15,

3651–3658. <https://doi.org/10.5194/hess-15-3651-2011>

Davis, C.A., Brown, B., Bullock, R., 2006a. Object-based verification of precipitation forecasts. Part I: Methodology and application to mesoscale rain areas. Mon. Weather Rev. 134, 1772–1784. <https://doi.org/10.1175/MWR3145.1>

Davis, C.A., Brown, B., Bullock, R., 2006b. Object-based verification of precipitation forecasts. Part I: Application to convective rain systems. Mon. Weather Rev. 134, 1785–1795. <https://doi.org/10.1175/MWR3146.1>

Dixon, M., Wiener, G., 1993. TITAN: thunderstorm identification, tracking, analysis, and nowcasting - a radar-based methodology. J. Atmos. Ocean. Technol. [https://doi.org/10.1175/1520-0426\(1993\)010<0785:TTITAA>2.0.CO;2](https://doi.org/10.1175/1520-0426(1993)010<0785:TTITAA>2.0.CO;2)

Donelan, M.A., 2004. On the limiting aerodynamic roughness of the ocean in very strong winds. Geophys. Res. Lett. 31, L18306. <https://doi.org/10.1029/2004GL019460>

Dudhia, J., 2015. WRF Physics, in: WRF Basic Tutorial Slide Presentations.

Dudhia, J., 1989. Numerical Study of Convection Observed during the Winter Monsoon Experiment Using a Mesoscale Two-Dimensional Model. J. Atmos. Sci. 46, 3077–3107. [https://doi.org/10.1175/1520-0469\(1989\)046<3077:NSOCOD>2.0.CO;2](https://doi.org/10.1175/1520-0469(1989)046<3077:NSOCOD>2.0.CO;2)

Dyer, A.J., Hicks, B.B., 1970. Flux-gradient relationships in the constant flux layer. Q. J. R. Meteorol. Soc. <https://doi.org/10.1002/qj.49709641012>

Ebert, E. , McBride, J. , 2000. Verification of precipitation in weather systems: determination of systematic errors. J. Hydrol. 239, 179–202. [https://doi.org/10.1016/S0022-1694\(00\)00343-7](https://doi.org/10.1016/S0022-1694(00)00343-7)

Ebert, E.E., 2009. Neighborhood verification: A strategy for rewarding close forecasts. Weather Forecast. 24, 1498–1510. <https://doi.org/10.1175/2009WAF2222251.1>

Ebert, E.E., 2008. Fuzzy verification of high-resolution gridded forecasts: a review and proposed framework. Meteorol. Appl. 15, 51–64.
<https://doi.org/10.1002/met.25>

Ebert, E.E., Gallus, W.A., 2009. Toward better understanding of the contiguous rain area (CRA) method for spatial forecast verification. Weather Forecast. 24, 1401–1415. <https://doi.org/10.1175/2009WAF2222252.1>

Eckley, I.A., Nason, G.P., Treloar, R.L., 2010. Locally stationary wavelet fields with application to the modelling and analysis of image texture. J. R. Stat. Soc. Ser. C Appl. Stat. <https://doi.org/10.1111/j.1467-9876.2009.00721.x>

Ekström, M., Gilleland, E., 2017. Assessing convection permitting resolutions of WRF for the purpose of water resource impact assessment and vulnerability work: A southeast Australian case study. Water Resour. Res. <https://doi.org/10.1002/2016WR019545>

ESRL, 2020. High Resolution Rapid Refresh (HRRR) [WWW Document]. URL <https://rapidrefresh.noaa.gov/hrrr/> (accessed 1.15.20).

Fast, J.D., Gustafson, W.I., Easter, R.C., Zaveri, R.A., Barnard, J.C., Chapman, E.G., Grell, G.A., Peckham, S.E., 2006. Evolution of ozone, particulates, and aerosol direct radiative forcing in the vicinity of Houston using a fully coupled meteorology-chemistry-aerosol model. J. Geophys. Res. 111, D21305. <https://doi.org/10.1029/2005JD006721>

Ferrier, B., Jin, Y., Lin, Y., Black, T., Rogers, E., DiMego, G., 2002. Implementation of a new grid-scale cloud and precipitation scheme in the NCEP Eta Model, in: Proc. 15th Conf. on Numerical Weather Prediction; San Antonio; 12–16 August 2002; TX. pp. 280–283.

Flocas, A.A., 1994. Meteorology and Climatology Courses. Ziti Publications, Thessaloniki.

Fritsch, J.M., Chappell, C.F., 1980. Numerical Prediction of Convectively Driven Mesoscale Pressure Systems. Part I: Convective Parameterization. J. Atmos. Sci. 37, 1722–1733. [https://doi.org/10.1175/1520-0469\(1980\)037<1722:NPOCDM>2.0.CO;2](https://doi.org/10.1175/1520-0469(1980)037<1722:NPOCDM>2.0.CO;2)

Gallus, W.A., Pfeifer, M., 2008. Intercomparison of simulations using 5 WRF microphysical schemes with dual-Polarization data for a German squall line. Adv. Geosci. <https://doi.org/10.5194/adgeo-16-109-2008>

Gebhardt, C., Theis, S.E., Paulat, M., Ben Bouallègue, Z., 2011. Uncertainties in COSMO-DE precipitation forecasts introduced by model perturbations and variation of lateral boundaries. Atmos. Res. <https://doi.org/10.1016/j.atmosres.2010.12.008>

Gerrity, J.P., Black, T.L., Treadon, R.E., 1994. The numerical solution of the Mellor-Yamada level 2.5 turbulent kinetic energy equation in the eta model. Mon. Weather Rev. [https://doi.org/10.1175/1520-0493\(1994\)122<1640:TNSOTM>2.0.CO;2](https://doi.org/10.1175/1520-0493(1994)122<1640:TNSOTM>2.0.CO;2)

Gill, D.O., 2015. WRF Software, in: WRF Basic Tutorial Slide Presentations.

Gilleland, E., Ahijevych, D., Brown, B.G., Casati, B., Ebert, E.E., 2009. Intercomparison of spatial forecast verification methods. Weather Forecast. 24, 1416–1430. <https://doi.org/10.1175/2009WAF2222269.1>

Gilleland, E., Ahijevych, D.A., Brown, B.G., Ebert, E.E., 2010. Verifying forecasts spatially. Bull. Am. Meteorol. Soc. 91, 1365–1373. <https://doi.org/10.1175/2010BAMS2819.1>

Gochis, D.J., Yu, W., Yates, D.N., 2015. The WRF- Hydro Model technical description and user's guide, version 3.0.

Gofa, F., Boucouvala, D., Louka, P., Flocas, H.A., 2018. Spatial verification approaches as a tool to evaluate the performance of high resolution precipitation forecasts.

- Atmos. Res. 208, 78–87. <https://doi.org/10.1016/j.atmosres.2017.09.021>
- Grabowski, W.W., Morrison, H., Shima, S.-I., Abade, G.C., Dziekan, P., Pawlowska, H., 2019. Modeling of Cloud Microphysics: Can We Do Better? Bull. Am. Meteorol. Soc. 100, 655–672. <https://doi.org/10.1175/BAMS-D-18-0005.1>
- Grams, J.S., Gallus, W.A., Koch, S.E., Wharton, L.S., Loughe, A., Ebert, E.E., 2006. The use of a modified Ebert-McBride technique to evaluate mesoscale model QPF as a function of convective system morphology during IHOP 2002. Weather Forecast. 21, 288–306. <https://doi.org/10.1175/WAF918.1>
- Green, B.W., Zhang, F., 2013. Impacts of Air–Sea Flux Parameterizations on the Intensity and Structure of Tropical Cyclones. Mon. Weather Rev. 141, 2308–2324. <https://doi.org/10.1175/MWR-D-12-00274.1>
- Grell, G.A., Peckham, S.E., Schmitz, R., McKeen, S.A., Frost, G., Skamarock, W.C., Eder, B., 2005. Fully coupled “online” chemistry within the WRF model. Atmos. Environ. 39, 6957–6975. <https://doi.org/10.1016/j.atmosenv.2005.04.027>
- Griffin, S.M., Otkin, J.A., Rozoff, C.M., Sieglaff, J.M., Cronic, L.M., Alexander, C.R., Jensen, T.L., Wolff, J.K., 2017. Seasonal analysis of cloud objects in the High-Resolution Rapid Refresh (HRRR) model using object-based verification. J. Appl. Meteorol. Climatol. <https://doi.org/10.1175/JAMC-D-17-0004.1>
- Haltiner, G.J., Williams, R.T., 1980. Numerical prediction and dynamic meteorology. John Wiley & Sons, Inc.
- Hess, P., Brezowsky, H., 1977. Katalog der Grosswetterlagen Europas(1881-2009). Berichte des Dtsch. Wetterdienstes 15.
- Hong, S.-Y., Dudhia, J., Chen, S.-H., 2004. A Revised Approach to Ice Microphysical Processes for the Bulk Parameterization of Clouds and Precipitation. Mon. Weather Rev. 132, 103–120. [https://doi.org/10.1175/1520-0493\(2004\)132<0103:ARATIM>2.0.CO;2](https://doi.org/10.1175/1520-0493(2004)132<0103:ARATIM>2.0.CO;2)

Hong, S.S., Lim, J.-O.J., 2006. The WRF Single-Moment 6-Class Microphysics Scheme (WSM6). J. Korean Meteorol. Soc. 42, 129–151.

Hong, S.Y., Noh, Y., Dudhia, J., 2006. A new vertical diffusion package with an explicit treatment of entrainment processes. Mon. Weather Rev. 134, 2318–2341.
<https://doi.org/10.1175/MWR3199.1>

Hong, S.Y., Pan, H.L., 1996. Nonlocal boundary layer vertical diffusion in a medium-range forecast model. Mon. Weather Rev. [https://doi.org/10.1175/1520-0493\(1996\)124<2322:NBLVDI>2.0.CO;2](https://doi.org/10.1175/1520-0493(1996)124<2322:NBLVDI>2.0.CO;2)

Iacono, M.J., Delamere, J.S., Mlawer, E.J., Shephard, M.W., Clough, S.A., Collins, W.D., 2008. Radiative forcing by long-lived greenhouse gases: Calculations with the AER radiative transfer models. J. Geophys. Res. Atmos. <https://doi.org/10.1029/2008JD009944>

Jacobson, M.Z., 2005. Fundamentals of atmospheric modeling second edition, Fundamentals of Atmospheric Modeling Second Edition. <https://doi.org/10.1017/CBO9781139165389>

Janjic, Z.I., 1994. The step-mountain eta coordinate model: further developments of the convection, viscous sublayer, and turbulence closure schemes. Mon. Weather Rev. [https://doi.org/10.1175/1520-0493\(1994\)122<0927:TSMECM>2.0.CO;2](https://doi.org/10.1175/1520-0493(1994)122<0927:TSMECM>2.0.CO;2)

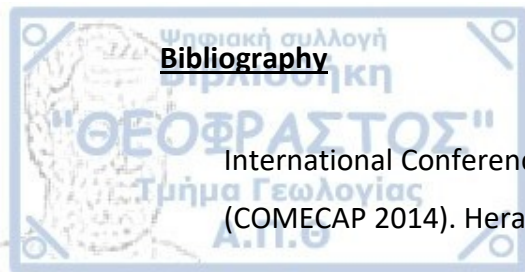
Janjić, Z.I., 2019. The surface layer parameterization in the NMM Models. NCEP Office Note, No. 497.

Janjić, Z.I., 2001. Nonsingular Implementation of the Mellor–Yamada Level 2.5 Scheme in the NCEP Meso model. NCEP Office Note, No. 437.

Janjić, Z.I., 2000. Comments on “Development and Evaluation of a Convection Scheme for Use in Climate Models.” J. Atmos. Sci. [https://doi.org/10.1175/1520-0469\(2000\)057<3686:codaeo>2.0.co;2](https://doi.org/10.1175/1520-0469(2000)057<3686:codaeo>2.0.co;2)

- Janjić, Z.I., 1994. The Step-Mountain Eta Coordinate Model: Further Developments of the Convection, Viscous Sublayer, and Turbulence Closure Schemes. Mon. Weather Rev. 122, 927–945. [https://doi.org/10.1175/1520-0493\(1994\)122<0927:TSMECM>2.0.CO;2](https://doi.org/10.1175/1520-0493(1994)122<0927:TSMECM>2.0.CO;2)
- Janjić, Z.I., 1990. The Step-Mountain Coordinate: Physical Package. Mon. Weather Rev. 118, 1429–1443. [https://doi.org/10.1175/1520-0493\(1990\)118<1429:TSMCPP>2.0.CO;2](https://doi.org/10.1175/1520-0493(1990)118<1429:TSMCPP>2.0.CO;2)
- Jiménez, P.A., Dudhia, J., 2012. Improving the Representation of Resolved and Unresolved Topographic Effects on Surface Wind in the WRF Model. J. Appl. Meteorol. Climatol. 51, 300–316. <https://doi.org/10.1175/JAMC-D-11-084.1>
- Jiménez, P.A., Dudhia, J., González-Rouco, J.F., Navarro, J., Montávez, J.P., García-Bustamante, E., 2012. A revised scheme for the WRF surface layer formulation. Mon. Weather Rev. <https://doi.org/10.1175/MWR-D-11-00056.1>
- Jolliffe, I.T., Stephenson, D.B., 2005. Comments on “Discussion of verification concepts in forecast verification: A practitioner’s guide in atmospheric science,” Weather and Forecasting. <https://doi.org/10.1175/WAF877.1>
- Kain, J.S., 2004. The Kain–Fritsch Convective Parameterization: An Update. J. Appl. Meteorol. 43, 170–181. [https://doi.org/10.1175/1520-0450\(2004\)043<0170:TKCPAU>2.0.CO;2](https://doi.org/10.1175/1520-0450(2004)043<0170:TKCPAU>2.0.CO;2)
- Kain, J.S., Fritsch, J.M., 1993. Convective Parameterization for Mesoscale Models: The Kain-Fritsch Scheme, in: The Representation of Cumulus Convection in Numerical Models. American Meteorological Society, Boston, MA, pp. 165–170. https://doi.org/10.1007/978-1-935704-13-3_16
- Kain, J.S., Fritsch, J.M., 1990. A One-Dimensional Entraining/Detraining Plume Model and Its Application in Convective Parameterization. J. Atmos. Sci. 47, 2784–2802. [https://doi.org/10.1175/1520-0469\(1990\)047<2784:AODEPM>2.0.CO;2](https://doi.org/10.1175/1520-0469(1990)047<2784:AODEPM>2.0.CO;2)

- Kain, J.S., Weiss, S.J., Levit, J.J., Baldwin, M.E., Bright, D.R., 2006. Examination of convection-allowing configurations of the WRF model for the prediction of severe convective weather: The SPC/NSSL Spring Program 2004. *Weather Forecast.* 21, 167–181. <https://doi.org/10.1175/WAF906.1>
- Karacostas, T., 2003. Synoptic, dynamic and cloud microphysical characteristics related to precipitation enhancement projects, in: *Regional Seminar on Cloud Physics and Weather Modification*. WMO-TD No 1227, p. 213.
- Karacostas, T., 1989. The Greek National Hail Suppression Program: Design and conduct of the experiment, in: *5th WMO Scientific Conference on Weather Modification and Applied Cloud Physics*. Beijing, China, pp. 605–608.
- Karacostas, T., 1984. The design of the Greek National Supression Program, in: *9th Conference Weather Modification*. Park City, Utah.
- Karacostas, T., Flocas, H.A., Flocas, A.A., Kakaliagou, O., Rizou, C., 1992. A study of the synoptic situations over the area of Eastern Mediterranean, in: *1st Greek Conference on Meteorology-Climatology-Physics of the Atmosphere*. pp. 469–477.
- Karacostas, T., Kartsios, S., Pytharoulis, I., Tegoulis, I., Bampzelis, D., 2018. Observations and modelling of the characteristics of convective activity related to a potential rain enhancement program in central Greece. *Atmos. Res.* 208, 218–228. <https://doi.org/10.1016/j.atmosres.2017.08.014>
- Karacostas, T., Pytharoulis, I., Tegoulis, I., Bampzelis, D., Kartsios, S., Kotsopoulos, S., Zanis, P., Katragkou, E., Mouskos, P., Tympanidis, K., 2015. The development of the DAPHNE conceptual model for the potentiality of designing a precipitation enhancement project in Thessaly, Greece, in: *95th AMS Annual Meeting*, Phoenix, Arizona, January 4–8.
- Kartsios, S., Karacostas, T., Pytharoulis, I., Dimitrakopoulos, A.P., 2014a. Coupled Weather – Wildland Fire Model for fire behaviour interpretation, in: *12th*



Bibliography

International Conference on Meteorology, Climatology and Atmospheric Physics (COMECAP 2014). Herakleion, Greece.

Kartsios, S., Karacostas, T., Pytharoulis, I., Dimitrakopoulos, A.P., 2014b. Simulating Atmosphere-Fire Interactions using a Coupled Weather – Wildland Fire Model, in: 10th Congress of the Hellenic Geographical Society. Thessaloniki, Greece.

Kartsios, S., Karacostas, T.S., Pytharoulis, I., Dimitrakopoulos, A.P., 2017. The Role of Heat Extinction Depth Concept to Fire Behavior: An Application to WRF-SFIRE Model, in: Karacostas, T., Bais, A., Nastos, P. (Eds.), Perspectives on Atmospheric Sciences. Springer International Publishing, Cham,. pp. 137–142. https://doi.org/10.1007/978-3-319-35095-0_20

Kartsios, S., Kotsopoulos, S., Karacostas, T., Tegoulis, I., Pytharoulis, I., Bampzelis, D., 2015. Statistical evaluation of the simulated convective activity over Central Greece, in: Geophysical Research Abstracts EGU General Assembly.

Kartsios, S.B., 2020. Study of Atmosphere-Wildland Fires Interactions, using Numerical Models, in Greece. Aristotle University of Thessaloniki, School of Geology, Department of Meteorology and Climatology, Annex Number of Scientific Annals of the School of Geology No 197, 229p.

Kassomenos, P., Flocas, H.A., Lykoudis, S., Petrakis, M., 1998. Analysis of Mesoscale Patterns in Relation to Synoptic Condition over an Urban Mediterranean Basin. Theor. Appl. Climatol. 59, 215–229. <https://doi.org/10.1007/s007040050025>

Katragkou, E., García-Díez, M., Vautard, R., Sobolowski, S., Zanis, P., Alexandri, G., Cardoso, R.M., Colette, A., Fernandez, J., Gobiet, A., Goergen, K., Karacostas, T., Knist, S., Mayer, S., Soares, P.M.M., Pytharoulis, I., Tegoulis, I., Tsikerdekis, A., Jacob, D., 2015. Regional climate hindcast simulations within EURO-CORDEX: evaluation of a WRF multi-physics ensemble. Geosci. Model Dev. 8, 603–618. <https://doi.org/10.5194/gmd-8-603-2015>

Katsafados, P., Mavromatidis, E., Gkikas, N., Papadopoulos, A., 2012. The numerical

weather prediction system of Harokopio University and statistical evaluation of the forecasts. *Geographies* 20, 79–98.

Keil, C., Craig, G.C., 2009. A displacement and amplitude score employing an optical flow technique. *Weather Forecast.* 24, 1297–1308.
<https://doi.org/10.1175/2009WAF2222247.1>

Keil, C., Craig, G.C., 2007. A displacement-based error measure applied in a regional ensemble forecasting system. *Mon. Weather Rev.* 135, 3248–3259.
<https://doi.org/10.1175/MWR3457.1>

Khain, A.P., Beheng, K.D., Heymsfield, A., Korolev, A., Krichak, S.O., Levin, Z., Pinsky, M., Phillips, V., Prabhakaran, T., Teller, A., Van Den Heever, S.C., Yano, J.I., 2015. Representation of microphysical processes in cloud-resolving models: Spectral (bin) microphysics versus bulk parameterization. *Rev. Geophys.*
<https://doi.org/10.1002/2014RG000468>

Kotroni, V., Lagouvardos, K., 2004. Evaluation of MM5 high-resolution real-time forecasts over the urban area of Athens, Greece. *J. Appl. Meteorol.*
<https://doi.org/10.1175/JAM2170.1>

Krestenitis, Y., Pytharoulis, I., Karacostas, T.S., Androulidakis, Y., Makris, C., Kombiadou, K., Tegoulas, I., Baltikas, V., Kotsopoulos, S., Kartsios, S., 2017. Severe Weather Events and Sea Level Variability Over the Mediterranean Sea: The WaveForUs Operational Platform. pp. 63–68. https://doi.org/10.1007/978-3-319-35095-0_9

Lagouvardos, K., Kotroni, V., Defer, E., Bousquet, O., 2013. Study of a heavy precipitation event over southern france, in the frame of HYMEX project: Observational analysis and model results using assimilation of lightning. *Atmos. Res.* <https://doi.org/10.1016/j.atmosres.2013.07.003>

Lakshmanan, V., Kain, J.S., 2010. A Gaussian mixture model approach to forecast verification. *Weather Forecast.* 25, 908–920.

<https://doi.org/10.1175/2010WAF2222355.1>

Lamb, H.H., 1972. British Isles weather types and a register of the daily sequence of circulation patterns 1861-1971.

Lang, S., Tao, W.K., Cifelli, R., Olson, W., Halverson, J., Rutledge, S., Simpson, J., 2007. Improving simulations of convective systems from TRMM LBA: Easterly and westerly regimes. J. Atmos. Sci. <https://doi.org/10.1175/JAS3879.1>

Laprise, R., 1991. The Euler equations of motion with hydrostatic pressure as an independent variable. Mon. Weather Rev. [https://doi.org/10.1175/1520-0493\(1992\)120<0197:teeomw>2.0.co;2](https://doi.org/10.1175/1520-0493(1992)120<0197:teeomw>2.0.co;2)

Lawson, J.R., Gallus, W.A., 2016. Adapting the SAL method to evaluate reflectivity forecasts of summer precipitation in the central United States. Atmos. Sci. Lett. 17, 524–530. <https://doi.org/10.1002/asl.687>

Lean, H.W., Clark, P.A., Dixon, M., Roberts, N.M., Fitch, A., Forbes, R., Halliwell, C., 2008. Characteristics of High-Resolution Versions of the Met Office Unified Model for Forecasting Convection over the United Kingdom. Mon. Weather Rev. 136, 3408–3424. <https://doi.org/10.1175/2008MWR2332.1>

Lin, Y.L., Farley, R.D., Orville, H.D., 1983. Bulk parameterization of the snow field in a cloud model. J. Clim. Appl. Meteorol. [https://doi.org/10.1175/1520-0450\(1983\)022<1065:BPOTSF>2.0.CO;2](https://doi.org/10.1175/1520-0450(1983)022<1065:BPOTSF>2.0.CO;2)

Locatelli, J.D., Hobbs, P. V., 1974. Fall speeds and masses of solid precipitation particles. J. Geophys. Res. <https://doi.org/10.1029/jc079i015p02185>

Lompar, M., Ćurić, M., Romanic, D., 2017. Simulation of a severe convective storm using a numerical model with explicitly incorporated aerosols. Atmos. Res. <https://doi.org/10.1016/j.atmosres.2017.04.037>

Lynch, P., 2006. The Emergence of Numerical Weather Prediction Richardson's Dream. Cambridge University Press.

- Maheras, P., Patrikas, I., Karacostas, T., Anagnostopoulou, C., 2000. Automatic classification of circulation types in Greece: Methodology, description, frequency, variability and trend analysis. Theor. Appl. Climatol. <https://doi.org/10.1007/s007040070010>
- Mahrt, L.T., Sun, J., 1995. The Subgrid Velocity Scale in the Bulk Aerodynamic Relationship for Spatially Averaged Scalar Fluxes. Mon. Weather Rev. 123, 3032–3041. [https://doi.org/10.1175/1520-0493\(1995\)123<3032:TSVSIT>2.0.CO;2](https://doi.org/10.1175/1520-0493(1995)123<3032:TSVSIT>2.0.CO;2)
- Mariani, S., Casaioli, M., 2018. Effects of model domain extent and horizontal grid size on contiguous rain area (CRA) analysis: A MesoVICT study. Meteorol. Zeitschrift 27, 481–502. <https://doi.org/10.1127/metz/2018/0897>
- Marzban, C., Sandgathe, S., 2010. Optical flow for verification. Weather Forecast. 25, 1479–1494. <https://doi.org/10.1175/2010WAF2222351.1>
- Marzban, C., Sandgathe, S., 2009. Verification with variograms. Weather Forecast. 24, 1102–1120. <https://doi.org/10.1175/2009WAF2222122.1>
- Marzban, C., Sandgathe, S., 2008. Cluster analysis for object-oriented verification of fields: A variation. Mon. Weather Rev. 136, 1013–1025. <https://doi.org/10.1175/2007MWR1994.1>
- Marzban, C., Sandgathe, S., 2006. Cluster analysis for verification of precipitation fields. Weather Forecast. 21, 824–838. <https://doi.org/10.1175/WAF948.1>
- Marzban, C., Sandgathe, S., Lyons, H., 2008. An Object-Oriented Verification of Three NWP Model Formulations via Cluster Analysis: An Objective and a Subjective Analysis. Mon. Weather Rev. 136, 3392–3407. <https://doi.org/10.1175/2007MWR2333.1>
- Marzban, C., Sandgathe, S., Lyons, H., Lederer, N., 2009. Three spatial verification techniques: Cluster analysis, variogram, and optical flow. Weather Forecast. 24,

1457–1471. <https://doi.org/10.1175/2009WAF2222261.1>

Mass, C.F., Ovens, D., Westrick, K., A., C.B., 2002. Does Increasing Horizontal Resolution Produce More Skillful Forecasts. Bull. Am. Meteorol. Soc. 83, 407–430. [https://doi.org/http://dx.doi.org/10.1175/1520-0477\(2002\)083](https://doi.org/http://dx.doi.org/10.1175/1520-0477(2002)083)

Mazarakis, N., 2010. Observational and numerical study of the dynamical and physical processes associated with the summer convective activity in Greece. Phd, University of Patras.

McCumber, M., Wei-Kuo Tao, Simpson, J., Penc, R., Su-Tzai Soong, 1991. Comparison of ice-phase microphysical parameterization schemes using numerical simulations of tropical convection. J. Appl. Meteorol. <https://doi.org/10.1175/1520-0450-30.7.985>

Mellor, G.L., Yamada, T., 1982. Development of a turbulence closure model for geophysical fluid problems. Rev. Geophys. 20, 851. <https://doi.org/10.1029/RG020i004p00851>

Mellor, G.L., Yamada, T., 1974. A Hierarchy of Turbulence Closure Models for Planetary Boundary Layers. J. Atmos. Sci. [https://doi.org/10.1175/1520-0469\(1974\)031<1791:ahotcm>2.0.co;2](https://doi.org/10.1175/1520-0469(1974)031<1791:ahotcm>2.0.co;2)

Mittermaier, M., Roberts, N., Thompson, S.A., 2013. A long-term assessment of precipitation forecast skill using the Fractions Skill Score. Meteorol. Appl. 20, 176–186. <https://doi.org/10.1002/met.296>

Miyakoda, K., Sirutis, J., 1977. Comparative integrations of global models with various parameterized processes of subgrid-scale vertical transports: Description of the parameterization. Beitr. Atmos. Phys 445–488.

Möbis, B., Stevens, B., 2012. Factors controlling the position of the Intertropical Convergence Zone on an aquaplanet. J. Adv. Model. Earth Syst. 4, n/a-n/a. <https://doi.org/10.1029/2012MS000199>

Monin, A.S., Obukhov, A.M., 1954. Basic laws of turbulent mixing in the surface layer of the atmosphere. Tr. Akad. Nauk SSSR Geophiz. Inst. 24, 163–187.

Muller, R.A., 1977. A Synoptic Climatology for Environmental Baseline Analysis: New Orleans. J. Appl. Meteorol. [https://doi.org/10.1175/1520-0450\(1977\)016<0020:ascfeb>2.0.co;2](https://doi.org/10.1175/1520-0450(1977)016<0020:ascfeb>2.0.co;2)

Nachamkin, J.E., 2004. Mesoscale verification using meteorological composites. Mon. Weather Rev. 132, 941–955. [https://doi.org/10.1175/1520-0493\(2004\)132<0941:MVUMC>2.0.CO;2](https://doi.org/10.1175/1520-0493(2004)132<0941:MVUMC>2.0.CO;2)

Nachamkin, J.E., Chen, S., Schmidt, J., 2005. Evaluation of heavy precipitation forecasts using composite-based methods: A distributions-oriented approach. Mon. Weather Rev. 133, 2163–2177. <https://doi.org/10.1175/MWR2975.1>

Nachamkin, J.E., Schmidt, J., 2015. Applying a neighborhood fractions sampling approach as a diagnostic tool. Mon. Weather Rev. 143, 4736–4749. <https://doi.org/10.1175/MWR-D-14-00411.1>

Ooyama, K. V., 1990. A thermodynamic foundation for modeling the moist atmosphere. J. Atmos. Sci. [https://doi.org/10.1175/1520-0469\(1990\)047<2580:ATFFMT>2.0.CO;2](https://doi.org/10.1175/1520-0469(1990)047<2580:ATFFMT>2.0.CO;2)

Paulson, C.A., 1970. The Mathematical Representation of Wind Speed and Temperature Profiles in the Unstable Atmospheric Surface Layer. J. Appl. Meteorol. 9, 857–861. [https://doi.org/10.1175/1520-0450\(1970\)009<0857:TMROWS>2.0.CO;2](https://doi.org/10.1175/1520-0450(1970)009<0857:TMROWS>2.0.CO;2)

Peralta, C., Ben Bouallègue, Z., Theis, S.E., Gebhardt, C., Buchhold, M., 2012. Accounting for initial condition uncertainties in COSMO-DE-EPS. J. Geophys. Res. Atmos. <https://doi.org/10.1029/2011JD016581>

Petalas, C., Pisinaras, V., Koltsida, K., Tsihrintzis, V.A., 2005. The Hydrological Regime of the East Basin of Thessaly, Greece, in: Proceedings of the 9th International

Conference on Environmental Science and Technology, Rhodes Island.

Pielke, R.A., 2013. Mesoscale Meteorological Modeling, Mesoscale Meteorological Modeling. <https://doi.org/10.1016/C2009-0-02981-X>

Powell, M.D., Vickery, P.J., Reinhold, T.A., 2003. Reduced drag coefficient for high wind speeds in tropical cyclones. *Nature*. <https://doi.org/10.1038/nature01481>

Pytharoulis, I., 2008. Numerical Weather Prediction. Notes of the postgraduate course on “Meteorology, Climatology and Atmospheric Environment.” Department of Meteorology and Climatology, School of Geology, Aristotle University of Thessaloniki, Greece (in Greek).

Pytharoulis, I., Kartsios, S., Tegoulis, I., Feidas, H., Miglietta, M., Matsangouras, I., Karacostas, T., 2018. Sensitivity of a Mediterranean Tropical-Like Cyclone to Physical Parameterizations. *Atmosphere* (Basel). 9, 436. <https://doi.org/10.3390/atmos9110436>

Pytharoulis, I., Kotsopoulos, S., Tegoulis, I., Kartsios, S., Bampzelis, D., Karacostas, T., 2016. Numerical modeling of an intense precipitation event and its associated lightning activity over northern Greece. *Atmos. Res.* 169, 523–538. <https://doi.org/10.1016/j.atmosres.2015.06.019>

Pytharoulis, I., Tegoulis, I., Kotsopoulos, S., Bampzelis, D., Karacostas, T., Katragkou, E., 2015a. Verification of the operational high-resolution WRF forecasts produced by WaveForUs project, in: 16th Annual WRF Users’ Workshop. Boulder, CO, USA.

Pytharoulis, I., Tegoulis, I., Kotsopoulos, S., Bampzelis, D., Karacostas, T., Katragkou, E., 2014a. Evaluation of the Operational Numerical Weather Predictions of the Wave4Us Project, in: 12th International Conference of Meteorology, Climatology and Physics of the Atmosphere. Heraklion, pp. 96–101.

Pytharoulis, I., Tegoulis, I., Kotsopoulos, S., Bampzelis, D., Kartsios, S., Zanis, P.,

- Katragkou, E., Karacostas, T., 2015b. High-resolution WRF hindcasts over central Greece: Characteristics of simulated convective activity and model evaluation, in: 15th Annual WRF Users' Workshop. Boulder, CO, USA.
- Pytharoulis, I., Tegoulis, I., Kotsopoulos, S., Bampzelis, D., Katragkou, E., Karacostas, T., 2014b. A high-resolution numerical weather prediction system for Greece: model setup and performance analysis, in: Proceedings of the 10th International Congress of the Hellenic Geographical Society, 22-24 October, Thessaloniki, Greece. pp. 135–145.
- Radanovics, S., Vidal, J., Sauquet, E., 2018. Spatial Verification of Ensemble Precipitation: An Ensemble Version of SAL. Weather Forecast. 33, 1001–1020. <https://doi.org/10.1175/WAF-D-17-0162.1>
- Richardson, L.F., 1922. Weather prediction by numerical process. Cambridge University Press.
- Roberts, N.M., Lean, H.W., 2008. Scale-selective verification of rainfall accumulations from high-resolution forecasts of convective events. Mon. Weather Rev. 136, 78–97. <https://doi.org/10.1175/2007MWR2123.1>
- Roberts, R.D., Rutledge, S., 2003. Nowcasting storm initiation and growth using GOES-8 and WSR-88D data. Weather Forecast. [https://doi.org/10.1175/1520-0434\(2003\)018<0562:NSIAGU>2.0.CO;2](https://doi.org/10.1175/1520-0434(2003)018<0562:NSIAGU>2.0.CO;2)
- Rogers, E., Black, T., Ferrier, B., Lin, Y., Parrish, D., DiMego, G., 2001. Changes to the NCEP Meso Eta Analysis and Forecast System: Increase in Resolution, New Cloud Microphysics, Modified Precipitation Assimilation, Modified 3DVAR Analysis.
- Rutledge, S.A., Hobbs, P. V., 1984. The Mesoscale and Microscale Structure and Organization of Clouds and Precipitation in Midlatitude Cyclones. XII: A Diagnostic Modeling Study of Precipitation Development in Narrow Cold-Frontal Rainbands. J. Atmos. Sci. 41, 2949–2972. <https://doi.org/10.1175/1520->

0469(1984)041<2949:TMAMSA>2.0.CO;2

Ryan, B.F., 1996. On the global variation of precipitating layer clouds. Bull. Am. Meteorol. Soc. [https://doi.org/10.1175/1520-0477\(1996\)077<0053:OTGVOP>2.0.CO;2](https://doi.org/10.1175/1520-0477(1996)077<0053:OTGVOP>2.0.CO;2)

Sindosi, O.A., Bartzokas, A., Kotroni, V., Lagouvardos, K., 2012. Verification of precipitation forecasts of MM5 model over Epirus, NW Greece, for various convective parameterization schemes. Nat. Hazards Earth Syst. Sci. <https://doi.org/10.5194/nhess-12-1393-2012>

Skamarock, W.C., Klemp, J.B., Dudhia, J., Gill, D.O., Barker, D.M., Duda, M.G., Huang, X.-Y., Wang, W., Powers, J.G., 2008. A description of the Advanced Research WRF Version 3. NCAR/TN-475+STR. <https://doi.org/10.5065/D68S4MVH>

Stein, T.H.M., Hogan, R.J., Clark, P.A., Halliwell, C.E., Hanley, K.E., Lean, H.W., Nicol, J.C., Plant, R.S., 2015. The DYMECS Project: A Statistical Approach for the Evaluation of Convective Storms in High-Resolution NWP Models. Bull. Am. Meteorol. Soc. 96, 939–951. <https://doi.org/10.1175/BAMS-D-13-00279.1>

Stensrud, D.J., 2011. Parameterization schemes: Keys to understanding numerical weather prediction models, Parameterization Schemes: Keys to Understanding Numerical Weather Prediction Models. <https://doi.org/10.1017/CBO9780511812590>

Stolaki, S., Pytharoulis, I., Karacostas, T., 2012. A Study of Fog Characteristics Using a Coupled WRF–COBEL Model Over Thessaloniki Airport, Greece. Pure Appl. Geophys. 169, 961–981. <https://doi.org/10.1007/s00024-011-0393-0>

Stratman, D.R., Coniglio, M.C., Koch, S.E., Xue, M., 2013. Use of multiple verification methods to evaluate forecasts of convection from hot- and cold-start convection-allowing models. Weather Forecast. 28, 119–138. <https://doi.org/10.1175/WAF-D-12-00022.1>

Tallapragada, V., Coauthors, 2014. Hurricane Weather Research and Forecasting (HWRF) Model.

Tao, W.-K., Lang, S., Zeng, X., Li, X., Matsui, T., Mohr, K., Posselt, D., Chern, J., Peters-Lidard, C., Norris, P.M., Kang, I.-S., Choi, I., Hou, A., Lau, K.-M., Yang, Y.-M., 2014. The Goddard Cumulus Ensemble model (GCE): Improvements and applications for studying precipitation processes. *Atmos. Res.* 143, 392–424. <https://doi.org/10.1016/j.atmosres.2014.03.005>

Tao, W.-K., Simpson, J., 1993. Goddard Cumulus Ensemble Model. Part I: Model Description. *Terr. Atmos. Ocean. Sci.* 4, 035. [https://doi.org/10.3319/TAO.1993.4.1.35\(A\)](https://doi.org/10.3319/TAO.1993.4.1.35(A))

Tao, W.K., Simpson, J., Baker, D., Braun, S., Chou, M.D., Ferrier, B., Johnson, D., Khain, A., Lang, S., Lynn, B., Shie, C.L., Starr, D., Sui, C.H., Wang, Y., Wetzel, P., 2003. Microphysics, radiation and surface processes in the Goddard Cumulus Ensemble (GCE) model. *Meteorol. Atmos. Phys.* <https://doi.org/10.1007/s00703-001-0594-7>

Tartaglione, N., Mariani, S., Accadia, C., Speranza, A., Casaioli, M., 2005. Comparison of raingauge observations with modeled precipitation over Cyprus using Contiguous Rain Area analysis. *Atmos. Chem. Phys. Discuss.* 5, 2355–2376. <https://doi.org/10.5194/acpd-5-2355-2005>

Tegoulas, I., Kartsios, S., Pytharoulis, I., Kotsopoulos, S., Karacostas, T.S., 2017. The Influence of WRF Parameterisation Schemes on High Resolution Simulations Over Greece, in: Karacostas, T., Bais, A., Nastos, P. (Eds.), *Perspectives on Atmospheric Sciences*. Springer International Publishing, Cham,. pp. 3–8. https://doi.org/10.1007/978-3-319-35095-0_1

Tegoulas, I., Pytharoulis, I., Kotsopoulos, S., Bampzelis, D., Kartsios, S., Karacostas, T., 2014a. The influence of WRF parameterisation schemes on high resolution simulations over Central Greece, in: *15th Annual WRF Users' Workshop*. Boulder, CO, USA.

Tegoulas, I., Pytharoulis, I., Kotsopoulos, S., Karacostas, T., 2014b. Numerical weather prediction sensitivity to sea-surface temperatures, in: 12th International Conference on Meteorology, Climatology and Atmospheric Physics (COMECAP2014). Herakleion, Crete, Greece. pp. 203–208.

The NCAR Command Language (Version 6.5.0) [Software], 2018. Boulder, Colorado: UCAR/NCAR/CISL/TDD. <https://doi.org/10.5065/D6WD3XH5>

Troen, I.B., Mahrt, L., 1986. A simple model of the atmospheric boundary layer; sensitivity to surface evaporation. *Boundary-Layer Meteorol.* <https://doi.org/10.1007/BF00122760>

Tustison, B., Harris, D., Foufoula-Georgiou, E., 2001. Scale issues in verification of precipitation forecasts. *J. Geophys. Res. Atmos.* 106, 11775–11784. <https://doi.org/10.1029/2001JD900066>

Tymvios, F., Charalambous, D., Michaelides, S., Lelieveld, J., 2018. Intercomparison of boundary layer parameterizations for summer conditions in the eastern Mediterranean island of Cyprus using the WRF - ARW model. *Atmos. Res.* <https://doi.org/10.1016/j.atmosres.2017.09.011>

Tzabiras, J., Loukas, A., Vasiliades, L., 2016. A hybrid downscaling approach for the estimation of climate change effects on droughts using a geo-information tool. Case study: Thessaly, Central Greece. *Open Geosci.* <https://doi.org/10.1515/geo-2016-0069>

Wałaszek, K., Kryza, M., Szymanowski, M., Werner, M., Ojrzyńska, H., 2017. Sensitivity Study of Cloud Cover and Ozone Modeling to Microphysics Parameterization. *Pure Appl. Geophys.* 174, 491–510. <https://doi.org/10.1007/s00024-015-1227-2>

Wang, W., Bruyere, C., Duda, M.G., Dudhia, J., Gill, D.O., Kavulich, M., Keene, K., Lin, H.-C., Michalakes, J., Rizvi, S., Zhang, X., 2014. ARW Version 3 modeling system users's guide, NCAR-MMM. ed.

Webb, E.K., 1970. Profile relationships: The log-linear range, and extension to strong stability. Q. J. R. Meteorol. Soc. <https://doi.org/10.1002/qj.49709640708>

Wei-Kuo Tao, Simpson, J., McCumber, M., 1989. An ice-water saturation adjustment. Mon. Weather Rev. 117, 231–235. [https://doi.org/10.1175/1520-0493\(1989\)117<0231:aiwsa>2.0.co;2](https://doi.org/10.1175/1520-0493(1989)117<0231:aiwsa>2.0.co;2)

Weisman, M.L., Davis, C., Wang, W., Manning, K.W., Klemp, J.B., 2008. Experiences with 0-36-h explicit convective forecasts with the WRF-ARW model. Weather Forecast. 23, 407–437. <https://doi.org/10.1175/2007WAF2007005.1>

Weniger, M., Friederichs, P., 2016. Using the SAL Technique for Spatial Verification of Cloud Processes: A Sensitivity Analysis. J. Appl. Meteorol. Climatol. 55, 2091–2108. <https://doi.org/10.1175/JAMC-D-15-0311.1>

Weniger, M., Kapp, F., Friederichs, P., 2017. Spatial verification using wavelet transforms: a review. Q. J. R. Meteorol. Soc. 143, 120–136. <https://doi.org/10.1002/qj.2881>

Wernli, H., Hofmann, C., Zimmer, M., 2009. Spatial forecast verification methods intercomparison project: Application of the SAL technique. Weather Forecast. 24, 1472–1484. <https://doi.org/10.1175/2009WAF2222271.1>

Wernli, H., Paulat, M., Hagen, M., Frei, C., 2008. SAL - A novel quality measure for the verification of quantitative precipitation forecasts. Mon. Weather Rev. 136, 4470–4487. <https://doi.org/10.1175/2008MWR2415.1>

Wicker, L.J., Skamarock, W.C., 2002. Time-splitting methods for elastic models using forward time schemes. Mon. Weather Rev. [https://doi.org/10.1175/1520-0493\(2002\)130<2088:TSMFEM>2.0.CO;2](https://doi.org/10.1175/1520-0493(2002)130<2088:TSMFEM>2.0.CO;2)

Wilks, D.S., 1995. Statistical Methods in the Atmospheric Sciences: An Introduction. Academic Press.

Yano, J.I.I., Ziemian'ski, Mi.Z., Cullen, Mi., Termonia, Pi., Onvlee, J., Bengtsson, L.,

- Carrassi, A., Davy, R., Deluca, A., Gray, S.L., Homar, V., Köhler, M.I., Krichak, S., Michaelides, S., Phillips, V.T.J., Soares, P.M.M., Wyszogrodzki, A.A., 2018. Scientific challenges of convective-scale numerical weather prediction. Bull. Am. Meteorol. Soc. <https://doi.org/10.1175/BAMS-D-17-0125.1>
- Yarnal, B., 1993. Synoptic climatology in environmental analysis. Belhaven Press, London.
- Zacharov, P., Řezáčová, D., Brožková, R., 2019. The verification of the QPF produced by ALADIN-CZ model. Meteorol. Zprávy 72, 140151.
- Zhang, D., Anthes, R.A., 1982. A High-Resolution Model of the Planetary Boundary Layer—Sensitivity Tests and Comparisons with SESAME-79 Data. J. Appl. Meteorol. 21, 1594–1609. [https://doi.org/10.1175/1520-0450\(1982\)021<1594:AHRMOT>2.0.CO;2](https://doi.org/10.1175/1520-0450(1982)021<1594:AHRMOT>2.0.CO;2)
- Zilitinkevich, S.S., 1995. Non-local turbulent transport: pollution dispersion aspects of coherent structure of convective flows, in: Air Pollution III — Volume I. Air Pollution Theory and Simulation, Eds. H. Power, N. Moussiopoulos and C.A. Brebbia. Computational Mechanics Publications, Southampton Boston, 53–60.
- Zinner, T., Mannstein, H., Tafferner, A., 2008. Cb-TRAM: Tracking and monitoring severe convection from onset over rapid development to mature phase using multi-channel Meteosat-8 SEVIRI data. Meteorol. Atmos. Phys. 101, 191–210. <https://doi.org/10.1007/s00703-008-0290-y>